

**Reaction monitoring using SABRE-
hyperpolarised benchtop (1 T) NMR spectroscopy**

Olga Semenova

PhD

University of York

Chemistry

June 2019

Abstract

This thesis develops novel methods for reaction monitoring using a low field (1 T, 43 MHz) benchtop NMR spectrometer combined with hyperpolarisation using the signal amplification by reversible exchange (SABRE) technique. Industry-friendly benchtop NMR spectrometers suffer from insensitivity, which is overcome here by hyperpolarisation. This work is focused on N-heterocyclic primary amines and amides as the target SABRE substrates. The optimisation of substrate concentration and polarisation transfer field was performed for individual compounds and their mixtures. Reaction monitoring studies were completed on an amide formation reaction, specifically conversion of 4-aminopyridine (**4-AP**) with benzoic anhydride to form N-(4-aminopyridyl)benzamide (**4-PBA**), and the reactivity of the SABRE catalyst itself. The transformation of the pre-catalyst $[\text{Ir}(\text{Cl})(\text{COD})(\text{IMes})]$ with the substrates **4-AP** and **4-MP** under hydrogen to form $[\text{Ir}(\text{H})_2(\text{IMes})(\text{substrate})_3]\text{Cl}$ was investigated. In addition, hydrogen isotope exchange (HIE) on the substrate in the presence of the SABRE complexes was explored in methanol- d_4 , where the source of the deuterium was the solvent. A new method was developed to monitor this reactivity using the lifetime of the SABRE-hyperpolarised ^1H NMR response. For this purpose, a single-shot hyperpolarisation lifetime ($\text{hyper}T_1$) measurement based on variable flip angles was developed that takes just five times the T_1 time constant, typically tens of seconds, to complete with high SNR. This method was implemented with both high-field (9.4 T, 400 MHz) and low-field (1 T, 43 MHz) ^1H NMR detection and comparable results were obtained using both instruments. In addition, the low sensitivity of the benchtop (1 T) NMR enabled the use of a *protio* solvent, which allowed for the differentiation between the effects of the catalyst formation and substrate deuteration. Calibration SABRE lifetime measurements fitted well to an analytical model of the kinetics of the SABRE process proposed in the literature. However, the quantification of the reaction monitoring data using this calibration revealed limitations of this simplified kinetic model.

Table of contents

Abstract	3
Table of contents.....	5
Table of figures.....	10
Table of tables	25
Accompanying Material.....	31
Acknowledgements.....	35
Declaration	37
Chapter 1: Introduction.....	39
Chapter 2: Theory	47
2.1 Principles of NMR	47
2.2 Low-field benchtop NMR spectroscopy.....	51
2.3 Hyperpolarisation in NMR.....	53
2.3.1 Para-hydrogen Induced Polarisation (PHIP)	54
2.3.1.1 Para-hydrogen	54
2.3.1.2 Production of para-hydrogen	56
2.3.1.3 Principles of Para-hydrogen Induced Polarisation (PHIP) ..	57
2.3.1.4 PASADENA.....	58
2.3.1.5 ALTADENA.....	59
2.3.2 SABRE and SABRE-Relay	61
2.3.2.1 Optimisation of SABRE conditions	62
2.3.2.1.1 Role of the SABRE catalyst	62
Chapter 3: Hyperpolarisation of N-heterocyclic amines	69
3.1 Introduction.....	69
3.2 Background.....	69
3.3 SABRE catalyst activation	71

3.4	Hyperpolarisation of 4-AP and 4-PBA by SABRE	73
3.4.1	Effect of the polarisation transfer field.....	76
3.4.1.1	Introduction	76
3.4.1.2	Results	77
3.4.2	Effect of substrate concentration on SABRE enhancement ...	81
3.4.2.1	Introduction	81
3.4.2.2	Results	84
3.5	Detection with SABRE of the compounds in mixtures	86
3.5.1	Reproducibility study.....	90
3.5.2	SABRE signal dependence on concentration in mixture	94
3.5.3	SABRE signal dependence on PTF in mixture	96
3.5.4	Polarisation of mixtures at 1 T.....	99
3.6	Conclusions.....	101
Chapter 4: Reaction monitoring with SABRE-hyperpolarised NMR		103
4.1	Introduction	103
4.2	Background	103
4.3	Choice of model reaction.....	104
4.4	Mixture analysis.....	107
4.5	Reaction monitoring in standard conditions.....	110
4.6	Reaction monitoring in SABRE conditions	112
4.7	Conclusions and future work.....	115
Chapter 5: Relaxation times of N-heterocyclic amines		119
5.1	Introduction	119
5.2	Background	119
5.2.1	Methods for measuring T_1	122
5.3	Thermal relaxation times of N-heterocyclic amines	125

5.3.1	Effect of air on relaxation times	126
5.3.2	Role of solvent on thermal T_1 values and SABRE signal	127
5.3.3	Effect of the SABRE catalyst on relaxation times	130
5.3.3.1	Effect of unactivated catalyst on relaxation	130
5.3.3.2	Effect of active catalyst on relaxation.....	132
5.3.3.3	Measurement of T_1 values in the absence of fast exchange	135
5.4	Single-shot hyperpolarised relaxation time measurements	137
5.4.1	Introduction	137
5.4.2	Constant flip angle sequence	141
5.4.3	Variable flip angle sequence	145
5.4.4	Sensitivity of single-shot sequences to the pulse calibration	152
5.4.5	Single-shot measurements with variable delays.....	156
5.5	Effect of the chemical change in the SABRE system on T_1	159
5.6	Measurement of enhancement factors and hyperpolarisation relaxation times for variety of amines	161
5.7	Conclusions and future work	166
Chapter 6: Hydrogen isotope exchange (HIE) in SABRE systems.....		169
6.1	Introduction.....	169
6.2	Background.....	169
6.3	Observations of HIE in SABRE systems	173
6.4	Investigation of the active catalyst for HIE.....	179
6.4.1	Lineshape analysis	180
6.4.2	Substrate and hydride SABRE signal.....	181
6.4.3	EXSY measurements.....	184
6.4.4	Conclusions	184

6.5	Monitoring the HIE reaction during catalyst activation	185
6.5.1	Investigation of the deuterated species kinetics	187
6.6	Investigation of kinetic intermediates	192
6.7	Conclusions and future work.....	196
Chapter 7: Reaction monitoring using SABRE-enhanced benchtop (1 T) NMR spectroscopy		
7.1	Introduction	199
7.2	Results.....	200
7.2.1.1	Reaction monitoring with SABRE signal intensity	202
7.2.1.1.1	HIE equilibrium effect on <i>ortho</i> position in 4-AP	204
7.2.1.2	Reaction monitoring using SABRE hyperpolarisation lifetimes	206
7.2.1.3	Calibration of SABRE hyperpolarisation lifetimes.....	212
7.2.1.3.1	Calibration model	212
7.2.1.3.2	Results	214
7.3	Conclusions.....	220
Chapter 8: Conclusions and future work.....		
8.1	Conclusions.....	223
8.2	Future work	230
Chapter 9: Experimental.....		
9.1	Sample preparation	235
9.2	NMR data acquisition	235
9.3	Measurement of hyperpolarised signals	236
9.4	Calculation of enhancement factors and polarisation levels	237
9.5	Automated flow system for hyperpolarisation (Chapter 3).....	237
9.5.1.1	Reproducibility study using flow system in a mixture	240

9.5.1.2	PTF for individual compounds and mixtures.....	240
9.6	Screening for the model reaction in the flask (Chapter 4)	241
9.6.1	HPLC-MS-UV instrument	241
9.7	Reaction monitoring of amide formation with standard and SABRE- enhanced ¹ H NMR (Chapter 4)	241
9.7.1	Reaction monitoring in the absence of the SABRE catalyst..	241
9.7.2	Reaction monitoring in SABRE conditions.....	242
9.8	Hyperpolarised single-shot T ₁ measurement (Chapter 5).....	242
9.9	SABRE catalyst activation and HIE monitoring using standard ¹ H NMR (Chapter 6)	243
9.9.1	Quantification of the level of deuterium incorporation	244
9.10	NMR Exchange Spectroscopy (EXSY)	244
9.11	Mean and error calculation.....	247
9.11.1	Error propagation.....	248
9.12	Characterisation	248
Abbreviations		257
Appendix.....		259
Additional information		259
References		271

Table of figures

Figure 2.1 Spin states energy splitting in magnetic field.	47
Figure 2.2 a) Scheme of nuclear spin state populations for two spin $\frac{1}{2}$ nuclei. b) Schematic representation of the NMR spectrum showing two doublets.....	48
Figure 2.3 a) Vector model illustrating the creation of transverse magnetisation M_{xy} through rotation by a RF pulse. b) Evolution of the NMR signal with the length of the applied pulse.	50
Figure 2.4 a) Schematic design of the static magnetic field based on permanent magnets. b) Halbach array. ¹⁶	51
Figure 2.5 ^1H NMR spectra of 25 mM 4-methylpyridine and 5 mM $[\text{Ir}(\text{COD})(\text{IMes})(4\text{-methylpyridine})]\text{Cl}$ in MeOD acquired at (a) 9.4 T and (b) 1 T.	52
Figure 2.6 Schematic representation of hydrogen nuclear spin states, which include three <i>ortho</i> -hydrogen states and one <i>para</i> -hydrogen state. The conversion between the two hydrogen forms is symmetry forbidden.	55
Figure 2.7 <i>Para</i> -hydrogen enrichment dependence on interconversion temperature in presence of a paramagnetic catalyst.	57
Figure 2.8 a) Scheme of spin energy state population in PASADENA for two spin $\frac{1}{2}$ nuclei. b) Schematic representation of the NMR spectrum showing two antiphase doublets as a result of PASADENA.	58
Figure 2.9 a) Scheme of spin energy states population in ALTADENA for two spin- $\frac{1}{2}$ nuclei. b) Schematic representation of the NMR spectrum showing two singlets, antiphase relatively to each other, as a result of ALTADENA.	59
Figure 2.10 Under <i>para</i> -hydrogen, the indicated substrate exchange processes enables hyperpolarisation transfer so that free substrate NMR resonances can be detected more readily. This transfer occurs in low magnetic field through the complex's scalar coupling network and due to reversibility operates continuously when <i>p</i> - H_2 is present.....	61

Figure 2.11 Activation of Crabtree's complex to the active SABRE catalyst under addition of <i>para</i> -hydrogen and pyridine as a substrate (py = pyridine).	63
Figure 2.12 Plot of the relative absolute signal strengths for the three pyridine proton sites (relative to signals for free pyridine at equilibrium). Results represent an average of five measurements, each recorded immediately after shaking the NMR tube in the Earth's field (50 μ T). These samples in methanol- <i>d</i> ₄ contained [Ir(COD)(py) ₂]BF ₄ , one equivalent of PR ₃ and of pyridine. Reprinted with permission from K. D. Atkinson, M. J. Cowley, P. I. P. Elliott, S. B. Duckett, G. G. R. Green, J. López-Serrano and A. C. Whitwood, <i>J. Am. Chem. Soc.</i> , 2009, 131 , 13362–13368. Copyright (2018) American Chemical Society.	64
Figure 2.13 Ligands used for complex synthesis, compound number, abbreviation, Tolman Electronic Parameter (cm ⁻¹), buried volume (%). B. J. A. van Weerdenburg, S. Glöggler, N. Eshuis, A. H. J. (ton) Engwerda, J. M. M. Smits, R. de Gelder, S. Appelt, S. S. Wymenga, M. Tessari, M. C. Feiters, B. Blümich and F. P. J. T. Rutjes, <i>Chem. Commun.</i> 2013, 49 , 7388 - Published by The Royal Society of Chemistry.	65
Figure 2.14 SABRE catalysts: 1) Crabtree's pre-catalyst; 2) IMes catalyst; water-soluble IDEG pre-catalyst; deuterated IMes- <i>d</i> ₂₂ pre-catalyst; 3) water-soluble SABRE pre-catalyst; 4) neutral SABRE pre-catalyst; 5) SABRE activated catalyst with phosphine and IMes carbene.....	66
Figure 3.1 Chemical changes occurring during SABRE pre-catalyst activation. Upon addition of substrate, [IrCl(COD)(IMes)] (1) transforms into [Ir(COD)(IMes)(substrate)]Cl (2). 2 then oxidatively adds H ₂ to form octahedral [Ir(H) ₂ (COD)(IMes) (substrate)]Cl (3), which is not stable at room temperature. Further addition of H ₂ causes COD hydrogenation and two further substrate molecules to bind, yielding the SABRE active complex [Ir(H) ₂ (IMes)(substrate) ₃]Cl (4).	72
Figure 3.2 Structures of 4-aminopyridine (4-AP) and N-(4-pyridyl)benzamide (4-PBA) with colour-labelled protons.....	73

Figure 3.3 Single scan ^1H NMR spectra of 4-AP under thermal (256-fold vertical expansion) and SABRE conditions. The SABRE ^1H NMR spectrum of 4-AP at a 35 mM excess relative to the activated SABRE catalyst was acquired with PTF = 65 G in methanol- d_4 . All spectra were acquired at 9.4 T (400 MHz).	74
Figure 3.4 Single scan ^1H NMR spectra of 4-PBA under thermal (16-fold vertical expansion) and SABRE conditions. The SABRE ^1H NMR spectrum of 4-PBA at a 35 mM excess relative to the activated SABRE catalyst was acquired with PTF = 65 G in methanol- d_4 . All spectra were acquired at 9.4 T (400 MHz).	75
Figure 3.5 Dependence of SABRE enhancement factor on polarisation transfer field (PTF) for 50 mM of 4-AP (10 equivalents relative to catalyst 1) in methanol- d_4 . 7% error bars represent the standard deviation determined in section 3.5.1.....	79
Figure 3.6 Dependence of SABRE enhancement factor on the polarisation transfer field (PTF) for 50 mM (10 equivalents relative to catalyst 1) of N-(4-pyridyl)benzamide. 7% error bars represent the standard deviation determined in section 3.5.1.....	80
Figure 3.7 Dissociative substrate exchange pathway.	82
Figure 3.8 Dependence of the absolute SABRE enhancement factor on the substrate to pre-catalyst ratio for 4-PBA acquired at PTF = 65 G in methanol- d_4 at 9.4 T. 7% error bars represent the standard deviation determined in section 3.5.1.....	85
Figure 3.9 Comparison of 1 scan thermal (64-fold vertical expansion) and SABRE ^1H NMR spectra of a mixture of 4-AP (5 eq rel. to 1) and 4-PBA (5 eq rel. to 1) in methanol- d_4 in the presence of the active catalysts based on $[\text{Ir}(\text{H})_2(\text{IMes})(\mathbf{4-AP})_x(\mathbf{4-PBA})_{3-x}]\text{Cl}$ where $x = 0, 1, 2$ and 3. The overall SABRE polarisation level for this mixture was estimated as 0.53%, compared to 0.0032% for the Boltzmann derived polarisation.	88
Figure 3.10 a) Combinations of SABRE complexes which can form in the presence of two substrates in solution. The SABRE ^1H NMR spectra of the	

hydride region of (b) pure **4-PBA**, (c) pure **4-AP** and (d) the 5eq:5 eq mixture of **4-AP** and **4-PBA**. 89

Figure 3.11 Reproducibility of the enhancement values for **4-AP** *ortho* (a) and *meta* (b) protons and **4-PBA** *ortho* (c) and *meta* (d) protons in a 5 eq: 5 eq mixture acquired with PTF = 65 G. Reproducibility of the ratios of the enhancements (e) of the *ortho* and *meta* protons within **4-AP**, and (f) of the *ortho* protons of **4-AP** and **4-PBA**, respectively. The mean enhancement value (solid line) and one standard deviation from mean (dashed lines) and percentage standard deviation are presented in each graph. Each graph y-axis is scaled to $\pm 15\%$ from the mean. 92

Figure 3.12 Dependence on concentration of the enhancement factor of the **4-PBA** *ortho* proton in pure solution (grey line, square markers) and in a mixture with **4-AP** (red line, circle markers), where the concentration of **4-AP** was varied in such way that the total substrate concentration in the solution was 50 mM. The error bars of 7% represent the standard deviation determined in section 3.5.1. 94

Figure 3.13 a) SABRE signal integral of the *ortho* proton of **4-AP** (grey squares) and **4-PBA** (red circles) as a function of concentration in a mixture. The concentrations of **4-AP** and **4-PBA** were varied in such way that the total substrate concentration in the solution was 50 mM, which is 10 eq relative to the 5 mM SABRE pre-catalyst. b) Ratio of the SABRE signal integrals of the **4-AP** and **4-PBA** *ortho* protons as a function of their concentration ratios. The error bars represent three times the standard deviation for the SABRE signal integral as determined in the reproducibility study discussed above. The error bars represent a standard deviation of 7% in (a), determined in section 3.5.1, and of 10% in (b), calculated using error propagation. 95

Figure 3.14 Enhancement factor of (a) **4-PBA** and (b) **4-AP** *ortho* protons dependence on PTF at the concentrations of 12.5 mM, 25 mM and 37.5 mM mixture (50 mM total) with the other substrate which is **4-PBA** or **4-AP** respectively and of 50 mM individual substrate solution. The error bars of 7% represent the standard deviation determined in section 3.5.1. 97

Figure 3.15 Comparison of 1 scan thermal (300-fold scaled) and SABRE ¹ H NMR spectra of 4-AP (5 eq) and 4-PBA (5 eq) mixture in methanol- <i>d</i> ₄	100
Figure 4.1 General scheme of an amide formation reactions of substituted aminopyridines with benzoic anhydride and ethyl benzoate screened below.	105
Figure 4.2 Model reaction of amide formation with the mechanism ¹³⁰ for reaction monitoring by SABRE NMR.	107
Figure 4.3 Structure of proposed pyridinium carboxylate salt formed by BAH and 4-AP or 4-PBA	108
Figure 4.4 ¹ H NMR chemical shift changes in a mixture of (a) 4-AP and (b) 4-PBA with BA in DCM compared to the ¹ H NMR spectra of the pure compounds. (*) Peak is assigned to either 4-PBA pyridinium proton or amide proton.	109
Figure 4.5 Standard reaction monitoring of amide formation by ¹ H NMR (400 MHz) in DCM. ¹ H NMR spectra of 4-AP before the addition of BAH (bottom trace) and after 140.6 min of the reaction proceeding (top).	110
Figure 4.6 Kinetics of the amide formation reaction assessed from the ¹ H NMR integrals of peaks at 8.51 ppm (1), 8.08 ppm (2), 7.90 ppm (3), 7.43 ppm (4) and 6.52 ppm (5) using Bruker's Dynamics Center software.	112
Figure 4.7 Thermal spectra collected during reaction monitoring of amide formation by NMR (400 MHz) in presence of the SABRE catalyst [Ir(H) ₂ (IMes)(4-AP or 4-PBA) ₃]Cl in DCM- <i>d</i> ₂	113
Figure 4.8 ¹ H NMR (400 MHz) SABRE enhanced spectra of (a) 4-AP in presence of activated complex, Ir(H) ₂ (IMes)(4-AP) ₃]Cl, before addition of BAH , (b, c) the reaction mixture collected during reaction monitoring of amide formation in the presence of the SABRE catalyst [Ir(H) ₂ (IMes)(4-AP or 4-PBA) ₃]Cl, (d) 4-PBA in presence of activated SABRE complex, [Ir(H) ₂ (IMes)(4-PBA) ₃]Cl, for comparison.	114

Figure 5.1 Inversion recovery pulse sequence for T_1 measurement.....	123
Figure 5.2 Pulse sequence for saturation recovery relaxation time measurement.	124
Figure 5.3 Evolution of the of ^1H NMR signal intensities in the (a) inversion recovery and (b) saturation recovery measurements for free (8.47 ppm) and bound (8.26 ppm) <i>ortho</i> -protons of N-(4-pyridyl)benzamide (2-fold excess) in presence of 5 mM $[\text{Ir}(\text{N}-(4\text{-pyridyl})\text{benzamide})_3(\text{IMes})(\text{H}_2)]$ in methanol- d_4 at 253 K measured at 400 MHz. The resultant relaxation curve for free (8.47 ppm) <i>ortho</i> resonance which yields a T_1 of 2.59 ± 0.01 s from both (c) inversion and (d) saturation recovery measurements when fitted to Equation (5.2) and (5.3) respectively.	124
Figure 5.4 Change in 4-AP T_1 values in presence of unactivated catalyst $[\text{Ir}(\text{COD})(\text{IMes})(\mathbf{4-AP})]\text{Cl}$ (5 mM) with increase of 4-AP concentration. Error bars represent the fitting errors.....	131
Figure 5.5 Annotation for substrate protons bound to the catalyst <i>trans</i> to hydride ligands (sub') and <i>trans</i> to IMes carbene (sub'') and in free solution (sub).	133
Figure 5.6 Constant flip angle sequence proposed by Kaptein to determined T_1	138
Figure 5.7 Schematic representation of a single-shot hyperpolarised T_1 measurement using a small flip angle NMR pulse sequence.....	139
Figure 5.8 Thermal polarisation increase during constant 5 degree flip angle sequence for hyper T_1 measurement for the 4-PBA free <i>ortho</i> peak at 8.46 ppm.....	142
Figure 5.9 Experimental and corrected absolute signal intensities for the constant flip angle hyper T_1 measurement of 4-PBA free <i>ortho</i> proton.....	144
Figure 5.10 Evolution of the hyperpolarised and thermal magnetisation in a variable flip angle single-shot measurement for the free 4-methylpyridine (4-MP) <i>ortho</i> proton (8.39 ppm) in the presence of $[\text{Ir}(\text{H})_2(\text{IMes})(\mathbf{4-MP})_3]\text{Cl}$	

in methanol- d_4 at 298 K. The decay of the hyperpolarised signal with time is presented in red circles. The corresponding thermal polarisation build-up curve is shown in grey squares. The corrected hyperpolarisation decay curve (the difference between the hyperpolarised and thermal reference measurements) is presented in blue triangles. Inset is an expanded region of the graph illustrating the thermal polarisation increase with time in the reference scan. 149

Figure 5.11 Change of phase during hyperpolarised relaxation times measurement with variable flip angle sequence observed for the *meta* proton of N-(4-pyridyl)benzamide (**4-PBA**). 150

Figure 5.12 a) First NMR spectrum from hyperpolarised variable (vfa, red) and constant (cfa, black) flip angle measurements for free 4-methylpyridine (**4-MP**) in the presence of $[\text{Ir}(\text{H})_2(\text{IMes})(\text{4-MP})_3]\text{Cl}$ in methanol- d_4 at 298 K. b) Logarithmic relaxation plots for the resonance at 8.39 ppm (*ortho* protons of free **4-MP**) of these samples (variable (red) and constant (black) flip angle results). 151

Figure 5.13 In both graphs simulated magnetisation percentage sampled when the accurate variable flip angles (vfa) are applied is shown in blue circles. Orange and green circles represent magnetisation (%) obtained when the variable flip angles a) decreased 8 and 16%, b) increased 8 and 16% from the accurate ones. 153

Figure 5.14 Chemical shift annotation for 3-amino-5-methylpyridine in methanol- d_4 at 400 MHz. 153

Figure 5.15 Hyperpolarisation relaxation plots as a function of pulse length for the free 3-amino-5-methylpyridine proton H_a at 7.78 ppm that were acquired with variable (vfa) and constant flip angle sequences (cfa). The 90 degree pulse lengths were assumed to be 12.5 μs , 11.5 μs and 10.5 μs . The corresponding theoretical fit is presented via the solid lines. The sample included 3-amino-5-methylpyridine (2-fold excess) with 5 mM activated SABRE catalyst in methanol- d_4 under 4 bar $p\text{-H}_2$ 154

Figure 5.16 Simulated signal decay using equation $y = \exp - xT1$ with relaxation times of 0.5 s (grey squares) and 10 s (red circles), (a, b) when time points are spaced evenly with (a) short (0.2 s) and (b) long (4 s) time delays, (c) when time points are spaced with variable (0, 0.2, 0.4, 0.6, 0.9, 1.1, 1.5, 2, 3, 5, 10, 20, 30, 40, 50 s) time delays. 157

Figure 5.17 a) The thermal relaxation time graph of the *ortho* peak of **4-PBA** (5 eq) measured with inversion recovery (IR) sequence acquired over 12.3 hrs while deuteration was occurring at the same time in presence of $[\text{Ir}(\text{H})_2(\text{IMes})(\text{4-PBA})_3]\text{Cl}$ in methanol- d_4 at 298 K. The bottom time-axis in seconds presents the time delays implemented in the inversion recovery experiment, the upper time-axis in hours gives the reaction time during the experiment. The upper axis scales non-linearly with the bottom axis, e.g. 3 hrs in the upper trace is associated with 1.5 s in the bottom trace. The fit to mono-exponential is shown in blue line. b) ^1H NMR spectra acquired before and after IR T_1 measurement with 16 hr 26 min time difference in between the spectra. 160

Figure 5.18 Hyperpolarised relaxation times and enhancement factors (in bold) for free protons of different amines (5 eq, IMes, MeOD) at 3 bar *para*- H_2 at 65 G, 10 sec shaking acquired with variable and constant flip angle pulse sequence at 298 K. Error bars represent standard errors calculated from 3 repeated measurements, except 3-amino-5-methylpyridine, which was repeated 4 times. 162

Figure 5.19 Hyperpolarised relaxation times and enhancement factors (in bold) for free protons of different amines (5 eq, IMes, MeOD) at 3 bar *p*- H_2 at 65 G, 10 sec shaking acquired with variable and constant flip angle pulse sequence at 298 K (continuation). Error bars represent standard errors calculated from 3 repeated measurements. 163

Figure 5.20 The resonance forms for 4-amino-3-methylpyridine (left) and 3-amino-5-methylpyridine (right) showing the mesomeric electron donating effect. 165

Figure 6.1 Scheme of deuteration reaction of organic molecules with different functionality promoted by Crabtree's catalyst. ¹⁶⁶	170
Figure 6.2 Simplified mechanism of the exchange process in the presence of deuterium oxide. Reprinted from Tetrahedron, 57, G. J. Ellames, J. S. Gibson, J. M. Herbert and A. H. McNeill, The scope and limitations of deuteration mediated by Crabtree's catalyst, 2001, 9487–9497, Copyright (2018), with permission from Elsevier.	170
Figure 6.3 Postulated process for incorporation of deuterium at C6 of pyridines. Reprinted from Tetrahedron, 57, G. J. Ellames, J. S. Gibson, J. M. Herbert and A. H. McNeill, The scope and limitations of deuteration mediated by Crabtree's catalyst, 2001, 9487–9497, Copyright (2018), with permission from Elsevier.....	171
Figure 6.4 The complexes containing pyridylidene ligands. Tp^{Me_2} = hydrotris(3,5-dimethylpyrazolyl)borate.....	172
Figure 6.5 Evolution of the hydride ^1H NMR peaks for the $[\text{Ir}]-(\text{H})_2$ and $[\text{Ir}]-(\text{H})(\text{D})$ catalyst forms during the activation of the SABRE catalyst and substrate deuteration for the case where the substrate is 4-PBA	175
Figure 6.6 Change in <i>meta</i> peak appearance with the deuteration of the <i>ortho</i> position as a function of reaction time. No significant change in splitting was detected for methanol- d_4 residual peak that suggests that the reactivity is the cause of the substrate's lineshape change.....	177
Figure 6.7 Deuteration of 4-AP in the <i>ortho</i> positions.....	177
Figure 6.8 ^{13}C NMR SABRE signals demonstrating the deuteration of 4-AP (10 mM in the activated sample) in presence of 5 mM activated catalyst $[\text{Ir}(\text{IMes})(\text{H})_2(\mathbf{4-AP})_3]\text{Cl}$ (4a) in MeOD under 4 bar $p\text{-H}_2$. The <i>ortho</i> carbon resonance of free and bound 4-AP shows splitting from deuterium ($J_{\text{CD}} = 26.6$ Hz) in these ^{13}C and $^{13}\text{C}\{^1\text{H}\}$ spectra. This splitting is removed on ^2H decoupling which confirms its origin from deuteration of the <i>ortho</i> position. The <i>meta</i> carbon signal is weaker and produces an antiphase signal which disappears in the $^{13}\text{C}\{^1\text{H}\}$ SABRE NMR spectrum.	178

Figure 6.9 Chemical changes occurring during SABRE pre-catalyst activation.....	180
Figure 6.10 <i>Meta</i> proton resonance of 4-AP bound to 2 at 6.35 ppm, 3 at 6.28 ppm and 4 at 6.17 ppm (equatorial, bound <i>trans</i> to hydride) and 6.06 ppm (axial, bound <i>trans</i> to carbene) as a function of reaction time. Significant changes in peak lineshape demonstrate slow substrate exchange in 2 and 3 and fast exchange in 4	181
Figure 6.11 Increase in 4-AP SABRE signal intensity parallels the formation of 4a , which is confirmed by observation of the hydride region of these SABRE NMR spectra.....	182
Figure 6.12 Hyperpolarised hydride resonances in 3a and 4a detected with a 45 degree pulse: a) the first PHIP spectrum acquired after addition of <i>p</i> -H ₂ to 2a ; b) and c) subsequent PHIP spectra with fresh <i>p</i> -H ₂ do not show further hydride hyperpolarisation; d) PHIP NMR spectrum acquired after addition of fresh 2a and <i>p</i> -H ₂ , e) subsequent PHIP spectrum acquired with fresh <i>p</i> -H ₂ . Thermally polarised NMR spectra acquired after the corresponding PHIP spectra are presented for all sets except for (d) where two subsequent PHIP spectra were acquired in order to quickly detect 3a signals.....	183
Figure 6.13 In red: Catalyst [Ir(H) ₂ (IMes)(substrate) ₃]Cl 4 proportion as formed with 4-AP (7.32 ppm) (a), 4-MP (6.68 ppm) (b), 4-PBA (6.74 ppm) (c), pyridine (6.65 ppm) (d) where their initial substrate concentration was 25 mM in methanol- <i>d</i> ₄ under hydrogen gas (4 bar) and the employed carbene resonance is given in brackets. In grey: corresponding deuteration level of the substrates' <i>ortho</i> position. The deuteration curve for 4-MP shows an initial fall that is not real, but instead reflects a decrease in the free <i>meta</i> peak (7.30 ppm) integral due to partial overlap with initial catalysts' resonances (7.24 ppm and 7.35 ppm), a change in line-broadening also contributes to this.	186
Figure 6.14 In red: Extent of [Ir(H) ₂ (IMes)(substrate) ₃]Cl 4 formation for 4-MP (6.68 ppm) (a), 4-PBA (6.74 ppm) (b) and pyridine (6.65 ppm) (c), when	

their concentration is 25 mM in the starting methanol- <i>d</i> ₄ solution under hydrogen gas (4 bar) and the employed carbene resonance is given in brackets. In grey: deuteration level for the substrate's <i>ortho</i> position. Changes shown over an 80 min timescale.....	187
Figure 6.15 a) Scheme of expected evolution of the iridium deuterated species. b) Scheme of the HIE processes occurring in the SABRE system.	188
Figure 6.16 Increase in HD gas ¹ H NMR peak integral at 4.43 ppm with reaction time for a) 4-MP, b) 4-PBA, c) pyridine.....	188
Figure 6.17 Change in [Ir]-(H) ₂ , [Ir]-(H)(D) and [Ir]-(D) ₂ species relative concentration (%) with the reaction time. Zoom up to 60 min for a) pyridine, b) 4-PBA , c) 4-MP and up to 300 min for d) 4-AP	190
Figure 6.18 Change in [Ir]-(H) ₂ , [Ir]-(H)(D) and [Ir]-(D) ₂ species relative concentration (%) with the reaction time for a) pyridine, b) 4-PBA , c) 4-MP and d) 4-AP	191
Figure 6.19 <i>J</i> couplings obtained by simulation for 4-AP , 4-PBA and pyridine.	193
Figure 6.20 a) Experimental and (b-d) simulated spectra of <i>ortho</i> and <i>meta</i> proton peak lineshape for 4-AP , 4-PBA and pyridine.....	194
Figure 6.21 Simulated change in fractions of <i>protio</i> - and deuterated substrates with time of deuteration reaction using experimental ¹ H NMR data.	195
Figure 7.1 ¹ H NMR spectra acquired using a 43 MHz (1 T) benchtop NMR spectrometer before addition of <i>p</i> -H ₂ (bottom trace) and at 1.5 min after <i>p</i> -H ₂ addition (upper trace) to a sample of 25 mM 4-AP in presence of the SABRE catalyst (5 mM) in methanol- <i>d</i> ₄	200
Figure 7.2 Standard ¹ H NMR spectra (top) compared with SABRE-enhanced ¹ H NMR spectra (bottom) of 4-AP (5 eq, 2-fold-excess, 10 mM) in the presence of [Ir(H) ₂ (IMes)(4-AP) ₃] (4a) (5 mM) in methanol- <i>d</i> ₄ acquired in a	

magnetic field of 9.4 T at 328 min from start of activation (a) and at 1 T at 320 min from start of activation (b). 201

Figure 7.3 (a) Concentration of free **4-AP** as a function of time determined from standard ^1H NMR spectra acquired at 9.4 T in parallel with the SABRE measurements. The time to activation (235 min) was determined from a fit to a mono-exponential decay. Normalised raw SABRE-enhanced ^1H NMR signal intensity of the *ortho* (blue circles) and *meta* (violet triangles) protons of **4-AP** (5.2 eq relatively to **1**) during the activation of 5 mM SABRE complex in methanol- d_4 as measured using detection at (b) 9.4 T and (c) 1 T..... 203

Figure 7.4 Standard ^1H NMR signal integral of the *ortho* (blue circles) and *meta* (violet triangles) signal intensity during the reaction monitoring under (a) *p*- H_2 when the sample was monitored with alternate thermal and hyperpolarised measurements and *para*-hydrogen gas was refreshed for each hyperpolarised scan (b) H_2 , when H_2 was added once in the beginning, and (c) *p*- H_2 , when the catalyst was activated to 37% using shaking under *p*- H_2 and then the sample was monitored without additional *p*- H_2 refreshment. 205

Figure 7.5 (a) **4-AP** concentration assessed by acquisition of non-hyperpolarised ^1H NMR signal intensity of the **4-AP** *meta* proton resonance, acquired as a function of time following the addition of H_2 to the methanol- d_4 solution alongside parallel hyperpolarisation lifetime measurements in (b) at 400 MHz. The *ortho* (blue circles) and *meta* (purple triangles) encode the corresponding hyper T_1 values, (c) portrays the analogous lifetime results in methanol- d_4 at 1 T, while (d) reflect the same data from *protio* methanol at 1 T. The initial concentration of **4-AP** used was 25 mM, giving a net 2-fold excess relative to $[\text{Ir}(\text{H})_2(\text{IMes})(\text{4-AP})_3]\text{Cl}$ (5 mM) once the reaction is complete. Error bars represent the standard errors of the fit for each point. The time for the activation step to go to completion was estimated from an exponential fit of the ^1H NMR data in (a) and is indicated by the vertical dotted line..... 207

Figure 7.6 Change in the relative intensity and line-shape of the *ortho* and *meta* proton resonances of **4-AP** as a function of reaction time in the regime

where the *p*-H₂ was refreshed between each scan. The *ortho* resonance line shape loses some of the second order splitting, which is characteristic of progressive ²H substitution at the second *ortho* position on the ring, but retains the doublet line-shape indicating that the *meta* resonance itself is not undergoing deuteration. The line-shape of the *meta* resonance evolves into a singlet over time which suggests that the *ortho* position has been significantly deuterated. Time zero denotes the time at which the H₂ gas was introduced to the sample.209

Figure 7.7 Hyperpolarisation lifetimes of the *ortho* and *meta* protons of **4-MP** as a function of time during the activation of the SABRE complex at 1 T (a) in methanol-d₄ and (b) in *protio* methanol. Initial concentration of **4-MP** is 25 mM which results in a 2-fold excess to the activated complex [Ir(H)₂(IMes)(**4-MP**)₃]Cl (5 mM). Error bars represent the standard error from the fit of each hyperpolarisation decay curve to mono-exponential.211

Figure 7.8 Change in the relative intensity of the **4-MP** *ortho* and *meta* resonances as a function of reaction time in the regime when the *p*-H₂ was refreshed between each scan acquired at 400 MHz. The initial solution was prepared with 9 eq of **4-MP** relative to **1**. Eleven *p*-H₂ refreshments were done in 89 min. The ¹H NMR spectra presented here were acquired (bottom) before *p*-H₂ addition, (middle) 39 min and (top) 89 min after the first *p*-H₂ addition. No significant change was observed in the line-shapes of the *ortho* and *meta* peaks of **4-MP**, indicating no significant deuteration on this timescale. Time zero denotes the time at which the *p*-H₂ gas was introduced to the sample.211

Figure 7.9 a) Scheme for the exchange of the hyperpolarised substrate (S*) on the SABRE catalyst (C) via the formation of the intermediate 16-electron complex (C₁). b) Scheme illustrating the rates of association (k_s^a) and dissociation (k_s^d) and the relaxation rates for the free (R_s) and bound substrate (R_C), which are considered in the model proposed by Barskiy *et al.*⁴⁶213

Figure 7.10 Hyperpolarisation lifetimes of 4-AP in MeOH at 1 T benchtop NMR (a) at different concentrations (3.5 eq, 5 eq, 10 eq, 20 eq, 50 eq, 106 eq relatively to 1) in presence of 5 mM $[\text{Ir}(\text{IMes})(\text{H})_2(\mathbf{4-AP})_3]\text{Cl}$ and (b) at 10 mM 4-AP in the activated sample at different concentrations of $[\text{Ir}(\text{IMes})(\text{H})_2(\mathbf{4-AP})_3]\text{Cl}$ (0.5 mM, 1 mM, 1.5 mM, 2 mM, 3 mM, 3.5 mM, 4 mM, 4.5 mM, 5 mM).	215
Figure 7.11 The dependence of $R_{1,\text{avg}}$ on the relative concentration of the bound to the free substrate molecules, fitted to Equation 7.10. The concentration of the bound substrate was taken as the double of the catalyst concentration due to the equal probability of both two bound <i>trans</i> to hydrides substrate molecule to exchange with the free substrate. The inserted graph is the zoomed region shown in dashed line.	216
Figure 7.12 (a) The activated catalyst to substrate ratio dependence on reaction time according to the hyper T_1 data recorded at 1 T benchtop NMR spectrometer in <i>protio</i> -methanol in conjunction with Equation 7.11 for the <i>ortho</i> and <i>meta</i> sites (without an outlier data point at 173 min). (b) <i>Ortho</i> proton data from (a) alongside the activated catalyst to substrate ratio as determined from the substrate <i>meta</i> proton and the catalyst carbene signals for a thermal control measurement recorded at 400 MHz NMR for an analogous sample in methanol- d_4 based on the data in Figure 7.5a.....	218
Figure 9.1 1 – Hydrogen generator; 2 – Bruker <i>para</i> -hydrogen generator; 3 – reaction chamber and the coil used to generate the polarisation transfer field; 4 – flow cell for sample monitoring inside the NMR spectrometer.	239
Figure 9.2 1D selective NOESY gradient pulse sequence for EXSY experiment.	245
Figure 9.3 Scheme representing the exchange between substrate species in free solution and bound to the catalyst.	246
Figure A9.4 Polarisation transfer field (PTF) and relative concentrations dependence on enhancement factor of 4-AP <i>ortho</i> proton.	262

Figure A9.5 Polarisation transfer field (PTF) and relative concentrations dependence on enhancement factor of 4-AP <i>meta</i> proton.	262
Figure A9.6 Polarisation transfer field (PTF) and relative concentrations dependence on enhancement factor of 4-PBA <i>ortho</i> proton.	263
Figure A9.7 Polarisation transfer field (PTF) and relative concentrations dependence on enhancement factor of 4-PBA <i>meta</i> proton.....	263
Figure A9.8 Hyperpolarisation lifetime curves for 3,5-diaminopyridine (3,5-DAP) <i>ortho</i> (7.35 ppm) and <i>para</i> (6.47 ppm) protons acquired in presence of [Ir(H) ₂ (IMes)(3,5-DAP) ₃]Cl in methanol- <i>d</i> ₄ on a 1 T NMR spectrometer with constant time delays of a) 1.26 s and b) 7.06 s and c) variable time delays.	265
Figure A9.9 ¹ H NMR signal intensities of the 4-AP <i>meta</i> proton peak of the free substrate in solution and bound to 2a , 3a and 4a as a function of reaction time when <i>para</i> -hydrogen is refreshed between NMR measurements.	266
Figure A9.10 ¹ H NMR signal intensity of the 4-AP <i>meta</i> proton peak of the substrate in free solution and bound to 2a , 3a and 4a as a function of reaction time when <i>para</i> -hydrogen was refreshed between measurements over the first 50 mins of reaction.....	266
Figure A9.11 MS-ESI spectrum for pure solution of 4-AP in methanol- <i>d</i> ₄	267
Figure A9.12 MS-ESI spectrum of 4-AP when its <i>ortho</i> position is deuterated to the level of ~60% (by ¹ H NMR spectroscopy) in presence of [Ir(H) ₂ (IMes)(4-AP) ₃]Cl in methanol- <i>d</i> ₄ under hydrogen gas.....	268
Figure A9.13 The activated catalyst to substrate ratio dependence on reaction time according to the hyperT ₁ data recorded at 1 T benchtop NMR spectrometer in <i>protio</i> -methanol in conjunction with Equation 7.11 in Chapter 7 for the <i>ortho</i> and <i>meta</i> sites.	270

Table of tables

Table 3.1 Maximum enhancements for <i>ortho</i> and <i>meta</i> protons of 4-AP and 4-PBA within all mixtures in the range 0-10 eq. of each substrate and in the range of PTF values from 0.5 – 140 G.	98
Table 4.1 Model reactions for potential investigation under SABRE conditions. The ratio of starting materials used was 1:1, and their concentration was 50 mM, unless otherwise stated.....	105
Table 4.2 (continuation) Model reactions for potential investigation under SABRE conditions. The ratio of starting materials used was 1:1, and their concentration was 50 mM, unless otherwise stated.....	106
Table 5.1 Thermal relaxation times for free N-(4-pyridyl)benzamide (25 mM) protons in methanol- <i>d</i> ₄ under hydrogen atmosphere. Error bars represent fitting errors.....	126
Table 5.2 Thermal relaxation times for free N-(4-pyridyl)benzamide (25 mM) protons in THF- <i>d</i> ₈ under hydrogen atmosphere. Error bars represent fitting errors.	126
Table 5.3 Thermal relaxation times for N-(4-pyridyl)benzamide (50 mM) under air and hydrogen in methanol- <i>d</i> ₄ at 298 K. Error bars represent fitting errors.	127
Table 5.4 <i>T</i> ₁ values for free 3,5-diaminopyridine protons after the activation of 5 mM [Ir(Cl)(COD)(IMes)] with 10 eq 3,5-diaminopyridine in methanol- <i>d</i> ₄ , 50:50 (by volume) mixture of methanol- <i>d</i> ₄ and <i>protio</i> -methanol and dichloromethane- <i>d</i> ₂ at 9.4 T. The quoted errors represent fitting errors.	128
Table 5.5 Enhancement values (per proton) for free 3,5-diaminopyridine protons after the activation of [Ir(Cl)(COD)(IMes)] with 10 eq 3,5-diaminopyridine in methanol- <i>d</i> ₄ , 50:50 (by volume) mixture of methanol- <i>d</i> ₄ and <i>protio</i> -methanol and dichloromethane- <i>d</i> ₂ when a PTF value of 65 G and detection field of 9.4 T.	129

Table 5.6 Relaxation times for free N-(4-pyridyl)benzamide protons and those of free and bound N-(4-pyridyl)benzamide in presence of $[\text{Ir}(\text{H})_2(\text{IMes})(\text{N}-(4\text{-pyridyl})\text{benzamide})_3]\text{Cl}$ (5 mM) in methanol- d_4 solution under a hydrogen atmosphere. Error bars represent fitting errors.	133
Table 5.7 Relaxation times for free 3,5-diaminopyridine protons and those of free and bound 3,5-diaminopyridine in presence of $[\text{Ir}(\text{H})_2(\text{IMes})(3,5\text{-diaminopyridine})_3]\text{Cl}$ (5mM) in methanol- d_4 under hydrogen atmosphere. Error bars represent fitting errors.	133
Table 5.8 Relaxation times for free 4-methylpyridine protons and those of free and bound 4-methylpyridine (10 eq, 7-fold excess) in presence of $[\text{Ir}(\text{H})_2(\text{IMes})(4\text{-methylpyridine})_3]\text{Cl}$ (5mM) in methanol- d_4 under hydrogen atmosphere. Error bars represent fitting errors.	134
Table 5.9 Thermal relaxation times for free N-(4-pyridyl)benzamide (2-fold excess) protons in MeOD in presence of $[\text{Ir}(\text{H})_2(\text{IMes})(\text{N}-(4\text{-pyridyl})\text{benzamide})_3]\text{Cl}$ under 4 bar hydrogen atmosphere at 298 K and 253 K. Error bars represent fitting errors.	135
Table 5.10 Thermal relaxation times for free and bound 3,5-diaminopyridine (2-fold and 7-fold excess) protons in presence of 5 mM $[\text{Ir}(\text{H})_2(\text{IMes})(3,5\text{-diaminopyridine})_3]\text{Cl}$ (5mM) in methanol- d_4 under 4 bar hydrogen atmosphere at 298 K and 260 K. Error bars represent fitting errors.	136
Table 5.11 Hyperpolarised relaxation times for free and bound N-(4-pyridyl)benzamide protons (4-PBA) (5 eq, 2-fold excess) determined in presence of $[\text{Ir}(\text{H})_2(\text{IMes})(\text{N}-(4\text{-pyridyl})\text{benzamide})_3]\text{Cl}$ by application of a constant 5° pulse flip angle. Error bars represent fitting errors for individual T_1 values and standard errors for the average T_1 values (in bold).	142
Table 5.12 Hyperpolarised relaxation times for free and bound N-(4-pyridyl)benzamide protons (5 eq, 2-excess) in the presence of $[\text{Ir}(\text{H})_2(\text{IMes})(\text{N}-(4\text{-pyridyl})\text{benzamide})_3]\text{Cl}$ determined with a constant flip angle pulse sequence, without and with thermal correction. Error bars	

represent fitting errors for individual T_1 values and standard errors for the average T_1 values (in bold).	145
Table 5.13 Variable flip angles and corresponding z-magnetisation and xy-magnetisation levels (%) for an optimised variable flip angle sequence with $N = 15$ according to Equations 5.10, 5.11, 5.14 and conditions (1) and (2).	148
Table 5.14 Hyperpolarised relaxation times for the <i>ortho</i> and <i>meta</i> free and <i>ortho</i> bound N-(4-pyridyl)benzamide (4-PBA) proton signals (5 eq, 2-excess) in the presence of $[\text{Ir}(\text{H})_2(\text{IMes})(\text{N}-(4\text{-pyridyl})\text{benzamide})_3]\text{Cl}$ determined by the variable flip angle pulse sequence. Each experiment was repeated three times with the average given in bold. Error bars represent fitting errors for individual T_1 values and standard errors for the average T_1 values.	150
Table 5.15 Hyperpolarised relaxation time dependence on pulse duration for free 3-amino-5-methylpyridine acquired with the variable and constant flip angle pulse sequences (thermal polarisation corrected and magnetisation corrected for cfa). The error bars represent the standard error determined from 3 repeat measurements for all T_1 values, except vfa 12.5 μs T_1 which was repeated 4 times. The sample included 3-amino-5-methylpyridine (2-fold excess) with 5 mM activated SABRE catalyst in methanol- d_4 under 4 bar $p\text{-H}_2$	155
Table 5.16 Percentage difference between the T_1 values for free 3-amino-5-methylpyridine determined by cfa and vfa, calibrated according to 10.5 μs and 11.5 μs pulse lengths for the 90 degree pulse, compared to the T_1 values acquired with a 12.5 μs 90 degree pulse. The sample involved 3-amino-5-methylpyridine (2-fold excess) and 5 mM activated SABRE catalyst in methanol- d_4 under 4 bar $p\text{-H}_2$	155
Table 5.17 Comparison of hyper T_1 values acquired using the variable flip angle sequence with constant and variable time delays for activated 3,5-diaminopyridine (3-fold excess) in the presence of $[\text{Ir}(\text{H})_2(\text{IMes})(3,5\text{-diaminopyridine})_3]\text{Cl}$ (5 mM) in MeOD on a 9.4 T NMR	

spectrometer. Error bars represent standard errors calculated from 3 (constant, <i>ortho</i>), 5 (constant, <i>para</i>) and 6 (variable) repeated measurements.	158
Table 5.18 Comparison of hyper T_1 values acquired using the variable flip angle sequence with constant and variable time delays for activated 3,5-diaminopyridine (2-fold excess) in the presence of $[\text{Ir}(\text{H})_2(\text{IMes})(3,5\text{-diaminopyridine})_3]\text{Cl}$ (5 mM) in MeOD on a 1 T NMR spectrometer. Error bars represent standard errors calculated from 3 repeated measurements.	158
Table 5.19 Hyperpolarised (measured with variable flip angle sequence on freshly activated sample and after 16 hrs 55 min) for free N-(4-pyridyl)benzamide (2-fold excess) in presence of $[\text{Ir}(\text{H})_2(\text{IMes})(\text{N}-(4\text{-pyridyl})\text{benzamide})_3]\text{Cl}$ in methanol- d_4 at 298 K. Error bars represent fitting errors.	160
Table 6.1 Hydride ligands' chemical shifts for the activated SABRE complexes formed with 4-AP , 4-MP , pyridine and 4-PBA in MeOD at 250 K alongside is the ratio of the dihydride isotopologues when the substrate deuteration level is ~30%, except for 4-AP which deuterates faster and so has a substrate deuteration level of 89%.	176
Table 7.1 T_1 values of the <i>ortho</i> and <i>meta</i> protons of the free and bound substrate obtained under hyperpolarisation from fitting the data presented in Figure 7.11 to Equation 7.10. The last column refers to data measured on a sample of 150 mM 4-AP in MeOH in presence of 5 mM $[\text{Ir}(\text{COD})(\text{IMes})(\text{4-AP})]\text{Cl}$ under areduced pressure atmosphere.	216
Table A1 Standard deviation and standard error for the <i>ortho</i> and <i>meta</i> protons of 4-AP and 4-PBA assessed for their 5 eq : 5 eq mixture in presence of the activated SABRE catalyst in methanol- d_4	259
Table A2 Reproducibility of the enhancement factors measured for the 4-AP and 4-PBA <i>ortho</i> and <i>meta</i> protons in the 5 eq : 5 eq mixture in presence of the SABRE catalyst in methanol- d_4 under 4 bar <i>p</i> - H_2	260

Table A3 Reproducibility of the ratios of enhancement factors measured for the 4-AP and 4-PBA <i>ortho</i> and <i>meta</i> protons in the 5 eq : 5 eq mixture in presence of the SABRE catalyst in methanol- <i>d</i> ₄ under 4 bar <i>p</i> -H ₂	261
Table A4 NMR chemical shifts of individual compounds and mixtures in DCM for reaction monitoring characterisation.	264
Table A5 Change in 4-AP <i>T</i> ₁ values in presence of unactivated catalyst [Ir(COD)(IMes)(4-AP)]Cl (5 mM) with increase of 4-AP concentration. Error bars represent the fitting errors.....	265
Table A6 <i>J</i> -couplings and linebroadening parameters used in the analysis of 4-AP	269
Table A7 <i>J</i> -couplings and linebroadening parameters used in the analysis of pyridine.....	269
Table A8 <i>J</i> -couplings and linebroadening parameters used in the analysis of 4-PBA	269

Accompanying Material

An electronic copy of this thesis, an electronic copy of the publication based on the results reported in this thesis and the permissions to reprint figures from published sources are included on the accompanying CD. This is attached to the back page of this thesis.

“no success comes on a silver platter...”

Acknowledgements

I would like to say a great thank you to my supervisors Dr. Meghan Halse and Prof. Simon Duckett who lead me through this PhD journey. I am grateful for this wonderful scientific opportunity they have given me, their invaluable advice and enthusiasm at all times. Thanks to Dr. Jason Lynam who challenged me on research I have done and encouraged me to be critical when analysing my results. I really enjoyed my time in both Simon's and Meghan's research groups and would love to thank all of the people who supported and helped me through the happy and hard times. Thanks to Liz, Jenny, Emma, Barby, Kate, Amy, Rhianna, both Petes, Ben, Alastair, Phil, Will, Aminata, Mirjam, Richard, Vicky, Denise, Lyndsay, Inna, Marianna, Robin, Anand, Aneurin, Marie, Wissam, Graham, Fadi, Frida, Sarah, Hannah, James, Matheus, Soumya, Dan, Chris, Fraser, Kieran, Adel and Ahmed for good times, games nights and CHyM trips around Yorkshire. Special thanks to Pete Richardson who I learnt a lot from and who always stepped in to help me.

I also would like to thank Dr. Alison Nordon and Dr. Andrew Parrott for collaboration on the project.

I would like to sincerely thank Mojgan Moshgbar and Polina Kishinevskaya who supported me during my internship in Pfizer and encouraged me to apply for a PhD. Great thanks to Pfizer, GSK, Dr. Tony Wild and EPSRC for funding my PhD project.

Thanks to all staff from the University of York. Special thanks to Sharon, Rachel and Alice from the graduate office, and Adina from the International Admissions.

Last but not least I want to take time to thank my family for encouragement and support, and for our close relationship despite being in different countries. Especially a big thank you to my beloved husband who moved with me to the UK for my PhD, for all the dinners he learnt to make when I got home late and for the trips around the UK he organised for us.

Declaration

I declare that this thesis is a presentation of original work and I am the sole author. This work has not previously been presented for an award at this, or any other, University. All sources are acknowledged as References.

Some work presented in this thesis has been previously published in a peer-reviewed article of which I am the primary author:

O. Semenova, P. M. Richardson, A. J. Parrott, A. Nordon, M. E. Halse and S. B. Duckett, *Anal. Chem.*, 2019, **91** (10), 6695-6701.

Chapter 1: Introduction

Process analytical technology (PAT) is defined as a system for designing, analysing, and controlling manufacturing during processing with the goal of ensuring final product quality.¹ PAT tools find applications in process understanding, process verification and monitoring and process control in industry. Employment of PAT allows real-time feedback about the process and rapid troubleshooting. The real-time monitoring is useful when the sampling for the off-line analysis is complicated due to degradation, the need for the frequent analysis and when the batch process does not include isolation steps.² Requirements for PAT are reliability, low-cost, and easy implementation in real-time detection analysis.

Optical molecular spectroscopy methods (NIR, MIR, UV, Raman) are often employed in many steps of the process control.²⁻⁴ The identity of raw materials, synthesis, crystallisation and drying are monitored using these methods. Reaction monitoring is an important part of quality control and is required from the initial steps of the synthesis design and optimisation to the final batch manufacturing process. PAT methods, such as infrared (IR) and Raman detection, are employed for kinetic and mechanism elucidation in industrial processes on the initial optimisation steps.³ These methods are commonly used to monitor the composition of bulk components; however, they are not suitable for the detection of trace reactants due to their insensitivity.⁵ For example, the near infrared (NIR) method is limited due to water signal interference and reduced sensitivity. Another disadvantage of optical spectroscopy is insufficient specificity for the measurement of compounds close in chemical structure, such as products and by-products.⁶ On-line collection of the spectral information usually does not allow for sample pretreatment. Broad and overlapping bands in optical spectroscopy may have many wavelength variables, thus, the assignment to the specific chemical group is complicated.^{7, 8} Thus, detection of degradants, trace contaminants and reactants often has to be achieved off-line in an external laboratory using, for example, high performance liquid chromatography

(HPLC). To conclude, PAT remains limited for the real-time control applications, including reaction-monitoring.^{2, 8}

Nuclear magnetic resonance (NMR) is a powerful technique that provides structural and quantitative information that is in some cases more useful than chromatography and optical spectroscopy.^{9, 10} This technique usually does not require removal of impurities and gives additional structural information. NMR is specific and highly reproducible. NMR is convenient for reaction monitoring, as a measurement of the ratio of starting material to the product will give a direct result because of the linear relationship between intensity and observed nuclei concentration independent of a compound-specific response factor.¹¹ Reaction monitoring using NMR can also identify reaction intermediates with sufficient lifetimes, for example at lower temperatures. New approaches to mechanistic understanding have been developed. These include kinetic studies on ligand exchange and intramolecular haptotropic shift using NMR.¹² Thus, NMR analysis can be beneficial for the understanding and optimisation of important chemical processes in industry.^{13, 14} Nevertheless, NMR remains a laboratory-based method as it is expensive to purchase and maintain.

Recently, low-field low-cost benchtop NMR spectrometers, based on permanent magnets with field strengths around 1 - 2 T, have become available. Benchtop NMR instruments that use permanent magnets do not require cryogenics or large amounts of space. These offer an opportunity to address the issue of cost whilst also providing a level of detector portability.¹⁵⁻²⁰ Several research groups have studied in-line reaction monitoring, kinetics and reaction optimisation using benchtop NMR spectrometers.²¹⁻²⁴ Musio *et al.* investigated the reaction conditions and the process design for the reaction of CF_3H gas with a range of carbonyl compounds which resulted in a 71 - 97% yield of fluorinated ethers and carbinols.²⁴ Cronin and co-workers employed benchtop NMR to follow the formation of imine ligands and their complexation in Cu(I) and Cu(II) complexes in-line, electrophilic fluorination and Diels–Alder cycloaddition reactions.^{21, 22} The acid-catalysed acetalization of *p*-nitrobenzaldehyde with

ethylene glycol was studied at a range of temperatures and catalyst loadings by Singh *et al.*²³ Thus, benchtop NMR spectroscopy has been shown to be applicable to real-time monitoring of various chemical processes, where the characterisation of the reactant does not require its isolation. However, these instruments suffer from relatively low sensitivity and reduced chemical shift dispersion due to their lower magnetic field strengths, limiting their viability for the study of low concentration analytes and nuclei with low NMR receptivity such as ¹³C. Indeed, all examples of reaction monitoring highlighted above were performed in the concentration range of 0.1 – 1 M.²¹⁻²⁴

Benchtop NMR has the potential to be developed for bulk process control in industry; however, the main limitation of these instruments is the low magnetic field that leads to lower sensitivity and second order effects in spectra due to reduced chemical shift dispersion.^{15, 16, 18, 19} The spectral crowding can be reduced by employing selective NMR pulse sequences, which use both radiofrequency pulses and magnetic field gradient pulses to simplify spectra, like the pure shift homonuclear decoupling sequence.²⁵ Chemometric procedures, based on principal component analysis and partial least squares methods, can be used in conjunction with NMR sequences to separate and identify the peaks of interest.²⁶ However, the pure shift methods typically sacrifice SNR and have a problem of sideband peaks similar in intensity to the signals of minor components. The insensitivity and selectivity problem can in principle be addressed by combining hyperpolarisation with low-field NMR measurements.

Hyperpolarisation is a term used to describe methods that generate NMR signal responses that are enhanced relative to those associated with nuclear spins at thermal equilibrium in the detection field.^{27, 28} In the context of industrial process monitoring, it is essential that the hyperpolarisation process itself is low-cost and compact so that it does not compromise the advantages of benchtop NMR. Some of the most popular hyperpolarisation methods today are dynamic nuclear polarisation (DNP),²⁹ spin-exchange optical pumping (SEOP)^{30, 31} and *para*-hydrogen induced

polarisation (PHIP).^{32, 33} The SEOP method is limited to the hyperpolarisation of noble gases. Dissolution DNP has been integrated with benchtop NMR for monitoring the conversion of [1-¹³C] pyruvate to [1-¹³C] lactate *in vitro* and *in vivo*.^{34, 35} However, the generation of hyperpolarised compounds by dissolution DNP is time consuming (ca. 90 mins per hyperpolarised sample) and hyperpolarises one sample at a time, which then can be used only until the hyperpolarisation has decayed (typically tens of seconds). The DNP technique is also costly, and the equipment is non-portable and requires significant lab space, maintenance and expensive cryogenics.

In contrast to DNP, PHIP methods are lower cost and yield hyperpolarisation in seconds. Due to relatively cheap methods for generating and storing *p*-H₂ and the comparative simplicity of the PHIP methods, this is an attractive approach for industrial process monitoring using hyperpolarised benchtop NMR.^{36, 37} Hydrogenative and non-hydrogenative PHIP methods can be considered. In the former technique, an analyte becomes hyperpolarised once the pair of protons from *p*-H₂ is incorporated into it. Reaction monitoring was reported recently using low-field NMR combined with the hydrogenative PHIP hyperpolarisation technique, where the kinetics of the hydrogenation reaction were explored.³⁸ Time-resolved non-uniform sampling was used to help spectral resolution.³⁸ In this case, the hyperpolarised signal can only be observed for unsaturated molecules and for the period of time until the starting material is consumed.

This work focuses on the non-hydrogenative PHIP method called Signal Amplification By Reversible Exchange (SABRE).³⁹ This hyperpolarisation technique provides fast and continuous enhanced NMR signal without changing the identity of the substrate molecule, which is beneficial for reaction monitoring applications. ¹H and ¹³C NMR signal enhancements of 20000-fold and 8000-fold, respectively were obtained when SABRE conditions were optimised and signals were detected at 9.4

T.⁴⁰ SABRE has successfully been combined with benchtop NMR to enhance ¹H, ¹³C and ¹⁵N NMR signals.⁴¹⁻⁴⁴

One of the key challenges of the use of NMR hyperpolarisation methods for analytical applications is the quantification of hyperpolarised NMR response. In contrast to a conventional quantitative NMR measurement, SABRE signal intensity does not scale linearly with the analyte (substrate) concentration. Several research groups are developing methods to better understand the relationship between the SABRE-enhanced NMR signal and the concentration of the detected compound.⁴⁵⁻⁴⁷ A linear SABRE signal response was achieved for low concentration analytes (< 1 μ M) by Tessari and co-workers.^{45, 48} This result was obtained as a consequence of SABRE complex stabilisation in presence of an excess of co-ligand and *p*-H₂ so that the target analyte amount was the only limiting concentration. Thus, first-order kinetics were observed for an analyte, where the response factor was dependent on exchange rates and relaxation effects. An analytical model, which predicts the relationship between the hyperpolarised substrate concentration, theoretical SABRE enhancement, T₁ relaxation times in the system and concentration of the catalyst and substrate was proposed by Barskiy *et al.*⁴⁶ This model accounts for the linearity in SABRE signal observed previously in the presence of a large excess of co-substrate.^{45, 46} Importantly, SABRE-enhanced NMR signals of the substrate scales linearly with the *p*-H₂ enrichment. This was explored by Richardson *et al.* who assessed the efficiency of SABRE transfer for several substrates and showed that maximum enhancement can be predicted if enhancement factors are measured at two different *p*-H₂ concentrations.⁴⁷ Despite these important advances, a robust method to quantify the SABRE signal has not yet been achieved and requires further investigation.

This thesis describes novel methods for reaction monitoring using a low-field benchtop NMR spectrometer with SABRE hyperpolarisation. The literature review in Chapter 2 discusses the theory of low-field NMR spectroscopy and the SABRE hyperpolarisation technique. In addition to

this general background, each results chapter includes a section that provides further context for the data acquired.

In order to evaluate the potential for the SABRE process to be used for reaction monitoring, first, the SABRE signal for two N-heterocyclic compounds, 4-aminopyridine (**4-AP**) and N-(4-aminopyridyl)benzamide (**4-PBA**) was optimised, both individually and in mixtures. In particular, the dependence of the SABRE enhancement on the so-called polarisation transfer field (PTF) and substrate concentration was measured and compared. The results of these experiments are discussed in Chapter 3.

In Chapter 4, the choice of an amide formation reaction as the target model reaction to monitor using SABRE-enhanced NMR is discussed. A range of starting materials was used to select the reaction with optimal parameters for monitoring with the SABRE response. Then, the thesis explores if the reaction proceeds in presence of SABRE catalyst and hydrogen using standard and hyperpolarised NMR spectroscopy. Perspectives for quantitative reaction monitoring using the SABRE signal intensity are evaluated.

In Chapter 5 the lifetime of the SABRE response is studied, which is proportional to the spin-lattice relaxation time constant (T_1). The influence of the SABRE conditions on T_1 , such as the presence of a hydrogen atmosphere and the different forms of the SABRE catalyst is described. Conventional methods for measuring relaxation are discussed. Then, a single-shot method to measure SABRE signal lifetimes is developed and compared to a method proposed in literature. Finally, this method is applied to assess the relationship between SABRE signal enhancement and hyperpolarisation lifetime for a range of N-heterocyclic amines.

In Chapter 6, the reaction monitoring studies are performed with an investigation of the chemical transformations of the SABRE catalyst and of an associated hydrogen isotope exchange (HIE) reaction. A study of the HIE is important as the incorporation of deuterium into the substrate molecule disturbs the J coupling network, which is crucial to the SABRE process. The

deuterium labelling is also widely applicable in pharmacokinetic studies. Four SABRE systems for the HIE reaction are investigated. Evidence is presented for H/D-labelling in pyridine, 4-AP, 4-PBA and 4-methylpyridine (4-MP) and the associated catalysts are explored in order to identify which is the key complex driving the HIE reaction. The time-dependence trends are obtained for each substrate, iridium catalyst and hydrogen isotopologues in order to compare the kinetics and explore the mechanism. In addition, the kinetics of the deuterium incorporation into the substrate using simulations of the line-shape for the mono- and di-substituted isotopologues is discussed.

Chapter 7 investigates the conversion of the SABRE pre-catalyst into the activated dihydride catalyst and the HIE reaction using hyperpolarised benchtop NMR spectroscopy. These reactions are probed with the SABRE signal intensity and lifetime using low field NMR spectroscopy for detection and compare these results to high-field NMR data as a proof-of-concept. The standard non-hyperpolarised ^1H NMR signal at 400 MHz is used as a reference for comparison with the SABRE measurements. The insensitivity of the benchtop NMR instrument allows for the detection in *protio*-solvent, which is used to remove the HIE effect. The formation of the Ir(III) catalysts is followed in the presence of two different substrates and discuss the differences in the obtained trends. Additionally, calibration data are collected in *protio*-methanol using the benchtop NMR spectrometer and apply a quantification model for the SABRE process proposed in the literature.⁴⁶ The parameters extracted from the calibration data are applied to the reaction monitoring data to obtain kinetic curves for this process, which are compared to reference ^1H NMR experiments at high-field.

Chapter 8 presents conclusions and a discussion of future work and Chapter 9 provides experimental details and methods used throughout the thesis.

Chapter 2: Theory

2.1 Principles of NMR

Nuclear Magnetic Resonance (NMR) is based on the interaction of nuclear spins ($I \neq 0$) with a static magnetic field which leads to the Zeeman splitting of the nuclear spin energy levels. In the absence of a magnetic field the nuclear spin energy levels are degenerate. However, in a magnetic field there are $2I+1$ non-degenerate states. The magnetic quantum number $m = -I, \dots, +I$ defines the energy states that are created in the magnetic field. For example, for a nucleus with $I = \frac{1}{2}$ there are two spin states with $m = \frac{1}{2}$ (α) and $m = -\frac{1}{2}$ (β) (Figure 2.1).⁴⁹ The frequency (ω_0) of the transition is called the Larmor frequency and is specific to the nucleus involved and depends on the gyromagnetic ratio of the nucleus (γ) and the magnetic field (B_0) (Equation 2.1). The energy of the spin state m is defined by Equation 2.2 and the energy difference between α and β states is given by Equation 2.3.⁵⁰

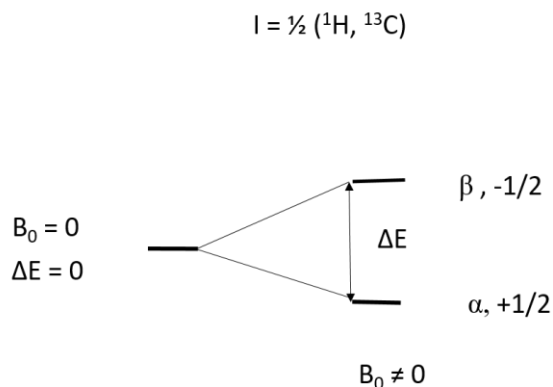


Figure 2.1 Spin states energy splitting in magnetic field.

$$\omega_0 = \gamma B_0 \quad (2.1)$$

$$E_m = -m\hbar\gamma B_0 \quad (2.2)$$

$$\Delta E = E_\beta - E_\alpha = \hbar\gamma B_0 \quad (2.3)$$

In an AX type spin system the four product states typically used to describe two coupled $I = \frac{1}{2}$ nuclei are: $\alpha\alpha, \beta\beta, \alpha\beta, \beta\alpha$. These result in two doublets in the NMR spectrum split by J -coupling (Figure 2.2).

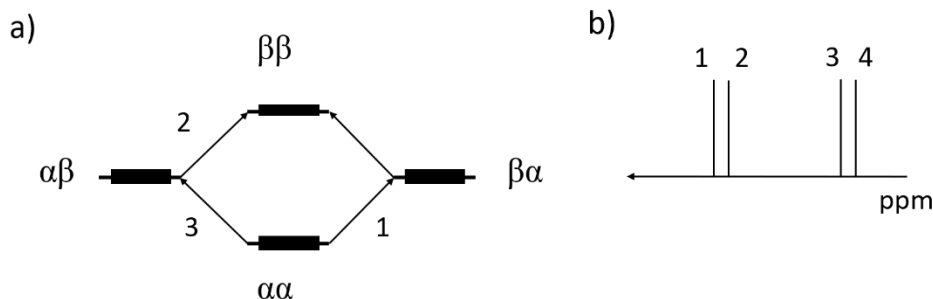


Figure 2.2 a) Scheme of nuclear spin state populations for two spin $\frac{1}{2}$ nuclei. b) Schematic representation of the NMR spectrum showing two doublets.

The population difference between the nuclear spin states dictates the strength of the NMR signal. The populations of the spin states obey the Boltzmann distribution. The polarisation (P) describes the population difference as a fraction of the total number of spins. Equation 2.4 reflects the polarisation for a single nucleus ($I = \frac{1}{2}$), where N_α and N_β are the populations of the α and β states, \hbar is reduced Planck constant, k_B is the Boltzmann constant and T is temperature. The equation for polarisation is simplified according to the so-called “high temperature approximation” as the energy gap is small compared with $k_B T$.

$$P = \frac{N_\alpha - N_\beta}{N_\alpha + N_\beta} = \tanh\left(\frac{\gamma B_0 \hbar}{2k_B T}\right) \approx \frac{\gamma B_0 \hbar}{2k_B T} \quad (2.4)$$

From Equation 2.4, there are three factors that affect the population difference: magnetic field, B_0 , gyromagnetic ratio, γ , and temperature, T . In a 1 T magnetic field at room temperature the polarisation for ^1H nuclei is $P = 0.0003\%$. In other words there are 500 003 spin states α for 500 000 spin states β . Increasing the sample concentration and the number of scans can help low sensitivity. Superconducting magnets, which produce high magnetic fields, increase the population difference and therefore achieve higher NMR signal. The use of an inverse broadband probe, which contains the ^1H coil closest to the sample, instead of a regular broadband probe,

additionally maximises the ^1H NMR signal sensitivity. Cryoprobes, cooled with the liquid helium, increase the sensitivity of NMR signal due to the decrease in background noise and reach about 2-3-times higher signal-to-noise ratio (SNR) compared to the conventional probes.⁵¹

The population difference in Equation 2.4 gives rise to a net magnetisation along the axis of the applied magnetic field B_0 (z-axis).⁵² This magnetisation is represented by the vector M_0 in Figure 2.3a. In order to detect the net z-magnetisation, a radiofrequency (RF) pulse at the Larmor frequency is applied perpendicular to B_0 using an appropriately oriented coil. The RF pulse can be represented as a vector, B_1 , in the xy-plane. B_1 rotates around z-axis at the Larmor frequency in the “laboratory frame” of reference. In the “rotating frame” of reference, defined by coordinates x' , y' and z' , the x' and y' axes rotate around the z' axis at the Larmor frequency. As a consequence, B_1 appears static and B_0 disappears in this reference frame. During the RF pulse, M_0 is rotated from z' -axis, around B_1 , into the transverse $x'y'$ -plane. The angle of rotation of the magnetisation is proportional to the rotation frequency, which is in turn proportional to the amplitude of the RF pulse, B_1 , and the duration of the pulse (t , microseconds) (Equation 2.5). The dependence of the M_z and M_{xy} components of the magnetisation on the RF pulse angle is described by Equations 2.6 and 2.7. In the laboratory frame, the transverse magnetisation M_{xy} rotates around B_0 and this precession can be observed using the same coil that generated the RF pulse.⁵⁰

The NMR signal is proportional to the M_{xy} component of the magnetisation and so, according to Equations 2.5 and 2.7, it depends on the pulse duration. In practice, the angle of the RF pulse can be calibrated by observing the NMR signal intensity as a function of RF pulse duration. This shows a sinusoidal dependence on the pulse duration (Figure 2.3b), where the maximum signal is obtained with a 90-degree pulse ($\pi/2$).

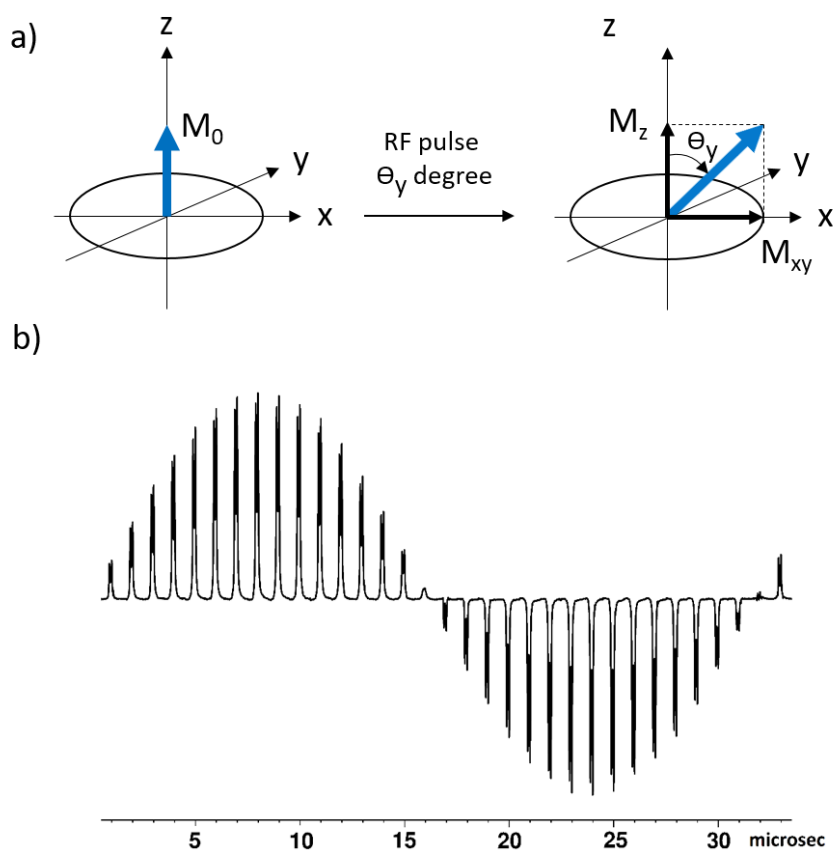


Figure 2.3 a) Vector model illustrating the creation of transverse magnetisation M_{xy} through rotation by a RF pulse. b) Evolution of the NMR signal with the length of the applied pulse.

$$\theta = \omega_1 t = \gamma B_1 t \quad (2.5)$$

$$M_z = M_0 \cos \theta \quad (2.6)$$

$$M_{xy} = M_0 \sin \theta \quad (2.7)$$

The NMR signals are dependent on the nuclear isotope (e.g. ^1H , ^{13}C , ^{15}N etc.) and the electronic environment of the nucleus. The NMR peak is characterised by its position on the chemical shift scale (ppm), which is defined by Equation 2.8, where δ is chemical shift value in ppm, ω is Larmor frequency of the detected nucleus and ω_{ref} is the frequency of the peak from reference compound, which is tetramethylsilane for ^1H NMR.

$$\delta = 10^6 \frac{\omega - \omega_{ref}}{\omega_{ref}} \quad (2.8)$$

The integral intensity of the NMR signal is proportional to the number of detected nuclei. Therefore, NMR spectroscopy provides qualitative and quantitative information about molecular structure.

2.2 Low-field benchtop NMR spectroscopy

The new generation of low-field benchtop NMR instruments show large potential to be used for research and industrial applications.¹⁵⁻¹⁹ These instruments are based on permanent magnets which can be arranged in parallel to the sample or in a Halbach array design (Figure 2.4).¹⁶ The Halbach design (Figure 2.4b), where small permanent magnets are arranged around a sample placed in the middle of the cylinder, provides high magnetic field homogeneity in a chosen direction based on magnet orientation. These Halbach arrays produce very little stray field outside the spectrometer.

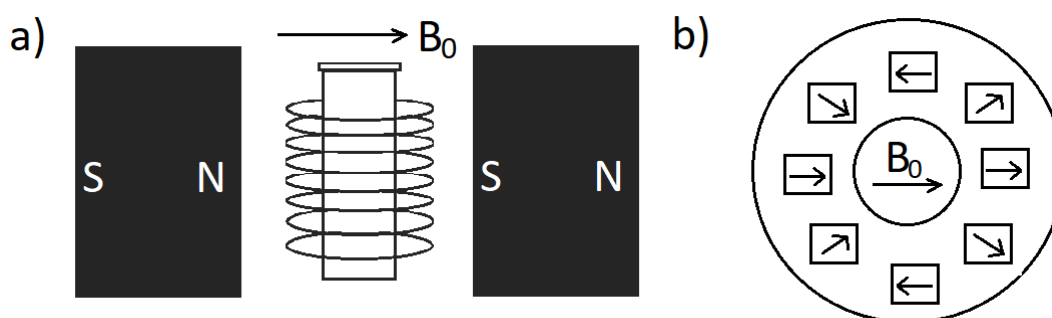


Figure 2.4 a) Schematic design of the static magnetic field based on permanent magnets. b) Halbach array.¹⁶

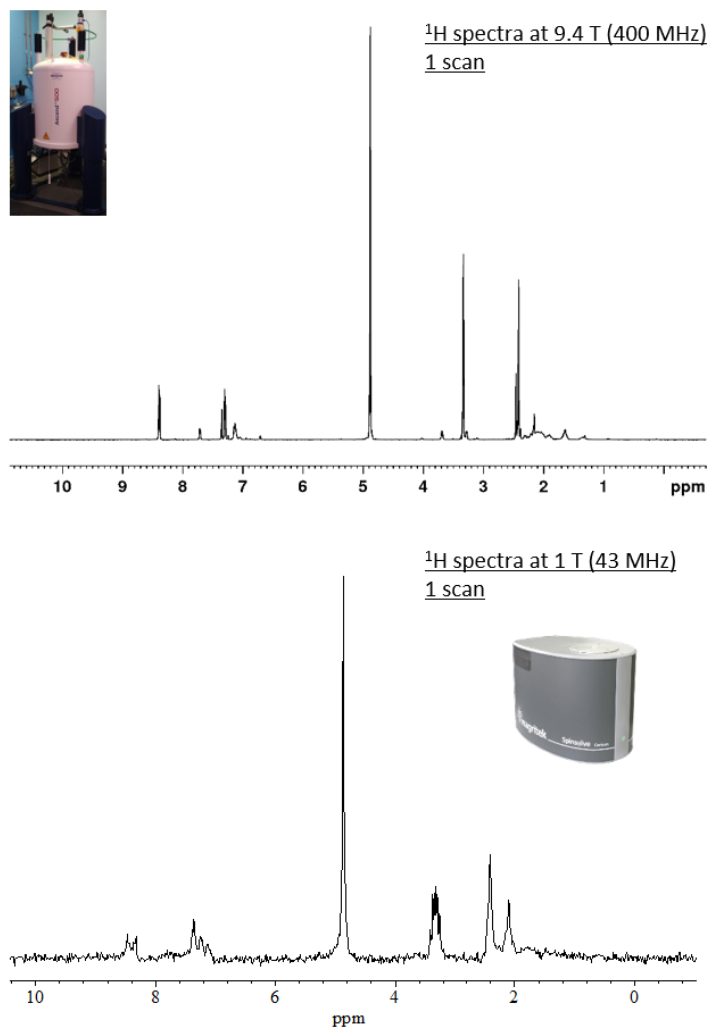


Figure 2.5 ¹H NMR spectra of 25 mM 4-methylpyridine and 5 mM [Ir(COD)(IMes)(4-methylpyridine)]Cl in MeOD acquired at (a) 9.4 T and (b) 1 T.

Benchtop NMR spectrometers provide several advantages. They are relatively cheap to purchase and do not require maintenance associated with cryogens like their high-field NMR counterparts.¹⁷ However, the consequences of their relatively low magnetic fields are low sensitivity and spectral dispersion, often resulting in more complex spectra. Compared to 9.4 T, the spin polarisation at 1 T is 9.4-times smaller and as such results in a decreased SNR (Figure 2.5). In addition, lower magnetic field strength leads to low spectral dispersion, such as at 9.4 T 1 ppm reflects 400 Hz in ¹H NMR spectrum compared to 43 Hz at 1 T field. Second order effects, such as ‘roofing’, take place when the difference in chemical shift (in Hz) between the signals is comparable to the *J* coupling between them.⁵³

Therefore, at lower magnetic field second order effects are more likely, and J coupling splittings become more prominent in the spectrum. To demonstrate these points, Figure 2.5 is presented which shows spectra for the same sample acquired at 9.4 T and 1 T.

Modern low-field NMR spectrometers can detect ^1H and a heteronuclei, such as ^2H , ^7Li , ^{11}B , ^{13}C , ^{15}N , ^{19}F , ^{27}Al , ^{31}P .¹⁷ In contrast to the high-field NMR spectrometers, the benchtop instruments generally have two channels, which are responsible for detection of $^1\text{H}/^{19}\text{F}$ and only one heteronucleus. For instance, this limits opportunities for decoupling, as usually only ^1H but not ^2H can be decoupled. Relaxation and diffusion weighted measurements can be performed using low-field instruments as well as 2D homonuclear and heteronuclear correlation NMR experiments.¹⁸

54

Benchtop NMR spectrometers from a range of vendors, such as Bruker, Anasazi, Thermo Scientific, Nanalysis, Magritek, Oxford instruments, are available on the market. The instrument used in this thesis is a Magritek Spinsolve Carbon 1 T (43 MHz) NMR spectrometer. This spectrometer is characterised by high temperature stability, good resolution (< 0.5 Hz at 50% linewidth) and the ability to apply pulsed field gradients. The Spinsolve Carbon instrument acquires ^1H , ^{19}F and ^{13}C nuclei. However, to achieve a different X nucleus a different NMR spectrometer is required due to the hardware limitations. This instrument is able to perform gradient-assisted spectroscopy due to the implemented gradient coil as well as 2D NMR (COSY, HETCOR, HMQC, HMBC). Due to the low sensitivity, there is no problem with the dynamic range of the amplifier and as such measurements in *protio*-solvent can be acquired. Field lock is achieved with built-in external ^{19}F sample which is a more sensitive probe than deuterium and can be easily detected at 1 T.

2.3 Hyperpolarisation in NMR

Hyperpolarisation is a term used to describe methods that generate NMR signal responses that are enhanced relative to those associated with

nuclear spins at thermal equilibrium in the detection field.^{27, 28} Some of the most popular hyperpolarisation methods today are dynamic nuclear polarisation (DNP),²⁹ spin-exchange optical pumping (SEOP)^{30, 31} and *para*-hydrogen induced polarisation (PHIP).^{32, 33} The hyperpolarisation technique used in this project is based on the long-lived state of *para*-hydrogen and the transfer of latent polarisation from *para*-hydrogen to analyte nuclei.

2.3.1 *Para-hydrogen Induced Polarisation (PHIP)*

2.3.1.1 *Para-hydrogen*

Each hydrogen nucleus in a dihydrogen molecule contains one proton that possess a nuclear magnetic moment with nuclear spin quantum number $I = 1/2$. Particle physics states that for a fermion like H₂, the overall wave function must be antisymmetric with respect to particle interchange. According to the Born Oppenheimer approximation the quantum mechanical descriptions of the translation, rotational, vibrational, electronic, and nuclear spin wave functions of H₂ can be treated as a direct product because they are far apart in energy.^{37, 55} Hence the total wavefunction for a hydrogen molecule can be written simply as follows:

$$\psi_{tot} = \psi_{trans}\psi_{vib}\psi_{elec}\psi_{rot}\psi_{nuc}. \quad (2.9)$$

The vibrational, translational, and electronic wave functions are always symmetric as the nuclei remain in the same relative positions. In contrast, quantised rotation about the center of mass interchanges the positions of H₁ and H₂ when the rotational wave number (j) is odd. When j is even they remain in the same relative orientation. Hence, these two distinct manifolds are antisymmetric and symmetric with respect to particle interchange.^{37, 55} The nuclear spin wave function can also be symmetric or antisymmetric with respect to particle interchange and hence there are two forms of the total wave function (Equation 2.10 and 2.11).

$$\psi_{tot}(\text{antisym}) = \psi_{trans}(\text{sym})\psi_{vib}(\text{sym})\psi_{elec}(\text{sym})\psi_{rot}(\text{sym})\psi_{spin}(\text{antisym}) \quad (2.10)$$

$$\psi_{tot}(\text{antisym}) = \psi_{trans}(\text{sym})\psi_{vib}(\text{sym})\psi_{elec}(\text{sym})\psi_{rot}(\text{antisym})\psi_{spin}(\text{sym})$$

(2.11)

A hydrogen molecule with a symmetric rotational and antisymmetric nuclear spin wave function is called *para*-hydrogen (*p*-H₂). In contrast, that with an antisymmetric rotational and symmetric nuclear spin wave function is called *ortho*-hydrogen. The four product states typically used to describe two coupled I = ½ nuclei, αα, ββ, αβ, βα, are not the appropriate eigenstates for H₂ system because the two protons in H₂ are chemically and magnetically equivalent. In addition, the states αβ and βα are neither symmetric or anti-symmetric and do not fulfill the symmetry requirement for hydrogen molecule.⁵⁶ Their normalised linear combinations represent the eigenstates of H₂, αα, ββ, $\frac{1}{\sqrt{2}}(\alpha\beta + \beta\alpha)$, $\frac{1}{\sqrt{2}}(\alpha\beta - \beta\alpha)$, where the last anti-symmetric superposition state corresponds to *para*-hydrogen (Figure 2.6).

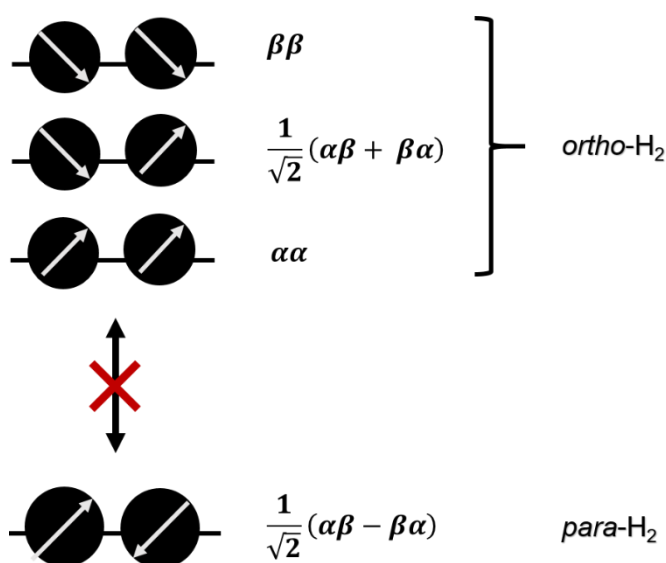


Figure 2.6 Schematic representation of hydrogen nuclear spin states, which include three *ortho*-hydrogen states and one *para*-hydrogen state. The conversion between the two hydrogen forms is symmetry forbidden.

As a consequence, *para*-hydrogen exists as a nuclear singlet (S₀) that has no net angular momentum. *Ortho*-hydrogen is restricted to higher energy odd rotational wave numbers and exists in three possible substates. Therefore, it is a nuclear triplet and made up of the αα (T₋₁), $\frac{1}{\sqrt{2}}(\alpha\beta + \beta\alpha)$ (T₀) and ββ(T₀) forms.

In general the conversion between the two hydrogen forms is symmetry forbidden. The two forms can only interconvert under special conditions discussed below. Therefore, if hydrogen gas can be enriched in one of the forms, it can be stored for long periods of time.^{37, 55, 57} The two forms exhibit different heat capacities, electrical conductivities and adsorption properties and these properties are exploited in different areas, for example in astrochemistry and liquid hydrogen fuel storage.^{58, 59}

2.3.1.2 Production of *para*-hydrogen

Para- and *ortho*- hydrogen have different energies; however, their interconversion requires the change of two quantum numbers and hence is forbidden. The equilibrium ratio of the two hydrogen isomers is temperature dependent. Therefore, they can be separated. At room temperature and above an equilibrium sample of hydrogen contains approximately 75% of *ortho*- and 25% of *para*-hydrogen because the four energy levels are roughly equally populated (Figure 2.7). At lower temperatures, the even rotational wave numbers are favoured because they are of lower energy. Equilibration between the hydrogen isomers takes a long time because their interconversion is forbidden by quantum mechanics. A paramagnetic material can be employed in order to break the magnetic symmetry of the *p*-H₂ nuclei and, therefore, establish equilibrium quicker. Hydrogen gas passed through a solid paramagnetic material interacts with magnetic dipoles of the unpaired electrons on the surface. As a result, at low temperatures and in presence of this paramagnetic catalyst *ortho-para* equilibration time is reduced to a few seconds.^{59, 60} Conventional catalysts for *ortho-para* hydrogen conversion are activated charcoal³⁷, nickel-silica⁶¹, hydrous ferric oxide⁵⁷, silica/FeCl₃⁶² and pure iron⁷. At around 19 K there is 99.75% of *para*-hydrogen achieved in normal hydrogen (Figure 2.7).^{37, 55, 63} Once produced, it can be stored at room temperature in the absence of the catalyst for weeks until its symmetry is broken again in a reaction or through interactions with a paramagnetic species.^{37, 64}

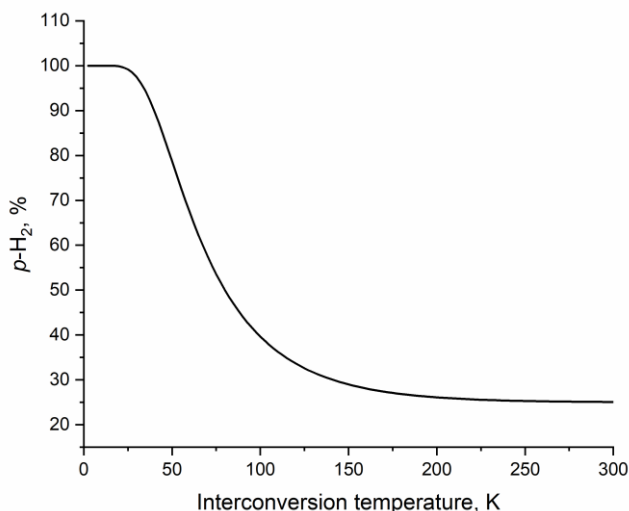


Figure 2.7 *Para*-hydrogen enrichment dependence on interconversion temperature in presence of a paramagnetic catalyst.

2.3.1.3 Principles of *Para*-hydrogen Induced Polarisation (PHIP)

All NMR experiments with *para*-hydrogen are covered by the term *Para*-hydrogen Induced Polarisation (PHIP). The observations of the *para*-hydrogen phenomenon in the 1980s were pioneered by Bargon, Eisenberg and Weitekamp and were initially attributed to CIDNP (Chemically Induced Dynamic Nuclear Polarisation).⁶⁴⁻⁶⁶ The NMR signal sensitivity enhancement obtained with PHIP was predicted theoretically in 1986 by Bowers and Weitekamp, and subsequently verified experimentally in 1987 by two research groups simultaneously. One of the first observations of PHIP was during an investigation by ¹H NMR spectroscopy of a hydrogenation reaction in the presence of a transition metal complex. Enhanced ¹H NMR signals for the product and the dihydride form of the catalyst were observed. The samples, which contained hydrogen, were frozen in liquid N₂ prior to investigation. This caused the H₂ to be enriched with *p*-H₂.^{64, 66} As described originally by Bowers and Weitekamp, the effect of NMR signal enhancement by *p*-H₂ in the detection field of the spectrometer is called *Para*-hydrogen And Synthesis Allow Dramatically Enhanced Nuclear Alignment (PASADENA).⁶⁴ A different PHIP effect was reported in 1988 by Pravica and Weitekamp, who observed enhanced in-phase NMR signals when the reaction was carried out in a weak magnetic

field and then the sample was transferred into the high-field NMR spectrometer for detection.⁶⁷ This type of PHIP that happens in a relatively low magnetic field is called Adiabatic Longitudinal Transport After Dissociation Engenders Nuclear Alignment (ALTADENA).⁶⁷

2.3.1.4 PASADENA

In a PASADENA experiment, the pairwise transformation of the *para*-hydrogen nuclear states occurs inside the NMR spectrometer and, therefore, at high magnetic field. This may correspond to a hydrogenation reaction or the formation of a metal dihydride product when *para*-hydrogen derived protons are incorporated into the product molecule. As a result of the reaction, the symmetry of *para*-hydrogen is broken and the new protons possess larger population differences across the nuclear spin states than those at thermal equilibrium. In an AX type of spin system, where the chemical shift difference between the protons from *p*-H₂ is much bigger than the *J* coupling between them, the *para*-hydrogen singlet state becomes longitudinal two spin order ($\alpha\beta$ and $\beta\alpha$) states (Figure 2.8).^{37, 56} Selective population of the $\alpha\beta$ and $\beta\alpha$ states leads to the observation of two strong antiphase doublets in the NMR spectrum.³⁷ This differs from the Boltzmann population of $\alpha\alpha, \beta\beta, \alpha\beta, \beta\alpha$ states (Figure 2.2) where the lower states are slightly more populated and the NMR spectrum shows absorption peaks.

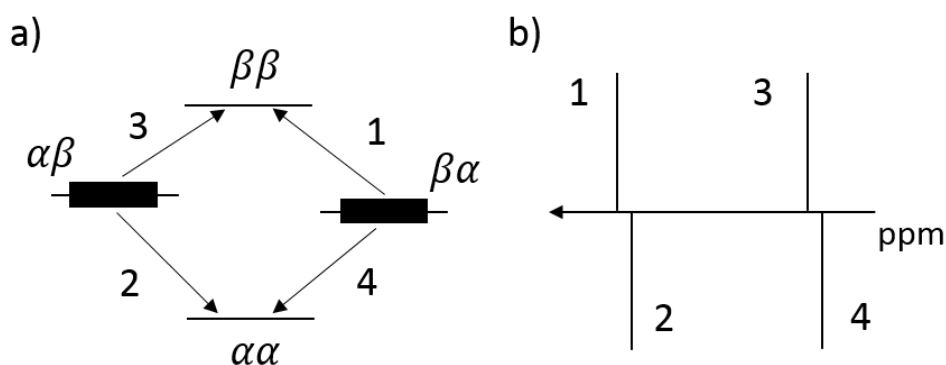


Figure 2.8 a) Scheme of spin energy state population in PASADENA for two spin $\frac{1}{2}$ nuclei. b) Schematic representation of the NMR spectrum showing two antiphase doublets as a result of PASADENA.

The experimental setup for PASADENA requires a capillary inside the NMR tube for *para*-hydrogen addition. After *p*-H₂ is bubbled through a

solution of the substrate and the catalyst, an NMR spectrum is acquired.^{68,}
⁶⁹ The capillary can be removed after bubbling is finished to improve spectral quality. In another approach, the sample solution is frozen in the NMR tube and *p*-H₂ is subsequently added, followed by the sample transfer into the NMR spectrometer. A series of NMR spectra are acquired to observe the progress of the hydrogenation reaction while the sample thaws inside the NMR spectrometer.^{70, 71}

2.3.1.5 ALTADENA

The ALTADENA effect is different from the previously discussed PASADENA because the strength of the magnetic field in which the product spin system is formed is low (0 – 20 mT). This means that the initial *para*-hydrogen-derived singlet state $\frac{1}{\sqrt{2}}(\alpha\beta - \beta\alpha)$ is created in a strongly coupled second order environment and evolves into an imbalance of the $\alpha\beta$ and $\beta\alpha$ states. This results in the exclusive population of one of the $\alpha\beta$ or $\beta\alpha$ states. Because of the adiabatic (in the quantum mechanical sense) transfer into the high magnetic field for detection, the created spin order does not alter. Therefore, when observed in a high magnetic field the overpopulation of either the $\alpha\beta$ or $\beta\alpha$ states generates a spectrum that is characteristic of just two transitions: one absorption and one emission (Figure 2.9).^{37, 67}

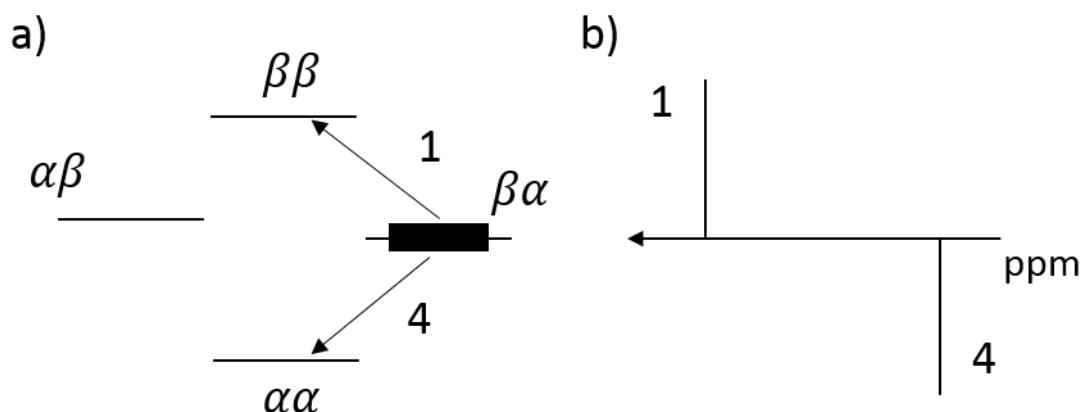


Figure 2.9 a) Scheme of spin energy states population in ALTADENA for two spin-¹/₂ nuclei. b) Schematic representation of the NMR spectrum showing two singlets, antiphase relatively to each other, as a result of ALTADENA.

To perform an ALTADENA experiment p -H₂ is added to the NMR tube with the substrate and the catalyst in solution. Then the NMR sample is shaken vigorously outside the NMR spectrometer in the Earth's magnetic field or in the stray field of the NMR spectrometer and quickly inserted into the spectrometer for detection.^{69, 72, 73} Alternatively, a flow system can be used that includes the reaction chamber placed inside a solenoid and a capillary that connects the reaction chamber with the NMR spectrometer. In the reaction chamber, p -H₂ is bubbled through the solution and a low magnetic field is applied by passing a current through the solenoid. After that, the solution is passed through the capillary to the detection field of the NMR spectrometer.^{74, 75} Polarisation transfer via ALTADENA was shown to happen due to both through-bond and through-space interactions leading to a superposition of these effects.⁶⁹

The hydrogenative PHIP techniques described above achieve high NMR signal enhancements; however, they change the structure of substrate and so can provide enhanced signals only until the hydrogenation is complete. This thesis focuses on a different non-hydrogenative version of PHIP called signal amplification by reversible exchange (SABRE).

2.3.2 SABRE and SABRE-Relay

A non-hydrogenative ALTADENA type method was introduced in 2009 by Duckett and co-workers called Signal Amplification By Reversible Exchange (SABRE).³⁹ It involves the reversible binding of *para*-hydrogen, as hydride ligands, and a target compound to a metal complex. At low magnetic field, spin polarisation is transferred from the hydride ligands to other nuclei in the complex via the scalar coupling network. Therefore, the NMR signal of the ligand after dissociation is greatly enhanced compared to the signal derived under Boltzmann equilibrium. Notably, the chemical structure of the ligand is not modified during SABRE (Figure 2.10).³⁹

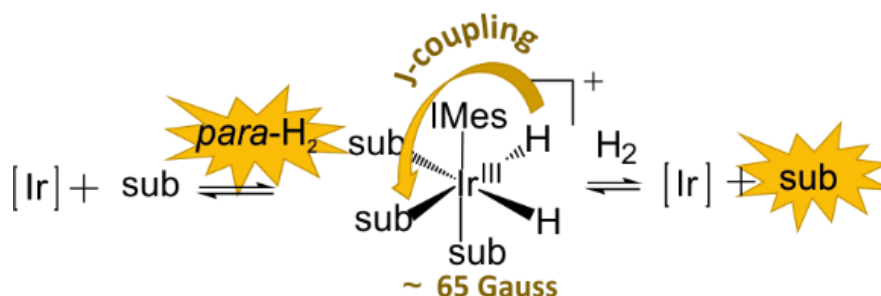


Figure 2.10 Under *para*-hydrogen, the indicated substrate exchange processes enables hyperpolarisation transfer so that free substrate NMR resonances can be detected more readily. This transfer occurs in low magnetic field through the complex's scalar coupling network and due to reversibility operates continuously when *p*-H₂ is present.

The rule for efficient SABRE polarisation transfer is that the dominant *J* coupling in the complex network has to be equal to the chemical shift difference between the hydride ligands and the substrate nuclei.⁷⁶ Usually the *J* coupling between the hydrides is around 7-10 Hz.⁷⁷ The level of transferred polarisation is magnetic field dependent due to the chemical shift term and for transfer to ¹H nuclei, optimal conditions are in the range of tens of Gauss.⁷⁶ In addition, the efficiency of the polarisation transfer also depends on the *J* coupling between the hydride and the substrate nucleus which is typically 1.2 Hz for a ⁴*J*^{HH} coupling.^{77, 78} When heteronuclei are considered, the chemical shift difference now requires lower polarisation transfer fields because of the larger difference in Larmor frequency.^{77, 79} Classically, the SABRE effect is observed in a high detection field where chemical shift difference leads to diagnostic NMR spectra.^{39, 80, 81} This

requires a physical transfer of the sample between the low polarisation transfer field and the detection field and, hence, adds time for relaxation.^{82,}
⁸³ Alternatively SABRE observation can be achieved by switching between the fields inside the spectrometer like in the case of zero-field⁸⁴ and Earth's field⁸⁵ NMR spectroscopy.

Hyperpolarisation on many different nuclei has been observed using SABRE, e.g. ^1H , ^{13}C , ^{15}N , ^{19}F , ^{29}Si , ^{31}P and ^{119}Sn .^{39, 41, 79, 86-88} The lower gyromagnetic ratio and natural abundance of heteronuclei makes them even more insensitive than thermal ^1H NMR. However, SABRE was shown to provide a strong signal that is of potential use, for example, for proton and heteronuclear MRI acquisition.^{32, 89, 90} Heteronuclear low natural abundance is particularly useful for MRI applications as it implies that there is low background signal.

2.3.2.1 *Optimisation of SABRE conditions*

The original SABRE measurements were performed with pyridine as the substrate. The level of hyperpolarisation obtained was $\sim 1\%$ for ^1H NMR signal.³⁹ Great progress has been made since then, and SABRE hyperpolarisation levels have been improved. For comparison pyridine was recently reported to give $\sim 4.8\%$ polarisation.⁴² This improvement in SABRE signal enhancement has been achieved by extensive optimisation of several parameters such as the SABRE catalyst, substrate relaxation times, polarisation transfer field (PTF), and concentration of $p\text{-H}_2$ in solution. The polarisation transfer field (PTF), substrate relaxation times and substrate concentration effects on SABRE hyperpolarisation are discussed in detail later in this thesis, specifically in Chapters 3 and 5. The optimisation of the catalyst is not studied in detail in this thesis. However, due to the importance of the catalyst to the SABRE technique, a historical overview of the optimisation of the SABRE catalyst is provided below.

2.3.2.1.1 Role of the SABRE catalyst

In the initial demonstration of SABRE, Crabtree's catalyst $[\text{Ir}(\text{COD})(\text{PCy}_3)(\text{py})][\text{BF}_4]$ (COD = cyclooctadiene; Cy = cyclohexyl), was

employed as a pre-catalyst.⁹¹ Upon reaction with pyridine and *para*-hydrogen gas the active complex, $[\text{Ir}(\text{H})_2(\text{PCy}_3)(\text{py})_3][\text{BF}_4]$, is formed. It contains a *J* coupling network between the pyridine and hydride ligands. This is required for hyperpolarisation transfer (Figure 2.11).⁹²

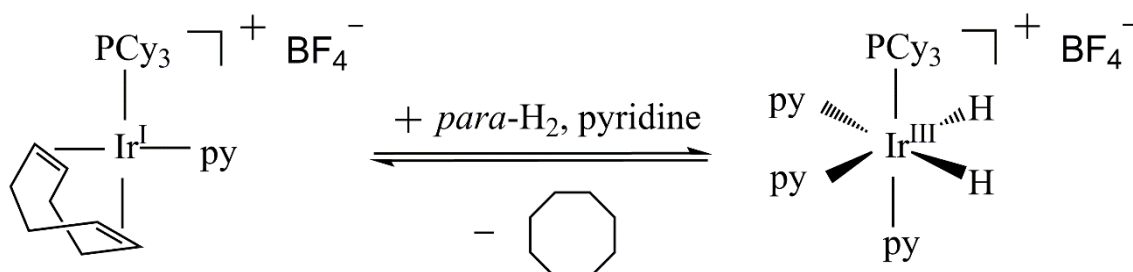


Figure 2.11 Activation of Crabtree's complex to the active SABRE catalyst under addition of *para*-hydrogen and pyridine as a substrate (py = pyridine).

The active catalyst undergoes reversible hydrogen and substrate elimination and, therefore, free pyridine in the solution can be polarised.³⁹ Moreover, other compounds capable of reversible binding to this catalyst, such as nicotinamide, 3-fluoropyridine, nicotine, pyridazine, quinoline, quinazoline, quinoxaline, and dibenzothiophene, can also be polarised.³⁹ In order to optimise the catalyst for the reversible exchange of substrate and hydrogen, a series of sterically bulky electron-donating phosphines were studied.⁹² Catalysts with PCy_3 , PPhCy_2 , PPh_2Cy , PEt_3 , P^iPr_3 , P^nBu_3 , P^tBu_3 and $\text{P}(1\text{-naphthyl})_3$ ligands were investigated under SABRE conditions. The properties of the phosphine ligand were shown to have an important effect on the NMR signal enhancement achieved for pyridine (Figure 2.12). One of the most sterically bulky and electron-rich phosphines, PCy_2Ph , was shown to give the best polarisation among all studied phosphine ligands, giving 2.5-times more polarisation compared to the Crabtree's catalyst.⁹²

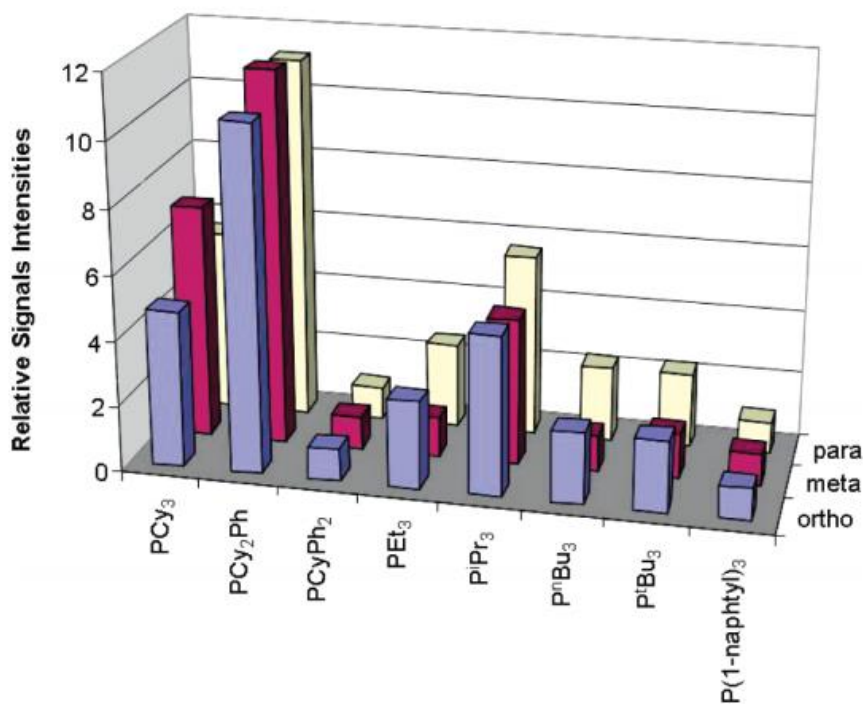


Figure 2.12 Plot of the relative absolute signal strengths for the three pyridine proton sites (relative to signals for free pyridine at equilibrium). Results represent an average of five measurements, each recorded immediately after shaking the NMR tube in the Earth's field (50 μ T). These samples in methanol-*d*₄ contained [Ir(COD)(py)₂]BF₄, one equivalent of PR₃ and of pyridine. Reprinted with permission from K. D. Atkinson, M. J. Cowley, P. I. P. Elliott, S. B. Duckett, G. G. R. Green, J. López-Serrano and A. C. Whitwood, *J. Am. Chem. Soc.*, 2009, **131**, 13362–13368. Copyright (2018) American Chemical Society.

Subsequently, the phosphine ligand was replaced with a monodentate N-heterocyclic carbene (NHC) ligand that provides more electron density to the metal via σ -bond and is stabilised by π backbonding from the metal.⁹³⁻⁹⁵ The substituents on the carbene have to be chosen to increase the steric bulk in order to promote substrate dissociation. While substrate dissociation is required for the SABRE effect, the substrate's residence time on the catalyst has to be long enough for hyperpolarisation to transfer. Hence, the pre-catalysts of type [Ir(Cl)(COD)(NHC)] were studied with *p*-H₂ and pyridine for their SABRE effect.⁹⁶ Additionally, the pyridine SABRE enhancement dependence on the Tolman electronic parameter⁹⁷ and the buried volume⁹⁸ have been measured for a variety of carbene ligands. No straightforward trend was found. The exchange rates of free and bound pyridine have been determined for these complexes and showed that the complex, [Ir(COD)(IMes)(Cl)] (IMes = 1,3-bis(2,4,6-trimethylphenyl)-

imidazole-2-ylidene) gives the best SABRE enhancement when the exchange rate for pyridine is $k_{\text{exchange}} = 9 \text{ s}^{-1}$ at 298 K.⁹⁶

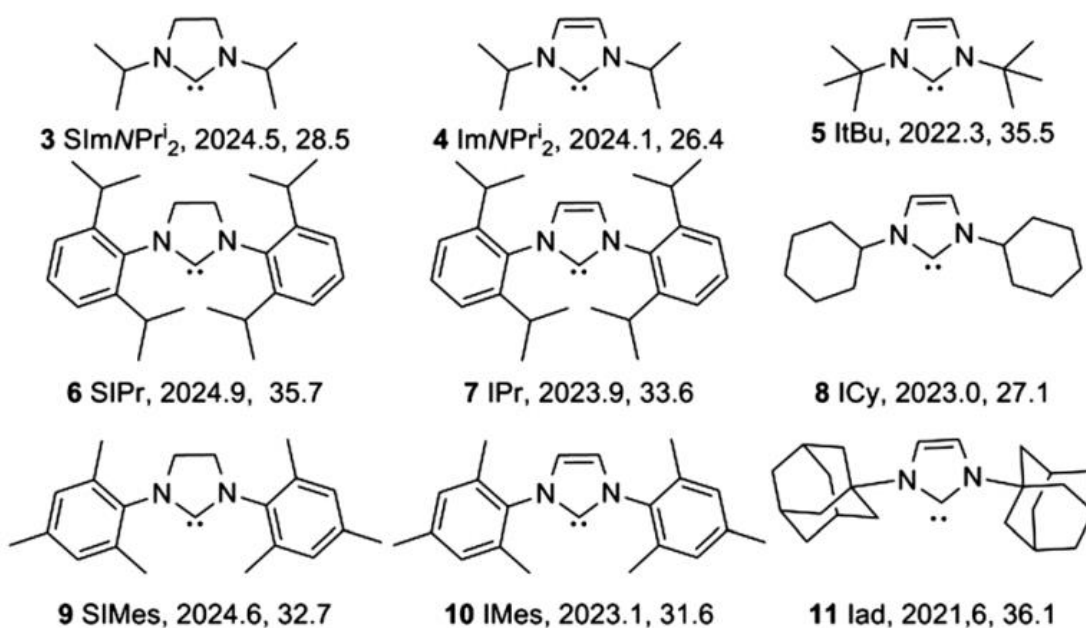


Figure 2.13 Ligands used for complex synthesis, compound number, abbreviation, Tolman Electronic Parameter (cm⁻¹), buried volume (%). B. J. A. van Weerdenburg, S. Glöggl, N. Eshuis, A. H. J. (ton) Engwerda, J. M. M. Smits, R. de Gelder, S. Appelt, S. S. Wymenga, M. Tessari, M. C. Feiters, B. Blümich and F. P. J. T. Rutjes, *Chem. Commun.* 2013, **49**, 7388 - Published by The Royal Society of Chemistry.

The combination of PCy₃ or PPh₃ phosphine ligands and the IMes carbene ligand was investigated for SABRE with a mixture of acetonitrile and pyridine as substrates (ligand 5 in Figure 2.13).⁹⁹ An interesting dependence of the substrate dissociation rate on the phosphine ligand has been observed for these complexes. When the PCy₃ ligand is employed, pyridine is the more favorable ligand to dissociate, followed by acetonitrile. In contrast, with a PPh₃ ligand, acetonitrile dissociates preferentially over pyridine.⁹⁹ Thus, the substrate with the optimal dissociation rate obtains higher SABRE hyperpolarised signal. These findings can be applied for selective hyperpolarisation of one of the compounds in the solution.

In order to apply SABRE-enhanced NMR spectroscopy to biological applications, bio-compatible conditions have to be achieved. For example, the ability to conduct SABRE experiments in water has been investigated. In the experiment performed by Zeng *et al.*, the water insoluble SABRE pre-

catalyst $[\text{Ir}(\text{Cl})(\text{COD})(\text{IMes})]$ was activated in methanol and water was added prior to methanol being evaporated. As a result SABRE NMR polarisation of 1% was achieved for 3-amino-1,2,4-triazine.¹⁰⁰ In order to improve the aqueous solubility of the SABRE catalyst, water soluble substituents have been incorporated on the ligands (complexes **2-IDEG**, IDEG = 1,3-bis(3,4,5-tris(diethyleneglycol)benzyl)-1H-imidazole-2-ylidene carbene and **3** in Figure 2.14).^{101, 102} Neutral bidentate NHC complexes have been developed in order to achieve better polarisation levels in non-polar solvents.¹⁰³ Also, attempts to create a heterogenous SABRE catalyst by immobilisation to 3-aminopropylfunctionalized silica gel has been shown to be successful. The resultant catalyst $(\text{SiO}_2)_x(\text{C}_3\text{H}_6)\text{NH Ir}(\text{COD})(\text{IMes})$ was created and provided a 100-fold NMR signal enhancement for ^{15}N in ^{15}N -pyridine with 50% $p\text{-H}_2$ employed.⁸⁸

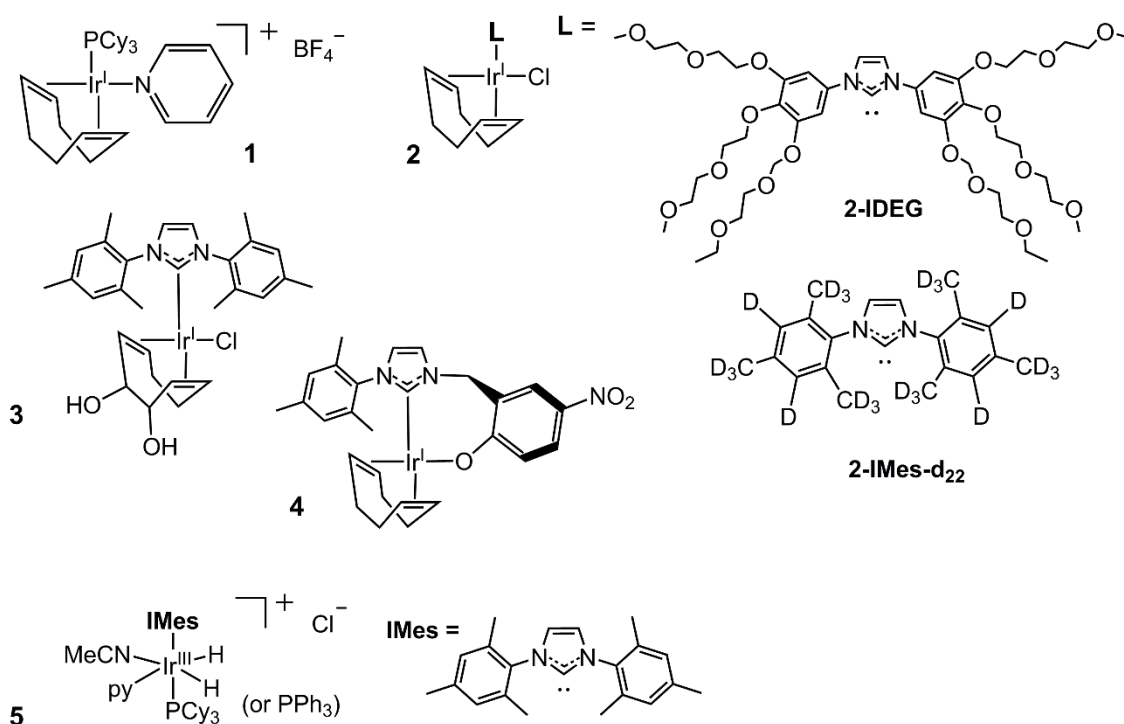


Figure 2.14 SABRE catalysts: 1) Crabtree's pre-catalyst; 2) IMes catalyst; water-soluble IDEG pre-catalyst; deuterated IMes- d_{22} pre-catalyst; 3) water-soluble SABRE pre-catalyst; 4) neutral SABRE pre-catalyst; 5) SABRE activated catalyst with phosphine and IMes carbene.

In addition, by decreasing the NHC ligand's ability to become polarised via J coupling by replacing the protons on the ligand with deuterium nuclei, polarisation of the substrate can be increased (complex

2-IMes- d_{22} in Figure 2.14).⁹⁰ Due to the lower gyromagnetic ratio of deuterium, and therefore reduced spin-spin coupling, this helps to transfer polarisation more efficiently into the nuclei of the target substrate. The T_1 values for the bound and free substrate increase in the presence of the deuterated catalyst compared to its protonated counterpart. This is beneficial because less hyperpolarisation is lost during the sample transfer to the detection field and higher SNR is achieved. An increase in polarisation level by 250 % was achieved with the IMes- d_{22} catalyst.⁹⁰

In conclusion, the catalyst determines the substrate exchange rates, affects relaxation and the J coupling network that drives the hyperpolarisation transfer. In this thesis the pre-catalyst [Ir(Cl)(COD)(IMes)] is used which has been shown to provide optimal NMR signal enhancement for most N-heterocycles via SABRE in organic solvents.

Chapter 3: Hyperpolarisation of N-heterocyclic amines

3.1 Introduction

In this chapter the SABRE hyperpolarisation of N-heterocyclic substrates containing an amino group that are potential candidates for participating in an amide formation reaction under conditions suitable for SABRE is described. Specifically, the hyperpolarisation level dependence on the polarisation transfer field and substrate concentration for the individual compounds and their mixtures are measured. The knowledge of how SABRE hyperpolarisation distributes between compounds in mixtures at different concentrations is key to the development of a method for quantitative reaction monitoring with hyperpolarised low-field benchtop NMR spectroscopy. In addition, the reproducibility of the SABRE signal with mixtures of substrates is explored and the distribution of the hyperpolarisation intra-molecularly and inter-molecularly is observed.

3.2 Background

Aromatic amines are biologically active and widely used in the pharmaceutical and chemical industries.¹⁰⁴⁻¹⁰⁸ For example, lisdexamfetamine, which is a central nervous system stimulant, is used for ADHD treatment.¹⁰⁴ Dopamine and noradrenalin are both hormones and neurotransmitters that play a significant role in several medical conditions.^{105, 106} In addition, aromatic amines are involved in polymer synthesis¹⁰⁹, oil refining¹¹⁰, food¹¹¹ and the textile industry.¹⁰⁷ The concentration of these compounds is controlled in industrial wastewaters due to their potential accumulative toxicity; safety concerns associated with arylamines in foods have been raised.^{107, 108, 111} In this study the substrate 4-aminopyridine (**4-AP**), a potassium channel blocker known as dalfampridine, is used that is registered as a drug for walking improvement in patients with multiple sclerosis.¹¹²

These types of compounds are of interest because they are suitable targets for reaction monitoring with SABRE. This will be discussed in

Chapter 4 in more detail. There are a few examples of the hyperpolarisation of compounds containing an amino group in the literature. Amino acids have been successfully hyperpolarised by the DNP method and used to investigate enzyme activity.^{113, 114} There are also examples of hyperpolarisation of dehydroaminoacids using PHIP, which occurs due to the addition of *para*-hydrogen through hydrogenation of these substrates.¹¹⁵ Amino acids, like glycine, histidine and phenylalanine, have been hyperpolarised with SABRE but the enhanced signal was detected in a 3.9 mT field where chemical shift resolution is limited.¹¹⁶ It should be noted that these results were not successfully reproduced in York. Hyperpolarisation of ¹⁵N-labelled amines using the SABRE-SHEATH method in ultra-low (mG) magnetic fields has been performed via their conversion to Schiff bases.¹¹⁷ ¹H hyperpolarisation of ammonia (~ 40-fold), phenylethylamine (~ 108-fold), phenoxyethylamine (~ 99-fold), benzylamine (~ 72-fold), phenylpropylamine (~ 46-fold), isobutylamine (~ 187-fold), allylamine (~ 76-fold) and tryptamine (~21-fold) have been observed once these substrates bind to the SABRE catalyst via the amino group nitrogen.^{118, 119} Additionally, these amines have been used as polarisation carriers in the recently described SABRE-Relay method. In this approach the amine obtains hyperpolarisation via binding to the SABRE catalyst and then acts as a carrier of hyperpolarisation due to the exchange of its hyperpolarised amino group protons with those in other molecules.¹¹⁸ The SABRE-Relay technique has been employed to detect a hyperpolarised signals for secondary amines, which do not bind to the iridium catalyst, such as isopropylamine (~ 220-fold) and dibenzylamine (~ 274-fold).¹¹⁹ In the same way, acetamide, ¹⁵N-¹³C-labeled urea, methacrylamide and cyclohexyl methacrylamide ¹H, ¹³C and ¹⁵N hyperpolarised resonances have been observed with SABRE-Relay.¹¹⁸ Higher levels of hyperpolarisation of amines and amides can be achieved with SABRE by tethering to a pyridine ring, which acts as a binding site to the iridium catalyst. For example, the SABRE conditions for the tertiary amine 3-(N,N-dimethylamino)pyridine have been optimised leading to an overall polarisation level of 3.6%.⁴⁰ It has also been successfully employed in case of amides, where up to 4.1% and 16.1%

polarisation has been reported for selectively deuterated 4,6- d_2 -nicotinamide and 2,5- d_2 -isonicotinamide, respectively.⁹⁰

3.3 SABRE catalyst activation

In order to observe SABRE hyperpolarised signals, an activated form of the SABRE catalyst with the substrate under investigation is prepared. For this purpose, the pre-catalyst (complex type 1, Figure 3.1) with the general formula $[\text{Ir}(\text{Cl})(\text{COD})(\text{NHC})]$, where COD is *cis,cis*-1,5-cyclooctadiene and NHC is a N-heterocyclic carbene, is mixed with an excess of the substrate and hydrogen. Initially, the substrate reacts with the pre-catalyst, by displacing the chloride ion to form complexes of type 2 $[\text{Ir}(\text{COD})(\text{NHC})(\text{sub})]\text{Cl}$ (Figure 3.1). When hydrogen gas is added, 2 oxidatively adds H_2 to form an octahedral dihydride complex of type 3 $[\text{Ir}(\text{H})_2(\text{COD})(\text{NHC})(\text{sub})]\text{Cl}$ (Figure 3.1). Upon further addition of H_2 , the hydrogenation of the cyclooctadiene ligand occurs to form cyclooctane (COA) which can no longer ligate. The activated SABRE catalyst that results from this process is type 4, $[\text{Ir}(\text{H})_2(\text{NHC})(\text{sub})_3]\text{Cl}$, and typically contains three ligated molecules of the substrate that are differentiated as *trans* to the hydride ligands (sub') and *trans* to the carbene ligand (sub'') as shown in Figure 3.1. In this thesis, solutions containing 5 mM loadings of the pre-catalyst are typically used, and the NHC is IMes (IMes = 1,3-bis(2,4,6-trimethyl-phenyl)imidazole-2-ylidene) unless specified otherwise.

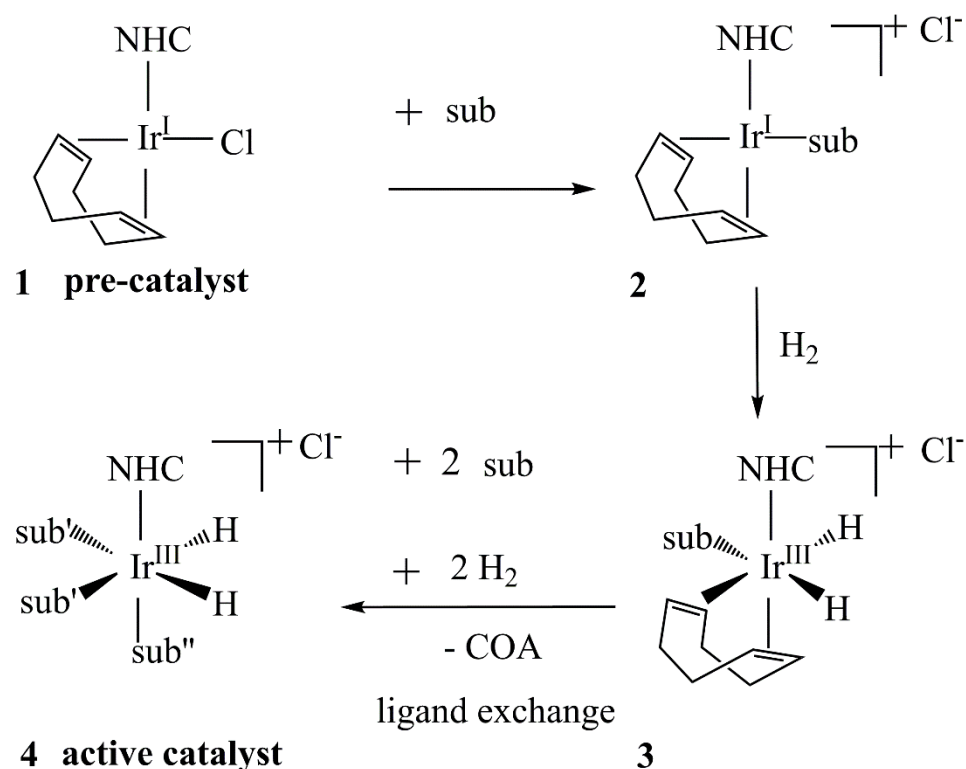


Figure 3.1 Chemical changes occurring during SABRE pre-catalyst activation. Upon addition of substrate, $[\text{IrCl}(\text{COD})(\text{IMes})]$ (**1**) transforms into $[\text{Ir}(\text{COD})(\text{IMes})(\text{substrate})]\text{Cl}$ (**2**). **2** then oxidatively adds H_2 to form octahedral $[\text{Ir}(\text{H})_2(\text{COD})(\text{IMes})(\text{substrate})]\text{Cl}$ (**3**), which is not stable at room temperature. Further addition of H_2 causes COD hydrogenation and two further substrate molecules to bind, yielding the SABRE active complex $[\text{Ir}(\text{H})_2(\text{IMes})(\text{substrate})_3]\text{Cl}$ (**4**).

Once the pre-catalyst is activated, complex **4** can be characterised by observing the hydride region which gives a singlet peak in the ^1H NMR spectrum at around -23 ppm. Complex **4** simultaneously and reversibly binds hydrogen (*para*-hydrogen) and the target substrate, enabling the transfer polarisation between them when in the presence of a small magnetic field, termed the polarisation transfer field (PTF). The value of the PTF is chosen in such a way as to maximise the level of polarisation transfer between the hydride and substrate nuclei. The underlying requirement for this optimised transfer of polarisation is that the chemical shift difference between the hydrides and the substrate nuclei are equal to the dominant J coupling within the spin network on the active catalyst. This is typically the coupling between the hydride ligands that is on the order of 10 Hz.⁷⁷ In case of proton nuclei, a typical optimal PTF is about 65 G. Once the hyperpolarisation has been transferred to the bound substrate it can be

shared the other substrate nuclei via intra-molecular J couplings. Due to the chemical exchange that takes place during this process, the substrate that is present in free solution becomes hyperpolarised. Additionally, this process converts *para*-hydrogen into normal hydrogen. Consequently, the SABRE procedure is reversible and can be repeated if the *para*-hydrogen is refreshed. It should be noted that the interactions with the catalyst can also reduce the SABRE NMR signal of the target due to the reversibility of the hyperpolarisation transfer and therefore there is an optimal residence time of the substrate on the catalyst to maximise polarisation transfer.

In summary, the final SABRE hyperpolarisation level depends on the PTF, the time allowed for the hyperpolarisation transfer, substrate exchange rates on the catalyst, the concentration of p -H₂, catalyst and substrate, the solubility of all components and the competitive binding efficiency when there are several substrates in solution. Hence there are a number of significant challenges associated with the optimisation and quantification of SABRE.

3.4 Hyperpolarisation of 4-AP and 4-PBA by SABRE

The result of SABRE on 4-aminopyridine (**4-AP**) and N-(4-pyridyl)benzamide (**4-PBA**) are now considered. These reagents have been selected because they are involved in the model reaction explored in Chapter 4, where one reflects a simple primary amine and the second its amide condensation product with benzoic anhydride (Figure 3.2).

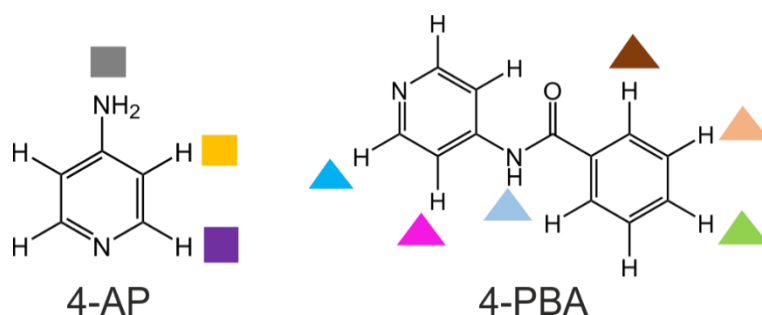


Figure 3.2 Structures of 4-aminopyridine (**4-AP**) and N-(4-pyridyl)benzamide (**4-PBA**) with colour-labelled protons.

Once **1** is activated with **4-AP** and H_2 in methanol- d_4 , $[Ir(H)_2(IMes)(4-AP)_3]Cl$ (**4a**) forms as revealed by the hydride resonance at -23.25 ppm. This is the fully active form of the SABRE catalyst. Figure 3.3 compares a single thermally polarised (this phrase is used to indicate that the sample was under Boltzmann equilibrium conditions when the spectrum was recorded) NMR scan (256-times vertical expansion) and the corresponding SABRE enhanced 1H NMR spectrum of **4-AP**. The SABRE process was conducted using a PTF of 65 G in methanol- d_4 solution and monitored at 400 MHz (9.4 T). The precise experimental conditions are detailed in Experimental, section 9.5.

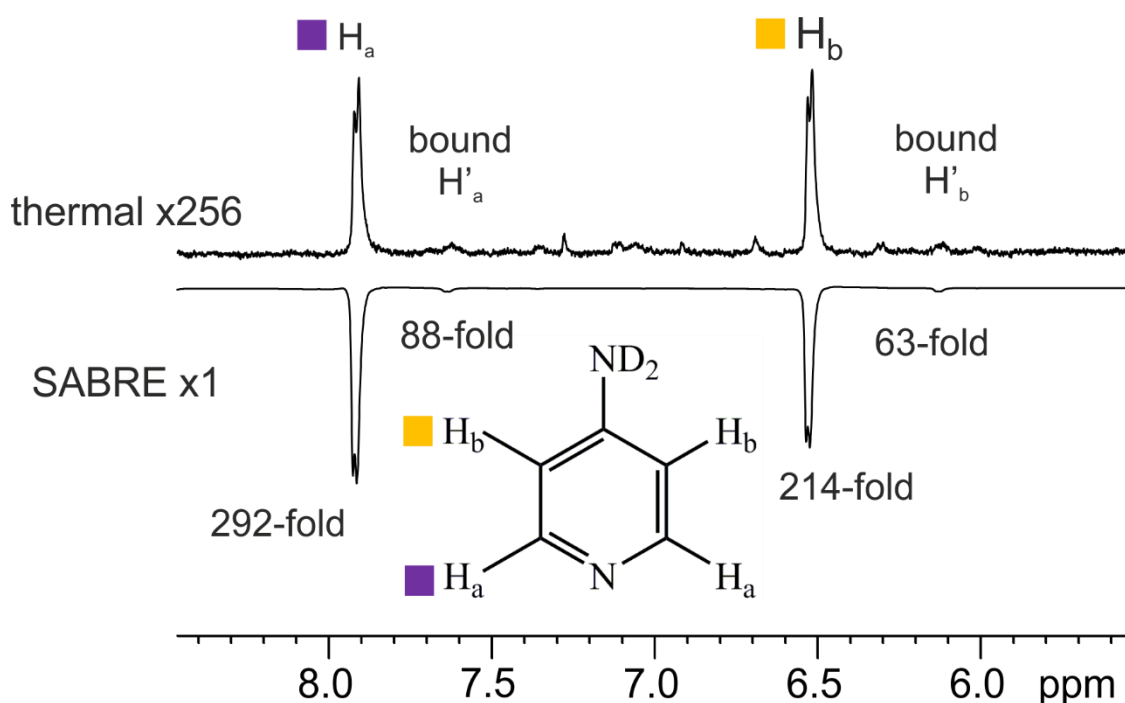


Figure 3.3 Single scan 1H NMR spectra of **4-AP** under thermal (256-fold vertical expansion) and SABRE conditions. The SABRE 1H NMR spectrum of **4-AP** at a 35 mM excess relative to the activated SABRE catalyst was acquired with PTF = 65 G in methanol- d_4 . All spectra were acquired at 9.4 T (400 MHz).

The aromatic protons of **4-AP** provide enhanced signals at δ 7.97 (violet square, H_a) and δ 6.56 (yellow square, H_b) in the SABRE spectrum. Weaker signals for the *ortho* and *meta* protons of the bound substrate are also observed at 7.68 ppm (H'_a) and 6.17 ppm (H'_b), respectively. Once **4-AP** has been dissolved in methanol- d_4 the NH_2 group becomes ND_2 and subsequently the signal is not observed for this site in these 1H NMR spectra.

The two spectra were collected with the same NMR parameters, therefore, the enhancement factor for these two SABRE enhanced NMR signals can be calculated from the ratio of their signal integrals. The enhancement values are detailed in Figure 3.3 and are larger for the protons adjacent to the binding site, which will possess larger couplings to the hydride ligands in catalyst **4**.

The prototype condensation reaction product, N-(4-pyridyl)benzamide (**4-PBA**), forms $[\text{Ir}(\text{H})_2(\text{IMes})(\mathbf{4-PBA})_3]\text{Cl}$ (**4b**) in a similar way, and yields a hydride resonance at -22.73 ppm. Figure 3.4 compares the analogous thermal (vertical scale increased 16-times) and SABRE ^1H NMR spectra.

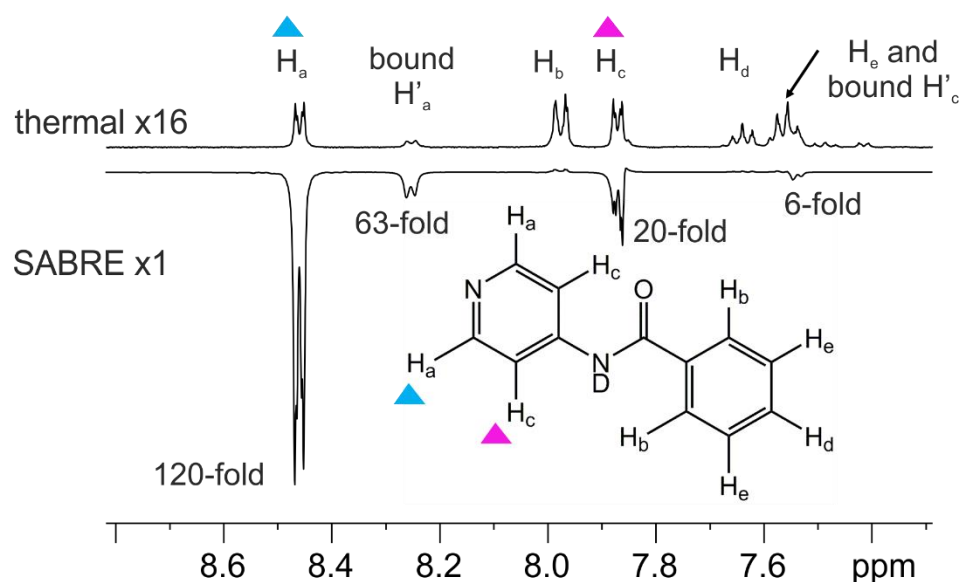


Figure 3.4 Single scan ^1H NMR spectra of **4-PBA** under thermal (16-fold vertical expansion) and SABRE conditions. The SABRE ^1H NMR spectrum of **4-PBA** at a 35 mM excess relative to the activated SABRE catalyst was acquired with PTF = 65 G in methanol- d_4 . All spectra were acquired at 9.4 T (400 MHz).

4-PBA possesses 6 groups of protons; however, only those on the nitrogen containing ring (*ortho* H_a at 8.46 ppm and *meta* H_c at 7.86 ppm) couple to each other and the hydride ligands and therefore obtain hyperpolarisation via SABRE. The remaining protons are separated by an amide group which acts as a J -coupling disrupter and receive no appreciable hyperpolarisation. In addition, the NH group is deuterated when the solvent is methanol- d_4 and does not therefore yield a ^1H NMR signal. The bound

substrate *ortho* and *meta* proton signals are detected at δ 8.25 and δ 7.54, respectively, in the SABRE enhanced spectrum. In the case of H_c' , peak overlap in the thermally polarised spectrum prevents easy peak assignment; however, the SABRE enhancement allows for the detection of these resonances. The results in Figure 3.3 and Figure 3.4 establish that SABRE can be used to acquire diagnostic signals in just one scan for **4-AP** and **4-PBA**. The higher signal gains seen for free **4-AP** are attributed to a more optimal ligand exchange rate and hence more efficient SABRE polarisation.⁴⁶

In the next sections the dependences of the SABRE enhanced ¹H NMR signal of **4-AP** and **4-PBA** on the PTF and substrate concentration are explored.

3.4.1 Effect of the polarisation transfer field

3.4.1.1 Introduction

The SABRE signal enhancement factor is dependent on the polarisation transfer field (PTF) due to the relative evolution of the hydride-hydride coupling and the chemical shift difference between the hydride and the substrate nuclei as a function of magnetic field. The optimal resonance condition for hyperpolarisation transfer is achieved once the hydride-hydride coupling is equal to the difference in chemical shift between the hydrides and the substrate nuclei. In case of the heteronuclei such as ¹³C or ¹⁵N this corresponds to the difference in Larmor frequencies. Hence, to fulfill the resonance condition for heteronuclei, magnetic fields below the Earth's magnetic field ($\sim 50 \mu\text{T}$) should be employed.^{56, 76} The equation identifying the optimum PTF condition for SABRE polarisation transfer from the hydrides to nucleus X, $B_{\text{resonance}}$, has been reported by Theis *et al.* A simplified version is presented in Equation 3.1, where J^{HH} and J^{XH} are the hydride-hydride coupling and the hydride-X nucleus coupling in Hz, γ_H and

γ_X are the gyromagnetic ratios of the ^1H and X nuclei in MHz T^{-1} , and δ_H and δ_X are the chemical shifts of the ^1H and X nuclei in ppm.⁷⁹

$$PTF = B_{Resonance} \approx \frac{J^{HH} - J^{XH}}{(\gamma_H(1 - \delta_H) - \gamma_X(1 - \delta_X))} \quad (3.1)$$

If the estimated parameters are: $J^{HH} \approx 7 \text{ Hz}$ ⁷⁶, $J^{XH} \approx 1 \text{ Hz}$ ⁷⁸, $\gamma_H = \gamma_X = 42.577 \text{ MHz T}^{-1}$, $\delta_H \sim -23 \text{ ppm}$ for the hydrides and $\delta_H \sim 7 \text{ ppm}$ for the aromatic substrate protons, the optimal PTF for ^1H is 6.3 mT (63 G). In the same manner, for ^{13}C the optimal PTF is calculated to be 0.3 μT (3 mG).¹²⁰

It has been reported previously that there are a range of magnetic states related to the nuclei in the SABRE complex that can be created during the SABRE process.⁵⁶ It has been shown that their relative levels of hyperpolarisation vary depending on the PTF.⁷⁴ Due to the fact that SABRE hyperpolarisation is transferred through the scalar coupling network, the amount of signal the nucleus exhibits is dependent on its relative position within this spin coupling network and hence the molecule. The strength of the hydride to substrate nucleus coupling is a driving force for the initial hyperpolarisation transfer step, for example, more strongly coupled *ortho* protons usually obtain more hyperpolarisation than other more weakly coupled substrate protons.⁷⁸ Therefore an accurate knowledge of the PTF dependence can enable selective detection of different species in a mixture. This has been shown for mixtures of pyridine and acetonitrile, which exhibited the highest SABRE signals at 140 G and 20 G respectively.⁹⁹ At the same time, due to the dependence of the optimal PTF on the J couplings within the complex, different enhancement levels are obtained with different catalysts.⁹⁹ Therefore, it is important to investigate the optimal PTF conditions for hyperpolarised signal detection for the substrate and catalyst systems under investigation.

3.4.1.2 Results

Here, the PTF dependence of the starting material, **4-AP**, and product, **4-PBA**, of a model condensation reaction is explored. For this purpose, an automated flow system for hyperpolarisation was used that

provides reproducible hyperpolarisation levels and allows for software control of the PTF, the polarisation transfer time (PTT) and the sample transfer times.⁷⁴ For each measurement the sample was enriched with *p*-H₂ by bubbling the gas through the solution within a reaction chamber. The reaction cell is housed inside a solenoid coil that is used to generate the desired PTF. Once polarisation has been built-up in solution (after a few seconds), the sample is pneumatically transferred using N₂ gas to the NMR spectrometer for signal detection. Prior to the PTF study, SABRE pre-catalyst **1** was activated with **4-AP** or **4-PBA** in methanol-*d*₄ through repeated periods of *p*-H₂ bubbling. The formation of the active SABRE complex of type **4** was confirmed spectroscopically using detection on a 400 MHz NMR spectrometer.

The activation of the SABRE catalyst with **4-AP** is relatively slow (hours) and therefore full conversion to the active catalyst species requires extended periods of bubbling and repeated transfers to the NMR spectrometer for detection. One limitation of the automated flow system is that due to solvent evaporation during bubbling and sample transfer, only a limited number of bubbling and transfer periods can be achieved on a single sample. Therefore, the following measurements on the SABRE response of **4-AP** were achieved with ~ 50% of the active complex in the solution relative to the initial concentration of the pre-catalyst. In order to avoid any systematic error associated with the continued activation of the complex during these PTF experiments, the variable PTF measurements were acquired in a random order. The PTF dependence for 10 eq of **4-AP** (50 mM) relative to the starting iridium catalyst **1** was obtained by performing repeated SABRE hyperpolarisation experiments with fixed experimental parameters (PTT, sample transfer time, NMR detection parameters) but with variable PTF. The variation in SABRE enhancement factor as a function of PTF for the *ortho* and *meta* resonances of **4-AP** (both in free solution and bound to **4**) are presented in Figure 3.5.

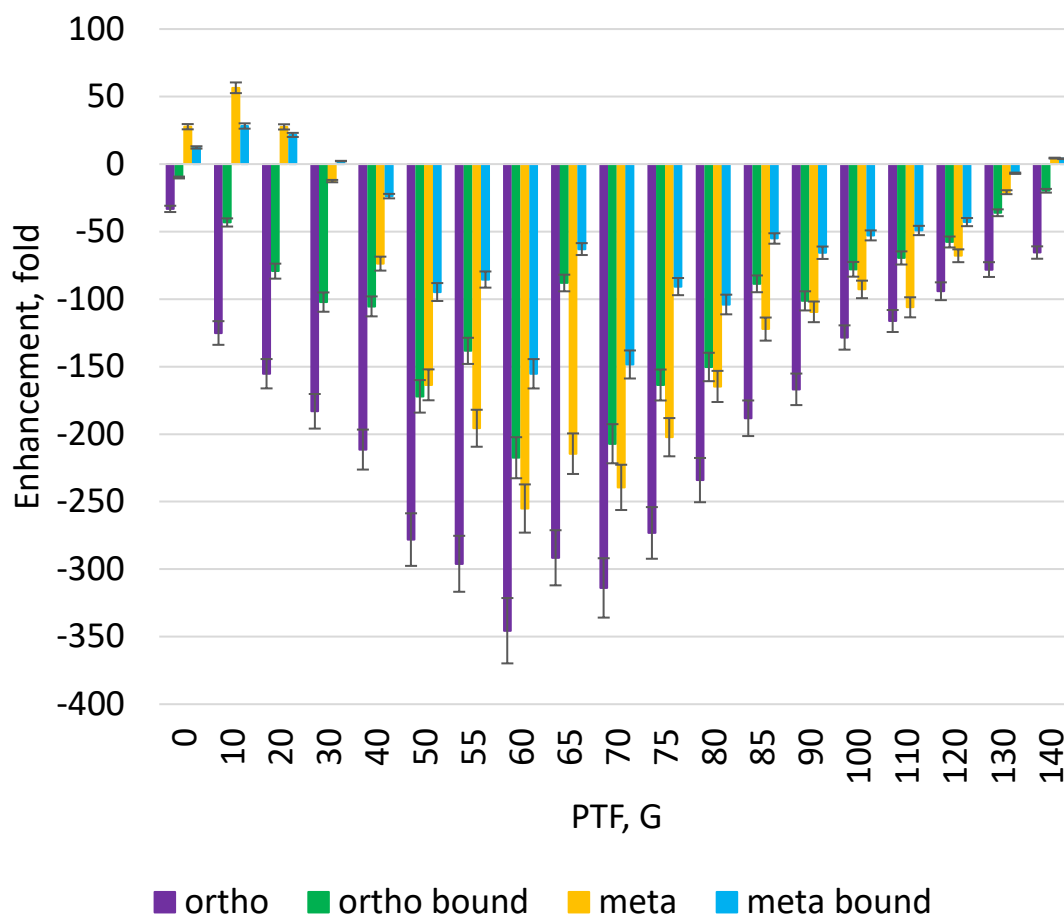


Figure 3.5 Dependence of SABRE enhancement factor on polarisation transfer field (PTF) for 50 mM of **4-AP** (10 equivalents relative to catalyst **1**) in methanol- d_4 . 7% error bars represent the standard deviation determined in section 3.5.1.

The SABRE enhancement factors for both the metal-bound and free substrate signals exhibit similar PTF dependence curves. The *ortho* and *meta* proton resonances of the free substrate show maximum SABRE enhancement at around 60 G and the bound substrate protons follow the same trend. Additionally, for the *meta* proton in bound and free substrate molecules, a change in sign of the SABRE enhancement factor is observed at 30 G. This PTF dependence is similar to other N-heterocyclic compounds such as pyridine, pyrazinamide and nicotinamide, which also reveal a maximum at around 60 G.^{43, 74, 78, 80} The sign change of the enhancement factor with PTF has been reported before but has not been fully understood.⁷⁴ Potentially it can be caused by the competition between direct and indirect polarisation transfer from the hydrides to the *meta* proton via the *ortho* proton.⁵⁶ Here, directly transferred hyperpolarisation refers to the

polarisation that has been transferred from the hydrides to the substrate nuclei without the involvement of an additional spin, while the hyperpolarisation shared within the molecule via the J couplings is considered indirect.

The PTF dependence for 50 mM (10 eq relative to the iridium catalyst **1**) of **4-PBA** was acquired following the same procedure and the results are presented in Figure 3.6. The SABRE enhanced spectra were acquired with 83% active catalyst in solution and the variable PTF measurements were performed in a random order to account for solvent evaporation during the experiment.

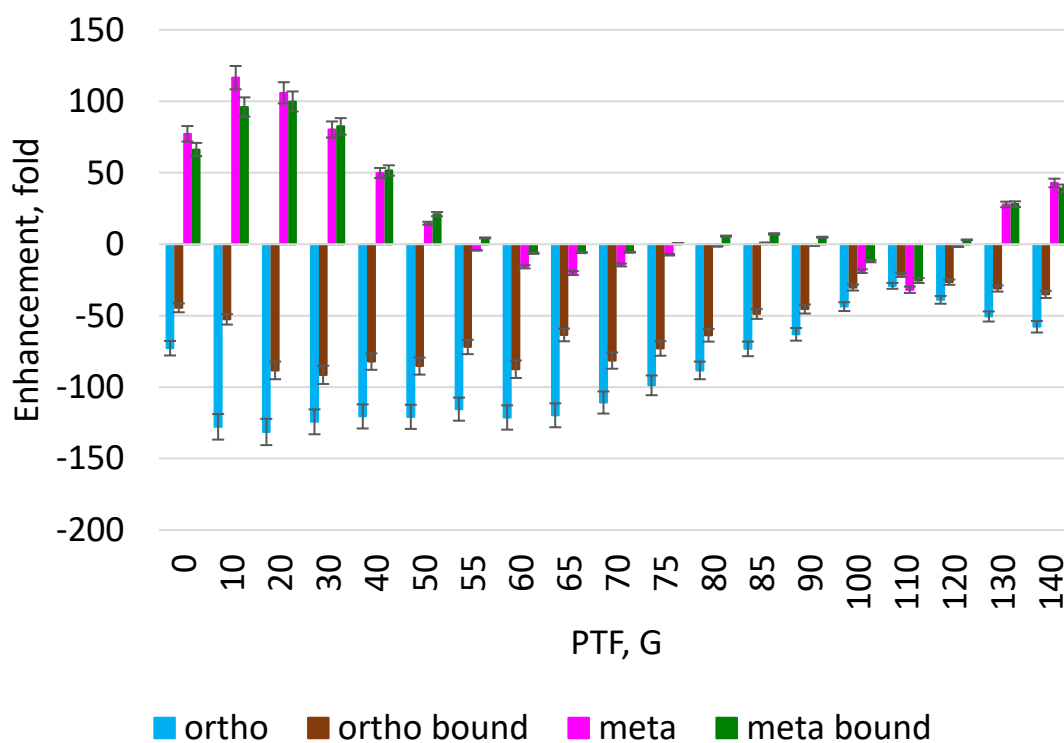


Figure 3.6 Dependence of SABRE enhancement factor on the polarisation transfer field (PTF) for 50 mM (10 equivalents relative to catalyst **1**) of N-(4-pyridyl)benzamide. 7% error bars represent the standard deviation determined in section 3.5.1.

Similar to the **4-AP** example, both bound and free **4-PBA** signals follow the same PTF dependence curves. However, in this case the maximum enhancement factor for the *ortho* proton resonance is observed at two different PTF values of 20 G and 60 G, and one maximum for the *meta* proton resonance at 20 G. Enhancements for the *ortho* protons are

comparable from 10 G to 70 G and thus show less dependence on PTF in this range. The *meta* proton response shows multiple changes in the sign of the SABRE created magnetisation at 55 G, 80 G, 100 G and 120 G. Therefore, the PTF dependence for **4-PBA** is significantly different from the trends observed for **4-AP**. A PTF curve similar to the one observed for **4-PBA** has been reported for isoniazid.⁸⁰ No particular dependence on the PTF plot can be drawn from the electronic effects of the substituents.^{74,80} It has been suggested that the form of the curve is caused by the differences in chemical structure and angle of binding of the substrates, and therefore, *J* coupling network in the SABRE complex.⁸⁰

The PTF curves can be used to optimise SABRE signal enhancements. In addition, the differences in these substrates' PTF curves can be used to resolve overlapping peaks by selectively hyperpolarising one substrate over another when in a mixture. For example, the *ortho* proton of **4-AP** and the *meta* proton of **4-PBA** appear close in chemical shift at 7.97 ppm and 7.86 ppm, respectively, and can overlap due to line broadening in a SABRE ¹H NMR spectrum. This can be resolved by acquiring SABRE ¹H NMR spectra at a range of PTF values between 80 – 90 G, where the NMR signal of the **4-PBA meta** proton is not enhanced and the **4-AP ortho** proton enhancement is –167 – –234-fold. Thus, the **4-AP ortho** proton can be detected individually without overlap with the peak from **4-PBA meta** proton. In contrast, at 0 G the **4-PBA meta** proton absolute enhancement is 2.3-times higher than that of the **4-AP ortho** proton. Accounting for the difference in signs of the enhancements of these protons when summed, the **4-PBA meta** proton will still be positively enhanced by about 44-fold which allows for its selective detection.

3.4.2 Effect of substrate concentration on SABRE enhancement

3.4.2.1 Introduction

The concentration dependence of the SABRE response has been studied previously.^{74, 121, 122} The SABRE-enhanced NMR signal has been shown to depend on the concentration of both the substrate and the catalyst

as they control the effective residence time of the substrate on the catalyst. Larger NMR signal enhancements have been observed when reducing the concentration of substrate relative to the catalyst because in this case more of the substrate molecules are likely to interact with the catalyst and obtain hyperpolarisation.^{74, 95, 122} At the lower substrate concentrations relative to the catalyst, the SABRE signal decreases as there are not enough substrate molecules to stabilise the SABRE complex and so additional Ir complexes, often involving binding of the solvent, can form.^{99, 122} In contrast, the effective time-averaged relaxation times of the free substrate have been shown to decrease with the higher catalyst to substrate ratio for many SABRE systems, which can lead to NMR signal decrease because it takes a finite time to move the sample to the point of measurement.^{74, 121} This effect will be discussed in more detail in Chapter 5.

Another factor which contributes to the effective SABRE enhancement is substrate exchange rate. The SABRE signal dependence on substrate relaxation time and concentration links to the lifetime of the SABRE active complex, which is controlled by its kinetic behaviour.⁷⁶ The substrate has to be bound to the catalyst for long enough for significant hyperpolarisation transfer to occur but not for so long that substrate depolarisation through relaxation dominates. It has been shown that the exchange of both the substrate and the *p*-H₂ involve substrate dissociation and the formation of a 16-electron five-coordinate complex of the type [Ir(H)₂(IMes)(substrate)₂]Cl (Figure 3.7).⁹⁵ The rate of loss of substrate is independent of substrate concentration in accordance with a dissociative exchange pathway.⁹⁵

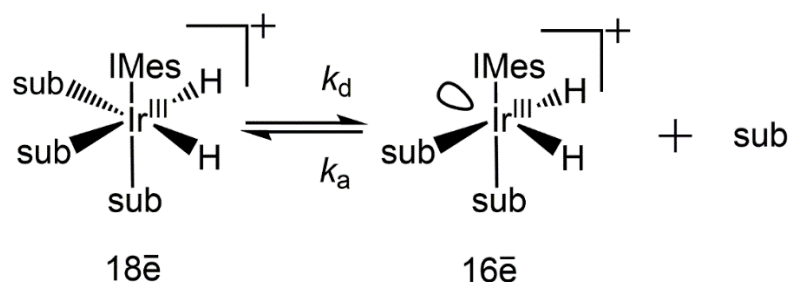


Figure 3.7 Dissociative substrate exchange pathway.

This process has been investigated by measurements of pyridine dissociation rate through EXSY methods for a range of different SABRE catalysts and this value has been compared to the resulting pyridine NMR signal enhancement levels achieved under these conditions.¹²¹ The catalyst, with what is termed optimal binding strength and, therefore, rate of dissociation, appeared to be $[\text{Ir}(\text{H})_2(\text{IMes})(\text{pyridine})_3]\text{Cl}$, which provided the highest enhancement levels for pyridine signal.¹²¹ Once the intermediate 16-electron five-coordinate complex is formed, it can undergo binding of either *p*-H₂, solvent or substrate. Thus, the reassociation of substrate should be dependent on its concentration and compete with the other two reaction pathways. In addition, the strength of the substrate-catalyst bond is likely to control the size of the *J* coupling between the hydride and substrate nuclei, which is the driving force of hyperpolarisation transfer. Recent studies are beginning to investigate this effect but it is complex and is not yet well understood.^{40, 78}

A study performed by Eshuis *et al.* has provided information on how substrate concentration affects the SABRE enhancements at trace substrate loadings in the presence of an excess of strongly ligating co-substrate.⁴⁵ The authors report a linear increase in SABRE NMR signal intensity with concentration of substrate as the exchange of the substrate on the catalyst is now in a pseudo first-order kinetic regime. Due to the SABRE complex stabilisation by the co-substrate, the concentration of the 16-electron complex discussed earlier is assumed to be constant as well as the *p*-H₂ concentration. Therefore, only substrate concentration affects the formation of the SABRE complex containing the bound target substrate for hyperpolarisation. However, the effect of non-hyperpolarised H₂ present in solution and hyperpolarisation transfer to the co-ligand in this process must be self-compensating. Additionally the differences in substrate relaxation within the complexes formed in the presence of the co-ligand are assumed negligible. The detection limit, where these conditions remain true has been found to be $< 1 \mu\text{M}$ of substrate.⁴⁵

To conclude, the effect of the SABRE catalyst and H₂ and substrate concentrations on the SABRE response is complex and in the absence of a robust theoretical model has to be explored empirically for the specific substrate and SABRE conditions used. This is especially true if an optimized response is desired and clearly reflects a current limitation of SABRE more generally. However, developing a quantitative model is still possible in principle because the SABRE enhancement results are reproducible.

3.4.2.2 Results

In this part of the study, the dependence of the SABRE NMR signal intensity on the **4-PBA** concentration in the mM range is explored. For this purpose, various relative concentrations of the substrate were used with a constant absolute catalyst concentration. The resulting SABRE NMR signal was measured using the flow system as previously described, at a specified PTF once the catalyst had been fully activated. The sample loadings of **4-PBA** were in the range of 2.5 - 10 equivalents relative to pre-catalyst **1** at 5 mM in methanol-*d*₄. The resulting PTF dependence plots over the range 0.5-140 G were measured. As a change in sign of the amplitude of magnetisation of the *meta* proton signal of **4-PBA** is observed with a change in PTF, absolute enhancement levels are presented. All of the resulting enhancement-concentration curves show the same trend regardless of PTF value and thus the graph for 65 G is shown in Figure 3.8. Determining the enhancement level for the signal arising from the *meta* protons of the bound substrate suffers in accuracy due to overlap with other signals from species within the sample. Therefore, the data for the *meta* peak of the bound substrate are not presented.

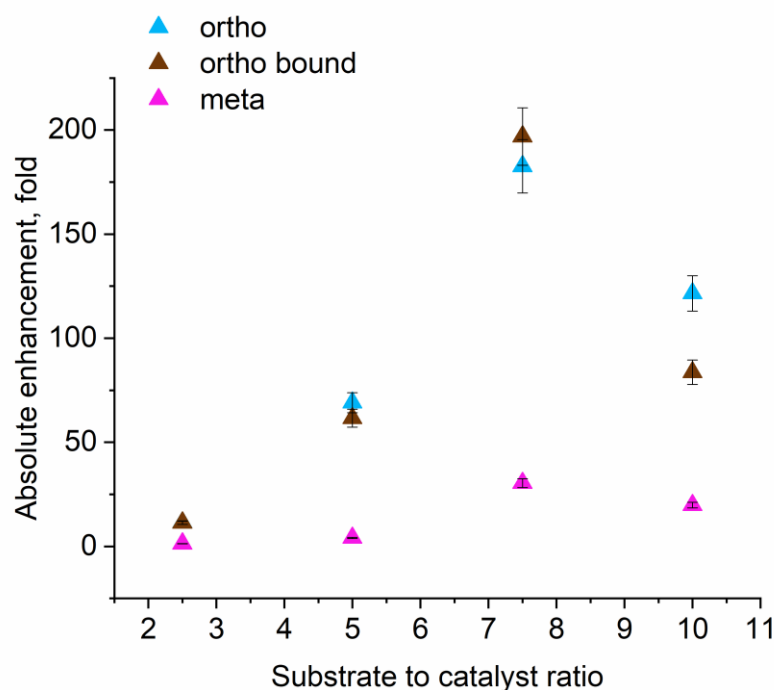


Figure 3.8 Dependence of the absolute SABRE enhancement factor on the substrate to pre-catalyst ratio for **4-PBA** acquired at PTF = 65 G in methanol- d_4 at 9.4 T. 7% error bars represent the standard deviation determined in section 3.5.1.

As Figure 3.8 shows, the level of the SABRE enhancement is not constant, which is the requirement for a linear increase of SABRE signal with concentration as is expected for a standard thermally polarised NMR signal. The maximum signal enhancement (~190-fold) was detected for both free *ortho* and *meta* protons at 7.5 equivalents of the substrate relative to the pre-catalyst **1** which corresponds to a 37.5 mM substrate concentration. It is suggested that this reflects the minimal substrate concentration for the stabilisation of the active SABRE complex with this substrate. A higher substrate to catalyst ratio is required for **4-PBA** compared to the other systems, for example in case of pyridine and nicotinic acid, where around 4 or 5-fold substrate excess gives the maximum enhancement.^{121, 122} This can be explained by the weak binding strength of **4-PBA**. The observed concentration dependence is in agreement with a complex interplay between relaxation time, which reduces with lower substrate to catalyst ratio, and the changes in the rates of ligand exchange due to substrate and *p*-H₂ binding. However, from such measurements an optimal concentration is suggested, at which the maximum SABRE signal

gain can be achieved. In this case further measurements would be required between 7.5 and 10 equivalents to produce a more accurate value.

3.5 Detection with SABRE of the compounds in mixtures

The hyperpolarisation of a mixture of several compounds at the same time using SABRE has been reported by Daniele *et al.*¹²³ and studied in a quantitative manner by Eshuis *et al.*¹²⁴ However, while a linear dependence was found for nanomolar concentration levels in the presence of a high relative concentration of a co-substrate, the challenge to quantify at higher concentration and in the absence of a co-substrate remains. Indeed, even in the low-concentration regime there remain some unanswered questions because there are multiple active SABRE complexes present in solution. The ability of these complexes to transfer hyperpolarisation would be expected to be different unless the J coupling network is the same in each complex. In addition, the bound substrate relaxation time is expected to change depending on the other ligands in the complex, while the relative concentrations of the SABRE complexes can change with the ligand concentration. These effects must be self-compensating, due to the similarities in structures of the substrates leading to the linear SABRE signal dependence on concentration observed by Eshuis *et al.*¹²⁴ It should be emphasised that these papers were published after the evaluations below were completed. In addition, the effect of PTF on the hyperpolarisation levels shown in a mixture of compounds of similar concentrations has not been described in the literature.

So far in this study, the SABRE polarisation of **4-AP** and **4-PBA** has been observed separately. Now our aim is to explore the hyperpolarisation of mixtures of the two compounds in order to calibrate the SABRE signal response and to create a model for subsequent quantitative reaction monitoring experiments. This is necessary because under reaction monitoring conditions both the starting material and product would be polarised through SABRE in the same measurement. Consequently, the following questions have to be answered: a) can these two substrates be

polarised at the same time from within a mixture? b) can the signals of these polarised compounds be distinguished from one another in the mixture? c) how does the level of polarisation observed for the two compounds in such a mixture depend on the PTF? and d) how is polarisation distributed between the two compounds in a mixture as a function of their relative concentration?

In this section the viability of the hyperpolarisation of both **4-AP** and **4-PBA** in a mixture is tested and the reproducibility of these measurements is investigated. The preliminary measurements were performed in order to explore the dependence of the SABRE hyperpolarisation level for **4-AP** and **4-PBA** in these mixtures as a function of the PTF and concentration (0 - 50 mM, see experimental section 9.5.1.2 for more details).

In order to test the viability of the hyperpolarisation of these two compounds at the same time, a SABRE enhanced ^1H NMR spectrum of a **4-AP** and **4-PBA** (5 eq : 5 eq relative to the pre-catalyst **1**) mixture was acquired after polarisation transfer in a PTF of 65 G. In this mixture the total substrate concentration was kept the same as in the samples of the individual compounds (Figure 3.3 and Figure 3.4). The resultant SABRE enhanced NMR spectrum along with a reference thermally polarised NMR spectrum are shown in Figure 3.9.

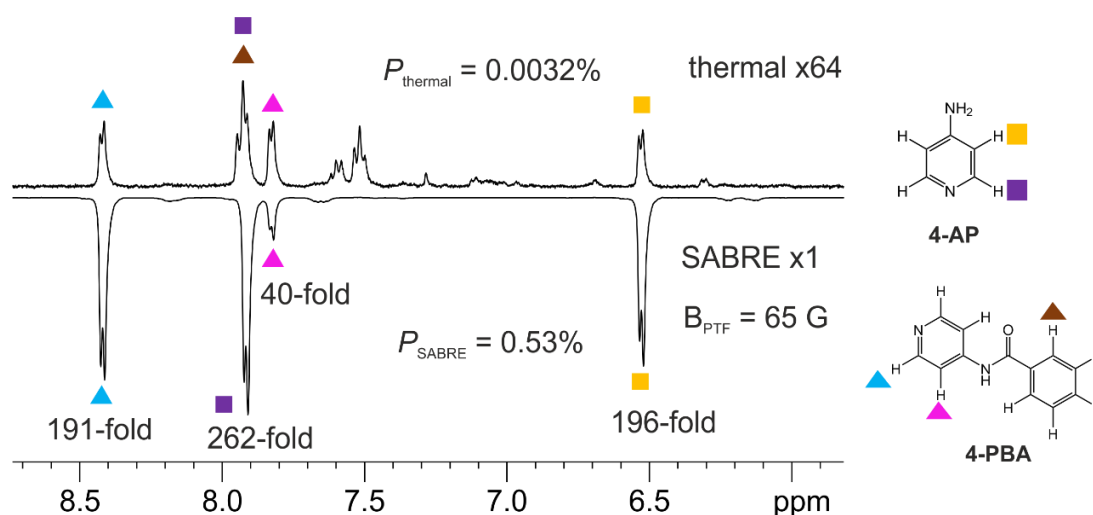


Figure 3.9 Comparison of 1 scan thermal (64-fold vertical expansion) and SABRE ^1H NMR spectra of a mixture of **4-AP** (5 eq rel. to **1**) and **4-PBA** (5 eq rel. to **1**) in methanol- d_4 in the presence of the active catalysts based on $[\text{Ir}(\text{H})_2(\text{IMes})(\text{4-AP})_x(\text{4-PBA})_{3-x}]\text{Cl}$ where $x = 0, 1, 2$ and 3 . The overall SABRE polarisation level for this mixture was estimated as 0.53%, compared to 0.0032% for the Boltzmann derived polarisation.

The SABRE-enhanced NMR spectrum in Figure 3.9 shows that all of the ^1H NMR signals due to free **4-AP** and **4-PBA** are enhanced. The chemical shifts of these resonances match those seen for the individual compounds in the presence of the corresponding SABRE complex. Both the *ortho* and *meta* ^1H NMR signals of free **4-AP**, and the *ortho* signal from free **4-PBA** are in fact strongly hyperpolarised, but the **4-PBA** *meta* proton shows little enhancement after polarisation transfer at 65 G. This behaviour is similar to that seen for the SABRE spectra of the individual substrates in Figure 3.3 and Figure 3.4. The corresponding thermal NMR signals are displayed in the upper trace for reference.

Even though the signal for the *ortho* proton of **4-AP** overlays with a peak of **4-PBA** that does not become SABRE polarised, the large SABRE gain means that it shows only a very limited distortion due to peak overlap. An enhancement factor for this *ortho* proton signal was calculated by using the thermal reference integral of the *meta* proton. The enhancement factors of the **4-AP** proton resonances were both found to decrease by 9% on average, while those for **4-PBA** increased by 43% on average when in the mixture relative to the corresponding values for the pure compounds when present at a 10 equivalent level relative to the catalyst. When compared to the

enhancements obtained from the sample of 5 equivalents of the **4-PBA** to the catalyst an increase of 77% on average was observed. This effect can be explained by **4-AP** exhibiting stronger binding that stabilises the active SABRE complexes. Thus, in this case, the SABRE signal enhancement of one substrate benefits from the presence of the other substrate in solution. In conclusion, Figure 3.9 shows that more than one compound can be polarised at the same time and, in this case, the selectivity of hyperpolarisation makes the peaks of the two substrates distinguishable despite the overlap in the thermal spectrum. The selectivity of hyperpolarisation will be particularly beneficial in the case of low-field NMR spectroscopy applications where there is reduced chemical shift dispersion.

In order to obtain information about the complexes that are formed from $[\text{Ir}(\text{Cl})(\text{COD})(\text{IMes})]$ upon reaction with **4-AP**, **4-PBA** and H_2 , a ^1H NMR spectrum of the hydride region was acquired for the same sample containing a 5 eq : 5 eq mixture of **4-AP** and **4-PBA**. There are 6 possible products that can be formed in the presence of the two substrates (Figure 3.10a). The SABRE ^1H NMR spectrum of the hydride region of the **4-AP** and **4-PBA** (5 eq : 5 eq) mixture is presented in Figure 3.10b.

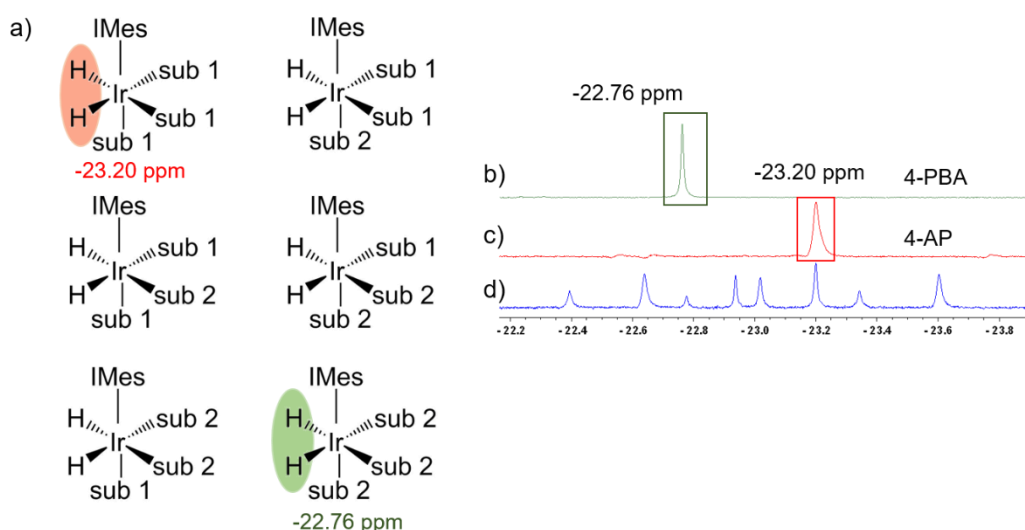


Figure 3.10 a) Combinations of SABRE complexes which can form in the presence of two substrates in solution. The SABRE ^1H NMR spectra of the hydride region of (b) pure **4-PBA**, (c) pure **4-AP** and (d) the 5eq:5 eq mixture of **4-AP** and **4-PBA**.

A comparison to the SABRE spectra of samples containing the individual substrates, confirms the presence of the 6 species as predicted (Figure 3.10). As expected, the tris-**4-AP** complex $[\text{Ir}(\text{H})_2(\text{IMes})(\text{4-AP})_3]\text{Cl}$ dominates due to the stronger binding of **4-AP**. The less intense hydride peak associated with the tris-**4-PBA** complex, $[\text{Ir}(\text{H})_2(\text{IMes})(\text{4-PBA})_3]\text{Cl}$ is also observed. This suggests that the other dominant complexes contain two **4-AP** bound molecules. The previous results show that the complex containing **4-AP** is significantly more efficient in SABRE hyperpolarisation transfer compared to the complex with **4-PBA** only. This correlates with the higher enhancement of the hydride resonance for this complex in the SABRE ^1H NMR spectrum in Figure 3.10. However, in order to investigate the relative ratio of these 8 complexes, a complete characterisation will be required. It is also unclear whether all of the detected complexes contribute to the **4-AP** and **4-PBA** hyperpolarisation. SABRE 2D NMR spectroscopy could be used to provide more information about this.

In conclusion, SABRE ^1H NMR signals of **4-AP** and **4-PBA** at millimolar concentration levels in a mixture were detected. A comparison of the hyperpolarised signals for the samples of the individual compounds and in the mixture showed increased SABRE signals from **4-PBA** protons in the presence of **4-AP** and the SABRE catalyst, while decreased signals from **4-AP**. The peaks for the *ortho* proton of **4-PBA** and the *meta* proton of **4-AP** are well separated in the hyperpolarised spectrum, which is of benefit for future applications in low-field NMR spectroscopy. The analysis of the hydride region of the SABRE enhanced ^1H NMR spectrum of the mixture revealed that 8 complexes are formed, as expected, for a mixture of **4-AP** and **4-PBA**; however, a full understanding of their individual contributions to the hyperpolarised signals would require further study.

3.5.1 Reproducibility study

In order to employ the hyperpolarisation of mixtures to develop a quantification model for reaction monitoring, the reproducibility of the SABRE NMR signal measurements has to be investigated. The variability in

the measurements performed using the flow system for hyperpolarisation have been reported previously as 5-6%.^{42, 74} Here, the reproducibility for a mixture of the compounds is studied, assessing the absolute enhancement factors and the intramolecular and intermolecular signal ratios.

This study was performed on a 5 eq : 5 eq mixture of **4-AP** and **4-PBA** with PTF = 65 G using the automated system for hyperpolarisation. A thermal ¹H NMR spectrum was acquired after each respective SABRE enhanced spectrum. This reference spectrum was used to compute the SABRE ¹H NMR signal enhancement values in order to reduce the contribution of solvent evaporation to the error in the measurements. In Figure 3.11a-d the enhancement factor for 11 repeated measurements is presented along with the mean (solid line) and the standard deviation from the mean (dashed lines) for the *ortho* and *meta* proton signals of **4-AP** and **4-PBA**. The reproducibility errors for the thermal and SABRE enhanced signal measurements, and enhancement factors calculated from them are presented in Table A1 in Appendix. Both substrates yield SABRE signal enhancements that exhibit a 1– 3% standard error and a 4-7% standard deviation over the 11 repeat measurements. The *meta* signal of **4-PBA** suffers from the highest deviation.

In order to show the reproducibility of the distribution of hyperpolarisation among the **4-AP** and **4-PBA** protons in the mixture, the intermolecular and intramolecular ratios of the ¹H NMR signal enhancements were calculated for each measurement. For instance, the *ortho* : *ortho* of **4-AP** : **4-PBA** and *ortho* : *meta* of **4-AP** enhancement ratios are presented in Figure 3.11e-f.

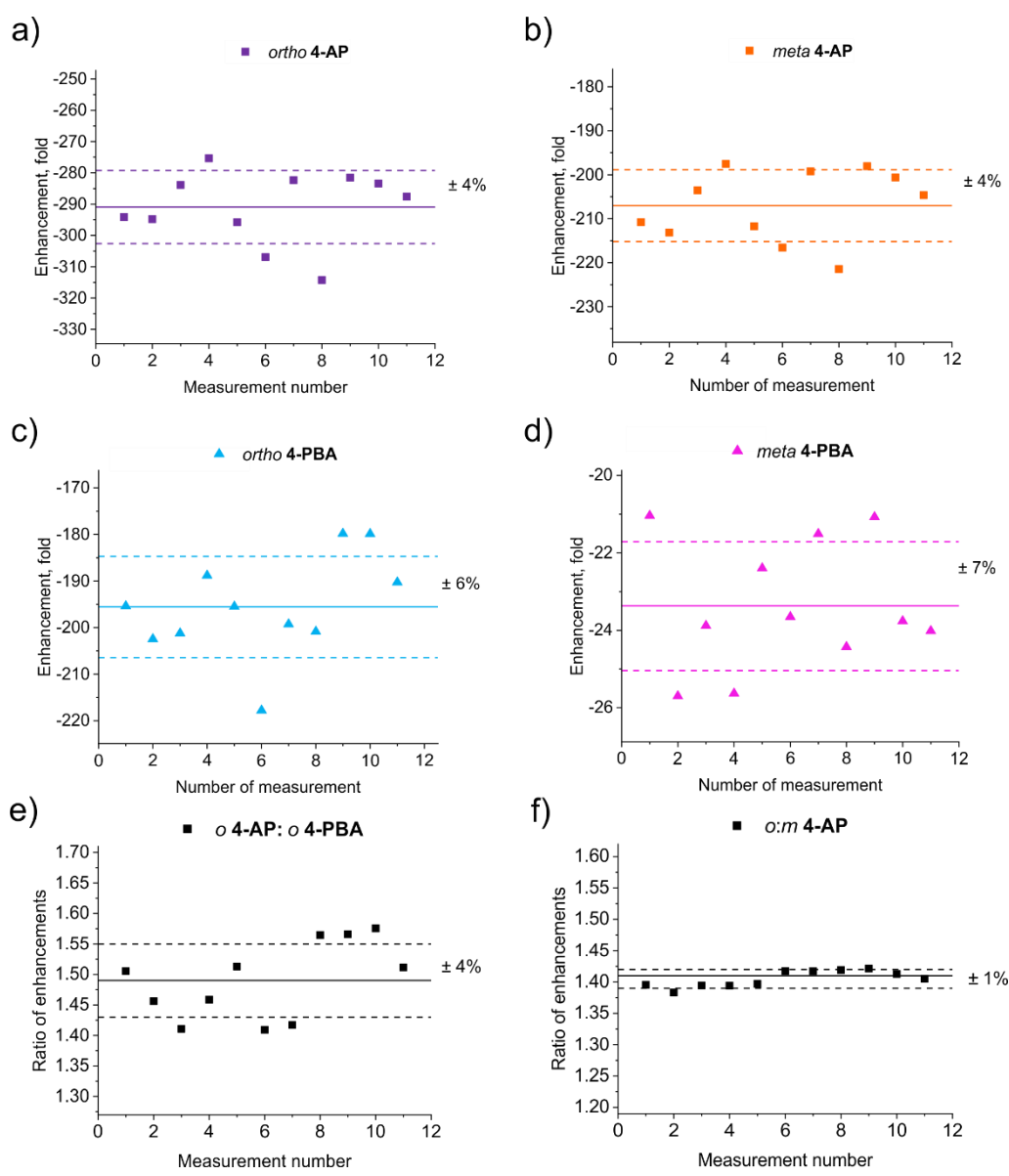


Figure 3.11 Reproducibility of the enhancement values for **4-AP** *ortho* (a) and *meta* (b) protons and **4-PBA** *ortho* (c) and *meta* (d) protons in a 5 eq: 5 eq mixture acquired with PTF = 65 G. Reproducibility of the ratios of the enhancements (e) of the *ortho* and *meta* protons within **4-AP**, and (f) of the *ortho* protons of **4-AP** and **4-PBA**, respectively. The mean enhancement value (solid line) and one standard deviation from mean (dashed lines) and percentage standard deviation are presented in each graph. Each graph y-axis is scaled to $\pm 15\%$ from the mean.

The ratio of the enhancements within the compound and between the two compounds yield a 0.3% standard error (1% standard deviation) for **4-AP** and 1.3% (4% standard deviation) for the ratio of the **4-AP** and **4-PBA** *ortho* protons. In this case, the distribution of the hyperpolarisation via *J* coupling within the molecule is more consistent than that between the two compounds in the mixture, where there are several complexes capable of SABRE. Noteworthy is the fact that the ratio of the **4-AP** enhancements are

more consistent than the individual enhancements of the **4-AP** *ortho* and *meta* protons. This confirms, as recently reported by P. Richardson *et al.*, that the distribution of SABRE hyperpolarisation within a molecule is highly reproducible and is more consistent than individual proton enhancement factors.⁴² The deviation in the ratios of the other **4-AP** and **4-PBA** proton enhancements were less consistent due to the high individual standard error of the **4-PBA** *meta* proton (2.2%). This led to the 2.4% standard error for the intramolecular ratio of the **4-PBA** *ortho* and *meta* proton enhancements and around 2.3% standard error for the intermolecular *meta* : *meta* **4-AP** : **4-PBA** and *ortho* : *meta* **4-AP** : **4-PBA** enhancement ratios. The *meta* : *ortho* **4-AP** : **4-PBA** possess a standard error of 1.2% as it does not include the highly variable **4-PBA** *meta* proton enhancement. Thus, for the **4-PBA** the reproducibility of the intramolecular enhancement ratio is less consistent than the individual proton enhancement factors. The data for the enhancement factors and their ratios for **4-AP** and **4-PBA** are summarised in Appendix (Table A2, Table A3).

In summary, the reproducibility of the enhancement factors for **4-AP** and **4-PBA** in a mixture was assessed and showed < 7% standard deviation for all resonances. The reproducibility of the ratio of the enhancement factors was shown to be more consistent for **4-AP**, and thus, can be used instead of the absolute values for quantification. However, this was not the case for the **4-PBA** substrate due to variability in *meta* proton enhancement factors. This approach can take account of variations in hyperpolarisation levels due to inconsistency in experimental parameters, like level of generated *p*-H₂, sample transfer time and solvent evaporation. Some of these parameters, like *p*-H₂ level and transfer time, are controlled by the flow system, however, some variations still exist and are reflected in the measured enhancement factors. Another source of the deviation in SABRE signal is provided by the process of ²H-¹H exchange in the substrate, catalysed by the activated SABRE complex. This phenomenon will be discussed in detail in Chapter 6. In the studies presented in the current chapter, no significant change in ¹H NMR peak line shape or relative

intensity was observed. Therefore, I infer that only limited or very slow ^2H - ^1H substitution has occurred during these experiments.

3.5.2 SABRE signal dependence on concentration in mixture

The next question of interest is how the ^1H NMR signal enhancements behave as a function of concentration in a mixture. In order to investigate this effect, SABRE ^1H NMR signal enhancements were measured for the *ortho* proton of **4-PBA** at different concentrations in a mixture with **4-AP** and compared to the **4-PBA** response in pure solution. These results are presented in Figure 3.12.

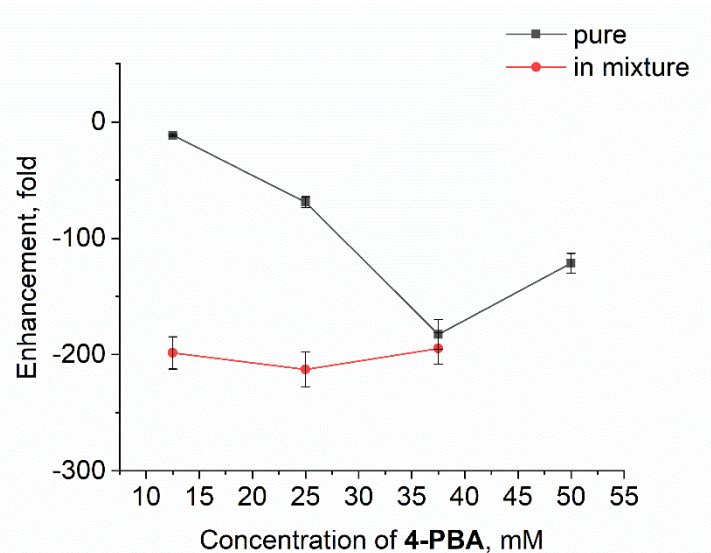


Figure 3.12 Dependence on concentration of the enhancement factor of the **4-PBA** *ortho* proton in pure solution (grey line, square markers) and in a mixture with **4-AP** (red line, circle markers), where the concentration of **4-AP** was varied in such way that the total substrate concentration in the solution was 50 mM. The error bars of 7% represent the standard deviation determined in section 3.5.1.

Figure 3.12 shows that the presence of **4-AP** in solution increases the **4-PBA** enhancement, which is consistent with the enhancement values measured for the 5 eq : 5 eq mixture previously (Figure 3.9). Additionally, the enhancement factors measured in the mixture vary with the concentration in a different way when compared to the trend seen for pure **4-PBA**. The enhancement factors are constant with concentration within the error. This reflects a linear dependence of the SABRE signal on the concentration of **4-PBA**. Indeed, when the SABRE signal is plotted against

the concentration of **4-AP** and **4-PBA** in the mixture, it shows a linear trend for both substrates (Figure 3.13). The slopes of the linear dependence differ for **4-AP** and **4-PBA**, while the intercept was forced to zero to keep the physical meaning of the enhanced signal. The ratio of the SABRE responses for the **4-AP** and **4-PBA** *ortho* protons also scales linearly with the ratio of their concentrations which can be useful for the quantification purposes (Figure 3.13).

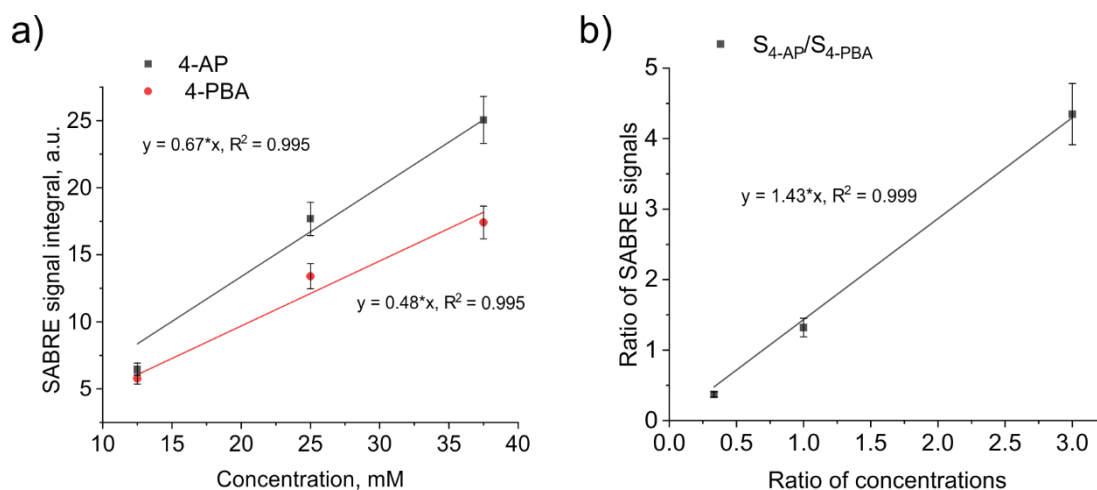


Figure 3.13 a) SABRE signal integral of the *ortho* proton of **4-AP** (grey squares) and **4-PBA** (red circles) as a function of concentration in a mixture. The concentrations of **4-AP** and **4-PBA** were varied in such way that the total substrate concentration in the solution was 50 mM, which is 10 eq relative to the 5 mM SABRE pre-catalyst. b) Ratio of the SABRE signal integrals of the **4-AP** and **4-PBA** *ortho* protons as a function of their concentration ratios. The error bars represent three times the standard deviation for the SABRE signal integral as determined in the reproducibility study discussed above. The error bars represent a standard deviation of 7% in (a), determined in section 3.5.1, and of 10% in (b), calculated using error propagation.

To conclude, the observed results show that the hyperpolarisation of **4-AP** and **4-PBA** in a mixture results in more efficient hyperpolarisation of **4-PBA** present in the mixture. This is explained by the role of more stable complexes containing **4-AP** and suggests that the time **4-PBA** spends on the catalyst is closer to the optimum residence time for hyperpolarisation transfer. The studied concentrations are much higher than the detection limit described in the research by Eshuis *et al.*⁴⁵, nevertheless, constant enhancement of the ¹H NMR signal is observed for both **4-AP** and **4-PBA**. The linearity of the substrate's enhanced signal with the concentration is very promising for quantification purposes, because then a model for

quantification is not required and a simple calibration will suffice instead. The condition described by Eshuis *et al.* is not fulfilled in this case, thus, more investigation is required to understand this effect and to explore the linear concentration range.

3.5.3 *SABRE signal dependence on PTF in mixture*

The next question of interest is how polarisation distributes between the two compounds in a mixture with PTF variation. Due to the mixture of complexes formed in the presence of the two substrates, the PTF dependence of the SABRE response might also vary from the original pure compound profiles. Considering future applications of low-field NMR to mixtures of compounds, the PTF at which both compounds obtain the highest hyperpolarisation and the PTF which allows for the selective detection of the one of the compounds are of interest. Known enhancement factors at a defined PTF will also help to quantify the concentration of the substrate in a mixture.

The mixtures of **4-AP** and **4-PBA** were probed for their SABRE response across the range of PTF = 0.5 - 140 G with concentrations of **4-AP** and **4-PBA** relative to the SABRE catalyst of: 10 eq : 0 eq; 7.5 eq : 2.5 eq; 5 eq : 5 eq; 2.5 eq : 7.5 eq; 0 eq : 10 eq. The comprehensive results are presented in Appendix (Figures A1 – A4). The effect of PTF is demonstrated for the 2.5 eq to 7.5 eq (12.5 mM to 37.5 mM), 5 eq to 5 eq (25 mM to 25 mM) and 7.5 eq to 2.5 eq (37.5 mM to 12.5 mM) mixtures in Figure 3.14. The PTF plot for the pure 50 mM substrate is presented alongside for comparison.

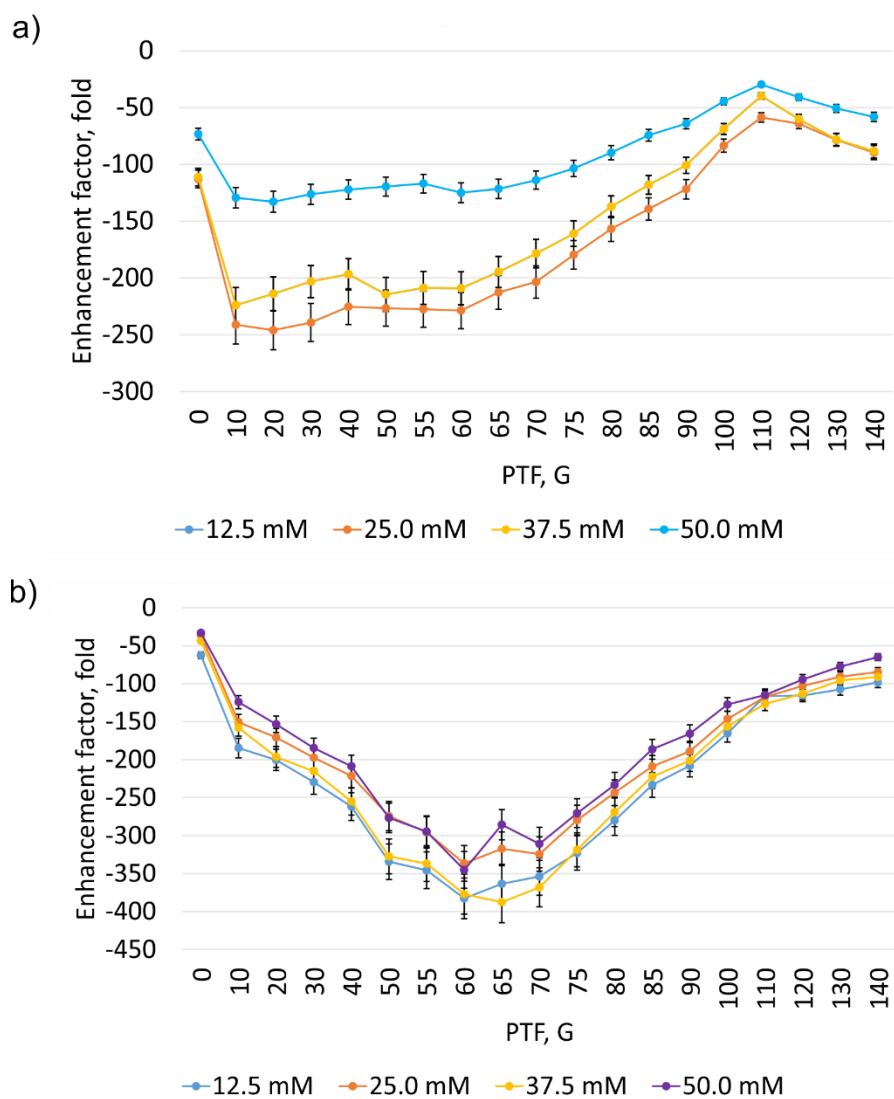


Figure 3.14 Enhancement factor of (a) **4-PBA** and (b) **4-AP** *ortho* protons dependence on PTF at the concentrations of 12.5 mM, 25 mM and 37.5 mM mixture (50 mM total) with the other substrate which is **4-PBA** or **4-AP** respectively and of 50 mM individual substrate solution. The error bars of 7% represent the standard deviation determined in section 3.5.1.

The PTF plots for both substrates yield similar trends with concentration in both the mixture and pure compound studied. In fact, the PTF curves for 12.5 mM and 37.5 mM **4-PBA** in these mixtures overlap with each other as shown in Figure 3.14a. This suggests that the distribution of the hyperpolarisation with polarisation transfer field is not affected by the changes in relative concentration of **4-AP** or **4-PBA** or their mixtures even though the enhancement value itself alters. This can be explained if there is little effect on the J couplings between the observed bound substrate and hydrides within the SABRE complex when the coordination sphere of the catalyst changes. This is supported by an Eshuis *et al.* study which suggests

similar *J* couplings exist in a range of active SABRE complexes employing 5 and 6-membered N-heterocycles.^{78, 125}

The maximum enhancement levels seen for **4-AP** and **4-PBA**, across all the investigated mixtures and PTF values are presented in Table 3.1. The changes in the enhancement factor result from the different PTF fields and concentrations.

Table 3.1 Maximum enhancements for *ortho* and *meta* protons of **4-AP** and **4-PBA** within all mixtures in the range 0-10 eq. of each substrate and in the range of PTF values from 0.5 – 140 G.

	Max. Enhancement factor, fold	Mixture ratio	PTF, G
<i>Ortho</i> 4-PBA	-246 ± 17	5 eq : 5 eq	20
<i>Meta</i> 4-PBA	206 ± 14	5 eq : 5 eq	10
<i>Ortho</i> 4-AP	-388 ± 27	7.5 eq : 2.5 eq	60
<i>Meta</i> 4-AP	-288 ± 20	7.5 eq : 2.5 eq	65

A comparison of concentration-PTF dependences for the mixtures showed that the *ortho* and *meta* protons of **4-PBA** are best polarised in the 5 eq : 5 eq mixture, while the protons of **4-AP** are optimally polarised in the 7.5 eq : 2.5 eq mixture. In spite of the fact that different PTF values give the best enhancement levels for the different resonances, the *ortho* proton of **4-PBA** and the *meta* proton of **4-AP** obtain hyperpolarisation above 0.4 % between 50 G and 80 G in all of the investigated mixtures. For example, at 60 G the enhancement factors are similar for the *ortho* proton of **4-PBA** (-229-fold) and the *meta* proton of **4-AP** (-232-fold) in the 5 eq : 5 eq mixture even though clearly the complexes that derive this enhancement are different. This means both compounds can be seen at trace concentrations with the same level of sensitivity if a single PTF value is used.

The fact that the protons of **4-AP** and **4-PBA** get the highest polarisation with different field settings can be employed for their selective detection. For example, at 30 G along the whole range of mixture

concentrations the *ortho* proton of **4-PBA** has a >200-fold enhancement while the *meta* protons of **4-AP** are poorly polarised <11-fold. For 140 G, the enhancements of the *ortho* protons of **4-PBA** lay from 74- to 90-fold while the enhancements of the *meta* protons of **4-AP** are just 3 - 4-fold. Thus, at 30 G, the dominance of the enhanced **4-PBA** *ortho* proton over the **4-AP** *meta* proton is 20-26-fold and at 140 G it is 24-28-fold. In the same manner, as discussed for the individual compounds in section 3.4.1, the differences in the SABRE enhancement at different PTF can be useful for distinguishing the *meta* proton of **4-PBA** and the *ortho* proton of **4-AP**, which are close in chemical shift and can overlap in a SABRE spectrum, e.g. if a low-field NMR spectrometer is used for detection. At 50 G and 55 G the enhancement of these protons is 12 to 45-times and 15 to 66-times more for the **4-AP** than for **4-PBA** across the mixtures. This allows us to detect the *ortho* proton of **4-AP** with good signal-to-noise even in the presence of the overlapping *meta* **4-PBA** proton peak. In contrast, the SABRE signal of the **4-PBA** *meta* proton exceeds the **4-AP** *ortho* proton counterpart only at 0 G with the benefit of 2-3-times higher enhancement in mixtures.

In general, for sensitivity purposes the PTF that gives the highest signal strength should be exploited in any detection study unless selectivity is required. The fact that the PTF plots for both substrates demonstrated similar trends in both the mixtures and pure compound studies, allows for the prediction of how the SABRE signal is going to scale with the PTF in reaction monitoring studies. The distribution of hyperpolarisation with the PTF was similar at different substrate concentrations, thus, the linearity of the SABRE response with the substrate concentration remains at different PTF values. This is a useful result for reaction monitoring applications as selective and quantitative detection could be achieved.

3.5.4 Polarisation of mixtures at 1 T

A preliminary study of the hyperpolarisation of **4-AP** and **4-PBA** in a mixture was completed using a low-field (1 T) benchtop NMR spectrometer. In this case, the hyperpolarisation process was conducted manually rather

than using a flow system. The same dependence of SABRE enhancement factors on PTF and concentration are expected. However, at low field (1 T) the ppm scale is compressed, as 1 ppm is equal to 43.3 Hz instead of 400.2 Hz at 9.4 T. This leads to reduced chemical shift dispersion. In this experiment the possibility to distinguish the hyperpolarised peaks in the low field regime was probed. Figure 3.15 presents thermal and hyperpolarised ^1H NMR spectra of the **4-AP** and **4-PBA** mixture (5 eq to 5 eq) acquired with 1 scan using a 1 T (43 MHz) benchtop NMR spectrometer.

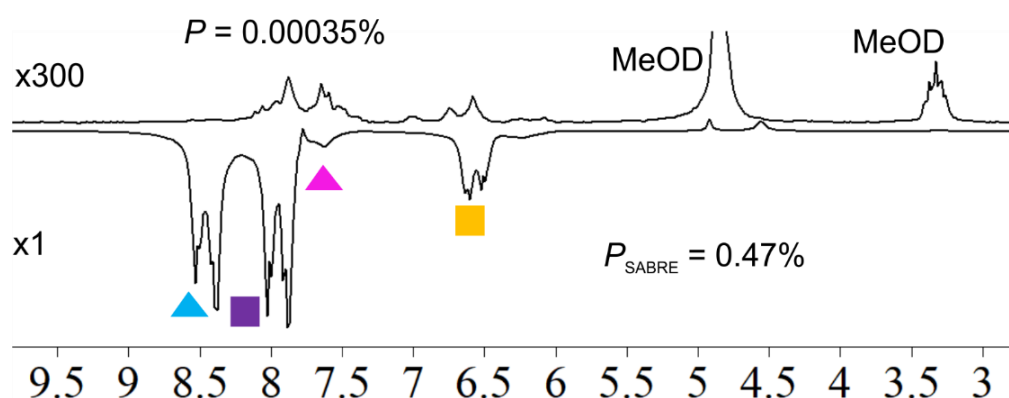


Figure 3.15 Comparison of 1 scan thermal (300-fold scaled) and SABRE ^1H NMR spectra of **4-AP** (5 eq) and **4-PBA** (5 eq) mixture in methanol- d_4 .

The 1 T SABRE NMR spectra of the **4-AP** and **4-PBA** mixture show just three hyperpolarised peaks because those for the *meta* proton of **4-PBA** and *ortho* proton of **4-AP** overlap. The two most separate peaks for the two compounds are of the most interest for reaction monitoring purposes on the low field NMR spectrometer. For this system, those are the **4-PBA** *ortho* proton and **4-AP** *meta* proton positions. While the intrinsic population difference at lower field is smaller, using SABRE hyperpolarisation measurements with benchtop NMR still yields high ^1H NMR signal strengths. The actual enhancement factor is dependent on the magnetic field of the spectrometer (B_0) because the polarised integral is divided by the thermal reference integral, which is field-dependent. Therefore, in order to provide a direct comparison, the SABRE polarisation percentage is presented. Note, thermal polarisation constitutes 0.0033 % at 9.4 T and is 0.00035 % at 1 T, at 295 K for ^1H . A comparison of the 9.4 T (Figure 3.9) and 1 T values reveals similar levels of polarisation (0.53 % and 0.47 %)

result in both cases, which allows for high levels of sensitivity at low field. Thus, here it has been shown that the **4-AP** and **4-PBA** peaks can be detected separately and high ^1H NMR signal strengths can be observed for these compounds using SABRE hyperpolarised benchtop NMR.

3.6 Conclusions

In this chapter the dependence of the SABRE response on PTF and the relative concentration of the substrate was probed for an N-heterocyclic amine and amide. The SABRE responses from **4-AP** and **4-PBA** at various relative concentrations and PTF values were measured in the range of concentrations from 0 to 50 mM for each substrate alone and in a series of mixtures (2.5 eq : 7.5 eq, 5 eq : 5 eq, 7.5 eq : 2.5 eq) and for PTF values between 0.5 and 140 G. Higher enhancement factors were observed for **4-PBA** in the presence of **4-AP**. This is explained by the higher binding strength of **4-AP** compared to the **4-PBA** which results in the stabilisation of the SABRE complex. Differences in the PTF curves were observed for **4-AP** and **4-PBA**. However, the PTF trends were similar in both the pure solutions and in the mixtures of **4-AP** and **4-PBA**. The differences in the SABRE ^1H NMR signal within the PTF range for **4-AP** and **4-PBA** could be used to aid with their selective detection in mixtures of the two. For example, the **4-AP** free *ortho* proton signal is 15- to 66-times higher in enhancement factor than that of **4-PBA** across the studied mixtures when the SABRE enhanced spectrum is measured at 55 G. Thus, **4-AP** *ortho* proton can still be detected with significant signal-to-noise ratio even if it overlaps with the *meta* proton signal of **4-PBA**. For instance, this approach can be applied when using a low-field NMR spectrometer for detection where signal frequency differences are reduced. At the same time, the *ortho* proton of **4-PBA** and the *meta* proton of **4-AP** were found to yield enhancement factors above 137-fold across all of the studied mixtures and a wide range of PTF values (50 – 80 G). This means that even if a single PTF value is used, significant sensitivity can be achieved.

Promising results were obtained by measuring the concentration dependence of the enhancement factors for **4-AP** and **4-PBA** in mixtures. The enhancement factors measured for **4-PBA** and **4-AP** in mixtures and at different PTF values were found to be independent of concentration within the error. This means that there is a linear dependence on the SABRE signal strength with concentration of each component of the mixture, when the total concentration is kept constant. Additionally, the ratio of the SABRE responses for the **4-AP** and **4-PBA** *ortho* protons also scaled linearly with the ratio of their concentrations. These linear effects are observed for samples at much higher concentrations than those reported previously and suggest our ultimate goal of quantitative reaction monitoring through a SABRE signal is viable.⁴⁵ As a consequence, a complicated analytical model is not required, and a simple calibration curve can be used. This a valuable result as both selective and quantitative detection can be achieved. However, in order to obtain a reliable quantification method, more rigorous investigation would be required to explore the limits of the range over which the SABRE response is linear.

Finally, preliminary studies using a low field (1 T) benchtop NMR spectrometer showed comparable polarisation levels to the high field spectrometer results. The *ortho* proton of **4-PBA** and the *meta* of **4-AP** are strongly hyperpolarised and well separated even at low field, and thus, can be used to characterise the two compounds if applied to reaction monitoring with high or low field NMR detection. In addition, high reproducibility of the ratio of the enhancements can aid in overcoming peak overlap, for example the integral of the overlapping peak can be found from its known ratio to another hyperpolarised peak. Therefore, this confirms the viability of the detection of mixtures at millimolar concentration with hyperpolarised low-field NMR spectroscopy, which is a lower cost option when compared to classic high field analysis.

The compounds **4-AP** and **4-PBA** investigated here will be used to explore reaction monitoring using SABRE enhanced ¹H NMR signal in Chapter 4.

Chapter 4: Reaction monitoring with SABRE-hyperpolarised NMR

4.1 Introduction

Here, reaction monitoring through the SABRE signal response is investigated using high-field ^1H NMR detection. A range of amide formation products are screened in order to find an optimal reaction model for this purpose. In addition, the challenges faced in the identification and quantification of the observed species through their SABRE hyperpolarised signals are discussed.

4.2 Background

Hyperpolarised low-field NMR can potentially reflect a low-cost analytical tool for reaction monitoring that can provide in-depth information, for example, about trace reaction components. The application of hyperpolarisation to reaction monitoring has been demonstrated using DNP. These experiments focused on metabolite conversion by an enzyme.^{34, 126, 127} Quantitative detection using DNP was reported by Lerche *et al.* who used bis-1,1-(hydroxymethyl)-[1- ^{13}C]cyclopropane- d_8 as an internal standard and the calibration curve of ^{13}C -labeled carbamazepine in rabbit blood plasma.¹²⁸ The results showed consistency between the DNP-NMR method and LC-MS detection of carbamazepine.¹²⁸ Regarding SABRE hyperpolarisation, there are fewer examples of studies dealing with reaction monitoring. In part this reflects the recent nature of the method, but Bae *et al.* has qualitatively detected inverse-demand Diels-Alder reaction components using ^{15}N hyperpolarised signals created by the SABRE-SHEATH technique.¹²⁹ The reaction proceeds in ~ 4 seconds, thus, it was not feasible to monitor the reaction's kinetic behaviour.¹²⁹ In 2014 Eshuis *et al.* commented on the linear dependence between the SABRE signal and trace substrate concentration (detection limit $< 1 \mu\text{mol}$) when measured in a mixture with a co-substrate present at a much higher concentration which remained fixed.^{45, 124} However this method has not been applied to reaction monitoring to date.

Reaction monitoring through SABRE-derived NMR signals faces several challenges that relate to the reaction conditions needed for SABRE hyperpolarisation to take place, which place limitations on the reactivity that can be investigated. These include, the need for non-aggressive reaction conditions so that the SABRE catalyst can remain in an active form in solution and the need for a reaction timescale that allows for a series of SABRE measurements during the monitoring stage. In addition, the solution has to be protected from air and paramagnetic reactants which can cause relaxation of $p\text{-H}_2$ and, therefore, SABRE signal loss.

The model reaction chosen for this work is a condensation reaction which leads to amide formation from a N-heterocyclic amine. In order to monitor a condensation reaction using hyperpolarisation, it is necessary that at least one of the components of the reaction is amenable to SABRE hyperpolarisation. This reaction is completed in a one-step process that can be performed at room temperature and does not require strong acids, bases or gaseous components. For these reasons, it is expected that the reaction could be carried out under SABRE conditions, i.e. in the presence of the Ir-based catalyst, $[\text{Ir}(\text{H})_2(\text{IMes})(\text{substrate})_3]\text{Cl}$, and *para*-hydrogen. In order to investigate the monitoring of the reactivity with SABRE, the optimal reaction, mixture analysis and reaction monitoring using standard and hyperpolarised high-field (9.4 T) NMR signals are explored in this chapter.

4.3 Choice of model reaction

Here, amide formation reactions of substituted aminopyridines with benzoic anhydride and ethyl benzoate (Figure 4.1) were screened in the indicated solvents using HPLC-MS-UV for product analysis and for assessing the reaction timescale (see experimental section 9.6 for more details). These reactions were performed in a flask and aliquots were extracted at fixed time points during the reaction for analysis. A summary of these screening experiments is presented in Table 4.1.

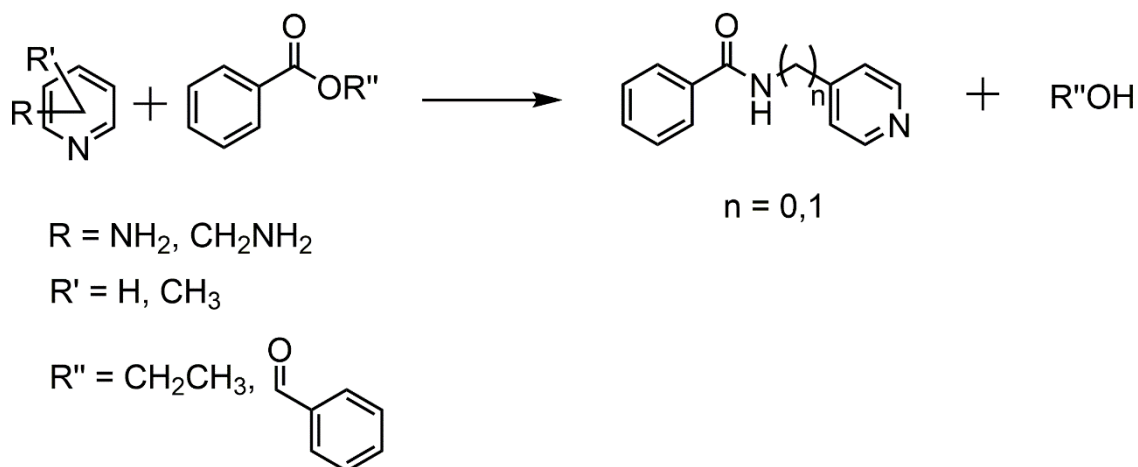


Figure 4.1 General scheme of an amide formation reactions of substituted aminopyridines with benzoic anhydride and ethyl benzoate screened below.

Table 4.1 Model reactions for potential investigation under SABRE conditions. The ratio of starting materials used was 1:1, and their concentration was 50 mM, unless otherwise stated.

<i>N</i>	<i>Amine</i>	<i>Benzoic anhydride/ethyl benzoate</i>	<i>Solvent</i>	<i>Result</i>
1	4-aminomethylpyridine	Benzoic anhydride	DCM	Instant
2	4-aminomethylpyridine	Benzoic anhydride	MeOH	Instant
3	4-amino-3-methylpyridine	Benzoic anhydride	DCM	~ 36% conversion in 19.5 hrs
4	4-amino-3-methylpyridine	Benzoic anhydride	MeOH	No product after 1 hr
5	4-amino-3-methylpyridine	Benzoic anhydride	MeCN	~ 63 % conversion in 6 hrs
6	4-aminopyridine	Benzoic anhydride	MeCN	~ 39 % conversion in 18 hrs
7	4-aminopyridine (100 mM)	Benzoic anhydride (100 mM)	MeOH	No product after 3.5 hrs

Table 4.2 (continuation) Model reactions for potential investigation under SABRE conditions. The ratio of starting materials used was 1:1, and their concentration was 50 mM, unless otherwise stated.

<i>N</i>	<i>Amine</i>	<i>Benzoic anhydride/ethyl benzoate</i>	<i>Solvent</i>	<i>Result</i>
8	4-aminopyridine (100 mM)	Benzoic anhydride (100 mM)	DCM	~ 24% conversion in 6.5 hrs
9	3,5-aminopyridine (90 mM)	Benzoic anhydride (90 mM)	MeOH	~ 64% conversion in 10 min
10	4-aminopyridine (100 mM)	Ethyl benzoate (100 mM)	MeOH	No product after 17.5 hr
11	4-aminopyridine (100 mM, at 40 °C)	Ethyl benzoate (100 mM)	MeOH	No product after 21.5 hr
12	3-amino-5-methylpyridine	Benzoic anhydride	DCM	No product after 1 hr, full conversion after 3 days (was not monitored between these time points)

The results in Table 4.1 show that several reactions proceed to the product on a timescale suitable for SABRE reaction monitoring. For example, the reaction of 4-amino-3-methylpyridine with benzoic anhydride in MeCN achieves ~ 63% conversion in 6 hrs. However, when this substrate was tested for SABRE activity in acetonitrile-*d*₃, weakly enhanced NMR signals (up to 3-fold) and significant peak overlap is observed. Further complexity is derived from the formation of a mixture of iridium complexes due to the solvent binding to the catalyst. In the case of 3,5-

diaminopyridine, the reaction appeared to be very fast, showing ~ 64% conversion in 10 minutes. In addition, this substrate suffers from the formation of a double-substituted product due to the two amino groups that are present in the starting material. In addition, solvent choice affects SABRE signal intensity because of the differences in solubility of *para*-hydrogen and the possibility of solvent binding to the SABRE catalyst differ, as in case of acetonitrile.⁹⁹ The reaction between 4-aminopyridine and benzoic anhydride proceeds in DCM, which is a compatible solvent for SABRE. This reaction yields N-(4-pyridyl)benzamide and benzoic acid and achieves ~ 24% conversion in 6.5 hrs according to HPLC-MS-UV (Figure 4.2). Therefore, amide formation was chosen as a model reaction for the further studies.

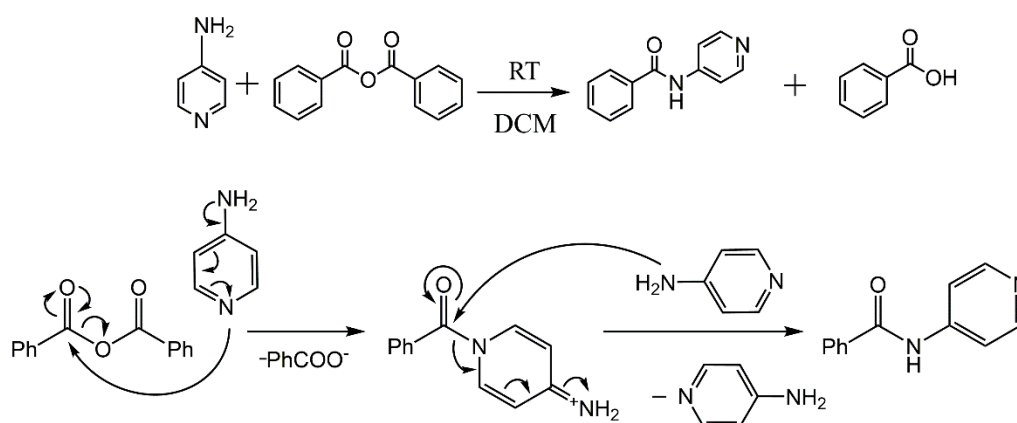


Figure 4.2 Model reaction of amide formation with the mechanism¹³⁰ for reaction monitoring by SABRE NMR.

In order to investigate the reaction by hyperpolarised NMR, an initial analysis of the reaction without the SABRE catalyst was performed. Secondly, the time evolution of the thermal and enhanced ¹H NMR spectra were studied in the presence of the catalyst and *para*-hydrogen. These preliminary studies were performed on a high-field (400 MHz) NMR spectrometer because of the better spectral resolution.

4.4 Mixture analysis

The exact NMR response of the individual compounds can change in mixtures due to chemical exchange, pH change, dielectric constant change

or the presence of other intermolecular interactions.¹³¹⁻¹³³ Samples containing mixtures of the compounds taking part in this model reaction were first characterised by ¹H NMR spectroscopy. Typical NMR chemical shifts of the individual compounds, benzoic anhydride (**BAH**), benzoic acid (**BA**), 4-aminopyridine (**4-AP**), N-(4-pyridyl)benzamide (**4-PBA**) and their mixtures are presented in Table A4 in Appendix.

The ¹H NMR spectroscopic analysis of the mixtures containing **4-AP** and **4-PBA** alongside **BA** showed the appearance of an additional broad singlet when compared to the pure compounds' response in DCM. This suggests that **BA** exists in equilibrium with its pyridinium carboxylate salt alongside **4-AP** and **4-PBA** (Figure 4.3); the aromatic nitrogen of the pyridine ring is protonated in this form. Due to this effect, the aromatic resonances of the substrate change their chemical shift as they are now in dynamic exchange. In the case of **4-AP**, both the *ortho* and *meta* protons' chemical shifts become deshielded and move downfield by 0.09 and 0.10 ppm, respectively (Figure 4.4a). The **4-PBA** proton resonances are affected less, showing a downfield shift of only 0.04 and 0.02 ppm, respectively for the *ortho* and *meta* protons of the pyridine ring (Figure 4.4b). Therefore, in the presence of benzoic acid, the peaks of **4-AP** and **4-PBA** move downfield. The effect of pH on the signals of related pyridine derivatives has been seen previously.¹²²

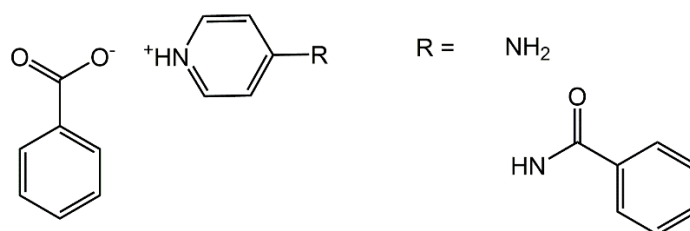


Figure 4.3 Structure of proposed pyridinium carboxylate salt formed by **BAH** and **4-AP** or **4-PBA**.

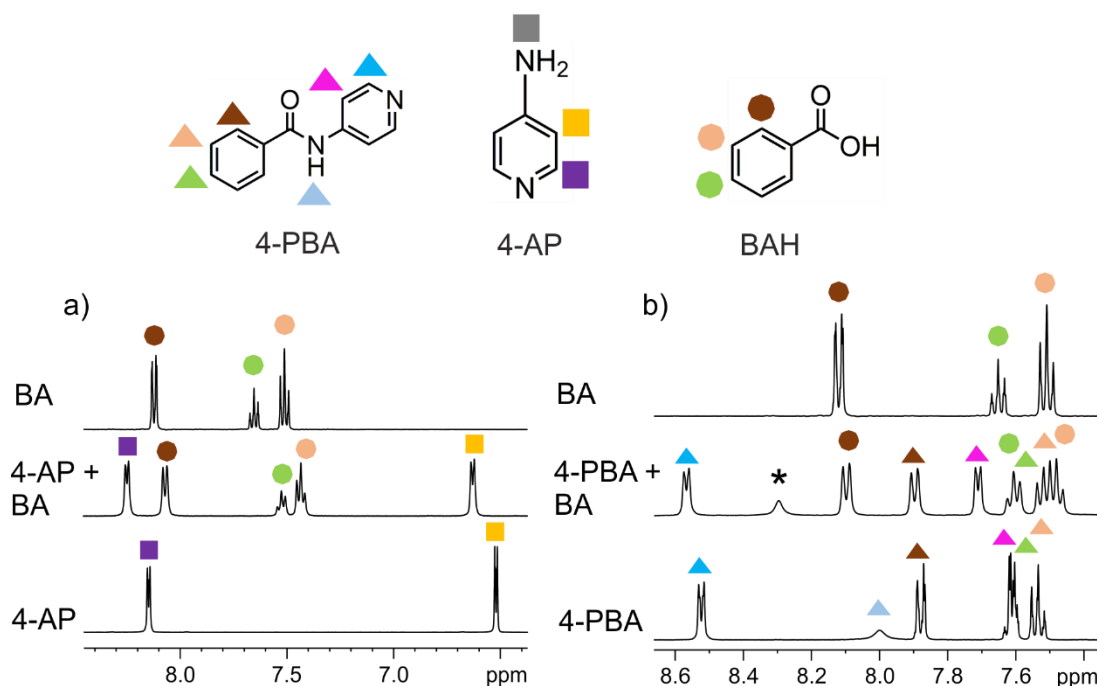


Figure 4.4 ^1H NMR chemical shift changes in a mixture of (a) **4-AP** and (b) **4-PBA** with **BA** in DCM compared to the ^1H NMR spectra of the pure compounds. (*) Peak is assigned to either **4-PBA** pyridinium proton or amide proton.

At the same time, the benzoic acid peaks move upfield by 0.05-0.1 ppm when in a mixture with **4-AP** and by 0.01-0.04 ppm with **4-PBA** (Figure 4.4). The presence of benzoic acid does not change the benzoic anhydride's chemical shifts. In addition, **4-AP** and **4-PBA** show slight changes in their chemical shifts once mixed. The *ortho* proton and the amino group resonances of **4-AP** move 0.01 ppm downfield and upfield respectively in the mixture. The aromatic protons of **4-PBA** exhibit a change in the range of 0.01-0.03 ppm, which beneficially leads to the *meta* (pyridine ring) and *para* (aryl ring) protons becoming distinct. A more significant change is observed for the **4-PBA** amide group protons which shift 0.7 ppm downfield.

These observations confirm that interactions between the reaction components lead to a change in the underlying NMR properties that will need careful analysis if NMR, or in fact SABRE, is to be used to monitor their reactivity.

4.5 Reaction monitoring in standard conditions

The model reaction was followed in DCM by 400 MHz ^1H NMR spectroscopy in a standard NMR tube. Equimolar amount of benzoic anhydride ($30\ \mu\text{mol}$) was added to the solution of 4-aminopyridine ($30\ \mu\text{mol}$) in DCM. Figure 4.5 shows a typical thermally polarised ^1H NMR spectrum of **4-AP** before the addition of **BAH** alongside an NMR spectrum recorded 140.6 min after the reaction started. The indicated changes in the appearance of these NMR spectra with time reflect the underlying reaction.

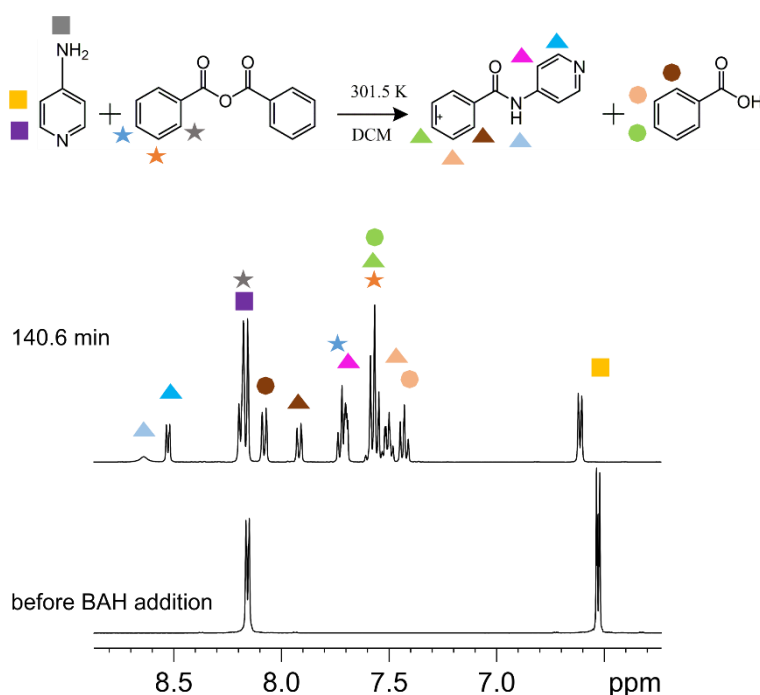


Figure 4.5 Standard reaction monitoring of amide formation by ^1H NMR (400 MHz) in DCM. ^1H NMR spectra of **4-AP** before the addition of **BAH** (bottom trace) and after 140.6 min of the reaction proceeding (top).

In Figure 4.5, the ^1H NMR spectrum recorded after 140.6 min reveals peaks for benzoic anhydride at 7.71 ppm (blue star) and 7.55 ppm (orange star) alongside **4-AP** peaks at 8.15 and 6.52 ppm. The formation of the product **4-PBA** is indicated by the peaks which appear at 8.51 ppm (*ortho* in pyridine ring, cyan triangle), 7.90 ppm (*ortho* in aryl ring, brown triangle) and 7.65 ppm (*meta* in pyridine ring, pink triangle). The other **4-PBA** peaks are difficult to distinguish due to overlap with the **BAH** and **BA** peaks. The **BA** peaks arise at 8.07 ppm (brown circle), 7.57 ppm (green circle), and 7.42 ppm (orange circle). The *meta* proton resonance of **4-AP** shifts from 6.52

ppm to 6.53 ppm (yellow square) in presence of the **BA**, in agreement with the mixture analysis detailed earlier. The residual water signal moves from 1.93 ppm to 2.87 ppm during the reaction while the amino group chemical shift changes from 4.24 ppm to 4.32 ppm. This reflects the change in the proton exchange rates in solution due to pH changes. Consistent with this observation, the amide group proton of **4-PBA** appears as a broad resonance at 8.77 ppm (grey-blue triangle). In order to assess the kinetics of this reaction, the integrals of the NMR peaks for these materials were extracted from the NMR data and plotted against the reaction time in Bruker's Dynamics Center software (Figure 4.6). Pseudo-first order experimental rate constants could be extracted from the integrals at 8.51 ppm, 8.08 ppm, 7.90 ppm, 7.43 ppm and 6.52 ppm. These were: $(2.200 \pm 0.002) \cdot 10^{-2} \text{ min}^{-1}$ based on the **4-PBA** *ortho* proton in pyridine ring and $(2.12 \pm 0.002) \cdot 10^{-2} \text{ min}^{-1}$ based on the **4-PBA** *ortho* proton in aryl ring, $(2.23 \pm 0.003) \cdot 10^{-2} \text{ min}^{-1}$ based on the **4-AP** *meta* proton, and $(1.40 \pm 0.001) \cdot 10^{-2} \text{ min}^{-1}$ based on **BA** *ortho* proton and $(1.37 \pm 0.001) \cdot 10^{-2} \text{ min}^{-1}$ based on **BA** *meta* proton. These rate constants show consistent results for both starting material and product of the reaction. It can be concluded that product formation can be followed by standard ^1H NMR at high field. In the next section the same reaction was monitored by thermal and hyperpolarised ^1H NMR in presence of the SABRE catalyst.

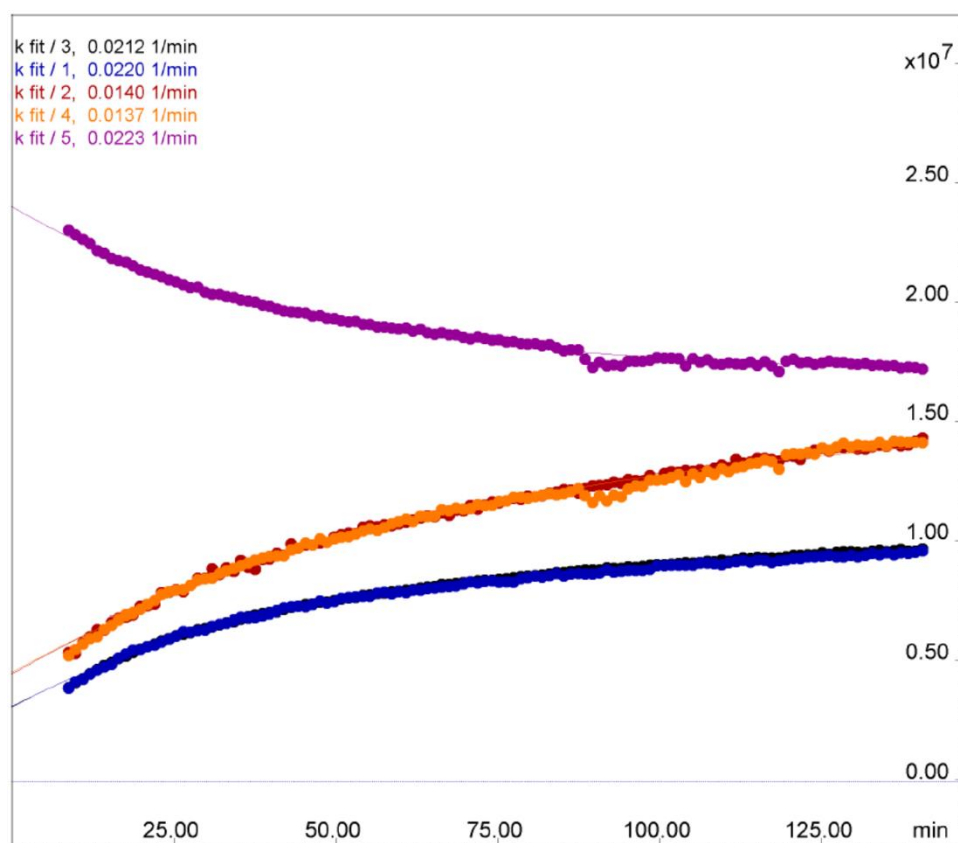


Figure 4.6 Kinetics of the amide formation reaction assessed from the ^1H NMR integrals of peaks at 8.51 ppm (1), 8.08 ppm (2), 7.90 ppm (3), 7.43 ppm (4) and 6.52 ppm (5) using Bruker's Dynamics Center software.

4.6 Reaction monitoring in SABRE conditions

In order to observe the amide formation reaction under SABRE conditions, the starting material **4-AP** (50 mM) was activated in presence of 5 mM $[\text{Ir}(\text{Cl})(\text{COD})(\text{IMes})]$ in $\text{DCM-}d_2$. **BAH** (50 mM) was added to the activated complex in the NMR tube to start the reaction. Standard and hyperpolarised ^1H NMR spectra were then acquired in parallel on a 400 MHz NMR spectrometer. Figure 4.7 shows two thermally-polarised ^1H NMR spectra that were recorded after 5 min 30 s and 95 min 30 s of reaction. The lower NMR spectrum of Figure 4.7 represents the **4-AP** response in the presence of the activated SABRE complex $[\text{Ir}(\text{IMes})(\text{4-AP})_3]\text{Cl}$ for comparison.

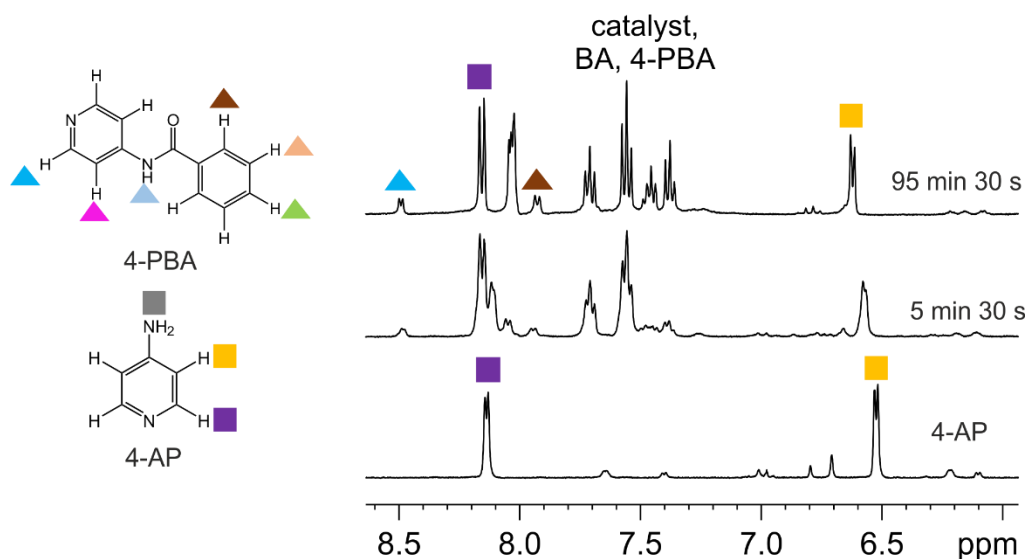


Figure 4.7 Thermal spectra collected during reaction monitoring of amide formation by NMR (400 MHz) in presence of the SABRE catalyst $[\text{Ir}(\text{H})_2(\text{IMes})(\mathbf{4}\text{-AP or } \mathbf{4}\text{-PBA})_3]\text{Cl}$ in $\text{DCM-}d_2$.

In Figure 4.7 the product **4-PBA** is detected as a series of signals at the same chemical shift as those in the earlier ^1H NMR spectra for reaction monitoring without the SABRE catalyst (Figure 4.5). As in the previous experiments, overlap of the peaks for **BAH** and **BA** with those of **4-PBA** is observed (8.15 ppm, 8.05 ppm, 7.3 – 7.8 ppm). Interestingly the **4-AP** *meta* proton (yellow square in Figure 4.7), the **4-AP** amino group and **4-PBA** amide proton resonances significantly change in chemical shift with reaction time. This is consistent with the presence of **BA** in solution as shown by the mixture analysis above (see section 4.4). Hence, the SABRE catalyst and *para*-hydrogen do not stop the formation of **4-PBA**. The continued observation of hydride peaks in the region from -22.6 to -23.5 ppm indicates that the complexes that are capable of SABRE hyperpolarisation transfer are also stable under these conditions. Significant product and starting material precipitation limits these ^1H NMR observations to around an hour and a half. Nevertheless, these observations confirm that to a first approximation the presence of the iridium complexes and hydrogen do not change the underlying reaction.

In order to learn whether the product can be seen via SABRE, hyperpolarised ^1H NMR spectra were acquired in parallel with the thermal

NMR spectra. Figure 4.8 confirms that hyperpolarised NMR spectra of the reaction mixture can be obtained. The hyperpolarised NMR spectra of **4-AP** (Figure 4.8a) and **4-PBA** (Figure 4.8d) are also presented for reference. No hyperpolarisation was observed for the signals of **BAH** with SABRE under these conditions.

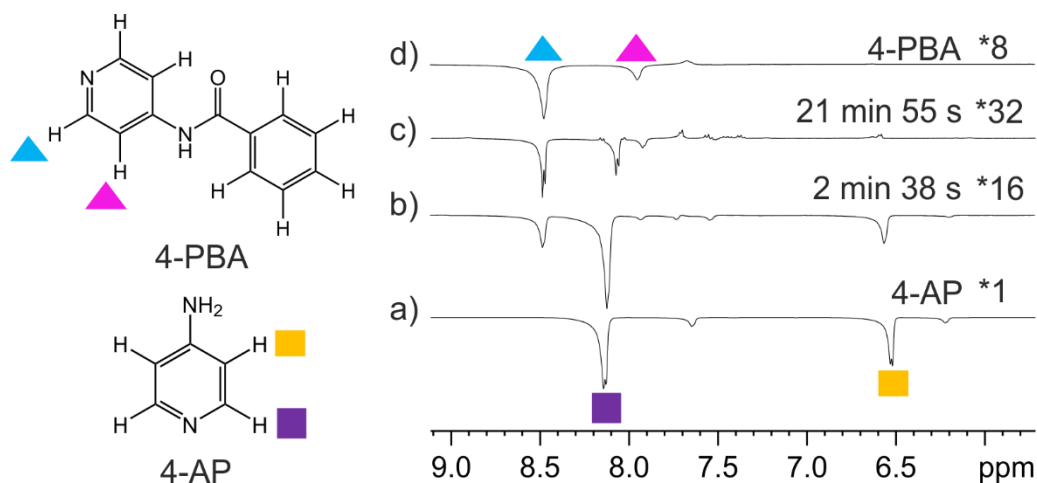


Figure 4.8 ^1H NMR (400 MHz) SABRE enhanced spectra of (a) **4-AP** in presence of activated complex, $[\text{Ir}(\text{H})_2(\text{IMes})(\text{4-AP})_3]\text{Cl}$, before addition of **BAH**, (b, c) the reaction mixture collected during reaction monitoring of amide formation in the presence of the SABRE catalyst $[\text{Ir}(\text{H})_2(\text{IMes})(\text{4-AP or 4-PBA})_3]\text{Cl}$, (d) **4-PBA** in presence of activated SABRE complex, $[\text{Ir}(\text{H})_2(\text{IMes})(\text{4-PBA})_3]\text{Cl}$, for comparison.

The hyperpolarised peaks at 8.48 ppm can be assigned to the *ortho* proton of free **4-PBA** by comparison with the reference SABRE NMR spectrum of pure **4-PBA** (Figure 4.8d). Comparison of Figure 4.8a and 5b shows that the enhancement factor exhibited by the *ortho* proton of **4-AP** at 8.12 ppm decreases from 325-fold to 24-fold over the first 2 min 38 s of the reaction. This is due in part to the substrate consumption in the reaction, and the protonation of the aromatic nitrogen that limits its binding to the catalyst. With further increase in the reaction time, the hyperpolarised peaks for the starting material disappear completely, while hyperpolarised peaks at 8.48 ppm and 7.93 ppm for **4-PBA** remain (Figure 4.8c). The **4-PBA** *ortho* proton at 8.48 ppm showed an enhancement value of 47-fold at 2 min 38 s which decreased to 22-fold at 21 min 55 s in between the spectra shown in Figure 4.8b and c. These results demonstrate that the product may also competitively bind to the SABRE catalyst during the reaction and, hence,

polarises. However, the presence of benzoic acid acts to reduce the enhancement levels of both substrates due to protonation of their aromatic nitrogens. This was confirmed by a separate SABRE experiment with **4-PBA** (50 mM) in presence of the 5 mM activated complex to which **BA** (50 mM) was added prior to acquisition of a hyperpolarised spectrum. The enhancement values obtained after addition of **BA** were 11-times smaller compared to the values for pure **4-PBA**.

In addition to the hyperpolarised peaks of **4-PBA**, there are new hyperpolarised peaks at 8.07 ppm, 7.93 ppm, 7.73 ppm and 7.54 ppm that appear during this reaction, which do not match the chemical shifts of the free starting material or the product. These peaks originate from the complexes with bound substrate molecules. These resonances could not be seen in the thermal spectra due to peak overlap (Figure 4.7). Comparison of the SABRE and thermal spectra (Figure 4.7 and Figure 4.8c) suggests that the starting material ceases to hyperpolarise even though it is still present in solution. Preferable binding of the product rather than the starting material would explain this. If **4-AP** protonates preferentially than **4-PBA**, it will be less able to bind and so to hyperpolarise.

In summary, the formation and detection of an amide redistribution product under SABRE validated the hypothesis that reaction monitoring is possible by hyperpolarised ^1H NMR spectroscopy. In this case, precipitation prevented quantitative rate data from being collected. Thus, it cannot be estimated whether the catalyst affects the mechanism and the kinetics of the reaction. In addition, the effect of pH on the SABRE process is dramatic, which adds complications by introducing changes in chemical shift and trapping of the key nitrogen center required for SABRE. However, this could be of benefit if pH measurement was required.

4.7 Conclusions and future work

This study establishes the potential ability of SABRE to monitor reactions through NMR signal enhancements at high field. The reaction conducted here yielded the same product both with and without the catalyst

and *para*-hydrogen. The reaction product's ^1H SABRE signal was enhanced 47-fold when compared to the thermal NMR signal. This signal gain reflects a substantial improvement in detectability and gives a potential to perform reaction monitoring with millimolar concentrations using high-field and low-field NMR spectrometers. Also noteworthy is the fact that the relatively crowded thermal ^1H NMR spectra are selectively enhanced by SABRE. This separation will be beneficial in case of complex mixture analysis, especially if low-field NMR spectroscopy is used due to its low chemical shift dispersion. Based on literature examples demonstrating heteronuclear (for example, ^{15}N , ^{31}P , ^{13}C) hyperpolarisation,^{39, 41, 79, 86-88} it could be used for reaction monitoring to avoid the peak overlap in such systems. Labelled compounds could also be of interest for reaction monitoring as they provide stronger and more selective thermal and SABRE signals. However, it must be remembered that resonances for the substrate in the asymmetric catalyst complexes must be accounted alongside any effects that result from a pH change.

The experiments described here were carried out within a sealed NMR tube and using a manual shaking SABRE procedure. However, a similar approach to reaction monitoring with SABRE can be performed using an automatic flow system for generating hyperpolarisation in order to obtain more control over the SABRE conditions.⁷⁴ Therefore, this method can be of a potential use for at-line by-product and contamination detection in industrial processes.

For accurate reaction monitoring, there is a need for precise quantification and kinetic studies. However, while hyperpolarisation provides a fast qualitative method for detecting trace species, the calibration of the SABRE signal is challenging (as discussed in Chapter 3, sections 3.4.2 and 3.5.2) unless a linear signal response regime is achieved as described by Eshuis *et al.*⁴⁵ This can be achieved when $< 1 \mu\text{M}$ concentrations are used and a co-ligand added to simplify the SABRE catalysis. However, the introduction of a co-ligand could be problematic if the new NMR peaks

overlap with those that are diagnostic of the reaction or it is itself reactive.^{45,}

48

One other potential way of assessing the SABRE response to the reactivity is to use hyperpolarisation lifetime instead of signal intensity. This approach to will be developed in Chapter 5.

Chapter 5: Relaxation times of N-heterocyclic amines

5.1 Introduction

In this chapter, the relaxation properties of a group of N-heterocyclic amines are explored. First, different methods for measuring T_1 relaxation times for both thermally polarised and hyperpolarised systems are compared to determine the optimal approach in terms of accuracy, repeatability and experiment time. Thermal polarisation lifetimes are measured with saturation and inversion recovery methods. Hyperpolarisation lifetime measurements are achieved using constant flip angle and variable flip angle sequences, which represent inversion recovery type methods where SABRE hyperpolarisation is used at the start. Second, these methods are used to study the T_1 values of a range of N-heterocyclic amines under SABRE conditions and to explain the SABRE enhancements observed. The effect of the SABRE catalyst and hydrogen atmosphere on substrate T_1 values is explored along with solvent effects.

5.2 Background

Relaxation in NMR is the phenomenon where bulk spin magnetisation reaches its equilibrium value. The rate of nuclear spin relaxation is dependent on the physical environment of the nuclei and Brownian molecular motion. These effects combine to create oscillating magnetic fields within the sample that interact with the magnetic moments of the nuclei causing nuclear spin transitions that drive relaxation. In NMR, relaxation is typically characterised by the spin-lattice and spin-spin relaxation processes which have corresponding time constants T_1 and T_2 , respectively. Spin-lattice (longitudinal) relaxation is the process of energy transfer between the spins and the environment via interactions with highly localised magnetic fields. This drives the z-magnetisation to an equilibrium value determined by the Boltzmann distribution of nuclei across the Zeeman energy states. Spin-spin (transverse) relaxation is the decay of transverse xy-magnetisation to equilibrium (zero) through a T_1 relaxation and loss of coherence due to dephasing of the spins.

This study focuses on using T_1 measurements to obtain insight into chemical interactions. The local magnetic fields, which return the system to thermal equilibrium, can originate from another spin's magnetic dipole, chemical shift anisotropy and unpaired electrons.¹³⁴ The dipole-dipole mechanism is typically the dominant form of relaxation for spin-1/2 nuclei in solution. It involves a spin experiencing a magnetic field generated by the dipole moment of another nucleus. This interaction is proportional to: a) the distance as $1/r^3$, b) the gyromagnetic ratio of each nucleus (the larger the gyromagnetic ratio, the larger the magnetic dipole moment), and c) the relative orientation of the spins with respect to the applied magnetic field, B_0 , along z-axis. Therefore, the closer the nuclei are to each other the more efficient the relaxation effect. Dipole-dipole relaxation varies with the molecular weight as well as being dependent on solvent viscosity. This is associated with the rate of molecular rotation in solution. A rotational correlation time is used as the measure of molecular motion. In the case where molecular motion is on the same timescale as the Larmor frequency, a resonance condition is achieved and relaxation is most efficient. As the timescale of molecular motion deviates away from this condition, such as for small molecules in non-viscous solvents, where molecular motion is much faster than the Larmor frequency, the T_1 value increases. Analogously, for larger molecules and viscous solutions, if the motion becomes much slower than the Larmor frequency, T_1 will increase. As changes in temperature cause variations in the correlation time, a change in T_1 is observed with temperature. The dependence of T_1 and T_2 as a function of correlation time and magnetic field was investigated by Bloembergen, Purcell and Pound, who developed a theory to estimate relaxation by dipole-dipole interactions.¹³⁵

The Chemical Shift Anisotropy (CSA) relaxation mechanism is caused by different spin orientations relative to the electron induced local magnetic field. These magnetic fields fluctuate due to molecular tumbling and cause relaxation via chemical shift anisotropy. The relaxation rate

caused by this mechanism is proportional to the square of applied magnetic field and the gyromagnetic ratio ($\gamma^2 B_0^2$).¹³⁴

The presence of a paramagnetic species, which create oscillating local magnetic fields through their unpaired electrons, is also a route to relaxation. Due to the strong magnetic moment of an unpaired electron this process can be efficient even when the paramagnetic species is present at low concentration.¹³⁴

Scalar relaxation occurs due to the time-dependent part of the J^{AB} coupling between the spins A and B, which varies due to internal molecular motions.¹³⁶ The scalar relaxation is contributed to mostly by 3J couplings as they are relatively big in value and vary with the molecular conformation according to the Karplus formula.¹³⁷ In the absence of chemical exchange, this type of relaxation is described by the same laws as dipolar relaxation.¹³⁸ This relaxation effect is much less efficient than dipolar relaxation with the exception of situations that involve very heavy nuclei.¹³⁸

Another relaxation mechanism, called the electric quadrupole interaction, takes place for nuclei with spin greater than $1/2$.¹³⁹ Such nuclei possess a quadrupole moment due to the uneven distribution of charge in the nucleus. Therefore, under interactions with local electric field gradients the nucleus experiences a random variation of charge orientation within itself. When this variation is at the nuclear resonant frequency it causes energy transfer between the spins and the environment as well as randomisation of nuclear spin phase. Therefore, the quadrupole mechanism contributes to both longitudinal and transverse relaxation. The rate of quadrupole relaxation is proportional to the square of the nuclear electric quadrupole moment and generally decreases with decrease in spin quantum number. Moreover, in contrast to spin-half nuclei, quadrupolar relaxation becomes slower with an increase in temperature.¹³⁹ In the case of scalar coupling to a fast-relaxing quadrupolar nucleus, the T_1 relaxation of a non-quadrupolar nucleus is not significantly affected unless the frequencies of both nuclei are close.¹⁴⁰⁻¹⁴²

Chemical exchange can also have an effect on T_1 relaxation. If the nuclei experience different relaxation rates on the exchanging sites, the resultant T_1 value is a weighted average. This effect forms the basis of chemical exchange saturation transfer (CEST) experiment.¹⁴³ In this method, exchangeable protons of a CEST agent are saturated with a frequency-selective RF pulse. This results in a water signal decrease due to magnetisation transfer via exchange. The effect of chemical exchange on T_1 within the SABRE catalytic process will be discussed in more detail in section 5.3.3.2 and Chapter 7.

In this thesis, where experiments are carried out in isotropic solution, I attribute the relaxation effects mostly to dipolar relaxation and discuss the effect of the chemical exchange on the T_1 . The applications of T_1 relaxation in NMR are extensive. For example, variable temperature T_1 measurements can yield the activation energy of molecular reorientation.^{144, 145} Due to the strong link between T_1 and the underlying chemical properties of the system, it can also be employed as an indicator of chemical change. Variance in T_1 values can be associated with the formation of intermediates, chemical exchange and isotope exchange.^{90, 146-148} T_1 is characteristic of the chemical environment and experimental conditions and can be used, for example, in the determination of surface microstructure¹⁴⁹ and of the bond length of metal dihydrogen ligands.¹⁵⁰ In addition, the amount of SABRE hyperpolarisation in a substrate has been reported to increase with increased substrate T_1 .¹⁵¹ The SABRE process involves a catalyst, and so relaxation within the catalyst whilst the substrate is bound will limit the efficiency of the polarisation transfer and hence the final level of SABRE hyperpolarisation.

5.2.1 *Methods for measuring T_1*

In order to estimate the spin-lattice time constant T_1 , the dynamics of the z-magnetisation vector (M_z) are observed with time. This can be described by the following differential Bloch equation (Equation 5.1).¹³⁴

$$\frac{dM_z(t)}{dt} = -R_1(M_z(t) - M_z^{eq}), \text{ where } R_1 = \frac{1}{T_1} \quad (5.1)$$

Equation 5.1 states that the rate of change of M_z is given by R_1 . This constant (R_1) is the inverse of T_1 . There are two robust methods to measure T_1 that are widely used in NMR spectroscopy, inversion recovery and saturation recovery.

The inversion recovery sequence measures the relaxation time by inverting M_z with a 180° degree pulse, waiting a specified time delay for magnetisation recovery and then detecting the available magnetization with a 90° degree pulse. By varying the delay between the 180° and 90° pulses a relaxation curve can be recorded. An inter-scan delay of $5 \cdot T_1$ is needed to ensure equilibrium magnetisation is probed and quantitative analysis possible.^{152, 153} Such a pulse sequence is presented in Figure 5.1, and the equation for M_z evolution shown in Equation 5.2.

$$M_z = M_0 \left(1 - 2e^{-t/T_1} \right) \quad (5.2)$$

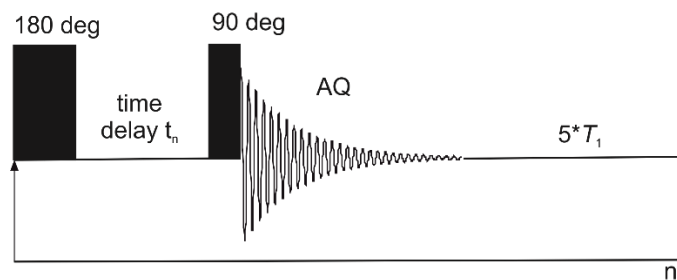


Figure 5.1 Inversion recovery pulse sequence for T_1 measurement.

A study by Look and Locker proposed an alternative and quicker saturation recovery sequence to measure T_1 .¹⁵⁴ In this method it is not necessary to wait $5 \cdot T_1$ to reestablish equilibrium magnetisation as the sequence first destroys all M_z with a series of 90° degree pulses that precede magnetic field spoiler gradients. The subsequent recovery of M_z is probed by applying a 90° degree pulse at a fixed time following this. The process is repeated for a range of delays up to $5 \cdot T_1$ (see Figure 5.2).¹⁵⁵ The relaxation curve for the saturation recovery experiment obeys Equation 5.3.

$$M_z = M_0 \left(1 - e^{-t/T_1} \right) \quad (5.3)$$

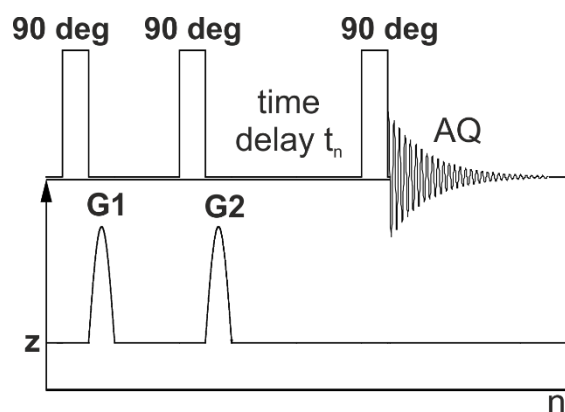


Figure 5.2 Pulse sequence for saturation recovery relaxation time measurement.

Examples of ^1H NMR signal intensity evolution during inversion and saturation recovery measurements are presented in Figure 5.3a and b. The integration of the peak intensities yield a T_1 recovery curve like those shown in Figure 5.3c and d for inversion and saturation recovery experiments respectively.

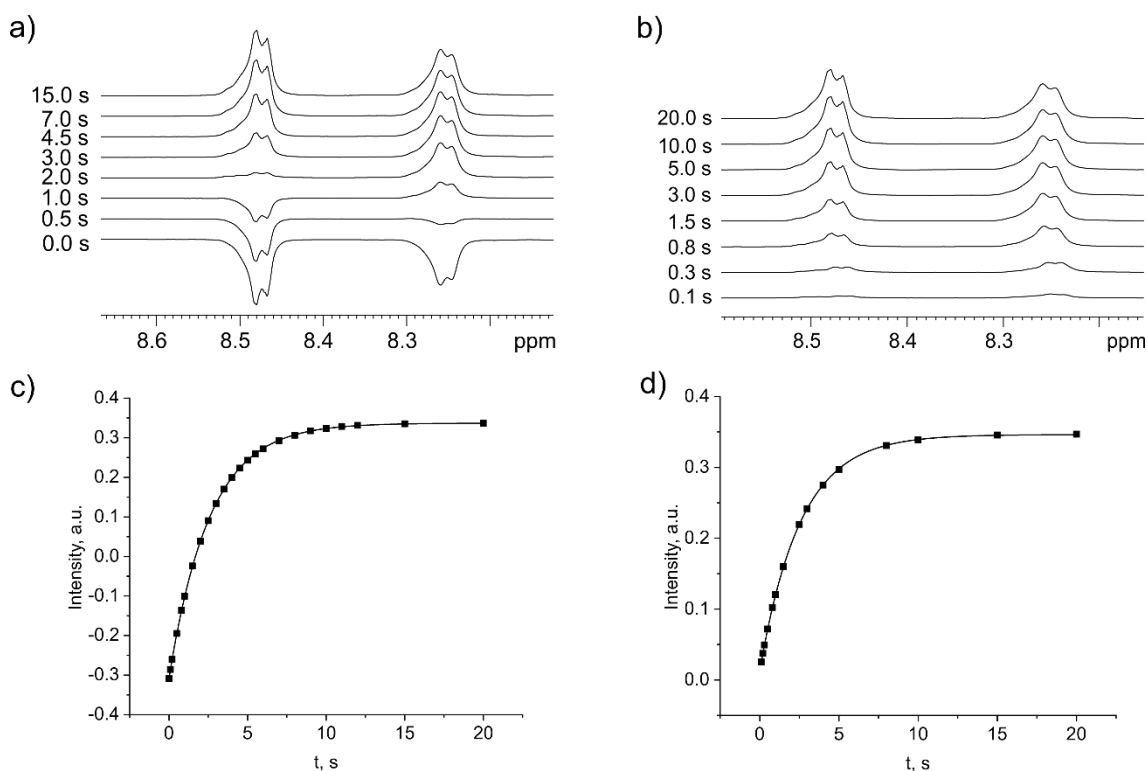


Figure 5.3 Evolution of the of ^1H NMR signal intensities in the (a) inversion recovery and (b) saturation recovery measurements for free (8.47 ppm) and bound (8.26 ppm) *ortho*-protons of N-(4-pyridyl)benzamide (2-fold excess) in presence of 5 mM $[\text{Ir}(\text{N}-(4\text{-pyridyl})\text{benzamide})_3(\text{IMes})(\text{H}_2)]$ in methanol- d_4 at 253 K measured at 400 MHz. The resultant relaxation curve for free (8.47 ppm) *ortho* resonance which yields a T_1 of 2.59 ± 0.01 s from both (c) inversion and (d) saturation recovery measurements when fitted to Equation (5.2) and (5.3) respectively.

In the case of the inversion recovery experiment depicted in Figure 5.3a and c, due to the $5 \cdot T_1$ wait between points, the total acquisition time exceeded 8 hours, while the resultant T_1 curve from the saturation recovery measurement was obtained in a total experiment time of just 50 min.

For systems with relatively long T_1 values, the saturation recovery measurement is much shorter when compared to inversion recovery because M_z does not have to recover before each data point. The signal is saturated between scans and therefore the observed signal starts from zero and builds-up with time. In order to obtain accurate T_1 values using saturation recovery, relaxation times should be long enough to avoid significant increase in M_z during the train of saturation pulses. For a time between pulses of $10 \mu\text{s}$, a relaxation time of 5 ms would lead to a recovery of less than 0.2% of the z-magnetization. Therefore saturation recovery is expected to give accurate results for the range of T_1 values explored in this thesis where $T_1 \gg 5 \text{ ms}$.

5.3 Thermal relaxation times of N-heterocyclic amines

As discussed above, the inversion recovery experiment takes much more time than saturation recovery to acquire, especially for samples exhibiting long T_1 values due to the requirement of a time delay of 3-5-times T_1 between scans to allow for the full recovery of the z-magnetization to equilibrium. Another limitation of the inversion recovery sequence is that an approximate value for T_1 is required before an accurate measurement can be achieved. In the saturation recovery experiment, the key limitation is that the z-magnetization recovery during the saturation and/or gradient pulses must be negligible. Here, the two methods of thermal polarisation lifetime measurement are evaluated. T_1 values were measured using the inversion recovery and saturation recovery sequences for 25 mM N-(4-pyridyl)benzamide (**4-PBA**) in two different solvents, methanol- d_4 and THF- d_8 , under a hydrogen atmosphere as detailed in Table 5.1 and Table 5.2.

Table 5.1 Thermal relaxation times for free N-(4-pyridyl)benzamide (25 mM) protons in methanol- d_4 under hydrogen atmosphere. Error bars represent fitting errors.

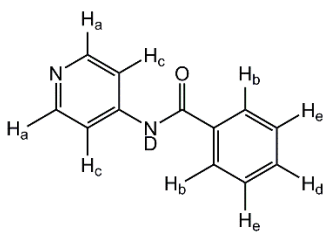
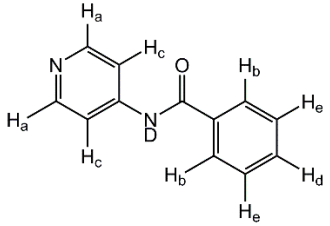
	Inversion T_1 , s	Saturation T_1 , s
H _a	5.28 ± 0.03	5.20 ± 0.05
H _b	6.04 ± 0.03	5.92 ± 0.05
H _c	5.349 ± 0.007	5.25 ± 0.02
H _d	9.4 ± 0.1	9.4 ± 0.2
H _e	4.90 ± 0.04	4.87 ± 0.05

Table 5.2 Thermal relaxation times for free N-(4-pyridyl)benzamide (25 mM) protons in THF- d_8 under hydrogen atmosphere. Error bars represent fitting errors.

	Inversion T_1 , s	Saturation T_1 , s
H _a	5.38 ± 0.01	5.34 ± 0.02
H _b	6.74 ± 0.03	6.78 ± 0.05
H _c	6.40 ± 0.05	6.44 ± 0.08
H _d	11.08 ± 0.08	11.2 ± 0.2
H _e	7.72 ± 0.03	7.93 ± 0.04
NH	3.04 ± 0.03	3.11 ± 0.04

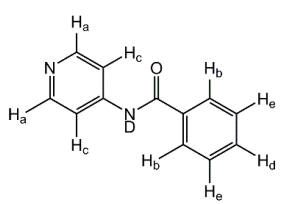
There is a good agreement between the two methods to within 2.7%; the presented fitting errors under estimate the real reproducibility error. These results prove therefore that saturation recovery is a reliable method for measuring T_1 (in this case of values from 3 to 11 s) in our system. At the same time, saturation recovery takes approximately 10-times less time for a complete measurement.

5.3.1 Effect of air on relaxation times

Due to the sensitivity of the relaxation time to paramagnetic components, oxygen that is dissolved in solution has a significant effect on the T_1 values of the substrate. Absence of air is also important for the SABRE process because paramagnetic oxygen can cause *para*-hydrogen to convert

into *ortho*-hydrogen, which decreases the level of hyperpolarisation achieved.⁴⁷ In the SABRE measurements the sample is degassed using a freeze-pump-thaw procedure using a bath of dry ice and acetone prior to hydrogen (H₂) addition. In order to compare the T_1 values under these conditions, one of the two samples of 50 mM **4-PBA** in methanol-*d*₄ was left under normal air atmosphere, while another was degassed and filled with 4 bar H₂. Table 5.3 presents the T_1 values measured for the two samples.

Table 5.3 Thermal relaxation times for N-(4-pyridyl)benzamide (50 mM) under air and hydrogen in methanol-*d*₄ at 298 K. Error bars represent fitting errors.

	T_1 , s	
	Air	H ₂
H _a	2.556 ± 0.008	4.790 ± 0.003
H _b	2.920 ± 0.009	5.590 ± 0.009
H _c	2.63 ± 0.01	4.960 ± 0.004
H _d	3.477 ± 0.006	8.82 ± 0.01
H _e	2.531 ± 0.008	4.62 ± 0.01

The comparison of the T_1 values for **4-PBA** under air and hydrogen atmosphere is presented in Table 5.3 and shows a significant reduction in T_1 for all resonances in the presence of oxygen. This is relevant to hyperpolarisation measurements because prolonging the substrate's T_1 value can help to obtain higher levels of polarisation in SABRE measurements. In addition, absence of air limits degradation of the active SABRE complex, which is typically air-sensitive once activated. Therefore, degassing is an important step in the preparation of SABRE samples.

5.3.2 Role of solvent on thermal T_1 values and SABRE signal

Solvent effects on SABRE catalysis have been discussed previously in the literature.^{90, 102, 103} A change of solvent can affect the T_1 values of the substrate, the ligand exchange rates, the composition and behaviour of exchangeable proton groups, as well as the solubility of the catalyst, substrate and *p*-H₂, and therefore, polarisation transfer. Hence it can be expected to find complex behaviour.

Here solvent effects on the T_1 values and the level of SABRE hyperpolarisation are studied for 3,5-diaminopyridine (**3,5-DAP**). Samples of 10 eq of **3,5-DAP** (50 mM) to 5 mM pre-catalyst **1** were prepared and activated with 4 bar (absolute) $p\text{-H}_2$ in the three solvents: a) methanol- d_4 , b) 50:50 (by volume) of methanol- d_4 and *protio*-methanol and c) dichloromethane (DCM). A characteristic hydride signal, at around -23.1 ppm in methanol and -23.5 ppm in DCM, indicates the formation of the $[\text{Ir}(\text{H})_2(\text{IMes})(\mathbf{3,5-DAP})_3]\text{Cl}$ complex in all three solvent systems. ^1H longitudinal relaxation time (T_1) values for free **3,5-DAP** were measured using the inversion recovery experiment in the presence of 5 mM $[\text{Ir}(\text{H})_2(\text{IMes})(\mathbf{3,5-DAP})_3]\text{Cl}$ in these solvent systems at 400 MHz (Table 5.4).

Table 5.4 T_1 values for free 3,5-diaminopyridine protons after the activation of 5 mM $[\text{Ir}(\text{Cl})(\text{COD})(\text{IMes})]$ with 10 eq 3,5-diaminopyridine in methanol- d_4 , 50:50 (by volume) mixture of methanol- d_4 and *protio*-methanol and dichloromethane- d_2 at 9.4 T. The quoted errors represent fitting errors.

	T_1, s		
	CD_3OD	50:50 $\text{CD}_3\text{OD} :$ CH_3OH	CD_2Cl_2
<i>ortho</i>	5.77 ± 0.02	2.86 ± 0.02	4.47 ± 0.02
<i>para</i>	18.09 ± 0.06	3.9 ± 0.2	5.12 ± 0.02
NH_2	Not visible	Not visible	1.524 ± 0.005

The measured T_1 values in the three solvents showed that in the 50:50 methanol mixture and DCM, the *ortho* and *meta* protons of **3,5-DAP** possess comparable T_1 values. In contrast, the T_1 values in methanol- d_4 are dramatically longer for the *para*-site adjacent to the deuterated amino groups. This is a consequence of proton-proton relaxation being more effective than proton-deuterium relaxation. The amino group signal is not visible in the methanol- d_4 : methanol (50:50) mixture due to hydrogen isotope exchange with the labile deuterium of the solvent deuterioxy group and peak broadening. However, the amino group is expected to be partially protonated. Thus, the T_1 of **3,5-DAP** *para* proton become shorter. It is hypothesised that proton exchange with the solvent creates an additional relaxation factor, which causes shorter T_1 values compared to the values measured in DCM where the amino groups are fully protonated. Due to the

presence of the *protio*-methanol in the 50:50 mixture, the overall relaxation effect is higher than of the other systems due to dipole-dipole interactions.

In order to investigate how the change in T_1 values correlates with the signal enhancements of **3,5-DAP** in the different solvents, SABRE measurements were performed using the stray field of the 400 MHz NMR spectrometer to provide a polarisation transfer field of ~ 65 G, determined using a Gaussmeter (GM08, Hirst Magnetic Instruments Ltd). Table 5.5 summarises the absolute SABRE enhancement factors of the ^1H NMR resonances of **3,5-DAP** in the three solvents.

Table 5.5 Enhancement values (per proton) for free 3,5-diaminopyridine protons after the activation of $[\text{Ir}(\text{Cl})(\text{COD})(\text{IMes})]$ with 10 eq 3,5-diaminopyridine in methanol- d_4 , 50:50 (by volume) mixture of methanol- d_4 and *protio*-methanol and dichloromethane- d_2 when a PTF value of 65 G and detection field of 9.4 T.

	CD_3OD	50:50 $\text{CD}_3\text{OD} : \text{CH}_3\text{OH}$	CD_2Cl_2
<i>ortho</i>	180-fold	278-fold	50-fold
<i>para</i>	370-fold	206-fold	30-fold
NH_2	Not visible	Not visible	2-fold

The results in Table 5.5 show that the **3,5-DAP** *ortho* and *para* protons achieve much greater polarisation in methanol- d_4 and the mixture of deuterated and *protio* methanol, while the amino groups are not visible in both thermal or SABRE spectra. Therefore, in methanol- d_4 and the 50:50 methanol mixture the polarisation is distributed across only the **3,5-DAP** *ortho* and *para* protons. DCM has a stronger C-D bond and does not provide deuterium-proton exchange in the solution, thus the amino group of **3,5-DAP** remains protonated and detectable. Higher signal enhancements in methanol compared to the values in DCM can be a result of $p\text{-H}_2$ better solubility in methanol. Although the data on $p\text{-H}_2$ solubility is not available for DCM.¹⁵⁶ In the 50:50 methanol mixture and DCM, the *ortho* protons obtain higher polarisation levels compared to the other substrate protons, as expected, as they are located closer to the hydrides within the complex. However, in the case of **3,5-DAP** in methanol- d_4 the proton in *para* position possesses higher enhancement than the *ortho* proton. This is associated with much longer T_1 of *para* proton in methanol- d_4 due to the effect of

deuteration, which results in a larger enhancement factor at the point of measurement. Although, in this case the change in T_1 values readily explain the differences in the SABRE enhancement levels seen in different solvents, the effect of solvent on the exchange rates of the bound substrate of the catalyst should clearly be taken into account for a rigorous analysis.

Therefore, variation of the solvent has been shown to improve SABRE hyperpolarisation levels whilst changing the distribution of the polarisation within a molecule. The underlying reasons for these effects were revealed by the T_1 measurements.

5.3.3 Effect of the SABRE catalyst on relaxation times

In this section, the effect of the SABRE catalyst on the substrate T_1 value is investigated. Substrate's T_1 values have been shown to be affected by SABRE catalysis and hence such a study is critical for understanding.^{90, 148} This change happens because while the substrate is bound to the metal centre it is thought to possess a much shorter T_1 than when in free solution. Hence exchange will lead to some form of weighted average of the free and bound T_1 values. If there is no chemical exchange, or it occurs on a timescale much slower than the relaxation times, a unique relaxation time would be observed for both the bound and free forms of the substrate. However, in the case of rapid exchange, an average T_1 value would be measured for both forms,^{90, 148} resulting in a weighted-average T_1 which is dependent on the catalyst and free substrate concentrations as well as the rate of chemical exchange.¹⁴⁸

5.3.3.1 Effect of unactivated catalyst on relaxation

In order to investigate the effect of the unactivated SABRE catalyst on T_1 , a series of 5 mM solutions of the pre-catalyst [Ir(Cl)(COD)(IMes)] containing various concentrations of the substrate (**4-AP**) were prepared. They were degassed to remove the effects of dissolved oxygen, which could mask the effect that is investigated here. [Ir(COD)(IMes)(**4-AP**)]Cl forms in this process. The resulting T_1 values for bound and free **4-AP**, determined by the saturation recovery technique, are presented graphically in Figure

5.4 (see Table A5 in Appendix for the T_1 values) as a function of **4-AP** concentration.

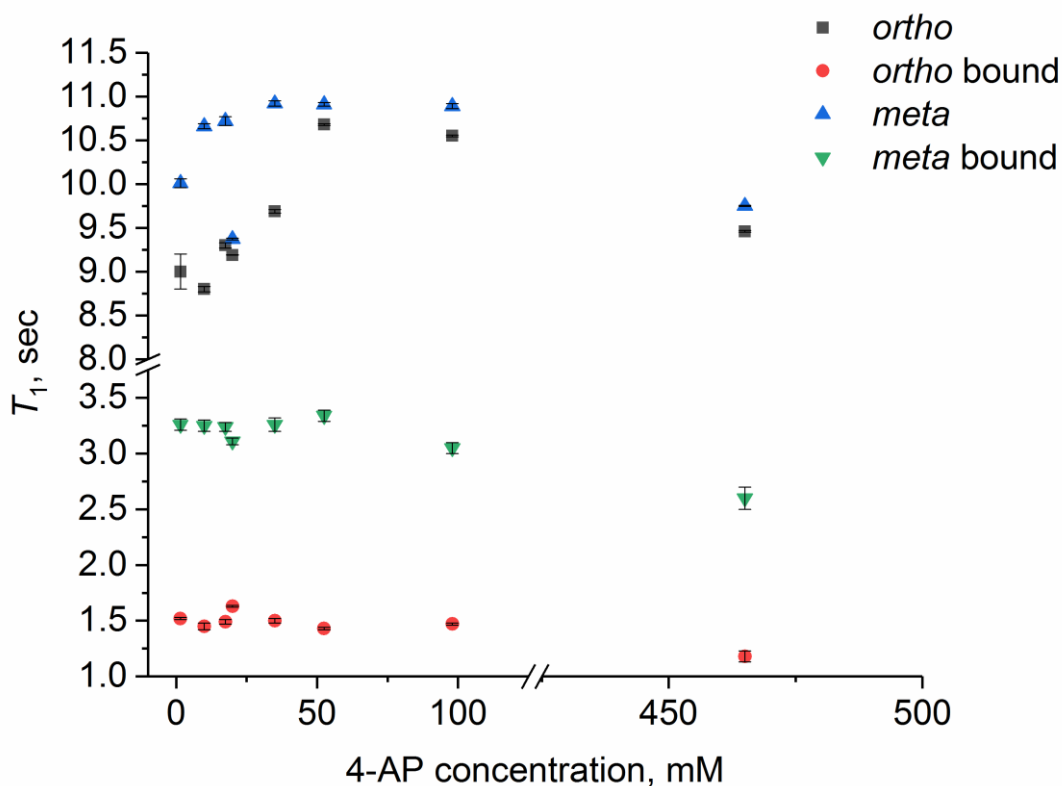


Figure 5.4 Change in **4-AP** T_1 values in presence of unactivated catalyst [Ir(COD)(IMes)(**4-AP**)]Cl (5 mM) with increase of **4-AP** concentration. Error bars represent the fitting errors.

Different T_1 values were found for the two forms of **4-AP** at all concentrations. The bound T_1 values appear to fall slightly with increase in substrate concentration. In contrast, the free T_1 values show a much more visually significant change where they first increase with substrate loading before subsequently falling. The higher loading reduction in T_1 is likely to be due to the effect of increasing solution viscosity and is reflected in all values. The other changes in free and bound substrate T_1 values are commensurate with slow ligand exchange which was not observed by EXSY experiments that measured exchange with mixing times of up to 1 s. The T_1 values for the free **4-AP** in the presence of unactivated catalyst lay in a range from 8.8 ± 0.03 s to 10.68 ± 0.01 s for the *ortho* proton and from 9.37 ± 0.01 s to 10.92 ± 0.03 s for the *meta* proton with the concentration (Table A5 in Appendix). These values are similar to the T_1 values measured for pure

4-AP in methanol- d_4 under H_2 at 25 mM ($T_{1,ortho} = 9.5 \pm 0.9$ s, $T_{1,meta} = 11.2 \pm 0.1$ s) and at 150 mM ($T_{1,ortho} = 8.14 \pm 0.05$ s, $T_{1,meta} = 10.2 \pm 0.04$ s). Therefore the reaction of pre-catalyst with substrate to form $[Ir(COD)(IMes)(\mathbf{4-AP})]Cl$ is found to have only a small effect on substrate T_1 .

5.3.3.2 Effect of active catalyst on relaxation

When H_2 gas was added to a solution of **4-AP** with the SABRE pre-catalyst, rapid 2H labelling of **4-AP** is observed and any T_1 effects can therefore no longer be attributed to a single change. However, solutions of N-(4-pyridyl)benzamide (**4-PBA**), 3,5-diaminopyridine (**3,5-DAP**) and 4-methylpyridine (**4-MP**) could be examined in this way as this HIE reaction occurs on a slower timescale. Free substrate relaxation times were determined for these materials in the absence of the SABRE catalyst in methanol- d_4 under a hydrogen atmosphere to produce control data. Analogous data were then collected at 298 K for these three substrates in the presence of the active SABRE catalyst and H_2 . These results are shown in Table 5.6, Table 5.7 and Table 5.8 respectively. The results for the free substrate protons are labelled (H_x), whilst when bound *trans* to hydride they are labelled (H_x') and *trans* to carbene (H_x'') as shown in Figure 5.5. The T_1 values for **4-PBA** and **3-DAP** were determined at two different concentrations to further examine catalyst effects.

There is an overlap for the free and bound resonances of **4-PBA** and hence aggregated T_1 values result. However, the *ortho* resonances H_a and H_a' do yield distinct T_1 values for the two forms. For the other substrates separate peaks are observable for all resonances.

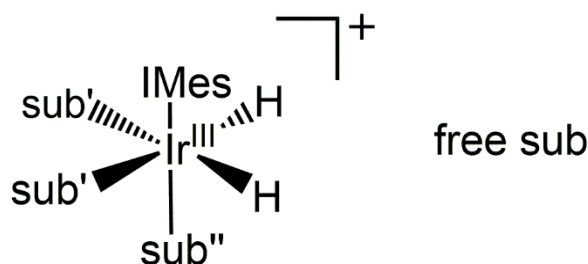


Figure 5.5 Annotation for substrate protons bound to the catalyst *trans* to hydride ligands (sub') and *trans* to IMes carbene (sub'') and in free solution (sub).

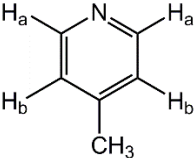
Table 5.6 Relaxation times for free N-(4-pyridyl)benzamide protons and those of free and bound N-(4-pyridyl)benzamide in presence of $[\text{Ir}(\text{H})_2(\text{IMes})(\text{N}-(4\text{-pyridyl})\text{benzamide})_3]\text{Cl}$ (5 mM) in methanol- d_4 solution under a hydrogen atmosphere. Error bars represent fitting errors.

	T_1, s			
	5 eq		10 eq	
	Pure	with 4	Pure	with 4
H_a	4.76 ± 0.01	0.63 ± 0.02	4.790 ± 0.003	2.40 ± 0.01
H_a'	-	0.56 ± 0.02	-	2.08 ± 0.06
H_b	5.44 ± 0.04	3.42 ± 0.06	5.59 ± 0.01	4.22 ± 0.01
H_c	4.83 ± 0.01	5.5 ± 0.2	4.960 ± 0.004	4.35 ± 0.02
H_d	8.3 ± 0.1	6.31 ± 0.08	8.82 ± 0.01	7.36 ± 0.01
H_e	4.45 ± 0.03	4.18 ± 0.05	4.62 ± 0.01	3.823 ± 0.003

Table 5.7 Relaxation times for free 3,5-diaminopyridine protons and those of free and bound 3,5-diaminopyridine in presence of $[\text{Ir}(\text{H})_2(\text{IMes})(3,5\text{-diaminopyridine})_3]\text{Cl}$ (5mM) in methanol- d_4 under hydrogen atmosphere. Error bars represent fitting errors.

	T_1, s			
	5 eq		10 eq	
	Pure	with 4	Pure	with 4
H_a	3.85 ± 0.01	3.49 ± 0.06	3.17 ± 0.02	5.60 ± 0.04
H_a'	-	3.24 ± 0.08	-	5.0 ± 0.2
H_a''	-	3.05 ± 0.07	-	2.54 ± 0.07
H_b	22.72 ± 0.05	13.54 ± 0.08	21.11 ± 0.04	17.56 ± 0.06
H_b'	-	13.30 ± 0.09	-	16.2 ± 0.2
H_b''	-	10.79 ± 0.08	-	9.68 ± 0.07

Table 5.8 Relaxation times for free 4-methylpyridine protons and those of free and bound 4-methylpyridine (10 eq, 7-fold excess) in presence of $[\text{Ir}(\text{H})_2(\text{IMes})(4\text{-methylpyridine})_3]\text{Cl}$ (5mM) in methanol- d_4 under hydrogen atmosphere. Error bars represent fitting errors.

	T_1 , s	
	Pure	with 4
H _a	18.66 ± 0.02	5.89 ± 0.03
H _a '	-	5.53 ± 0.03
H _a ''	-	1.67 ± 0.03
H _b	17.10 ± 0.07	8.3 ± 0.2
H _b '	-	8.0 ± 0.2
H _b ''	-	2.531 ± 0.001
CH ₃	5.90 ± 0.08	3.5 ± 0.1
CH ₃ '	-	3.2 ± 0.1

The resulting data confirm that the presence of the SABRE catalyst significantly shortens the associated substrate T_1 values. As an exception, the **3,5-DAP** *ortho* proton relaxation becomes slower for the 10 eq loading relative to the pure sample. A similar change has been seen for pyridine in presence of $[\text{Ir}(\text{H})_2(\text{NHC})(\text{py})_3]^+$, where the NHC is ICy, $\text{ImMe}_2\text{NPr}^i_2$ or IMe under 3 bar $p\text{-H}_2$.¹⁵⁷ However, the origin of this effect was not investigated but may result from the catalyst changing NH/ND exchange rates or the degree of hydrogen bonding in solution.

For all cases, the substrate molecules bound *trans* to the hydride in the active catalyst exhibit T_1 values that are similar to the associated free proton resonances. This suggests that the exchange between the free and bound substrate is fast on the timescale of the relaxation and an average results. These results also show that the relative catalyst loading affects the substrate T_1 . In general, T_1 values become longer at higher substrate to the catalyst ratios.

It should be possible to use the loading, $T_{1,\text{free}}$ and $T_{1,\text{average}}$ values to estimate the ligand exchange rates by manipulation of the model for SABRE exchange previously reported in the literature by Barskiy when the fast exchange limit is not achieved.⁴⁶ Conversely, this principle could be used in reverse to estimate a true bound proton T_1 values when exchange of the

associated groups is fast, even if their signals cannot be directly measured due to overlap. Alternatively, if the rates of ligand exchange are known alongside the $T_{1,\text{free}}$ and $T_{1,\text{average}}$ values such analyses can be deployed even if the system is not undergoing fast exchange. This type of approach will be more important for low field (1 T) NMR spectroscopy; see Chapter 7 for further results.

5.3.3.3 Measurement of T_1 values in the absence of fast exchange

Cooling the system to lower temperatures will slow the rate of exchange between the free and bound substrate. Once the rate of chemical exchange is sufficiently slow, unique T_1 values can be measured for the bound and free resonances. As a consequence of this temperature change the chemical shifts of some resonances may change. This change could be of benefit if overlapping proton peaks separate at lower temperature. However, it should be noted that the T_1 values are also dependent on temperature. Table 5.9 and Table 5.10 present the T_1 values of the free and bound *ortho* and *meta* protons of **4-PBA** and **3,5-DAP** at room temperature and at 253 K for **4-PBA** and 260 K for **3,5-DAP**.

Table 5.9 Thermal relaxation times for free N-(4-pyridyl)benzamide (2-fold excess) protons in MeOD in presence of $[\text{Ir}(\text{H})_2(\text{IMes})(\text{N}-(4\text{-pyridyl})\text{benzamide})_3]\text{Cl}$ under 4 bar hydrogen atmosphere at 298 K and 253 K. Error bars represent fitting errors.

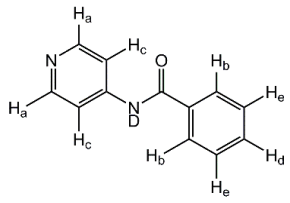
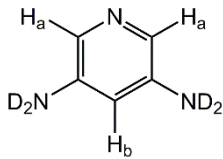
	T_1 , s	
	at 298 K	at 253 K
H_a	0.63 ± 0.02	2.579 ± 0.006
H_a'	0.56 ± 0.02	0.91 ± 0.01
H_c	5.5 ± 0.2	2.61 ± 0.01
H_c''	overlap at 298 K	2.3 ± 0.04

Table 5.10 Thermal relaxation times for free and bound 3,5-diaminopyridine (2-fold and 7-fold excess) protons in presence of 5 mM $[\text{Ir}(\text{H})_2(\text{IMes})(3,5\text{-diaminopyridine})_3]\text{Cl}$ (5mM) in methanol- d_4 under 4 bar hydrogen atmosphere at 298 K and 260 K. Error bars represent fitting errors.

	T_1 , s			
	5 eq		10 eq	
	at 298 K	at 260 K	at 298 K	at 260 K
H_a	3.49 ± 0.06	8.79 ± 0.05	5.60 ± 0.04	11.27 ± 0.06
H_a'	3.24 ± 0.08	1.04 ± 0.01	5.0 ± 0.2	1.01 ± 0.02
H_a''	3.05 ± 0.07	1.80 ± 0.03	2.54 ± 0.07	1.72 ± 0.09
H_b	13.54 ± 0.08	12.8 ± 0.1	17.56 ± 0.06	12.69 ± 0.08
H_b'	13.30 ± 0.09	5.78 ± 0.08	16.2 ± 0.2	5.25 ± 0.08
H_b''	10.79 ± 0.08	7.44 ± 0.07	9.68 ± 0.07	6.74 ± 0.07

The data in Table 5.9 and Table 5.10 show that in the low temperature regime the bound and free substrate protons now have distinct T_1 values, while an average value is observed at room temperature. At low temperature the difference between the **3,5-DAP** T_1 values (Table 5.10) for the free and bound substrate *ortho* protons (H_a and H_a') is bigger than the difference for *meta* protons (H_b and H_b'). Therefore, the effect of the catalyst on the observed T_1 values is reduced for the protons located further from the binding site to the metal centre. This suggests that interaction with the quadrupolar nucleus Ir ($I = 3/2$) may contribute to the relaxation time but reported ^2H -labelling studies on the NHC confirm there is an *intra* molecular effect.⁴⁰ It should be noted that the free and bound **4-PBA** *meta* peaks at 7.92 ppm and 7.44 ppm partially overlap with other proton peaks in the complex. This leads to an increase in the error associated with their T_1 values.

In conclusion, the measurement of T_1 values at low temperature and therefore in the absence of rapid chemical exchange provides a rough estimate of the T_1 values for the bound substrate protons, which are generally less than 2 s for the *ortho* positions. However, as T_1 values are dependent on temperature, these values can only be used as an approximation of the bound T_1 values at room temperature. As the SABRE polarisation builds up in the substrate with a rate proportional to its relaxation, the T_1 values are critical to the outcome of SABRE.¹⁵⁸

5.4 Single-shot hyperpolarised relaxation time measurements

5.4.1 Introduction

As discussed previously (see Introduction) interactions with the surroundings return an assembly of nuclei to a thermally controlled population distribution between nuclear spin state energy levels over time. In a traditional T_1 measurement, this equilibrium is disrupted by the action of a radiofrequency (RF) pulse and the changes are observed as it is reestablished. Alternatively, a hyperpolarised starting point can be used and its decay with time followed to yield the analogous lifetime, a hyperpolarised T_1 or $\text{hyper}T_1$, which may be the same as the unpolarised value. One way to achieve this in practice is to repeatedly rehyperpolarise the sample outside the magnet and wait a series of different but specified times to detect the NMR signal in the spectrometer.¹⁵¹ In this case, the T_1 values measured correspond to relaxation in the field where the sample was held during the waiting time. This technique requires consistency in the initial hyperpolarisation level for reliability and suggests an automated approach should be used. Notably, it is less time-consuming than the normal inversion recovery method as repolarisation with SABRE takes less time than the required $5 \cdot T_1$ of the normal method. However, the need to repolarise the sample means this method is not readily applicable to chemically transforming systems.

A further way to measure T_1 is to first invert the magnetisation and then use a series of small flip angle pulses to encode a whole T_1 curve in a single shot.¹⁵⁹ The sequence proposed by Kaptein *et al.* to do this is shown in (Figure 5.6). Homospoil pulses can be applied after the 180 degree pulse and FID acquisition to destroy any transverse magnetisation and reduce echo formation.¹⁵⁹ The relaxation curve created by this method therefore takes a total experiment time of $5 \cdot T_1$ for a single measurement.

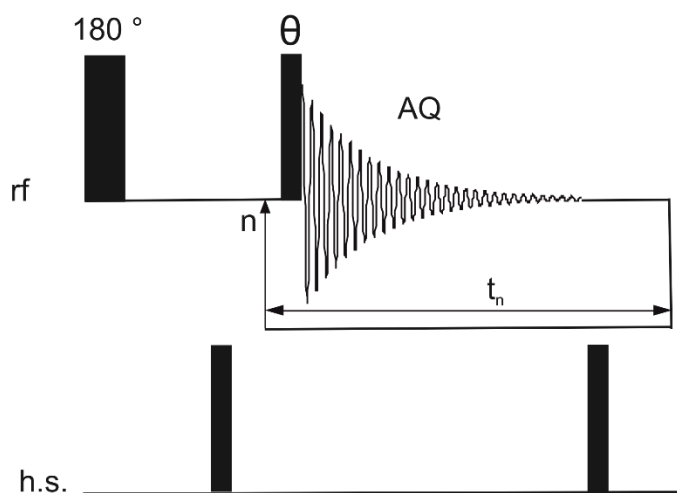


Figure 5.6 Constant flip angle sequence proposed by Kaptein to determine T_1 .

The choice of flip angle reflects a balance between the need for high signal-to-noise (SNR) and the destruction of z-magnetisation by the observation pulse. Consequently, fewer points can be acquired with larger flip angles as any magnetisation is consumed quickly. Small flip angles though use negligible amounts of magnetization in each pulse. For example, z-magnetisation drops with each pulse by 0.38% if $\theta = 5^\circ$, by 1.5 % if $\theta = 10^\circ$ and by 13.4 % if $\theta = 30^\circ$. This fall off can be corrected for according to Equation 5.4¹⁵⁹, where $\frac{1}{T_1^*}$ is the observed relaxation time, T_1 is real relaxation time, θ is the flip angle and τ the time delay between pulses. Hence the true T_1 can be obtained from a semi-logarithmic plot with time correction $T_c = \frac{\tau}{\ln \cos \theta}$.

$$\frac{1}{T_1^*} = \frac{1}{T_1} - \frac{\ln \cos \theta}{\tau} = \frac{1}{T_1} - \frac{1}{T_c} \quad (5.4)$$

The resulting low signal intensities however limit this approach when working with samples of low concentration, or when nuclei of low natural abundance are detected. A combination of a single-shot T_1 measurement with hyperpolarisation could solve the sensitivity problem. In such an experiment, the hyperpolarisation step replaces the 180 degree pulse and the observed signal decay is viewed using a train of low flip angle pulses. Figure 5.7 presents a schematic of this procedure. In practice, a pseudo 2D NMR spectrum is created containing n decaying SABRE hyperpolarised

spectra. The integrals of the hyperpolarised signals are then plotted against delay time and fitted to an exponential, to yield a decay constant.

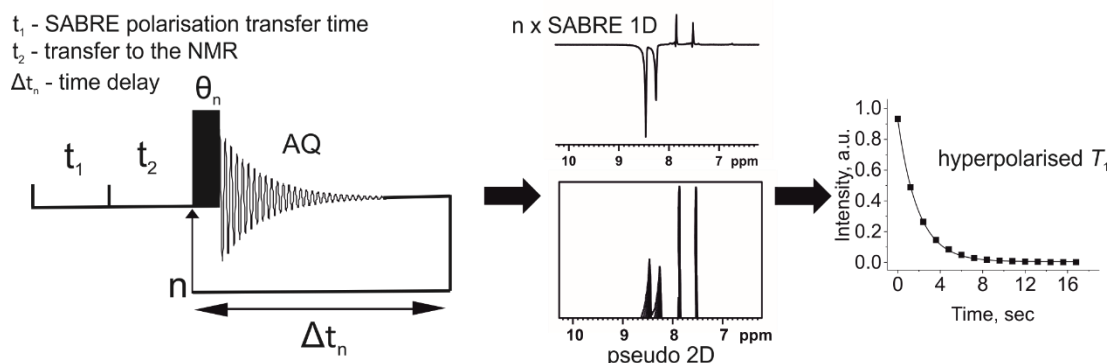


Figure 5.7 Schematic representation of a single-shot hyperpolarised T_1 measurement using a small flip angle NMR pulse sequence.

Once the sample is in the spectrometer for detection, the thermal magnetisation build-up occurs at the same time as the hyperpolarisation decay, and is also sampled in the same experiment. Day *et al.*¹⁶⁰, used DNP hyperpolarisation in combination with the single-scan T_1 methods for ^{13}C and ^{15}N relaxation assessment. The authors fitted the resultant hyperpolarised signal decay to Equation 5.5, which corrects for polarisation recovery after each RF pulse. Here $M_z(nt)$ is the magnetisation remaining after the n -th pulse, M_{DNP} is magnetisation produced initially by the DNP experiment, M_0 the thermal magnetisation, t the time between RF pulses, θ the flip angle of the RF pulse and T_1 the measured relaxation time constant. This approach assumes that the hyperpolarisation decays with the same time constant as the thermal magnetisation builds up.

$$M_z(nt) = M_{DNP}\alpha^n\beta^n + M_0(1 - \beta)\frac{1 - \alpha^n\beta^n}{1 - \alpha\beta} \quad (5.5),$$

where $\alpha = \cos\theta$ and $\beta = \exp(-t/T_1)$.

Hyperpolarisation relaxation times measured using both the constant flip angle sequence and the multiple hyperpolarised scans technique have been reported in the literature, and have been used to investigate the SABRE process.^{151, 161, 162} Knowledge of these values is also important in assessing the impact of solution transfer times during SABRE. The T_1 values

of metronidazole nuclei have been found with the small flip angle sequence in one hyperpolarised scan in a 9.4 T detection field.¹⁵¹ In this study, heteronuclear SABRE T_1 values have been shown to match the time constant for hyperpolarisation build-up in the case of metronidazole in a polarisation field of $<1 \mu\text{T}$, when measured using the multiple hyperpolarised scans method.¹⁵¹ Thus, the authors confirmed that the rise of the SABRE hyperpolarisation is controlled by the T_1 value in this case. Moreno *et al.* showed an example of a system, containing pyridine with the [Ir(Cl)(COD)(IMes)] catalyst and 5 mM HCl in methanol- d_4 , where SABRE lifetimes appear to be higher than the thermal T_1 value.¹⁶¹ Here the thermal values were 3-times higher for the solvent's residual protons (CD_3OH) and around 1.4-times higher for the pyridine protons. The authors suggest that repolarisation via cross-relaxation acts to reduce signal losses to explain this.¹⁶¹ Hyperpolarised T_1 values have also been used to investigate the effect of magnetic field and substrate to catalyst ratio on the achieved hyperpolarisation levels of pyridine and metronidazole.^{151, 162} Truong *et al.* showed that ^{15}N T_1 values for pyridine are higher at 9.4 T than in the polarisation transfer field (μT and mT range) and also increase with the substrate concentration.¹⁶²

In the study below the use of different single-shot sequences to measure the lifetime of the signal generated by the SABRE hyperpolarisation method is explored. First, the constant flip angle sequence (cfa) discussed above is combined with SABRE hyperpolarisation. Second, a variable flip angle (vfa) sequence is designed and tested by comparison to the cfa sequence. These measurements are performed as single-shot hyperpolarised experiments (Figure 5.7). The effect of the thermal signal contribution and the accuracy of the flip angles on the hyper T_1 values are investigated along with the resulting signal-to-noise ratios.

5.4.2 Constant flip angle sequence

For the constant flip angle study combined with SABRE the impact of thermal signal build-up is differentiated from the reduction in the z-magnetisation during the experiment. A reference scan and subsequent calculations are employed for this purpose. In the case when the SABRE signal level is not much higher than the thermal signal, the thermal contribution could significantly affect the result. Also, if the SABRE and thermal signals exhibit different signs (i.e. one emission and absorption) their combination leads to a reduction in the observed signal. Similarly, if they are the same sign, the acquired signal increases. Hence, it is important to assess these effects.

In order to map the thermally polarised signal, a series of constant 5 degree flip angle pulses were used to acquire a pseudo 2D spectrum of 15 spectra, separated by set time delays. This experiment was applied to an activated sample containing 5 eq of **4-PBA** relative to the pre-catalyst, [Ir(Cl)(COD)(IMes)], in methanol- d_4 . The sample first was held outside of the spectrometer for 1.5 min to ensure that any prepolarisation was effectively zero. Hence a thermal polarisation build-up curve is produced by the constant flip angle sequence. Figure 5.8 presents a projection of the **4-PBA** *ortho* proton NMR signal intensity from the pseudo 2D dataset as a function of the buildup time.

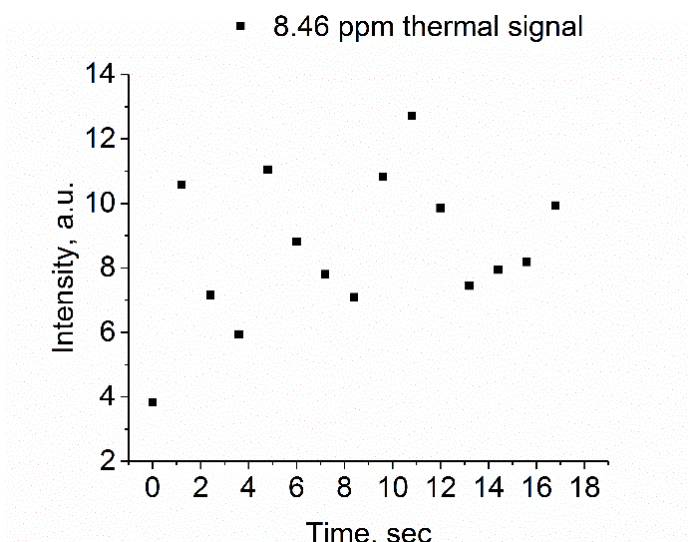


Figure 5.8 Thermal polarisation increase during constant 5 degree flip angle sequence for hyper T_1 measurement for the **4-PBA** free *ortho* peak at 8.46 ppm.

Figure 5.8 exhibits a weak, random thermal signal that is built up once the sample is inserted in the spectrometer for the hyper T_1 measurement. In the further measurements, the hyper T_1 values obtained by fitting the hyperpolarised signal reduced by the thermal signal acquired in a reference “blank” scan, like in Figure 5.8. These values are then compared to the values without such correction. Table 5.11 summarises the resulting hyperpolarised relaxation times for the free *ortho* and *meta* and bound *ortho* proton resonances of N-(4-pyridyl)benzamide (**4-PBA**) as determined when the constant pulse was 5°, with and without thermal subtraction.

Table 5.11 Hyperpolarised relaxation times for free and bound N-(4-pyridyl)benzamide protons (**4-PBA**) (5 eq, 2-fold excess) determined in presence of [Ir(H)₂(IMes)(N-(4-pyridyl)benzamide)₃]Cl by application of a constant 5° pulse flip angle. Error bars represent fitting errors for individual T_1 values and standard errors for the average T_1 values (in bold).

	Hyperpolarised T_1 , s		
	<i>ortho</i>	<i>meta</i>	<i>ortho'</i>
Without thermal signal correction	1.83 ± 0.01	5 ± 1	1.87 ± 0.01
	1.89 ± 0.02	4.0 ± 0.4	1.94 ± 0.02
	1.89 ± 0.02	4.6 ± 0.4	1.99 ± 0.01
	1.87 ± 0.03	5 ± 1	1.94 ± 0.02
With thermal signal correction	1.83 ± 0.01	5.3 ± 0.9	1.87 ± 0.01
	1.89 ± 0.02	3.9 ± 0.4	1.94 ± 0.01
	1.89 ± 0.02	4.6 ± 0.4	1.99 ± 0.01
	1.87 ± 0.03	5 ± 1	1.94 ± 0.03

There is no significant difference between hyper T_1 values calculated with and without the use of the thermal reference scan. These data show that by using a 5 degree pulse the contribution from the thermal polarisation is negligible when compared to the SABRE-derived signal enhancements. This reflects the fact that there is 338-fold signal enhancement for the 8.46 ppm and 83-fold for the 7.87 ppm resonances. However, for the higher concentration samples, thermal polarisation is expected to give stronger signals and the correction will be needed. It should also be noted that the hyperpolarised T_1 values for the equivalent free and bound protons exhibit very similar values as a consequence of fast chemical exchange at room temperature.

This analysis assumes that the amount of magnetisation consumed by each RF pulse is insignificant. This approximation will only be true for very small flip angle pulses as shown in section 5.3.1, however it will lead to lower overall detectable signal intensity. Conversely, for the larger flip angles a correction to the z magnetisation should be performed in order to take into account its consumption by the pulses. An equation for the signal change as a function of the number of pulses during a constant flip angle sequence is shown in Equation 5.6. The value $M_{xy}(t_n)$ represents the detected magnetisation, while $M_z \cos^n \theta$ is the residual magnetisation along z-axis after n pulses, where $t_n = \sum_{m=1}^{n-1} \Delta t_m$ and $n = 1, 2, 3 \dots N$ for $N = 15$ pulses.

$$M_{xy}(t_n) = M_0 \cos^{n-1} \theta \sin \theta \exp(-t_n/T_1) \quad (5.6)$$

The experimental value $M_{xy}(t)$, corrected by $\cos^n \theta$, reflects the loss of magnetisation along z-axis due to relaxation. Therefore, the equation for the magnetisation corrected T_1 curve is shown in Equation 5.7.

$$\frac{M_{xy}(t_n)}{\cos^n \theta} = M_0 \sin \theta \exp\left(-\frac{t_n}{T_1}\right) + M_{xy,offset} \quad (5.7)$$

These calculations were applied to the acquired experimental hyperpolarised signal integrals and the corrected signals were calculated.

The T_1 values were found from these data by fitting to Equation 5.7. The plot in Figure 5.9 shows the impact of this correction on the experimental data; in this case the difference is very small as detailed in Table 5.12. The results show no difference, within error, between the hyper T_1 values calculated with magnetisation correction and without. This suggests that a 5 degree flip angle is small enough to validate the assumption that the magnetisation along the z-axis remains approximately the same during the hyperpolarised T_1 measurement.

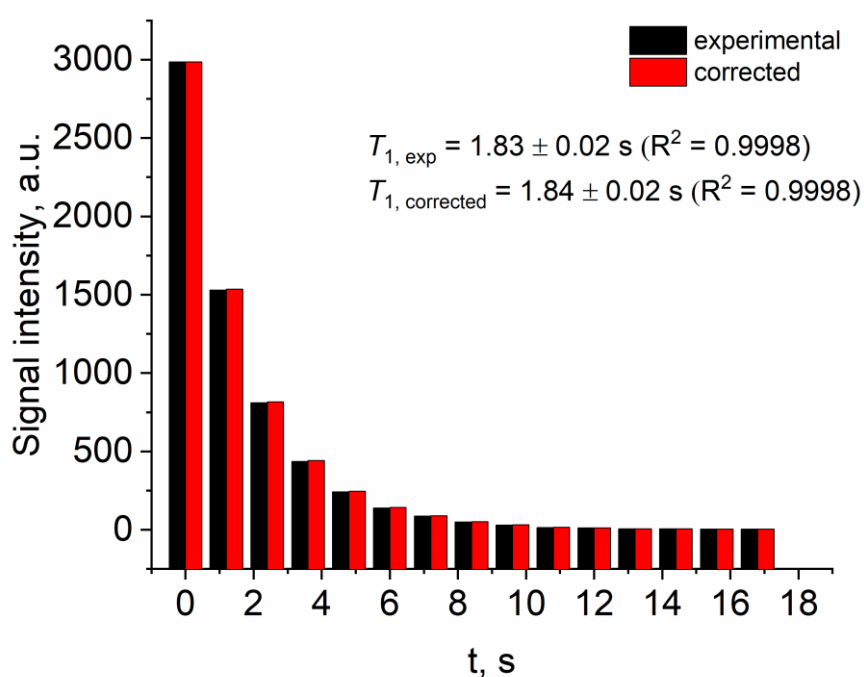


Figure 5.9 Experimental and corrected absolute signal intensities for the constant flip angle hyper T_1 measurement of **4-PBA** free *ortho* proton.

Table 5.12 Hyperpolarised relaxation times for free and bound N-(4-pyridyl)benzamide protons (5 eq, 2-excess) in the presence of $[\text{Ir}(\text{H})_2(\text{IMes})(\text{N}-(4\text{-pyridyl})\text{benzamide})_3]\text{Cl}$ determined with a constant flip angle pulse sequence, without and with thermal correction. Error bars represent fitting errors for individual T_1 values and standard errors for the average T_1 values (in bold).

	Hyperpolarised T_1 , s		
	<i>ortho</i>	<i>meta</i>	<i>ortho'</i>
Without	1.83 ± 0.01	5.3 ± 0.9	1.87 ± 0.01
magnetisation	1.89 ± 0.02	3.9 ± 0.4	1.94 ± 0.01
correction	1.89 ± 0.02	4.6 ± 0.4	1.99 ± 0.01
	1.87 ± 0.03	5 ± 1	1.94 ± 0.03
With	1.83 ± 0.02	4.8 ± 0.7	1.87 ± 0.01
magnetisation	1.89 ± 0.02	4.3 ± 0.4	1.94 ± 0.01
correction	1.89 ± 0.02	4.1 ± 0.3	1.99 ± 0.01
	1.87 ± 0.03	4.4 ± 0.9	1.93 ± 0.02

In conclusion, the hyperpolarisation lifetime can be measured on the timescale of a few minutes. The thermal signal contribution was identified and confirmed to be negligible for the resultant T_1 values due to the high SABRE signal enhancement. A 5 degree pulse angle has shown to provide a negligible influence on the reduction of the starting magnetisation along the z-axis due to the effect of the small flip angle pulses. However, due to the use of the small flip angle, the experiment does suffer from a low signal-to-noise ratio (SNR), which can affect the precision of the hyper T_1 measurement.

5.4.3 Variable flip angle sequence

During the constant flip angle sequence most of the polarisation remains unused due to the small pulse angles. An alternative single-shot sequence that replaces the constant angle pulses with variable flip angle pulses has been designed in order to produce higher signal-to-noise ratio (SNR) NMR spectra, and therefore measure hyper T_1 values more reliably.

In the variable flip angle pulse sequence a series of N FIDs is recorded where each FID is associated with an RF pulse with unique flip angle, θ_n . $M_{xy,n}$ and $M_{z,n}$ are defined as the amplitude of the transverse and longitudinal magnetization vectors immediately following the n th RF pulse, respectively. The time between RF pulses is Δt_n , where the subscript n

denotes the delay between θ_n and θ_{n+1} and $\Delta t_0 = 0$ by definition. The initial magnetisation along the z axis prior to the first RF pulse, M_0 , is the initial amplitude of the hyperpolarisation. Neglecting any thermal magnetisation, the following recursive relationships can be written to describe $M_{xy,n}$ and $M_{z,n}$, where T_1 is the hyperpolarisation lifetime and $M_{z,0} = M_0$:

$$M_{xy,n} = M_{z,n-1} \exp(-\Delta t_{n-1}/T_1) \sin \theta_n \quad (3.8)$$

$$M_{z,n} = M_{z,n-1} \exp(-\Delta t_{n-1}/T_1) \cos \theta_n \quad (3.9)$$

To directly monitor the decay of the magnetisation with an optimal signal-to-noise ratio, the variable flip angles are selected according to the following constraints:

- (1) In the absence of T_1 relaxation, the amount of transverse magnetisation resulting from each RF pulse should be the same for all N RF pulses.
- (2) As much of the magnetisation along the z -axis is sampled during the experiment as possible. Therefore the angles are chosen such that $M_{z,N} \rightarrow 0$ while not violating condition (1).

In the absence of T_1 relaxation, Equations 5.8 and 5.9 simplify to Equations 5.10 and 5.11 and the tangent of the flip angle, θ_n , is defined in terms of the ratio of the transverse and longitudinal magnetization (Equation 5.12).

$$M_{xy,n} = M_{z,n-1} \sin \theta_n \quad (5.10)$$

$$M_{z,n} = M_{z,n-1} \cos \theta_n \quad (5.11)$$

$$\tan \theta_n = \frac{M_{xy,n}}{M_{z,n}} \quad (5.12)$$

Substituting Equation 5.12 into Equation 5.10, the following is obtained:

$$\frac{M_{xy,n}}{M_{xy,n-1}} = \frac{\sin \theta_n}{\tan \theta_{n-1}} \quad (5.13)$$

To fulfil condition (1), $M_{xy,n} = M_{xy,n-1}$ for all n in the absence of T_1 relaxation. Therefore Equation 5.13 simplifies to Equation 5.14, which is defined for all N flip angles as long as $|\theta_{N-1}| \leq \frac{\pi}{4}$.

$$\sin \theta_n = \tan \theta_{n-1} \quad (5.14)$$

Condition (2) is met by determining the maximum value of θ_1 for which $|\theta_{N-1}| \leq \frac{\pi}{4}$. Table 5.13 presents the set of angles that fulfil conditions (1) and (2) where $N = 15$. In the absence of T_1 relaxation, 25.6% of the initial hyperpolarisation, M_0 , is excited by each of the 15 variable flip angles.

In the presence of relaxation, the transverse magnetisation created by each RF pulse is given by Equation 5.15.

$$M_{xy,n} = M_{z,n-1} \exp(-\Delta t_{n-1}/T_1) \tan \theta_{n-1} \quad (5.15)$$

Substituting in Equation 5.12, the following recurrence relationship for the transverse magnetisation is obtained:

$$M_{xy,n} = M_{xy,n-1} \exp(-\Delta t_{n-1}/T_1) = M_0 \sin \theta_1 \exp(-t_n/T_1) \quad (5.16)$$

where t_n is defined in Equation 5.17.

$$t_n = \sum_{m=1}^{n-1} \Delta t_m \quad (5.17)$$

Therefore, the signal observed using the variable flip angle sequence will have an initial amplitude of $M_0 \sin \theta_1$ and decay according to the hyperpolarisation lifetime. It is important to note that this analysis does not model the recovery of the thermal magnetisation during the experiment. These effects are removed by performing a reference measurement without hyperpolarisation as described below.

Table 5.13 Variable flip angles and corresponding z-magnetisation and xy-magnetisation levels (%) for an optimised variable flip angle sequence with $N = 15$ according to Equations 5.10, 5.11, 5.14 and conditions (1) and (2).

Experiment number	Flip angle / degrees	M_z / %	M_{xy} / %
1	15.0	96.6%	25.9%
2	15.5	93.1%	25.8%
3	16.1	89.4%	25.8%
4	16.8	85.6%	25.8%
5	17.5	81.6%	25.7%
6	18.4	77.5%	25.8%
7	19.5	73.0%	25.9%
8	20.7	68.3%	25.8%
9	22.2	63.3%	25.8%
10	24.1	57.7%	25.8%
11	26.6	51.6%	25.9%
12	30.0	44.7%	25.8%
13	35.2	36.5%	25.8%
14	44.9	25.9%	25.8%
15	86.2	1.7%	25.8%

One consequence of the larger flip angles in the variable flip angle sequence compared to the constant flip angle approach is that the amount of thermal signal built-up in the spectrometer during the hyper T_1 measurement can be significant. In order to test the effect of this, an activated sample of 5 eq of 4-methylpyridine (**4-MP**) relative to 5 mM of the pre-catalyst [Ir(Cl)(COD)(IMes)] in methanol- d_4 was held outside of the NMR spectrometer for 1.5 minutes to ensure the destruction of all polarisation. The sample was then transferred into the spectrometer and a single-shot variable flip angle experiment performed. The projection of the **4-MP** *ortho* thermal signal as a function of time, extracted from the pseudo 2D spectra of the “blank” scan, is presented in Figure 5.10 (grey squares). As expected, the thermal signal increases near the end of the hyper T_1 curve because the flip angles increase at longer times (zoomed region in Figure 5.10). In order to isolate the SABRE hyperpolarisation decay, the hyperpolarised signal integral is reduced by the thermal polarisation

integral, and is termed “corrected”. Figure 5.10 compares hyperpolarised uncorrected (red circles) and hyperpolarised corrected by thermal (blue triangles) signal as a function of time.

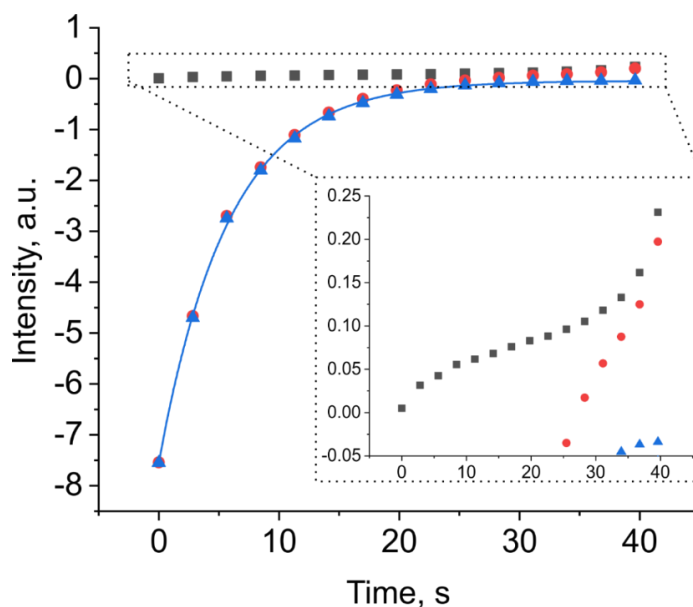


Figure 5.10 Evolution of the hyperpolarised and thermal magnetisation in a variable flip angle single-shot measurement for the free 4-methylpyridine (**4-MP**) *ortho* proton (8.39 ppm) in the presence of $[\text{Ir}(\text{H})_2(\text{IMes})(\mathbf{4}\text{-MP})_3]\text{Cl}$ in methanol- d_4 at 298 K. The decay of the hyperpolarised signal with time is presented in red circles. The corresponding thermal polarisation build-up curve is shown in grey squares. The corrected hyperpolarisation decay curve (the difference between the hyperpolarised and thermal reference measurements) is presented in blue triangles. Inset is an expanded region of the graph illustrating the thermal polarisation increase with time in the reference scan.

As seen from Figure 5.10, the difference between the uncorrected and corrected SABRE signal decay is small in this case. However, the thermal signal contribution is dependent on the relative intensities of the SABRE signal, which vary with the substrate and conditions, and the thermal signal. The necessity of the thermal signal correction for the variable flip angle sequence was explored using an activated sample of **4-PBA**. The hyper T_1 and reference scans were acquired according to the method described above. The results for the corrected and uncorrected relaxation curves are presented for the free *ortho* and *meta* and bound *ortho* protons of **4-PBA** in Table 5.14. Relaxation times, determined with and without the thermal signal correction, are the same within experimental error for the free and bound *ortho* protons. In the case of the free *meta*

proton, the variability is caused by the change in peak phase that cause signal cancelling that is highlighted in Figure 5.11 and reflects the creation of a second spin state by SABRE.^{37, 163}

Table 5.14 Hyperpolarised relaxation times for the *ortho* and *meta* free and *ortho* bound N-(4-pyridyl)benzamide (**4-PBA**) proton signals (5 eq, 2-excess) in the presence of $[\text{Ir}(\text{H})_2(\text{IMes})(\text{N}-(4\text{-pyridyl})\text{benzamide})_3]\text{Cl}$ determined by the variable flip angle pulse sequence. Each experiment was repeated three times with the average given in bold. Error bars represent fitting errors for individual T_1 values and standard errors for the average T_1 values.

	Hyperpolarised T_1 , s		
	<i>ortho</i>	<i>meta</i>	<i>ortho'</i>
Without thermal signal correction	1.85 ± 0.03	4.45 ± 0.2	1.89 ± 0.03
	1.93 ± 0.02	4.00 ± 0.4	1.96 ± 0.02
	1.88 ± 0.01	3.7 ± 0.8	1.91 ± 0.01
	1.89 ± 0.04	4.1 ± 0.9	1.92 ± 0.03
With thermal signal correction	1.84 ± 0.02	4.3 ± 0.2	1.87 ± 0.02
	1.95 ± 0.02	3.6 ± 0.3	1.98 ± 0.01
	1.856 ± 0.008	3.6 ± 0.7	1.87 ± 0.02
	1.88 ± 0.03	3.8 ± 0.2	1.91 ± 0.04

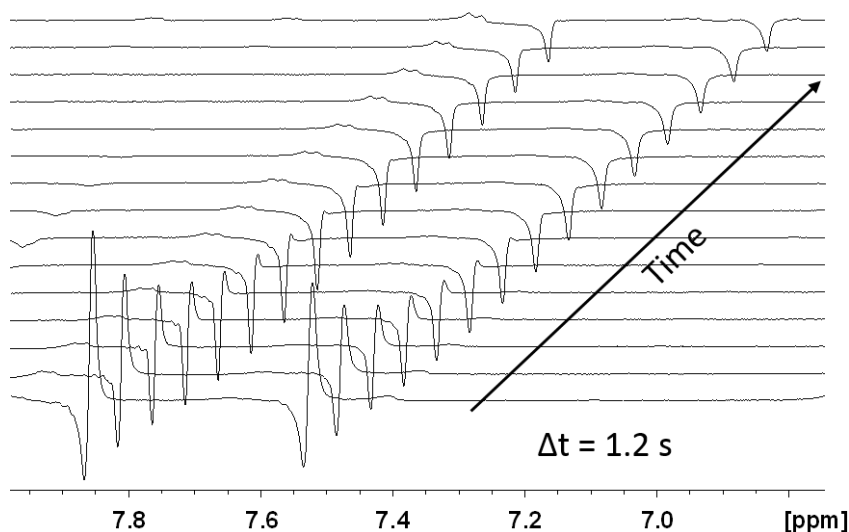


Figure 5.11 Change of phase during hyperpolarised relaxation times measurement with variable flip angle sequence observed for the *meta* proton of N-(4-pyridyl)benzamide (**4-PBA**).

Notably, this method gives the same hyper T_1 values as obtained using the constant flip angle sequence. Due to the bigger pulse angles employed in the variable flip angle sequence the SNR of these NMR spectra is significantly higher than those of the constant flip angle method. This view is confirmed by Figure 5.12a which shows a comparison of the first

spectrum from the variable (vfa) and constant flip angle (cfa) measurements for hyperpolarised 4-methylpyridine (**4-MP**). Figure 5.12b shows a logarithmic plot of the thermally corrected hyperpolarised **4-MP** *ortho* (7.78 ppm) signal intensities for both experiments. This confirms both approaches give the same T_1 with vfa yielding superior peak intensities.

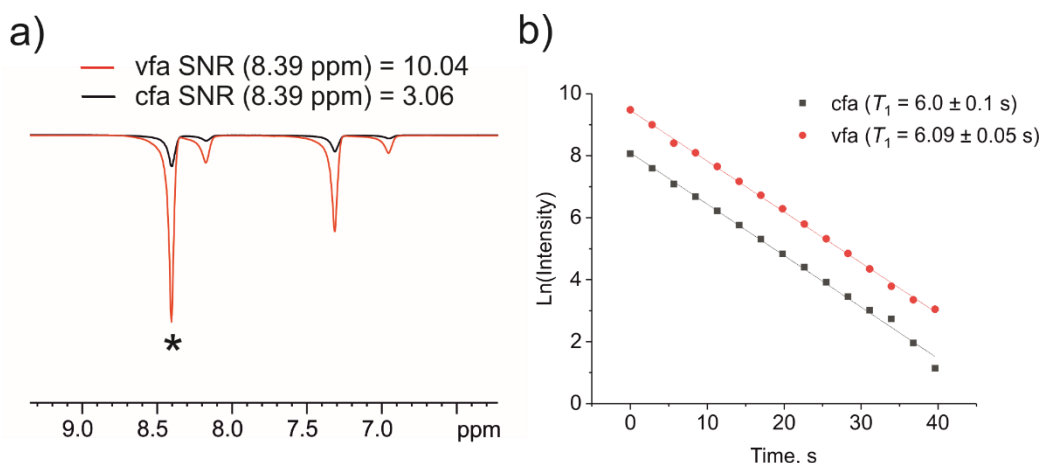


Figure 5.12 a) First NMR spectrum from hyperpolarised variable (vfa, red) and constant (cfa, black) flip angle measurements for free 4-methylpyridine (**4-MP**) in the presence of $[\text{Ir}(\text{H})_2(\text{IMes})(\mathbf{4}\text{-MP})_3]\text{Cl}$ in methanol- d_4 at 298 K. b) Logarithmic relaxation plots for the resonance at 8.39 ppm (*ortho* protons of free **4-MP**) of these samples (variable (red) and constant (black) flip angle results).

These findings have shown that single-shot variable and constant flip angle sequences allow the measurement of hyperpolarised T_1 values in a fast single-shot manner in a matter of minutes. The reference scan improves the T_1 value accuracy in the case of low hyperpolarisation levels, while it will not be necessary in case when the thermal signal is relatively low, for example when the detection is performed using a low-field NMR spectrometer. The variable flip angle method obtains higher SNR spectra and, therefore, more reliable T_1 values. Moreover, there is no need for a z-magnetisation correction, which makes the processing more straightforward. In the studies below the sensitivity of these methods to the accuracy of the flip angle is investigated and the results from both sequences for different substrates and at different detection fields are compared.

5.4.4 Sensitivity of single-shot sequences to the pulse calibration

In routine ^1H NMR experiments, the 90 degree pulse need not be calibrated for each measurement. In contrast, the variable (vfa) and constant flip angle (cfa) sequences previously described rely on the application of precise, reproducible radiofrequency pulse angles. Therefore, the 90 degree pulse should be calibrated before each experiment. This value is then used to calculate the smaller flip angles that are applied in both sequences. The cfa pulse sequence is not expected to be very sensitive to the precise pulse length if the angle is low because it uses the same angle every time and so the amplitude of the relaxation curve would change but not the slope of the corresponding logarithmic plot. Hence precise calibration is not needed. For the cfa sequence, when the angle is high there are fewer points, and therefore greater inaccuracy in the final T_1 value. However, if the angle is high and unknown then the correction for the reduction in z-magnetisation that is needed cannot be applied.

For the variable flip angle sequence there is a much greater impact if the pulses are uncalibrated. This results from the fact that the amount of magnetism sampled by each pulse would not be equal if the pulse angles are not the correct values. In Figure 5.13, the fraction of magnetisation that is detected with each pulse in the absence of the relaxation are presented for accurately calculated variable flip angles and for ones which deviate by 8% and 16% from the true value. If the angles are not accurate, the xy-magnetisation is no longer constant and its change contributes to the measured T_1 curve. Thus if the variable flip angles are lower than real ones (Figure 5.13a), the detected magnetisation starts lower and then increases, which can make observed T_1 values longer than should be the case. In contrast, with higher variable flip angles (Figure 5.13b), the magnetisation decreases and the measured T_1 values can appear shorter than true values. This hypothesis is now tested by reference to 3-amino-5-methylpyridine (Figure 5.14).

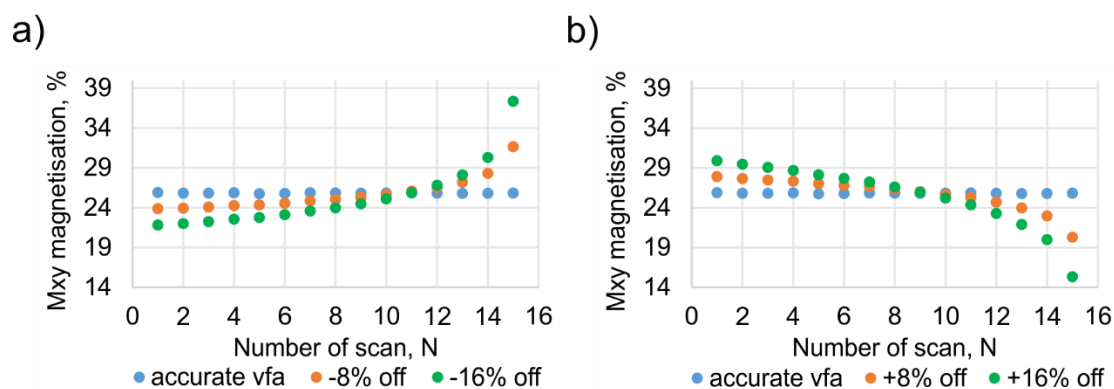


Figure 5.13 In both graphs simulated magnetisation percentage sampled when the accurate variable flip angles (vfa) are applied is shown in blue circles. Orange and green circles represent magnetisation (%) obtained when the variable flip angles a) decreased 8 and 16%, b) increased 8 and 16% from the accurate ones.

The effect of inaccurate 90 degree pulse calibration was assessed by assuming values of 12.5 μs (correct value), 11.5 μs (-8%), and 10.5 μs (-16%). The 8% and 16% deviation in the 90 degree pulse value is carried through to the constant and variable angles calculated from it. The resulting data is presented in Figure 5.15 and Table 5.15 to show the impact on the slopes of the corresponding linear relaxation plots as a function of time for the H_a proton at 7.78 ppm of 3-amino-5-methylpyridine.

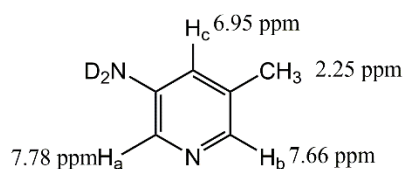


Figure 5.14 Chemical shift annotation for 3-amino-5-methylpyridine in methanol- d_4 at 400 MHz.

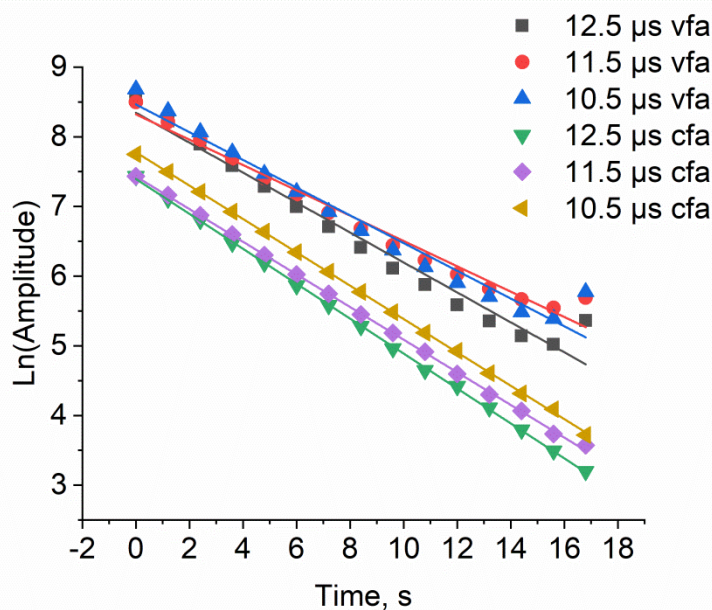


Figure 5.15 Hyperpolarisation relaxation plots as a function of pulse length for the free 3-amino-5-methylpyridine proton H_a at 7.78 ppm that were acquired with variable (vfa) and constant flip angle sequences (cfa). The 90 degree pulse lengths were assumed to be 12.5 μ s, 11.5 μ s and 10.5 μ s. The corresponding theoretical fit is presented via the solid lines.

The sample included 3-amino-5-methylpyridine (2-fold excess) with 5 mM activated SABRE catalyst in methanol- d_4 under 4 bar p - H_2 .

The relaxation data acquired with both methods fit well to a monoexponential decay. Despite the “blank scan” correction, all plots are affected by the build-up of thermal polarisation which is more visible at later times, however, this effect is more significant for the vfa experiments. This discrepancy is clear in the logarithmic plot. Furthermore, greater variation is observed in the T_1 values determined through the vfa method. The hyper T_1 values for all 3-amino-5-methylpyridine free protons obtained using the vfa and cfa sequences are presented in Table 5.15. Both sequences show similar results for hyper T_1 values across different pulse lengths. The slightly higher standard deviation for the extracted individual vfa T_1 values (<0.1%) compared to the cfa T_1 values (< 0.05%) supports the variance seen in the T_1 curves in Figure 5.15. In addition, the percentage difference between the T_1 values acquired with non-optimised (calculated from 10.5 and 11.5 μ s 90 degree pulses) and optimised 90 degree pulse angles (calculated from 12.5 μ s 90 degree pulses) were calculated for 3-amino-5-methylpyridine H_a , H_b and CH_3 protons and presented in Table 5.16. This difference was larger for the vfa T_1 values also supporting higher sensitivity of the vfa sequence to

the accurate flip angles. An isolated H_c proton at 6.95 ppm has a long T_1 and consequently the relaxation curve was not acquired for long enough which resulted in a larger error.

Table 5.15 Hyperpolarised relaxation time dependence on pulse duration for free 3-amino-5-methylpyridine acquired with the variable and constant flip angle pulse sequences (thermal polarisation corrected and magnetisation corrected for cfa). The error bars represent the standard error determined from 3 repeat measurements for all T_1 values, except vfa 12.5 μ s T_1 which was repeated 4 times. The sample included 3-amino-5-methylpyridine (2-fold excess) with 5 mM activated SABRE catalyst in methanol- d_4 under 4 bar p - H_2 .

Pulse length, μ s		Hyperpolarised T_1 , s			
		H_a	H_b	H_c	CH_3
vfa	10.5	4.0 ± 0.1	4.4 ± 0.3	12 ± 3	5.2 ± 0.4
	11.5	4.4 ± 0.2	4.3 ± 0.1	18 ± 4	5.7 ± 0.6
	12.5	3.7 ± 0.1	3.81 ± 0.06	11 ± 1	5.0 ± 0.4
cfa	10.5	4.2 ± 0.1	4.2 ± 0.2	20 ± 3	5.2 ± 0.4
	11.5	4.28 ± 0.05	4.16 ± 0.07	28 ± 6	5.3 ± 0.5
	12.5	3.89 ± 0.04	4.03 ± 0.05	18 ± 2	5.1 ± 0.3

Table 5.16 Percentage difference between the T_1 values for free 3-amino-5-methylpyridine determined by cfa and vfa, calibrated according to 10.5 μ s and 11.5 μ s pulse lengths for the 90 degree pulse, compared to the T_1 values acquired with a 12.5 μ s 90 degree pulse. The sample involved 3-amino-5-methylpyridine (2-fold excess) and 5 mM activated SABRE catalyst in methanol- d_4 under 4 bar p - H_2 .

Pulse length, μ s		Difference, %		
		H_a	H_b	CH_3
vfa	10.5	8	15	4
	11.5	19	13	14
cfa	10.5	7	3	2
	11.5	10	3	4

From these data it can be concluded that, as predicted, longer vfa T_1 values are measured when the lower angles are applied. In addition, the vfa T_1 values are clearly affected more than cfa ones by the deviation in the pulse length. An 8% error in pulse length is amplified to a 19% deviation in vfa T_1 . In contrast, similar errors in pulse lengths in the cfa sequence led to a 10% difference in the final T_1 value even though the angle should have no effect. Reduction in signal-to-noise associated with the smaller angles applied would produce a random error which reduces accuracy but would lead to the same T_1 value. There is no clear trend observed, as the larger deviation from angles does not result in the larger deviation in T_1 .

In summary, the cfa sequence is more suitable for use in the case where the accurate RF pulse angle is unknown, while the calibration of 90 degree pulse has to be performed prior to vfa measurements. In the following sections further optimisation of the variable flip angle sequence will be discussed.

5.4.5 Single-shot measurements with variable delays

Given the signal-to-noise requirements of the hyper T_1 measurement it is only realistic to have fifteen sampling points in the vfa sequence, which gives $\approx 26\%$ of M_z for each point. These points are encoded in one experiment. However, for many samples, a range of proton T_1 values will need to be measured during this period. Typically, to sample the full T_1 decay spectra are taken up to $5 \cdot T_1$ after the initial pulse and the time between samples is therefore $(5 \cdot T_1)/14$, if the time delay is constant. However, if the lifetime of one resonance is significantly higher than another then a T_1 decay curve sampled at fixed time steps cannot adequately yield full decay curves for all resonances unless many points are used. If too few points are acquired, the error in fitting will be substantial.

This effect is illustrated for T_1 values of 0.5 s and 10 s, in Figure 5.16. Constant time delays allow us to obtain a full curve for just one of the relaxation times (Figure 5.16a,b), while with variable delays both T_1 curves can be obtained reliably (Figure 5.16c). Thus, a sequence with variable time delays is optimal for samples with a range of T_1 values. It should be noted, that by acquiring different T_1 values in the same single-shot experiment, the number of relevant points for each curve is decreased. It is possible to calculate the flip angles so more points are measured in the vfa sequence, however, the decrease in SNR should be considered.

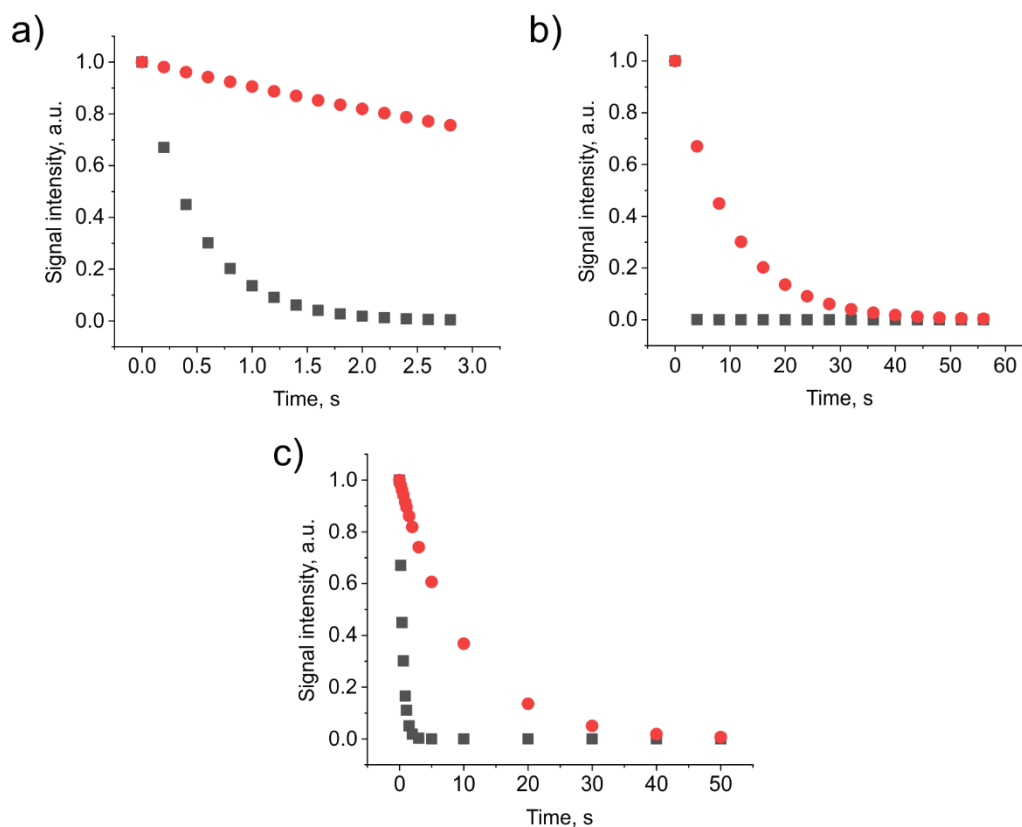


Figure 5.16 Simulated signal decay using equation $y = \exp(-x/T_1)$ with relaxation times of 0.5 s (grey squares) and 10 s (red circles), (a, b) when time points are spaced evenly with (a) short (0.2 s) and (b) long (4 s) time delays, (c) when time points are spaced with variable (0, 0.2, 0.4, 0.6, 0.9, 1.1, 1.5, 2, 3, 5, 10, 20, 30, 40, 50 s) time delays.

In this section, the sequence for the variable flip angle was amended to contain either a variable or a constant time delay time between pulses (Δt_n). To investigate the consistency of the variable delay sequence, experiments were carried out on an activated sample of 3,5-diaminopyridine (**3,5-DAP**) (2-3-fold excess) in the presence of $[\text{Ir}(\text{H})_2(\text{IMes})(\text{3,5-DAP})_3]\text{Cl}$ (5 mM) in MeOD using both the variable and constant delay approaches at 9.4 T and 1 T. **3,5-DAP** was selected because it has significantly different *ortho* and *para* proton T_1 values of 3 s and 13 s respectively. In order to accurately measure both relaxation times, two experiments were run for the constant time delay sequence with different fixed delay times between steps. In contrast, only one experiment was required with the variable time delay method. The results are presented in Table 5.17 (at 9.4 T) and Table 5.18 (at 1 T).

Table 5.17 Comparison of hyper T_1 values acquired using the variable flip angle sequence with constant and variable time delays for activated 3,5-diaminopyridine (3-fold excess) in the presence of $[\text{Ir}(\text{H})_2(\text{IMes})(3,5\text{-diaminopyridine})_3]\text{Cl}$ (5 mM) in MeOD on a 9.4 T NMR spectrometer. Error bars represent standard errors calculated from 3 (constant, *ortho*), 5 (constant, *para*) and 6 (variable) repeated measurements.

Type of time delay	<i>ortho</i>		<i>para</i>	
	T_1 , s	Error, %	T_1 , s	Error, %
Constant	3.1 ± 0.1	3.7	12.7 ± 0.2	1.6
Variable	3.3 ± 0.1	2.1	14.2 ± 0.6	4.2

Table 5.18 Comparison of hyper T_1 values acquired using the variable flip angle sequence with constant and variable time delays for activated 3,5-diaminopyridine (2-fold excess) in the presence of $[\text{Ir}(\text{H})_2(\text{IMes})(3,5\text{-diaminopyridine})_3]\text{Cl}$ (5 mM) in MeOD on a 1 T NMR spectrometer. Error bars represent standard errors calculated from 3 repeated measurements.

Type of time delay	<i>ortho</i>		<i>para</i>	
	T_1 , s	Error, %	T_1 , s	Error, %
Constant	3.11 ± 0.03	0.9	11.41 ± 0.07	0.6
Variable	2.98 ± 0.01	0.4	12.90 ± 0.3	2.3

The results show hyper T_1 values with high precision can be obtained by both the constant and variable time delay methods at 9.4 T and 1 T. In addition, the values at the different detection fields are similar. This fact can be attributed to the molecules being in the rapid tumbling regime, a characteristic of small molecules. There is, however, a discrepancy between the T_1 values obtained with the constant and variable time delay methods of 7% and hence the errors coming from the data analysis underestimate the real error. As previously mentioned, hyperpolarisation transfer or diffusion inside the spectrometer could account for this difference.^{164, 165} In such cases, when the constant time delays are used, the same amount of hyperpolarisation is expected to add to the decaying signal and the same systematic error is expected to contribute to each point, which is going to differ from that when variable time delays are applied.

Examples of hyperpolarisation relaxation curves acquired for **3,5-DAP** with constant and variable time delays are given in Figure A5 in the Appendix. As predicted, the employment of variable time delays allows for the acquisition of full relaxation curves for significantly different *ortho* and *para* proton T_1 values.

In summary, the variable flip angle method with variable time delays was implemented on both 9.4 T and 1 T NMR spectrometers. The data presented demonstrates that it is possible to measure significantly different relaxation times in one single-shot experiment with high SNR if variable flip angles and variable time delays are used. In the next studies the results from single-shot hyper T_1 measurements are compared with thermal T_1 and ^1H NMR data.

5.5 Effect of the chemical change in the SABRE system on T_1

It is possible that during relaxation time measurements, the chemical composition of the SABRE catalyst solution changes. Such changes can reflect reactions with the substrate that lead to its deuteration or the explicit reaction of the SABRE catalyst with the solvent.^{39, 96, 99, 121, 122, 166, 167} It might be expected that these changes will influence the measured T_1 values. As has been shown above, the thermal T_1 measurement is more time-consuming than the hyper T_1 , thus there is more time for such changes to occur. In the study now described the thermal and hyperpolarised T_1 values are investigated for a SABRE system that exhibits chemical change to probe its impact.

All the results were obtained on the same activated sample of N-(4-pyridyl)benzamide (**4-PBA**) with the SABRE catalyst in methanol- d_4 . Measurement involved two hyper T_1 determinations, one after sample activation and the other 16 hrs 55 min later. In the intervening time, one inversion recovery measurement was collected which took a total of 12 hrs 18 mins to acquire. Clearly the timescales associated with these observations mean that only extreme changes can be compared. Nonetheless, there is a difference in the associated T_1 values as detailed in Table 5.19. The increase in relaxation time for the *meta* proton can be explained by adjacent site deuteration. As a consequence of the gyromagnetic ratio of deuterium being ~ 6.5 -times smaller than that for a proton, an efficiency of dipole-dipole relaxation is reduced in heteronuclear ^1H - ^2H pair. In addition, the small quadrupolar ^2H magnetic moment results

in quadrupolar relaxation not being a dominant mechanism. More evidence for this effect is presented in Chapter 6.

Table 5.19 Hyperpolarised (measured with variable flip angle sequence on freshly activated sample and after 16 hrs 55 min) for free N-(4-pyridyl)benzamide (2-fold excess) in presence of $[\text{Ir}(\text{H})_2(\text{IMes})(\text{N}-(4\text{-pyridyl})\text{benzamide})_3]\text{Cl}$ in methanol- d_4 at 298 K. Error bars represent fitting errors.

	<i>ortho</i>	<i>meta</i>
After activation	1.91 ± 0.04	5.5 ± 0.6
After 16 hr 55 min	2.2 ± 0.1	7.1 ± 0.7

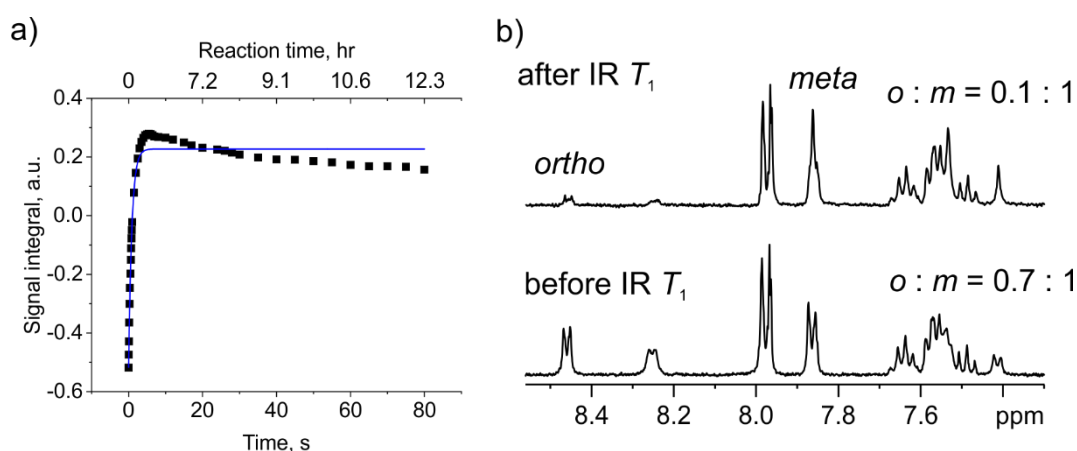


Figure 5.17 a) The thermal relaxation time graph of the *ortho* peak of **4-PBA** (5 eq) measured with inversion recovery (IR) sequence acquired over 12.3 hrs while deuteration was occurring at the same time in presence of $[\text{Ir}(\text{H})_2(\text{IMes})(\text{4-PBA})_3]\text{Cl}$ in methanol- d_4 at 298 K. The bottom time-axis in seconds presents the time delays implemented in the inversion recovery experiment, the upper time-axis in hours gives the reaction time during the experiment. The upper axis scales non-linearly with the bottom axis, e.g. 3 hrs in the upper trace is associated with 1.5 s in the bottom trace. The fit to mono-exponential is shown in blue line. b) ^1H NMR spectra acquired before and after IR T_1 measurement with 16 hr 26 min time difference in between the spectra.

Figure 5.17a reveals that the corresponding thermal T_1 data for the *ortho* proton resonance of **4-PBA** does not fit a mono-exponential build up curve. The bottom time-axis (seconds) presents the time delays implemented in the inversion recovery experiment, while the upper time-axis (hours) matches them to the reaction time at the end of the 8 scan T_1 point measurement. The intensity of ^1H signals that make up this curve should follow the predicted trace (blue). Instead they first grow and then fall. Based on the data above the T_1 should be constant during this period

and the fall must therefore be due to the expected deuteration. These deuteration effects are confirmed by the NMR spectra of Figure 5.17b where the *ortho* proton signal disappears.

Although, the inversion recovery experiment can be performed at low temperature to slow down the HIE, the T_1 value is likely to change as well due to the temperature dependence. It is proposed that by employing the single-shot method with SABRE hyperpolarisation a much more rigorous view of these changes can be obtained. This application will be discussed in Chapter 7.

5.6 Measurement of enhancement factors and hyperpolarisation relaxation times for variety of amines

In the previous results it was suggested that measurements of hyperpolarised lifetime can provide useful information about molecular structure and SABRE efficiency. To further develop this concept, hyper T_1 and SABRE enhancement values are determined for a variety of N-heterocyclic amines and amides. These samples were prepared according to experimental section 9 in methanol- d_4 . In all cases the catalyst concentration was 5 mM and the substrate was in a 5-fold excess relative to $[\text{Ir}(\text{Cl})(\text{COD})(\text{IMes})]$ (**1**) or $[\text{Ir}(\text{Cl})(\text{COD})(\text{IMes-}d_{22})]$ in case of 4,6-nicotinamide- d_2 . Figure 5.18 and Figure 5.19 show the average enhancement factors and hyperpolarised relaxation times for the free substrate protons used in this study.

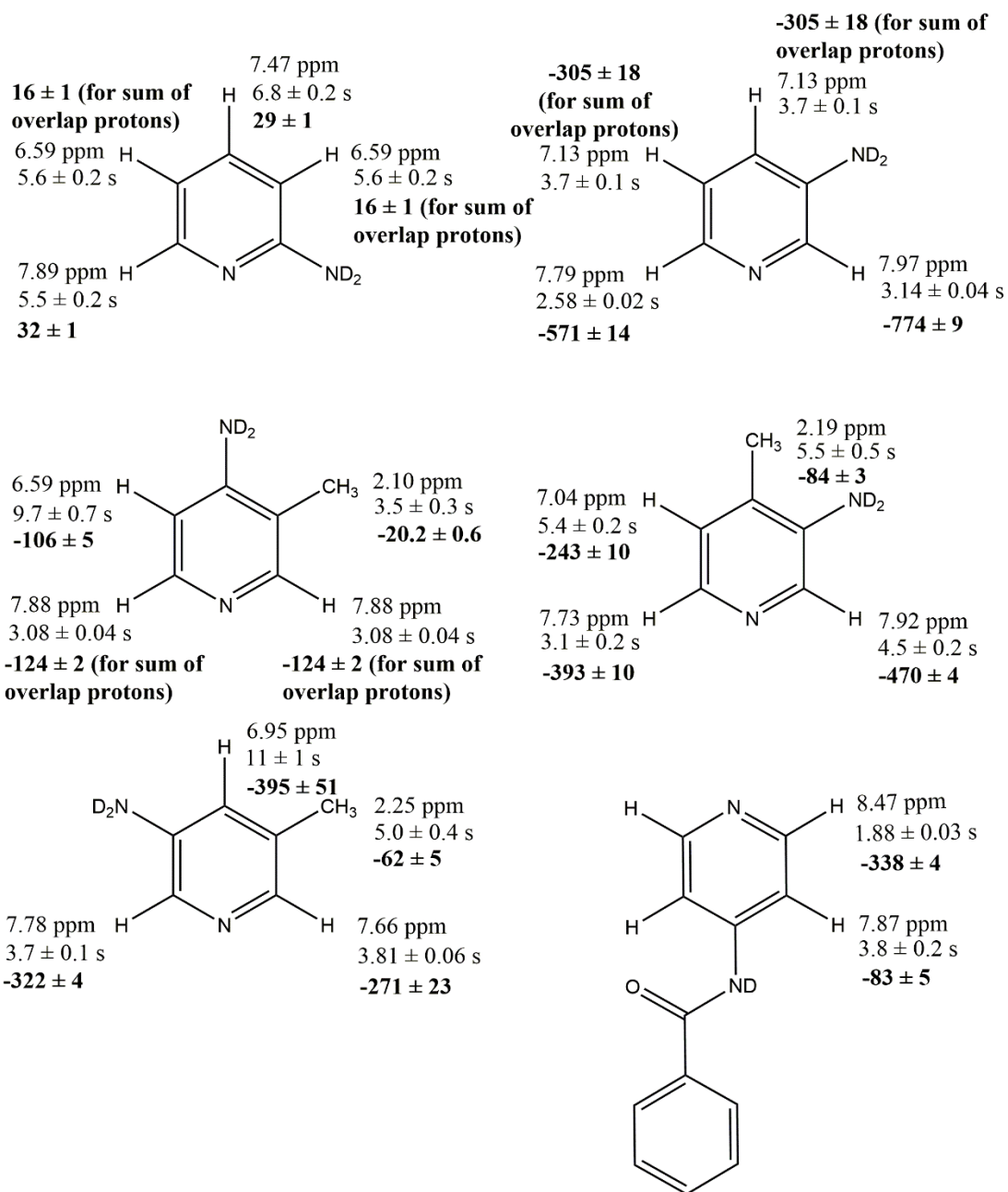


Figure 5.18 Hyperpolarised relaxation times and enhancement factors (in bold) for free protons of different amines (5 eq, IMes, MeOD) at 3 bar *para*-H₂ at 65 G, 10 sec shaking acquired with variable and constant flip angle pulse sequence at 298 K. Error bars represent standard errors calculated from 3 repeated measurements, except 3-amino-5-methylpyridine, which was repeated 4 times.

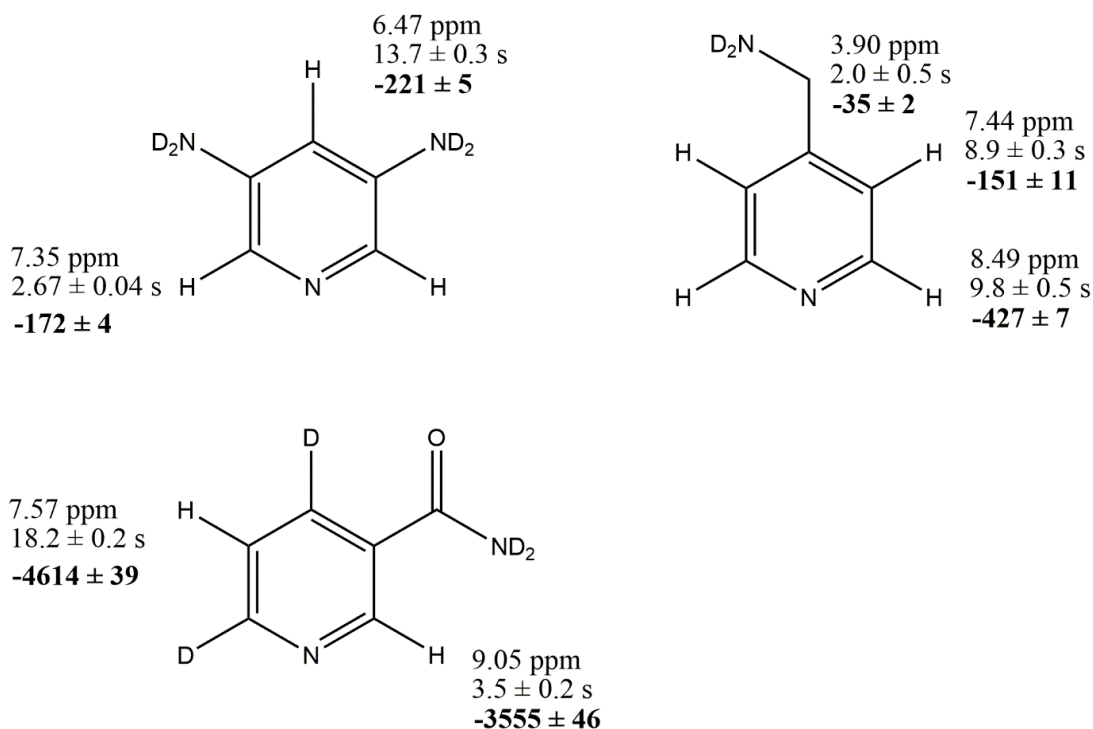


Figure 5.19 Hyperpolarised relaxation times and enhancement factors (in bold) for free protons of different amines (5 eq, IMes, MeOD) at 3 bar *p*-H₂ at 65 G, 10 sec shaking acquired with variable and constant flip angle pulse sequence at 298 K (continuation).

Error bars represent standard errors calculated from 3 repeated measurements.

A dependence of relaxation time and enhancement on the chemical structure of the various amines can be readily noted. The *ortho* protons are close to the binding nitrogen and relax quicker due to interactions with catalyst. Typically, a shorter T_1 subsequently results in more polarisation being lost during transfer between the polarisation transfer field and the detection field of the NMR spectrometer. These losses are observed in the reduced enhancement levels for the fast-relaxing protons. Exceptions are 4-(aminomethyl)pyridine and 2-aminopyridine, which have longer T_1 values of 9.8 ± 0.5 s and 5.5 ± 0.2 s when compared to the usual 2-4 s seen for the *ortho* protons of the other molecules. This has been attributed to the molecules binding through both aromatic and amino group nitrogens which is confirmed by the appearance of the hydride region of the associated ¹H NMR spectra. Despite the longer T_1 values exhibited by the *ortho* proton of 2-aminopyridine, the observed signal enhancement factors are actually small. This can be explained by the steric bulkiness of 2-aminopyridine which hinders binding to the catalyst and makes exchange non-optimal for SABRE.

In the case of the *ortho* protons, short T_1 and stronger J coupling to the hydrides interplay and yield the effective enhancement values. This results in the *ortho* protons obtaining higher or comparable levels of hyperpolarisation than the other longer relaxing protons.

Due to these experiments being conducted in methanol- d_4 , the amino groups of the substrates are deuterated and do not show a peak in these ^1H NMR spectra. Due to the smaller gyromagnetic ratio of deuterium compared to that for a proton, and therefore a reduction in the efficiency of dipole-dipole relaxation, the substrate protons adjacent to the deuterated amino groups relax more slowly. An apt example of this effect is observed for the *para* proton of 3,5-diaminopyridine which has a T_1 value of 13.7 ± 0.3 s.

The effect of substrate proton substitution with deuterium was shown with 4,6-nicotinamide- d_2 which possesses much higher hyperpolarisation levels than the other molecules. Due to the smaller magnetic moment of deuterium the measured T_1 of the *meta* proton is 18.2 ± 0.2 s. Interestingly, the *ortho* proton does not show the same long T_1 value due to the stronger interaction with the SABRE catalyst but still retains a high enhancement factor. The SABRE hyperpolarisation levels and thermal T_1 values were tested for a series of the deuterated nicotinamide molecules by Rayner *et al.*⁹⁰ The 4,6-nicotinamide- d_2 showed the best results in the ^1H NMR signal enhancement which suggested that the optimal conditions for the SABRE are when the strongly coupled to hydrides *ortho* proton shares the obtained hyperpolarisation with the other proton maintaining the SABRE signal for longer due to the long T_1 value. It should be noted that some deuteration was observed in the other compounds which were not initially ^2H -labelled due to the presence of the SABRE catalyst. The ^2H substitution of the *ortho* protons was assessed at $\approx 35\%$ in 2-aminopyridine, $\approx 27\%$ in 4-amino-3-methylpyridine, $\approx 15\%$ in 3-amino-4-methylpyridine, $\approx 30\%$ in 3-amino-5-methylpyridine and $\approx 21\%$ in N-(4-pyridyl)benzamide by the end of these experiments. Interestingly, no significant deuteration was observed for the remaining *ortho* proton of 4,6-nicotinamide- d_2 , 4-aminomethylpyridine, 3,5-

diaminopyridine or 3-aminopyridine. As illustrated earlier, HIE influences the T_1 values and is discussed in Chapter 6 and Chapter 7.

The substrates containing substituents in the *para* position that are able to donate electron density *via* mesomeric effects are observed to reduce the SABRE enhancement factor. For example, 4-amino-3-methylpyridine yields an average 93-fold signal enhancement compared to 3-amino-5-methylpyridine and 3-amino-4-methylpyridine, which have an amino group in the *meta* position, that gave 262-fold and 297-fold gains respectively. It is suggested that the *para* substituent reduces the ability for substrate dissociation from the SABRE catalyst due to increased electron density on the aromatic nitrogen which is shown through the resonance structures in Figure 5.20.

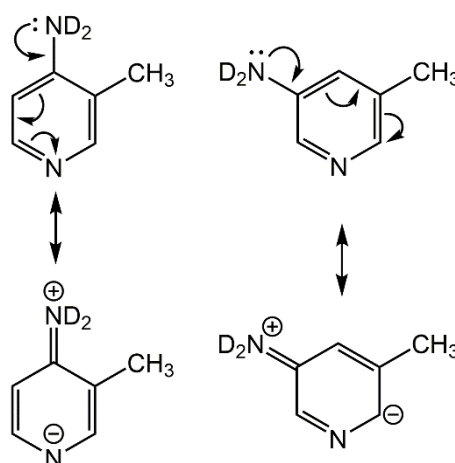


Figure 5.20 The resonance forms for 4-amino-3-methylpyridine (left) and 3-amino-5-methylpyridine (right) showing the mesomeric electron donating effect.

In summary, the substitution of the protons with deuterium in the amino group and aromatic ring prolongs the relaxation time of the adjacent protons, and therefore, allows for the higher hyperpolarisation levels to be observed. For example, the hyperpolarisation level reaches 13% in case of 4,6-nicotinamide- d_2 compared to the 0.032% of the Boltzmann thermal polarisation. Due to the J coupling network, the *ortho* protons which are more strongly coupled to hydrides obtain more hyperpolarisation, which is then distributed around the molecule and can be stored on the longer relaxing protons. The effect of the electronic structure of the substrate

showed the influence on the detected SABRE hyperpolarisation which is associated with the exchange rates on the catalyst. The effective measured SABRE enhancement level is a result of the contribution of several effects described above.

5.7 Conclusions and future work

In this chapter, different methods for measuring thermal and hyperpolarised T_1 values have been assessed, including the introduction of a single-shot variable flip angle measurement for hyperpolarisation lifetimes. The variable and constant flip angle sequences have proven to be a quick and efficient for determining the lifetimes of the hyperpolarised signal, and can be applied to any NMR active or SABRE active nuclei. The designed variable flip angle sequence shows consistent results when compared to the previously reported constant flip angle sequence. The use of SABRE served to increase the detection limit and provides a route to improve SNR of both flip angle methods, however, the use of the variable flip angles improved it further. For example, the vfa sequence provided the same T_1 value with the measured signal SNR 3-times higher than the cfa method for 4-methylpyridine (**4-MP**).

The vfa sequence was shown to be more sensitive to inaccurately calibrated flip angles than the cfa sequence. This is because if the vfa measurement uses uncalibrated pulses it is impossible to create the identical magnetisation levels needed in each measurement. For the cfa sequence, the absolute pulse applied is not critical as long as it uses a small fraction of the overall magnetisation each time. This makes the cfa sequence more convenient for use in case when an accurate RF pulse is unknown, while the calibration of the 90 degree pulse has to be performed prior to a vfa measurement. The implementation of a variable time delay into the variable flip angle sequence enabled data to be successfully obtained for protons with significantly different relaxation time constants in the same experiment, which further reduces the overall experimental time.

The NMR relaxation time constant T_1 is characteristic of the molecular environment and can help to elucidate species of different structure weighted concentrations in a mixture, for example bound to the catalyst and free substrate, starting material and product during a reaction, or partially deuterated species. The variable flip angle single-shot method was employed for a quick analysis of a variety of substrates providing accurate relaxation times in a fraction of the time that would not be possible via thermal relaxation time measurements. Based on this analysis, the dependence of T_1 values and SABRE hyperpolarisation levels on the substrate structure and chemical identity were investigated, revealing approaches to the higher hyperpolarised NMR signal. In addition, results presented in this chapter also highlight the dependence on the hyper T_1 values as a function of time in a sample undergoing hydrogen isotope exchange (HIE). This was shown in the different hyper T_1 values measured with reaction time, which correlated with the evidence of ^2H labelling in the associated ^1H NMR spectra. This method should be useful for the quick analysis of chemically changing systems, enabling the detection of reaction intermediates in the case of reaction monitoring, a premise that will be tested in Chapter 7.

Future work on hyperpolarised T_1 values can assist applications and fundamental knowledge of SABRE phenomenon. The studies by Tessari and co-workers show a linear dependence of SABRE signal size with concentration for low concentration samples in a mixture which ultimately allows for their quantification.¹²⁴ The implication of this is that T_1 is not varying significantly with concentration. The developed hyperpolarised single-shot T_1 measurement can provide rigorous information about the hyperpolarisation lifetime of substrates in a mixture to investigate this hypothesis.

Currently the model for the SABRE hyperpolarisation reported in the literature assumes fast exchanging systems.⁴⁶ Kinetic measurements can be performed in order to extend the model to include the effect of slow substrate exchange on the average T_1 . The bound substrate relaxation time

could then be estimated from the model based on a knowledge of the exchange rates, average T_1 values of associated resonances and free substrate T_1 values. For this purpose, an experiment with quenching of the SABRE catalyst between polarisation and hyper T_1 measurement can be undertaken in order to recover the initial T_1 of the free substrate in solution.¹⁴⁸

It might also be noted that comparison of the hyper T_1 and thermal T_1 values recorded at different magnetic fields could potentially reveal information on any spontaneous hyperpolarisation transfer that takes place inside the NMR spectrometer. This effect has been suggested to be caused by CSA relaxation which is field dependent.¹⁶⁴

In the further studies, see Chapter 7, the range of the substrate concentrations which allow for the hyper T_1 measurement is investigated. This is applied to the change in hyper T_1 in chemically changing systems. Prior to this, in Chapter 6 I investigate the reactivity which occurs in the SABRE system such as activation of the SABRE pre-catalyst with substrate under hydrogen and hydrogen isotope exchange (HIE) on the substrate.

Chapter 6: Hydrogen isotope exchange (HIE) in SABRE systems

6.1 Introduction

In this chapter observations that deal with hydrogen isotope exchange (HIE) in the substrate during the SABRE process are described and kinetic and mechanistic aspects of this reaction are investigated. This study is based on the detection of deuterium incorporation into the target SABRE substrate by NMR and mass-spectrometry (MS) measurements. Using standard (non-hyperpolarised) NMR methods, the role that the iridium complexes detected during the activation of the SABRE catalyst have on the HIE reaction is explored. Specifically, the kinetics of the incorporation of deuterium into a range of substrates including pyridine and its derivatives, **4-AP**, **4-PBA** and **4-MP**, is examined and the effect of catalyst concentration is evaluated. Finally, NMR line shape analysis is used to reveal further information about the mechanism of this process.

6.2 Background

The family of catalysts that are currently employed in SABRE were originally used to promote a hydrogen isotope exchange (HIE) reaction that involves C-H bond activation.^{39, 45, 96, 99, 158, 166} Early results in this area stem from the use of Crabtree's catalyst, which incorporates deuterium and tritium into an array of organic molecules.^{166, 168-171} In fact, Ellames *et al.* have studied the efficiency of this process extensively for aromatic ketones, carboxylic acids, aromatic amine derivatives and benzylic alcohols (Figure 6.1).¹⁶⁶ They showed that increasing the concentration of Crabtree's catalyst led to more efficient deuterium incorporation, which can reach a plateau or decrease after reaching a maximum.¹⁶⁶

Jones and Feher stated in 1989 that "*it is the product bond strengths (M-C) that dominate in the determination of the position of the hydrocarbon activation equilibria, not the reactant (C-H) bond strengths*"¹⁷², and hence by using directing groups it is possible to control selectivity in HIE.^{172, 173}

The proposed mechanism for the HIE reaction of Crabtree's catalyst proceeds through an octahedral cyclometalated dideuteride Ir^{III} species as detailed in Figure 6.2.¹⁶⁶

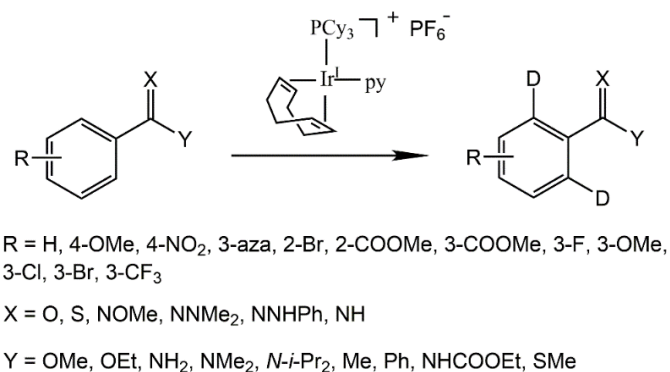


Figure 6.1 Scheme of deuteration reaction of organic molecules with different functionality promoted by Crabtree's catalyst.¹⁶⁶

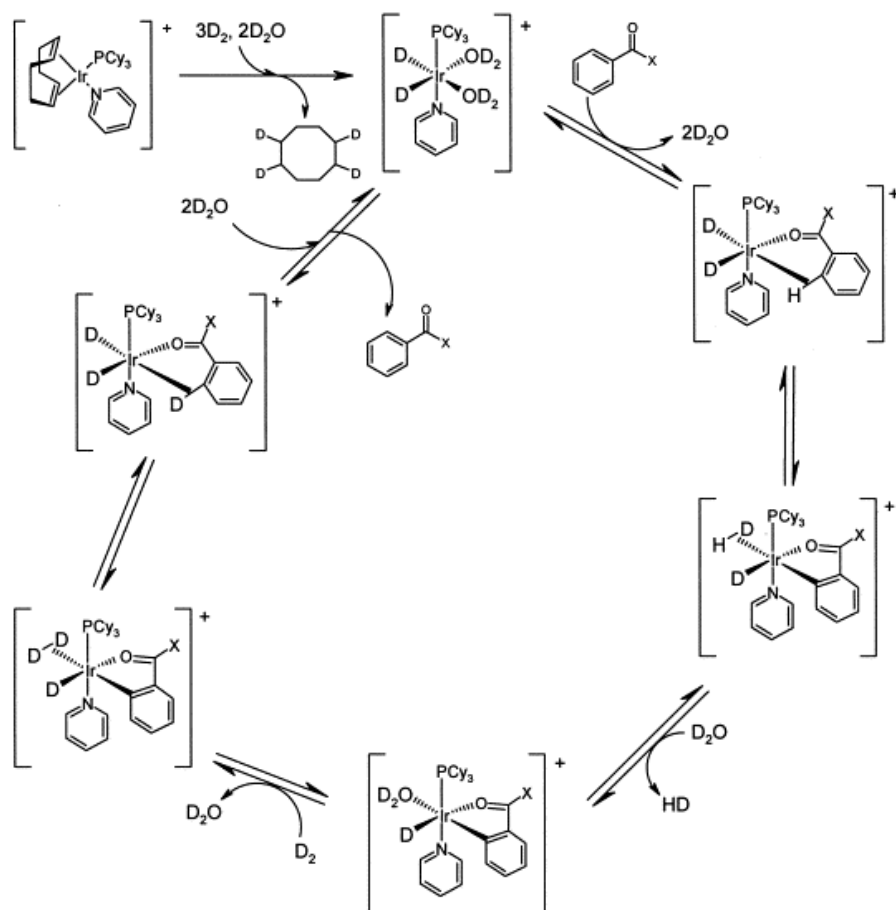


Figure 6.2 Simplified mechanism of the exchange process in the presence of deuterium oxide. Reprinted from *Tetrahedron*, 57, G. J. Ellames, J. S. Gibson, J. M. Herbert and A. H. McNeill, The scope and limitations of deuteration mediated by Crabtree's catalyst, 2001, 9487–9497, Copyright (2018), with permission from Elsevier.

Kerr and co-workers have further investigated this process by applying a variety of iridium catalysts with carbene and phosphine ligands, separately or combined on the same catalyst.^{171, 174, 175} The catalysts with mixed phosphine and carbene ligands were found to perform better for deuteration of the *ortho* position of a substrate's aromatic ring, providing up to 98% D incorporation.¹⁷¹ The presence of a chloride ligand on the catalyst has been shown to play an important role in aldehyde C-H bond activation as its substitution with a more labile ligand decreased the resulting HIE levels.¹⁷⁵ The C-H bond activation reactions of aromatic heterocycles such as those used as SABRE substrates have been less well studied. Deuteration of the proton positions adjacent to the aromatic nitrogen of pyridine has been reported to occur under SABRE conditions.^{39, 96, 166} A suggested step in the sequence is shown in Figure 6.3.¹⁶⁶

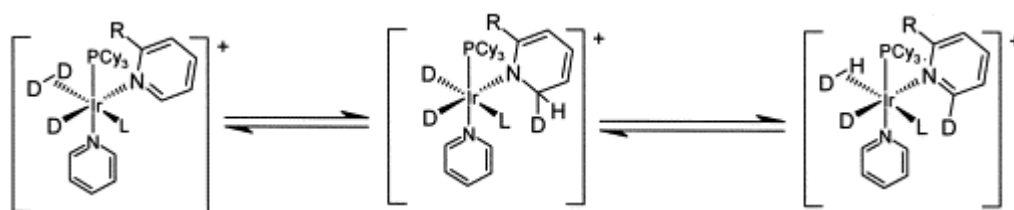


Figure 6.3 Postulated process for incorporation of deuterium at C6 of pyridines. Reprinted from *Tetrahedron*, 57, G. J. Ellames, J. S. Gibson, J. M. Herbert and A. H. McNeill, The scope and limitations of deuteration mediated by Crabtree's catalyst, 2001, 9487–9497, Copyright (2018), with permission from Elsevier.

Further research suggests that substrate tautomerism into a carbene may also play a role. This is reflected in the research of Alvarez *et al.*, who showed the formation of metal-carbon coordinated species for iridium and a 2-substituted pyridine, although the exact mechanism was not clearly stated (Figure 6.4a).¹⁷⁶ At the same time, while non-substituted, and 4-substituted pyridines have been reported to bind to iridium via their aromatic nitrogen, they were not seen to undergo further transformation.¹⁷⁶ In this case, steric factors were suggested to drive the formation of the pyridylidene type products.^{176, 177} A strategy to stabilise the NH tautomer, as was shown by Esteruelas *et al.*, which involved employment of a halide ligand that participates in Cl \cdots N-H bond formation within Os and Ru complexes of benzo[h]quinoline (Figure 6.4b for Ru).¹⁷⁸ A pyridylidene

bound to ruthenium was detected and shown to reflect a deactivation product in the formation of 2-(4-(trifluoromethyl)styryl)pyridine by Johnson *et al* (Figure 6.4c).¹⁷⁹ All these complexes were characterised by NMR and X-Ray methods.^{176, 178, 179}

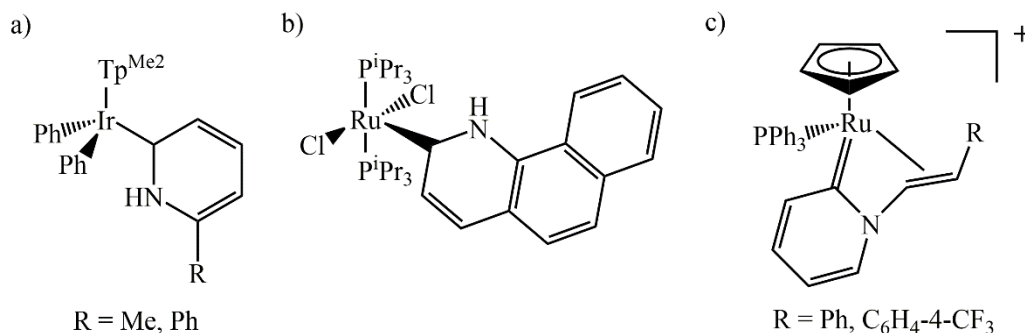


Figure 6.4 The complexes containing pyridylidene ligands. Tp^{Me_2} = hydrotris(3,5-dimethylpyrazolyl)borate.

An example of the C-H bond activation of an sp^3 -hybridised carbon centre in a 2-substituted pyridine has been reported by Crabtree and co-workers.¹⁸⁰ They isolated a cyclometalated iridium species with 2-dimethyl- and 2-diethyl-aminopyridine that proved to reflect Fischer carbene interactions.¹⁸⁰ The mechanism of their formation is proposed to proceed through two C-H bond activations of the alkyl group; the involvement of the heteroatom containing rings is proposed to produce an aromatic stabilized 10 π -electron intermediate.¹⁸⁰ Interestingly, the second α -proton transfer from the alkyl group is reversible.

C-H bond activation reactions are not limited to iridium, and in fact the deuteration of pyridine and its derivatives is readily achieved by the osmium (IV) tetrahydride catalyst, $\text{OsH}_4(\text{substrate})(\text{P}^i\text{Pr}_3)_2$, in benzene- d_6 .¹⁸¹ In the proposed mechanism, the dissociation of the substrate occurs before benzene- d_6 binds to the vacant site with subsequent C-D bond activation. Benzene- d_5 then eliminates and $\text{OsDH}_3(\text{P}^i\text{Pr}_3)_2$ is formed which subsequently exchanges H/D with pyridine. The catalyst therefore evolves to $\text{OsD}_x\text{H}_{4-x}(\text{P}^i\text{Pr}_3)_2$ while under HIE conditions. In this case, the deuteration of all three pyridine proton positions has been detected, with the rates of reaction decreasing as follows: $k_{para} > k_{meta} > k_{ortho}$.¹⁸¹ Alternatively, for 4-

methylpyridine k_{ortho} is bigger than k_{meta} . This change has been proposed to be a consequence of a steric clash with the methyl group.¹⁸¹ Generally, the success of the HIE reaction increases if the substrate binds more strongly to the catalyst.^{166, 172, 181} Although, pyridine C-H bond activation has been proposed to be rate-determining.¹⁸¹

In the SABRE systems studied in this work, the source of deuterium is methanol- d_4 . Therefore, a complex with bound methanol- d_4 may feature in this reaction. Complexes with MeCN⁹⁹, MeOH^{121, 182}, H₂O¹⁶⁷ and CH₂Cl₂¹⁸³ have been previously exemplified in the literature.^{99, 121, 167, 182, 183} However, the complex with bound methanol is short-lived and its hydride peaks have been detected at 265 K with an intensity 100-times less than the main pyridine coordination product.¹²¹ Interestingly a role for methanol has been demonstrated in hydrogen transfer to bound COD in a related iridium complex, which suggests its direct participation in HIE may be possible.¹⁸² It should be emphasized that the rates of deuteration during SABRE have been shown to be slower than SABRE polarization transfer and hence the two processes can be treated separately.¹²¹

As H/D incorporation levels play a role in spin-lattice relaxation and any change in deuteration level can change the final SABRE polarisation level the H/D exchange process is critical for SABRE optimisation.⁹⁰ Specifically, it will enable the observation of longer lived hyperpolarised signals and hence leads to measurements with higher signal-to-noise ratios. However, this second effect will be complicated because the catalyst's J coupling network will also change, which could impact the efficiency of the hyperpolarisation transfer step.^{56, 77-79} Here, I seek to explore the HIE reaction in SABRE systems using non-hyperpolarised high-field NMR. The effect of HIE on SABRE will be discussed in Chapter 7.

6.3 Observations of HIE in SABRE systems

The effects of HIE in SABRE systems can be detected by ¹H NMR spectroscopy in several different ways. First, the appearance of additional

NMR peaks in the hydride region and a 1:1:1 triplet peak near the chemical shift of H₂ (4.6 ppm) will indicate the formation of isotopologues of H₂ and the parent dihydride. A reduction in the signal intensity of particular substrate resonances with respect to others will be expected if there is HIE at the corresponding substrate position. In addition, the remaining substrate peaks would be expected to demonstrate significant lineshape changes due to the exchange of a ¹H-¹H coupling for a weaker ¹H-²H coupling. These key spectral changes will be explored to detect the presence of HIE in methanol-*d*₄ in the presence of the iridium SABRE catalyst [Ir(H)₂(NHC)(sub)₃]Cl for the N-heterocycles 4-aminopyridine (**4-AP**), 4-methylpyridine (**4-MP**), pyridine (**py**) and N-(4-pyridyl)benzamide (**4-PBA**).

The active tris-substrate-dihydride SABRE complex [Ir(H)₂(IMes)(sub)₃]Cl ([Ir]-(H)₂) yields a broad hydride peak at ~ -23 ppm. However, when measured in methanol-*d*₄ a further signal at ~ -22 ppm appears with time due to the formation of the partially deuterated complex [Ir(H)(D)(IMes)(sub)₃]Cl ([Ir]-(H)(D)), which eventually dominates as illustrated in Figure 6.5.^{39, 99, 121} The dideuterated form [Ir(D)₂(IMes)(sub)₃]Cl ([Ir]-(D)₂) is NMR silent in the hydride region of ¹H NMR spectrum; however, its presence in solution can be inferred by comparison of the relative NMR integrals for the organic parts of the complex and the hydride signals. For example, if the total integral of the carbene peaks corresponding to all three catalyst forms is not equal to the sum of hydride peak integrals, normalised to the same number of protons, this would indicate the presence of the dideuterated form.

An alternate explanation for a second hydride peak would be the formation of a new Ir complex. However, only one set of peaks in the organic region of these ¹H NMR spectra is observed for the bound substrate and the carbene ligand, which would suggest that just one product remains. The long-term retention of a single hydride peak for the activated SABRE complex when prepared in dichloromethane-*d*₂ further supports this HIE hypothesis, where the source of the deuterium is the methanol-*d*₄.

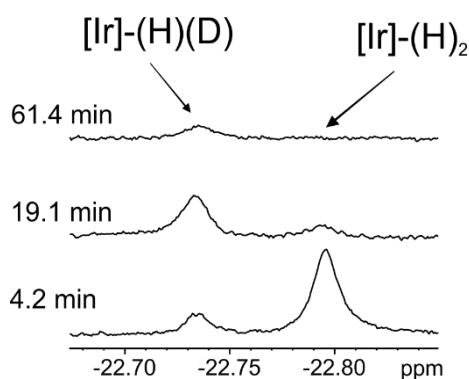


Figure 6.5 Evolution of the hydride ^1H NMR peaks for the $[\text{Ir}]-(\text{H})_2$ and $[\text{Ir}]-(\text{H})(\text{D})$ catalyst forms during the activation of the SABRE catalyst and substrate deuteration for the case where the substrate is **4-PBA**.

In order to assess the relative concentration of the catalyst isotopologues, the hydride peaks can be integrated at lower temperature, where both are sharp singlets due to the decrease in the hydrogen exchange rate on the catalyst. To achieve this, the SABRE complexes were activated at room temperature, and then the relative intensities of the hydride resonances were measured by ^1H NMR spectroscopy at 250 K. In the case of **4-MP**, pyridine and **4-PBA** the catalyst forms were quantified after deuteration levels had reached $\sim 30\%$. For **4-AP** the rate of HIE was faster and significant deuteration (89%) had been reached by the time the catalyst was activated. The absolute values for the hydride ligands' chemical shifts in $[\text{Ir}(\text{H})_2(\text{sub})_3(\text{IMes})]\text{Cl}$ (**4a**, **4b**, **4c**, **4d** with sub = **4-AP**, **4-PBA**, **4-MP** and **py**, respectively) and its isotopologue $[\text{Ir}(\text{H})(\text{D})(\text{sub})_3(\text{IMes})]\text{Cl}$ at 250 K are presented in Table 6.1. Measurements of the relative integrals of the hydride signals and use of a reference peak from the carbene ligand allow the amount of the $[\text{Ir}]-(\text{D})_2$ form to be estimated according to Equation 6.1, where I_{DD} is the relative integral of the $[\text{Ir}]-(\text{D})_2$ form, I_{ref} is the reference signal of the SABRE complex, n_{ref} is number of protons associated with the reference resonance, I_{HD} is relative integral of the $[\text{Ir}]-(\text{H})(\text{D})$ form, and I_{HH} is relative integral of the $[\text{Ir}]-(\text{H})_2$ form.

$$I_{DD} = \frac{I_{ref}}{n_{ref}} - I_{HD} - \frac{I_{HH}}{2} \quad (6.1)$$

Table 6.1 Hydride ligands' chemical shifts for the activated SABRE complexes formed with **4-AP**, **4-MP**, pyridine and **4-PBA** in MeOD at 250 K alongside is the ratio of the dihydride isotopologues when the substrate deuteration level is $\sim 30\%$, except for **4-AP** which deuterates faster and so has a substrate deuteration level of 89%.

	[Ir]-(H) ₂ , ppm	[Ir]-(H)(D), ppm	Substrate deuteration	Ratio of [Ir]-(H) ₂ : [Ir]-(H)(D) : [Ir]-(D) ₂ in %
pyridine	-22.54	-22.47	31	48 : 32 : 20
4-MP	-22.58	-22.51	29	49.5 : 31 : 19.5
4-PBA	-22.55	-22.49	28	21 : 21 : 58
4-AP	-22.95	-22.87	89	38.5 : 45 : 16.5

As shown in Table 6.1, the complexes with pyridine and **4-MP** ligands possess similar concentrations of their [Ir]-(D)₂ forms of $\sim 20\%$ at the point there is $\sim 30\%$ substrate deuteration. In contrast, the **4-PBA** and **4-AP** results are significantly different. At 28% deuteration of **4-PBA** the concentration of [Ir]-(D)₂ is much higher ($\sim 60\%$), while just 16.5% of the deuterated catalyst is present when **4-AP** is 89% deuterated. This confirms that the proportion of the deuterated catalyst form is not directly related to the level of ²H-substitution in substrate. This can be explained by the differences in the C-H bond strength in these substrates and by a more complicated pathway for ²H-incorporation. The full time dependence of these changes as a function of reaction time and substrate identity are investigated further in section 6.4.

One consequence of deuterium incorporation into the hydride ligand sites is the production of HD and D₂ gas.^{116, 158} The formation of HD gas is readily evident in these ¹H NMR spectra through the observation of a triplet HD signal centered at 4.6 ppm with a *J* coupling of 42.8 Hz.^{116, 158}

In addition to the evidence presented so far, further NMR observations confirm deuterium incorporation into the substrate in the position adjacent to the aromatic nitrogen. This is based on the significant line-shape changes observed for the *meta* resonance of the substrate **4-AP** that are detailed in Figure 6.6. This change in lineshape is due to incorporation of deuterium in the adjacent position (Figure 6.7).

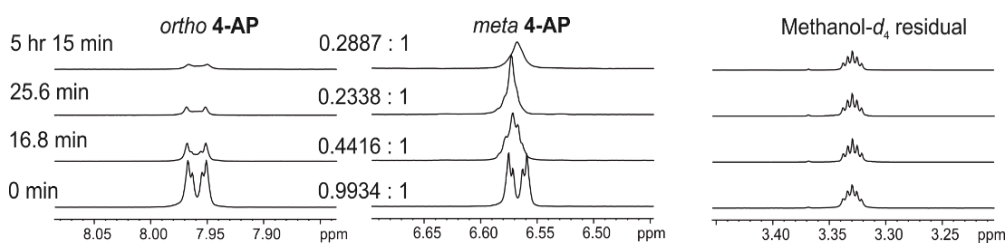


Figure 6.6 Change in *meta* peak appearance with the deuteration of the *ortho* position as a function of reaction time. No significant change in splitting was detected for methanol- d_4 residual peak that suggests that the reactivity is the cause of the substrate's lineshape change.

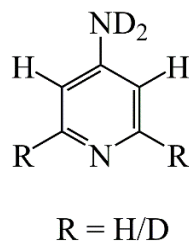


Figure 6.7 Deuteration of **4-AP** in the *ortho* positions.

Following H/D exchange, the proton in the *meta* position experiences a significant reduction in J coupling complexity, which is reflected in the resonance lineshape. This is due to the fact a proton-deuterium coupling J_{HD} is approximately 6.5-times smaller than the corresponding J_{HH} coupling due to their difference in gyromagnetic ratio. In the case of 2,6- d_2 -4-aminopyridine, this reduction in coupling causes the *meta* resonance to resemble a singlet. The exact lineshapes for the deuterated forms of the substrates can be simulated numerically, as discussed in section 6.5. A change in lineshape with time was observed for the *meta* resonance of all investigated substrates.

Further evidence of H/D exchange can be obtained from the corresponding ^{13}C NMR spectrum because when ^{13}C is directly bound to ^1H it gives a doublet with a one-bond $^1J_{\text{CH}}$ coupling of between 140 – 160 Hz. By contrast, when directly bound to ^2H a 1:1:1 triplet results with a $^1J_{\text{CD}}$ splitting that is around 6.5-times smaller than the $^1J_{\text{CH}}$ value. Due to the low natural abundance of ^{13}C , SABRE hyperpolarised ^{13}C NMR spectra were acquired to provide this information for the substrate, **4-AP** (10 mM) based on the action of $[\text{Ir}(\text{H})_2(\mathbf{4-AP})_3(\text{IMes})]\text{Cl}$ (**4a**) (5 mM). The ^{13}C NMR spectra were acquired using a 65 G PTF which is optimal for relayed polarisation transfer from

protons.^{76, 95, 120} These NMR spectra were obtained without decoupling, with ¹H decoupling and with ²H decoupling (Figure 6.8).

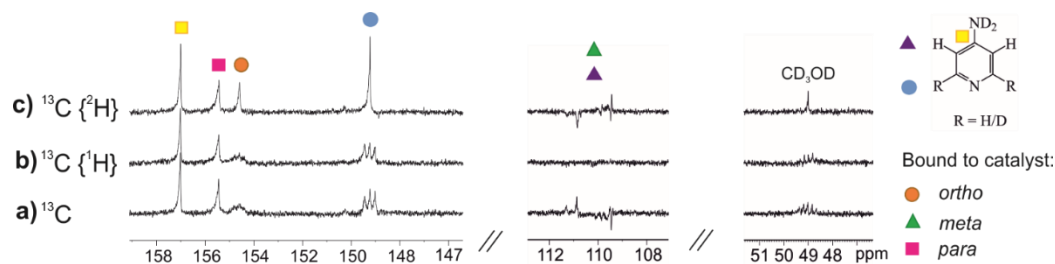


Figure 6.8 ¹³C NMR SABRE signals demonstrating the deuteration of **4-AP** (10 mM in the activated sample) in presence of 5 mM activated catalyst [Ir(IMes)(H)₂(**4-AP**)₃]Cl (**4a**) in

MeOD under 4 bar *p*-H₂. The *ortho* carbon resonance of free and bound **4-AP** shows splitting from deuterium ($J_{CD} = 26.6$ Hz) in these ¹³C and ¹³C {¹H} spectra. This splitting is removed on ²H decoupling which confirms its origin from deuteration of the *ortho* position. The *meta* carbon signal is weaker and produces an antiphase signal which disappears in the ¹³C {¹H} SABRE NMR spectrum.

The resonances corresponding to the *ortho* carbon of free (149.2 ppm) and bound (154.6 ppm) **4-AP** both show splitting from deuterium ($^1J_{CD} = 26.6$ Hz) in their ¹³C and ¹³C {¹H} SABRE NMR spectra (Figure 6.8a and b). This splitting is removed, and a singlet observed in the corresponding ¹³C {²H} SABRE NMR spectrum (Figure 6.8c). This confirms the incorporation of deuterium into the *ortho* position of **4-AP**. By contrast, the *meta* carbon resonances (109.7 ppm for the free and 111.0 ppm for the bound) do not exhibit the same behavior. Due to the indirect transfer of polarisation from ¹H to ¹³C via SABRE, the *meta* proton resonance is a weak antiphase doublet in the ¹³C and ¹³C {²H} spectra with $^1J_{CH} = 178.8$ Hz. The antiphase doublet peaks cancel (no signal observed) under ¹H decoupling (Figure 6.8b) but are unaffected by ²H decoupling, indicating the source of the doublet is coupling to ¹H and not ²H. Taken together, these spectra indicate ²H incorporation into only the *ortho* position of **4-AP**. It should be pointed out that the ²H-labelled material provides a superior enhancement to the ¹H-material, which accounts for the failure to see this form. It should be acknowledged that species which do not yield SABRE hyperpolarisation are not detected in these measurements. In agreement with the obtained ¹³C NMR data, around 90% deuteration for the *ortho* position was indicated,

while no deuteration for the *meta* resonance, in a standard ^1H NMR spectrum at the point where the spectra of Figure 6.8 were obtained.

6.4 Investigation of the active catalyst for HIE

In this section the form of the catalyst responsible for HIE in the substrate molecule is discussed. Specifically, I focus on probing the inorganic species that form during the activation of the SABRE catalyst. During this process, the iridium pre-catalyst $[\text{Ir}(\text{Cl})(\text{COD})(\text{IMes})]$ **1** normally transforms into the intermediates $[\text{Ir}(\text{COD})(\text{IMes})(\text{substrate})]\text{Cl}$ **2** and $[\text{Ir}(\text{COD})(\text{IMes})(\text{H})_2(\text{substrate})]\text{Cl}$ **3** before becoming $[\text{Ir}(\text{IMes})(\text{H})_2(\text{substrate})_3]\text{Cl}$ **4**, as discussed in Chapter 3. The activation scheme is repeated here in Figure 6.9 for convenience. Each of **2**, **3** and **4** contain bound substrate ligands that could potentially lead to HIE.

As methanol- d_4 is the source of deuterium in the systems under investigation, an intermediate complex with bound methanol should be present in solution. However, it has not been detected at room temperature or low temperature (260 K) due to instability and/or low concentration. Nevertheless, the solvent peak's enhancements of 2-4-fold, detected in the presence of the active SABRE complex with **4-MP** in MeOH and **4-AP** in MeOD under $p\text{-H}_2$, suggest its formation. In the case of **4-AP**, hyperpolarisation transfer into the methanol could also happen via exchange of the substrate's NH_2 protons under SABRE-Relay (see Chapter 2).¹¹⁸ Such a relayed process is consistent with the phase of the signal enhancement in methanol which is now opposite to that seen with **4-AP**.

Both the line-shape and the ratio of ^1H NMR signal integrals for the *ortho* and *meta* resonance of **4-AP** showed no signs of substrate deuteration when **4-AP** was left in presence of **2a** in MeOD for three months. Therefore, it is concluded that **2a** is not active for HIE. A similar analysis could not be performed for **3a** because this intermediate is short lived.

The deuteration of the substrate in free solution requires reversible binding of the substrate to the catalyst. In the next section, peak lineshapes,

SABRE signal intensities and selective exchange spectroscopy (EXSY) are used to investigate the hydrogen and substrate exchange in the different catalyst forms in order to further assess which one is likely to be responsible for HIE process.

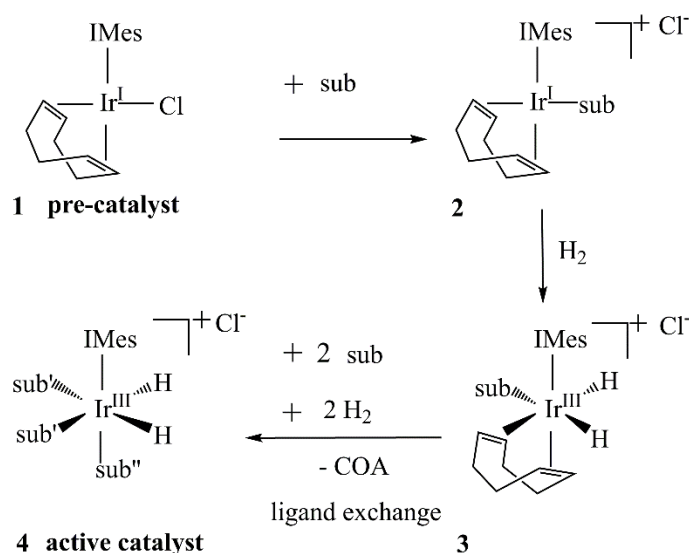


Figure 6.9 Chemical changes occurring during SABRE pre-catalyst activation.

6.4.1 Lineshape analysis

The deuteration of the substrate in free solution requires reversible binding of the substrate to the catalyst. When the catalyst activation is monitored by adding H₂ to a sample containing [Ir(COD)(IMes)(**4-AP**)]Cl **2a** and **4-AP** in methanol-*d*₄ by shaking the NMR tube once and then acquiring a series of ¹H NMR spectra overnight without refreshing the H₂ in solution, no peaks corresponding to [Ir(H)₂(COD)(IMes)(**4-AP**)]Cl **3a** were observed. However, when the sample is shaken between each experiment and the concentration of H₂ in solution is periodically replenished, signals for **4-AP** bound to **3** and its hydride ligands were observed in the corresponding early stage thermally-polarised ¹H NMR spectra. In fact, 1.5 minutes after H₂ addition, peaks corresponding to the *meta* protons of **4-AP** in the complexes **2a** (6.35 ppm), **3a** (6.28 ppm) and **4a** (trans to hydrides, sub', at 6.17 ppm, and trans to carbene, sub'', at 6.06 ppm) and can all be readily detected, as illustrated in Figure 6.10.

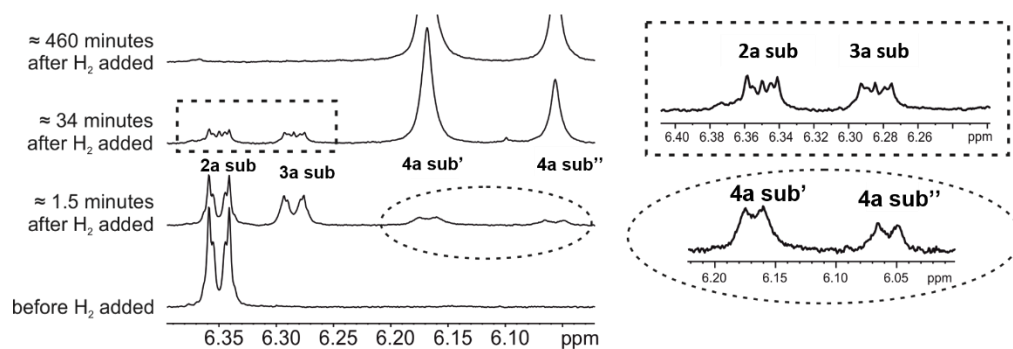


Figure 6.10 *Meta* proton resonance of **4-AP** bound to **2** at 6.35 ppm, **3** at 6.28 ppm and **4** at 6.17 ppm (equatorial, bound *trans* to hydride) and 6.06 ppm (axial, bound *trans* to carbene) as a function of reaction time. Significant changes in peak lineshape demonstrate slow substrate exchange in **2** and **3** and fast exchange in **4**.

In this NMR spectrum the bound **4-AP** *meta* proton resonance in **2a** and **3a** look very similar to that of the free **4-AP** before H₂ addition. Although an additional singlet-like peak appears in the middle of these resonances, it is not dominant, and in general the lineshapes suggest that the original H-H splitting is retained during the reaction. The corresponding signals from **4-AP** in **4a** that are located *trans* to the hydrides and *trans* to the carbene show a lineshape that transitions between that of the non-deuterated and deuterated forms of **4-AP**. After half an hour of monitoring, this situation becomes clear as the H-H coupling to an adjacent *ortho* proton is lost, thereby indicating substantial *ortho* position deuteration has occurred (Figure 6.10). Interestingly, the peaks for the *meta* protons of **4-AP** bound to **2a** and **3a** show a more subtle change in their lineshape, suggesting that there are significantly fewer deuterated molecules of **4-AP** bound to them than the proportion of this form in solution would suggest. This observation is consistent with slow ligand exchange in **2a** and **3a** and suggests **4a** plays a greater role in HIE catalysis than **3a**.

6.4.2 Substrate and hydride SABRE signal

Further evidence for slow substrate exchange in the intermediate SABRE complex **3a** comes from the weak SABRE signal associated with free **4-AP** when **3a** is the dominant catalyst form in solution. The overall SABRE signal gain increases with an increase in the proportion of **4a**. SABRE NMR spectra of **4-AP** in presence of the complexes **3a** and **4a** focused on the

aromatic and hydride regions are shown in Figure 6.11 to illustrate this point.

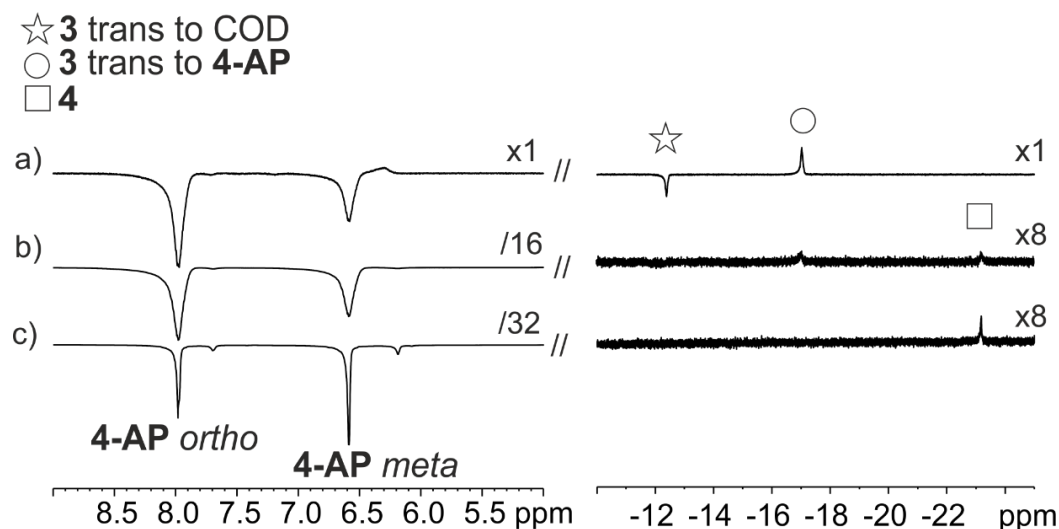


Figure 6.11 Increase in **4-AP** SABRE signal intensity parallels the formation of **4a**, which is confirmed by observation of the hydride region of these SABRE NMR spectra.

As discussed in the section 6.3, the HIE reaction is expected to involve a deuteride containing complex as well as HD and D₂ gas elimination.^{166, 181} Information about H₂ exchange within the catalyst is therefore important. As complex **3a** can undergo this process and yet it has not been reported in the literature, this process was studied in more detail below.

The hydride ligands of **3a** can be detected using their PHIP hyperpolarisation response (Figure 6.11a). Due to the two-spin order term created, the maximum signal intensity for these resonances is detected with a 45 degree pulse.^{65, 184} Thus, hyperpolarised ¹H NMR spectra were acquired with a series of 45 degree pulses after the addition and refreshment of *p*-H₂ (Figure 6.12 a, b and c). More complex **2a** and fresh *p*-H₂ was then added to the sample and hyperpolarised ¹H NMR spectra were acquired (Figure 6.12 d and e). Interestingly, peaks characteristic to ALTADENA are observed instead of the expected antiphase doublet PHIP peaks which are indicative of rapid initial addition but slow exchange.

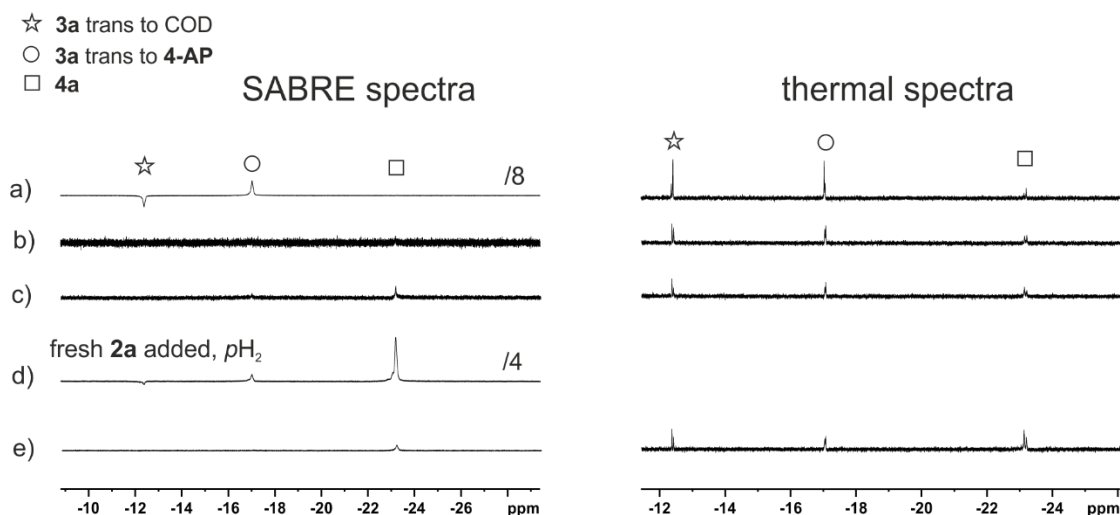


Figure 6.12 Hyperpolarised hydride resonances in **3a** and **4a** detected with a 45 degree pulse: a) the first PHIP spectrum acquired after addition of *p*-H₂ to **2a**; b) and c) subsequent PHIP spectra with fresh *p*-H₂ do not show further hydride hyperpolarisation; d) PHIP NMR spectrum acquired after addition of fresh **2a** and *p*-H₂, e) subsequent PHIP spectrum acquired with fresh *p*-H₂. Thermally polarised NMR spectra acquired after the corresponding PHIP spectra are presented for all sets except for (d) where two subsequent PHIP spectra were acquired in order to quickly detect **3a** signals.

Interestingly, PHIP hyperpolarisation of the hydride ligands of **3a** is observed only in the hyperpolarised ¹H NMR spectra recorded immediately following the addition of *p*-H₂ to solutions of **2a**. In contrast, the thermally polarised spectra confirm the presence of **3a** throughout the period of these observations. Figure 6.12 suggests that the signals for complex **3a** are enhanced only when it first forms and that hydrogen does not exchange on this timescale. After *p*-H₂ addition, the proton peak corresponding to the *meta* site of **4-AP** bound to **3a** increases rapidly and matches the intensity of the corresponding signal of **2a**. The intensities of these two peaks then remain equal as **4a** forms (see Figure A6 and Figure A7 in the Appendix). This observation suggests that either complexes **2a** and **3a** are in equilibrium or the rate of consumption of **2a** matches that for the formation of **4a**. In order to probe this process, more **2a** was added. Hyperpolarised signals for the hydride ligands of **3a** then reappear in the first PHIP NMR spectrum after addition but are not observed on the subsequent hyperpolarised spectra (Figure 6.12 d and e). This supports the idea that H₂ addition to **2a** is fast on the NMR timescale but **3a** forms more rapidly than subsequent hydrogen loss from **3a** allowing for rehyperpolarisation.

Consumption of **3a** seems to be faster than the H₂ exchange step required for hyperpolarisation.

6.4.3 EXSY measurements

The ligand exchange process in **2a** and **3a** that involves **4-AP** was probed explicitly by selective exchange spectroscopy (EXSY). For this purpose, the *meta* resonances of **4-AP** bound to **2a** or **3a** (6.35 ppm and 6.28 ppm, respectively) were selectively excited with a 180 degree pulse, and the effect observed in the ¹H NMR spectrum after a set time delay, allowing for exchange to be encoded during the delay. Changes in the associated relative peak integrals were then analysed. No signal was observed for the *meta* resonance of the free substrate up to 1 s suggesting an absence of exchange of the substrate with **2a** and **3a** on this timescale.

In contrast to the behaviour of **2a** and **3a**, the active SABRE catalyst is known to perform rapid reversible substrate and hydrogen exchange, which allows SABRE hyperpolarisation to be observed continuously for the free substrate in the solution.^{39, 96, 121} The rate of exchange for pyridine (10 eq to 1 mM of pre-catalyst, **1**) on the active catalyst **4** was reported to be $9.0 \pm 0.3 \text{ s}^{-1}$ at 298 K in MeOD.⁹⁶ The rates of substrate dissociation for **4-PBA** (10 eq to 5 mM **1**) and **4-AP** (5 eq to 5 mM **1**) in the associated complexes **4** were measured by this EXSY procedure (see Experimental) in MeOD at 293 K and 298 K respectively. The rates were found to be $4.62 \pm 0.08 \text{ s}^{-1}$ and $5.0 \pm 0.2 \text{ s}^{-1}$ for **4-PBA** and **4-AP**, respectively.

6.4.4 Conclusions

The results presented above suggest slow exchange for catalysts **2** and **3** and fast exchange for **4**. The EXSY measurements have shown that the activated SABRE catalyst performs much faster exchange than the unactivated and intermediate complexes. The lineshape analysis and SABRE-enhanced hydride resonance behavior also indicate slow exchange of H₂ in **3a**. Additional evidence dealing with ligand exchange in these complexes was gathered through the spin-lattice relaxation (*T*₁) times discussed in Chapter 5, section 5.4.1, which confirmed slow exchange on

the unactivated catalyst **2a** and much faster exchange on the activated species **4a**. Collectively this data suggests that **4** is likely to be a precursor for the HIE process. For future work, incorporation of deuterides into the intermediate catalyst **3** can be explored if stability of this complex is achieved.

6.5 Monitoring the HIE reaction during catalyst activation

In the previous section, the deuteration of the catalyst **4** was explored and its main role in the HIE reaction was confirmed. Here, I am interested in investigating ^2H -labelling in the substrate and the timescales of deuteration in different compounds. The active catalyst is unstable and formed *in situ* from pre-catalyst **1** (5 mM). In order to compare the HIE timescales, hydrogen gas (4 bar) was added to a solution of the unactivated complex **2** in the presence of the substrate (20 mM) in methanol- d_4 . ^1H NMR spectra show that pre-catalyst **1** exists in these solutions alongside **2** for all substrates except **4-AP**, where no peaks for **1** are observed. The proportion of **1** present immediately prior to H_2 addition was found by NMR to be 26% for pyridine, 18% for **4-MP** and 10% for **4-PBA**. The formation of **4**, and the deuteration of the substrate was monitored after rigorously shaking the sample for around 5 s to dissolve H_2 and inserting the sample into a 400 MHz NMR spectrometer. A series of ^1H NMR spectra were acquired over the following 15.5 hours (64 hrs for **4-PBA**) without further addition of H_2 or shaking of the NMR sample. The integrals of the peaks in these ^1H NMR spectra corresponding to the *meta* and *ortho* protons of the substrate were calculated. A decrease in the signals associated with the free substrate was expected due to the consumption of two equivalents of the substrate during the formation of the active SABRE catalyst, **4**. At the same time, a decrease in the relative intensities of the *ortho* and *meta* protons of the substrate is expected due to *ortho* deuteration. No evidence of significant deuteration of the *meta* position in any of the investigated substrates was observed. Figure 6.13 presents the catalyst activation and substrate *ortho* position deuteration curves for the four substrates: 4-aminopyridine (**4-AP**), pyridine (**py**), N-(4-pyridyl)benzamide (**4-PBA**), and 4-methylpyridine (**4-MP**). These

plots reveal information about the activation process and use the integrated intensity of one of the IMes carbene protons, either backbone (N-CH=CH-N) or aromatic protons for normalisation. The deuteration percentages were calculated using Equation 6.2, where S_{ortho} and S_{meta} are the integrated signal intensities for the *ortho* and *meta* resonances of each substrate, respectively. No decrease in relative intensity for the other substrates' protons was detected. In the case of **4-PBA**, activation and deuteration were observed over a longer timescale (Figure 6.13c).

$$D (\%) = 100 * \left(1 - \frac{S_{ortho}}{S_{meta}}\right) \quad (6.2)$$

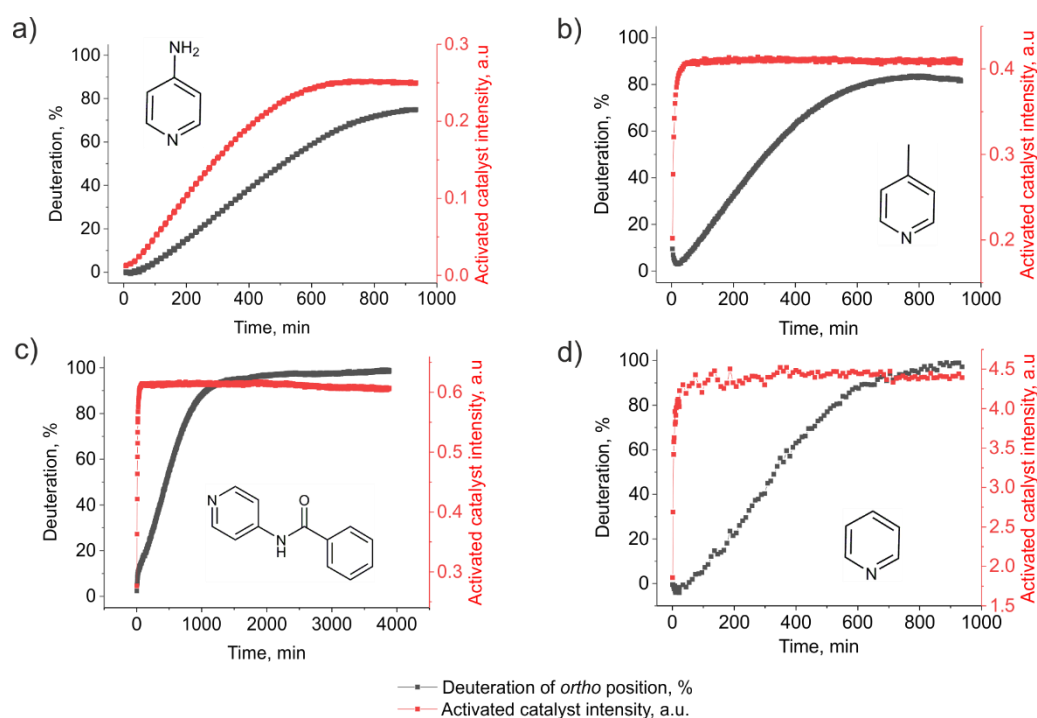


Figure 6.13 In red: Catalyst $[\text{Ir}(\text{H})_2(\text{IMes})(\text{substrate})_3]\text{Cl}$ **4** proportion as formed with **4-AP** (7.32 ppm) (a), **4-MP** (6.68 ppm) (b), **4-PBA** (6.74 ppm) (c), pyridine (6.65 ppm) (d) where their initial substrate concentration was 25 mM in methanol- d_4 under hydrogen gas (4 bar) and the employed carbene resonance is given in brackets. In grey: corresponding deuteration level of the substrates' *ortho* position. The deuteration curve for **4-MP** shows an initial fall that is not real, but instead reflects a decrease in the free *meta* peak (7.30 ppm) integral due to partial overlap with initial catalysts' resonances (7.24 ppm and 7.35 ppm), a change in line-broadening also contributes to this.

At 15.5 hrs following addition of H_2 , deuteration levels of 99% for **py**, 86 % for **4-PBA**, 82 % for **4-MP** and 75 % for **4-AP** were observed. In the case

of **4-PBA**, 98 % deuteration resulted after 50 hrs. The deuteration of **4-AP** takes place on the timescale of iridium catalyst formation (Figure 6.13 a). By contrast, **py**, **4-PBA** and **4-MP** undergo HIE on a longer timescale than activation (Figure 6.13 b, c, d). In these cases, **py**, **4-PBA** and **4-MP** are deuterated by less than 20% at the time when the activation is completed. To illustrate this point, Figure 6.14 reproduces the first 80 mins of the monitoring experiment from Figure 6.13 for **py**, **4-PBA** and **4-MP**. As deuteration continues in the absence of **2** and **3** they logically do not play a dominant role in this process.

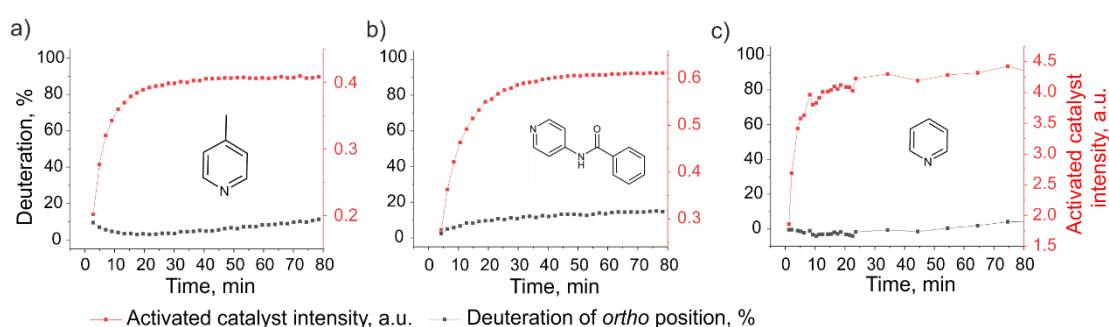


Figure 6.14 In red: Extent of $[\text{Ir}(\text{H})_2(\text{IMes})(\text{substrate})_3]\text{Cl}$ **4** formation for **4-MP** (6.68 ppm) (a), **4-PBA** (6.74 ppm) (b) and pyridine (6.65 ppm) (c), when their concentration is 25 mM in the starting methanol- d_4 solution under hydrogen gas (4 bar) and the employed carbene resonance is given in brackets. In grey: deuteration level for the substrate's *ortho* position. Changes shown over an 80 min timescale.

These results confirm a link to the presence of **4** and the success of the HIE reaction for all of the substrates studied. In addition, the data for **4-AP** suggests that small quantities of the active catalyst are capable of performing HIE, as **2** was shown previously to be inactive for the ^2H -substitution and the presence of **3** is not observed in ^1H NMR in the regime where the concentration of H_2 in solution is not periodically replenished. It should be noted that parts of deuteration curves do not follow a simple mono-exponential behaviour, thereby suggesting a complicated multistep mechanism.

6.5.1 Investigation of the deuterated species kinetics

Due to HIE with methanol- d_4 , activated dihydride iridium catalysts of the form $[\text{Ir}](\text{H})_2$ equilibrate with both $[\text{Ir}](\text{H})(\text{D})$ and $[\text{Ir}](\text{D})_2$ species. Depending on the speed of this process, such an exchange process could

follow the time course schematically shown in Figure 6.15a where the intermediate $[\text{Ir}]-(\text{H})(\text{D})$ first increases in intensity and then falls as the product $[\text{Ir}]-(\text{D})_2$ dominates. However, the substrate and H_2 gas based HIE processes that occur during SABRE will complicate this prediction (see Figure 6.15b). Thus, deuteration of the catalyst competes with its protonation via H/D exchange.

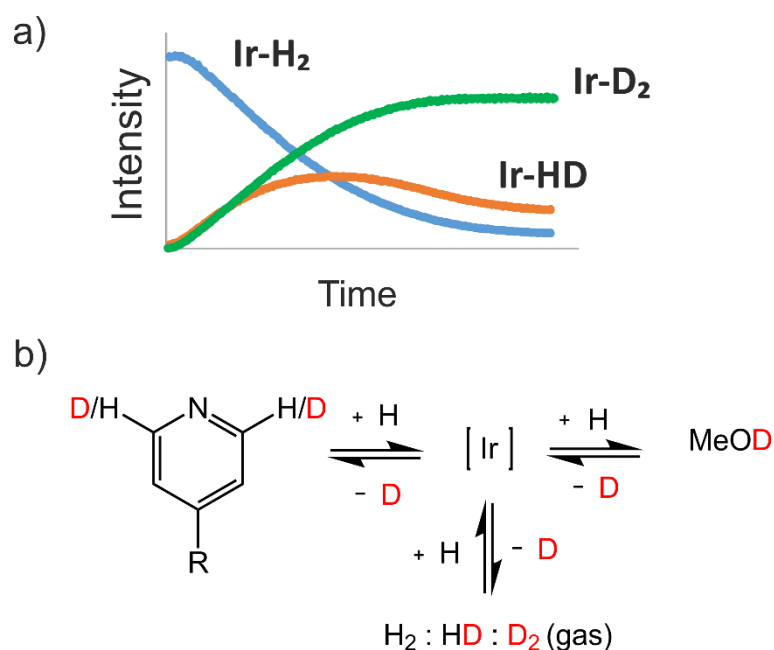


Figure 6.15 a) Scheme of expected evolution of the iridium deuterated species. b) Scheme of the HIE processes occurring in the SABRE system.

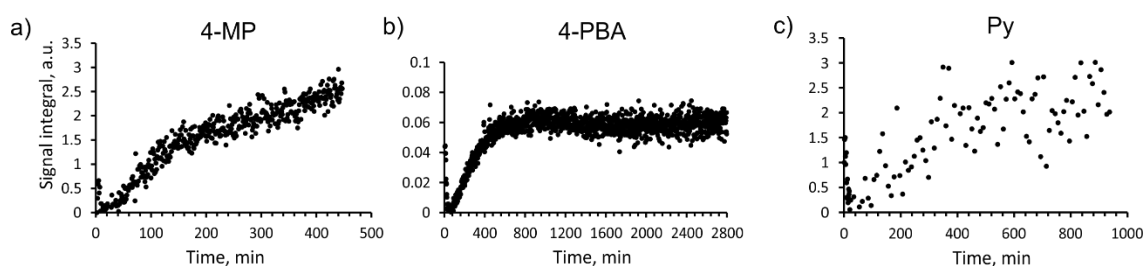


Figure 6.16 Increase in HD gas ^1H NMR peak integral at 4.43 ppm with reaction time for a) 4-MP, b) 4-PBA, c) pyridine.

Experimentally these effects are revealed in Figure 6.16, Figure 6.17 and Figure 6.18. The data used here were obtained from the experiments presented in Figure 6.13 of the previous section. In Figure 6.16, the ^1H NMR peak of HD gas at 4.43 ppm first decreases in intensity during early reaction

times in a profile which roughly matches that of catalyst activation for **4-MP**, **4-PBA** and pyridine; for **4-AP** the signal was too broad to integrate. Subsequently, the HD peak intensity increases with the reaction time, and in case of **4-PBA**, which was monitored on the longer timescale, reaches a plateau. Changes in the hydride signal appearance that were characteristic of $[\text{Ir}]-(\text{H})_2$ and $[\text{Ir}]-(\text{H})(\text{D})$ species were observed to happen on this timescale.

The relative concentrations of $[\text{Ir}]-(\text{H})_2$, $[\text{Ir}]-(\text{H})(\text{D})$ and $[\text{Ir}]-(\text{D})_2$ were assessed through the hydride and carbene ^1H signal integrals as described in section 6.2 (see equation 6.1). These results are presented in Figure 6.17 and Figure 6.18. For pyridine in Figure 6.17a, a fall in the hydride signal intensities of the $[\text{Ir}]-(\text{H})_2$ species and an increase in the amount of $[\text{Ir}]-(\text{D})_2$ is seen over the first 50 min, which matches the timescale of the catalyst formation (Figure 6.13b). The intermediate $[\text{Ir}]-(\text{H})(\text{D})$ is seen initially to rapidly increase and then to decrease on the same timescale as the catalyst activation (Figure 6.17a). On a longer timescale all species reach a plateau (Figure 6.18a). Similarly, the early reaction time plots for **4-PBA** and **4-MP** show the same trends for $[\text{Ir}]-(\text{H})_2$, $[\text{Ir}]-(\text{H})(\text{D})$ and $[\text{Ir}]-(\text{D})_2$ evolution (Figure 6.17b and c). This shows that the equilibration of H/D exchange between the hydrides and the solvent is fast and happens on the same time timescale as the catalyst formation.

In contrast, at longer reaction times **4-PBA** and **4-MP** show different behavior (Figure 6.18b,c). After the activation is complete, a growth of the **4-PBA** hydride signal for $[\text{Ir}]-(\text{H})(\text{D})$ and a corresponding decrease in calculated $[\text{Ir}]-(\text{D})_2$ form is observed before a plateau is reached after around 400 min. However, no signal corresponding to $[\text{Ir}]-(\text{H})_2$ is observed on this timescale (Figure 6.18b). When **4-MP** is considered, similar behavior is observed, but now an increase in the $[\text{Ir}]-(\text{H})_2$ form is also observed and it reaches a plateau at around the same time of 400 min (Figure 6.18c). Interestingly, the HD gas signal ceases to increase and reaches a plateau on the same timescale. The growth in the $[\text{Ir}]-(\text{H})_2$ and $[\text{Ir}]-(\text{H})(\text{D})$ can be explained by the return of the proton into the catalyst at the expense of the

substrate deuteration. The plateau would suggest that an equilibrium point was reached. A slight increase in the $[\text{Ir}]-(\text{D})_2$ form is seen in Figure 6.18c after 400 min, which could reflect measurement error due to peak widths and does not mean a further deviation from equilibrium. Interestingly, the slopes of the **4-MP** and pyridine deuteration curves (Figure 6.13b, d) are similar even though the associated catalysts exhibit different kinetic behavior.

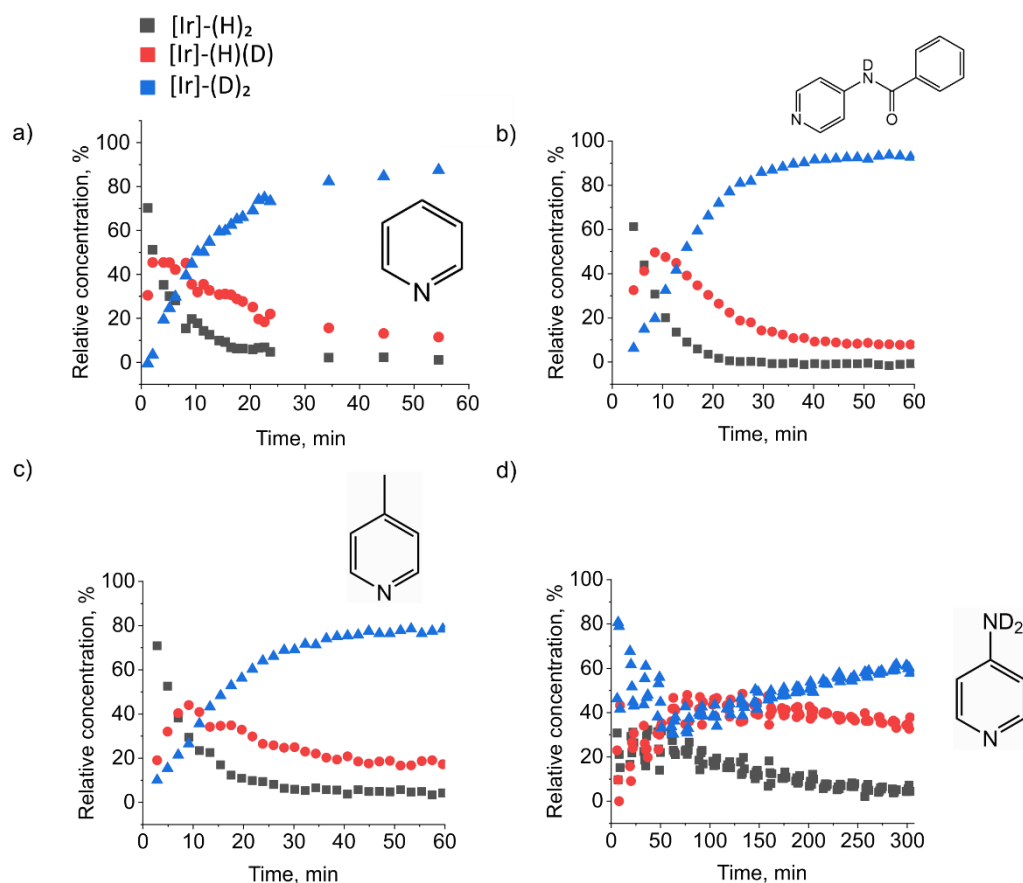


Figure 6.17 Change in $[\text{Ir}]-(\text{H})_2$, $[\text{Ir}]-(\text{H})(\text{D})$ and $[\text{Ir}]-(\text{D})_2$ species relative concentration (%) with the reaction time. Zoom up to 60 min for a) pyridine, b) **4-PBA**, c) **4-MP** and up to 300 min for d) **4-AP**.

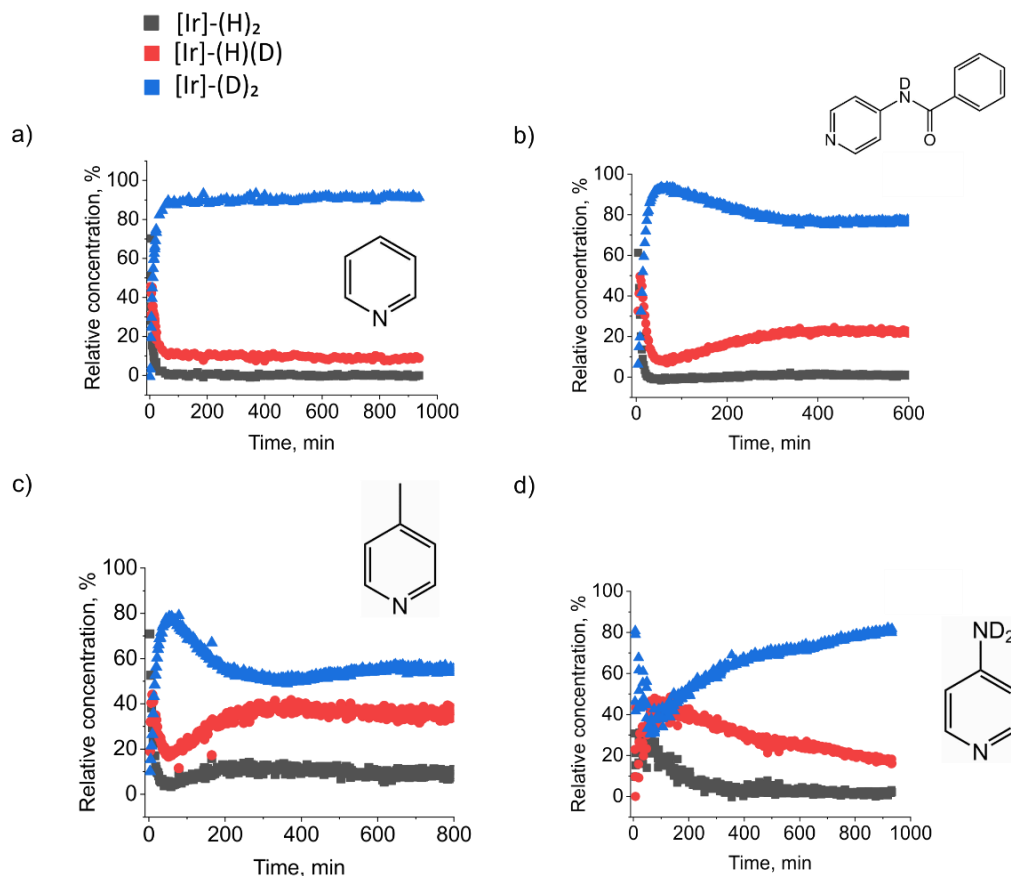


Figure 6.18 Change in $[\text{Ir}]-(\text{H})_2$, $[\text{Ir}]-(\text{H})(\text{D})$ and $[\text{Ir}]-(\text{D})_2$ species relative concentration (%) with the reaction time for a) pyridine, b) **4-PBA**, c) **4-MP** and d) **4-AP**.

The trends for **4-AP** discussed previously indicate much slower activation (900 minutes) when compared to the other substrates (Figure 6.13a), although the same behavior is seen. At short reaction times the hydride peaks are very broad with low SNR and therefore there is a high uncertainty in their integrals. Hence, the initial concentration of the $[\text{Ir}]-(\text{D})_2$ form is likely to be overestimated due to uncertainty in these peak integrals.

To conclude, the obtained trends in HD gas and hydride signal intensities for $[\text{Ir}]-(\text{H})(\text{D})$ and $[\text{Ir}]-(\text{H})_2$ are indicative of the competing processes that take place in these SABRE systems which undergo the HIE reaction and knowledge about this process can be extracted from their analysis. The return of the proton into the catalyst was observed for **4-MP** and **4-PBA** at the expense of the substrate deuteration after the activation is complete potentially indicates that the system reaches a new equilibrium position. This happens on a similar timescale to growth in HD gas peak.

During catalyst activation, hydrogen is consumed to form the cyclooctane and it exchanges into the hydrides sites through reductive elimination, it is only when activation is complete that exchange occurs alone. It is hypothesised that this change can cause the system to re-equilibrate.

6.6 Investigation of kinetic intermediates

The aim of this section is to use a lineshape analysis to differentiate between the loss of *ortho* signal intensity due to the formation of the mono-substituted **4-AP-*d*₁** and/or the double-substituted **4-AP-*d*₂**. As previously mentioned, the ¹H NMR lineshape for a nucleus will change if an adjacent proton to which it experiences a significant *J* coupling is substituted by deuterium. Therefore, the splitting patterns for couplings to the nuclei in **4-AP-*d*₁** and **4-AP-*d*₂** will be different. The presence of the mono-²H-labelled form was initially confirmed by independent ESI-MS. The sample of **4-AP** (5 eq to **1**) at about 60% deuteration showed the peaks for all three **4-AP** forms at 95.06 (**4-AP**), 96.07 (**4-AP-*d***) and 97.07 m/z (**4-AP-*d*₂**) when compared to the peak of the pure **4-AP** at 95.06 m/z (see Figure A8 and A9 in Appendix). However, this did not provide a quantitative response and so could not be used to assess changes in these species with the reaction time.

The lineshape analysis used here employed spectral simulations in Matlab written by Dr. Meghan Halse. For this purpose the proton-proton *J* couplings first need to be identified. However, the ¹H NMR spectra of the aromatic protons of N-heterocycles show strongly coupled multiplets and therefore the coupling constants cannot be directly measured from the spectra. Thus, an optimisation of the *J* couplings was performed using the *fminsearch* algorithm within a home-written Matlab macro that was interfaced with the SPINACH NMR simulation package.^{185, 186} This optimisation minimised the sum of squared differences between the points of the simulated and experimental NMR spectra. The ¹H-¹H *J* coupling constants, the chemical shift values and a single linebroadening parameter were included as parameters in the optimisation. The resultant coupling parameters for the three substrates considered here are presented in Figure

6.19 (see Tables A6 – A8 in Appendix for J coupling constants and line-broadening parameters)

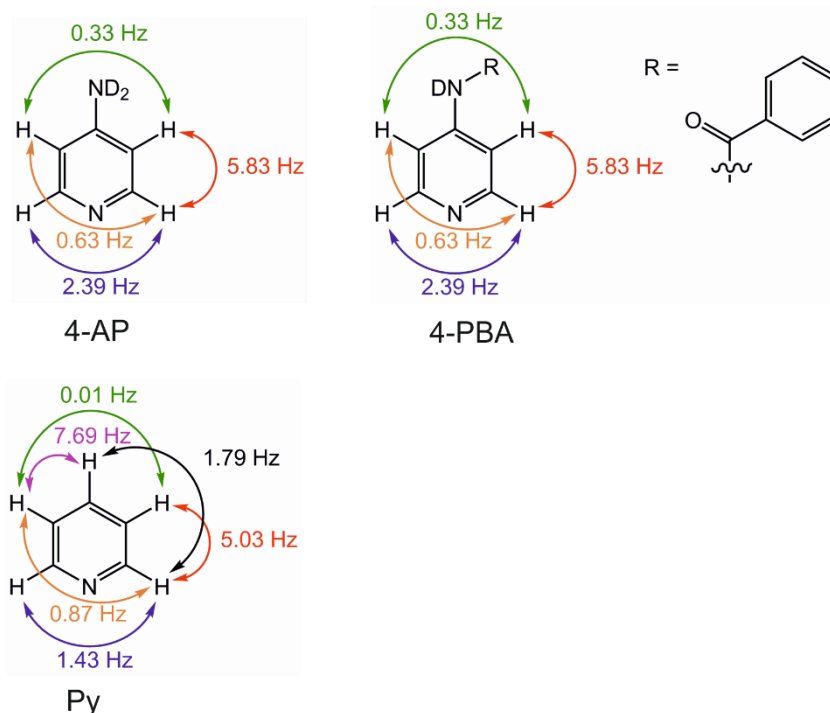


Figure 6.19 J couplings obtained by simulation for **4-AP**, **4-PBA** and pyridine.

Once the J couplings were known, the ^1H NMR spectra were simulated for **4-AP**, **4-AP- d_1** and **4-AP- d_2** . Figure 6.20 presents a comparison of (a) experimental ^1H NMR spectra, and simulated spectra of (b) fully protonated spectra, (c) mono-deuterium substituted and (d) di-deuterium substituted for the three substrates. Upon the substitution of one of the *ortho* protons with deuterium, the other proton retains its couplings to the *meta* and *para* protons, and forms a doublet of doublets in the case of **4-AP** and **4-PBA** and a doublet of doublets of doublets for pyridine. As the couplings, 0.63 Hz (for **4-AP** and **4-PBA**) and 0.01 Hz (for **Py**), are very small, these appear as a doublet and a doublet of doublets in the simulated spectra. When both *ortho* protons are substituted and the other protons are only coupled to the deuterium in the *ortho* positions, the *meta* signal appears to be a broad singlet in the case of **4-AP** and **4-PBA** and a doublet for pyridine (Figure 6.20).

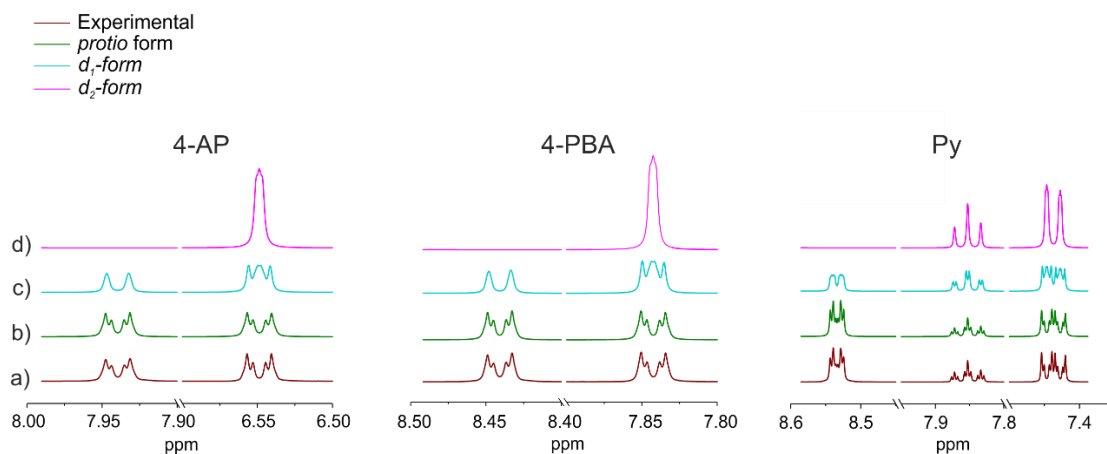


Figure 6.20 a) Experimental and (b-d) simulated spectra of *ortho* and *meta* proton peak lineshape for **4-AP**, **4-PBA** and pyridine.

The simulated spectra of the three substrate forms (non-labelled, mono- and double-deuterated) were used to determine the relative concentrations of these forms as a function of reaction time by comparison with the experimental spectra. Specifically, FIDs associated with each simulated spectrum (Figure 6.20) were combined with variable scaling factors and Fourier transformed. The sum-of-squared-differences between the simulated and experimental spectra was minimised by varying the scaling factors for the three forms. The optimised scaling factors were normalised to obtain the relative concentrations for the *protio* and deuterated substrate forms. Each point was processed independently and therefore no assumptions on the underlying mechanism were made. The results for the reactions involving **py**, **4-AP** and **4-PBA** are presented in Figure 6.21. The relative concentrations determined using this analysis are expected to be associated with a degree of uncertainty. However, the fact that each time point is analysed independently and the emergence of clear trends in the fitted data for all substrates in Figure 6.21 suggest that these changes are associated with real chemical processes rather than artefacts of the analysis.

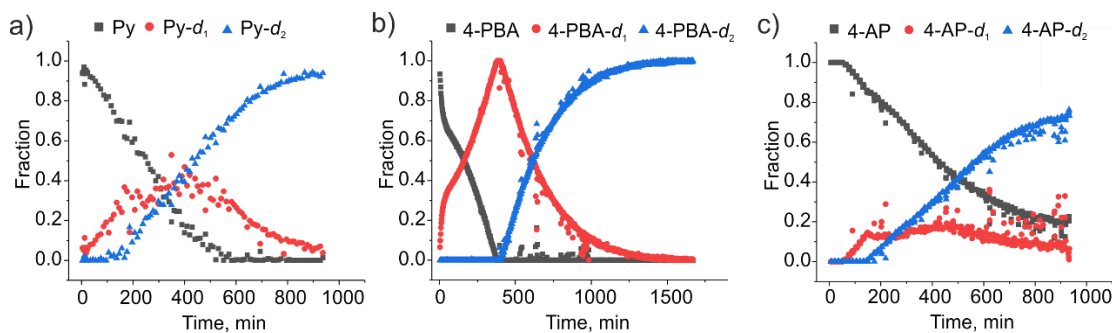


Figure 6.21 Simulated change in fractions of *protio*- and deuterated substrates with time of deuteration reaction using experimental ^1H NMR data.

The obtained plots show the presence of the d_1 -form with all of the analysed substrates thereby indicating the sequential substitution of the *ortho* protons with deuterium in all cases. Interestingly, pyridine and **4-PBA** show similar trends, where the *protio* and intermediate forms are almost fully converted to the d_2 -form by 1000 min. In contrast, **4-AP** still shows significant amounts of the protonated form at the end of the experiment. This difference could be due to the fact that the deuteration reaction has not reached completion by the end of the monitoring period; however it does appear that the system is approaching an equilibrium between the three forms. Surprisingly, in case of **4-PBA** full conversion to the mono-labelled form occurs prior to the insertion of the second label. It should also be noted, that due to peak overlap between the free **4-PBA** *meta* resonance and one of the signals from the activated complex with **4-PBA**, a slight distortion is evident in the curves up to the end of activation (~ 50 min) in the Figure 6.21b.

Therefore, in this part of the study lineshape analysis was successfully employed to track the precise fraction of mono- and double-labelled substrates with time. The results confirm that substrate dissociation from the catalyst occurs prior to the introduction of the second label. The differences in the kinetic plots for substrate *protio*, d_1 - and d_2 -forms were discussed.

6.7 Conclusions and future work

In this chapter, evidence for an indirect role for $[\text{Ir}(\text{H})_2(\text{IMes})(\text{substrate})_3]\text{Cl}$ in the HIE reaction has been obtained. Catalyst activation and substrate deuteration timescales were compared for 4-aminopyridine (**4-AP**), 4-methylpyridine (**4-MP**), pyridine (**py**) and N-(4-pyridyl)benzamide (**4-PBA**). Slowly exchanging intermediates $[\text{Ir}(\text{COD})(\text{IMes})(\text{4-AP})]\text{Cl}$ and $[\text{Ir}(\text{H})_2(\text{COD})(\text{IMes})(\text{4-AP})]\text{Cl}$ were detected and EXSY, lineshape analysis and PHIP hyperpolarisation studies suggest that they are not likely to be active species for HIE. The deuteration of the *ortho* position up to 99% has been observed and the activated catalyst found to be effective for HIE even when present at low concentration. Here, source of deuterium was methanol which suggests that the mechanism of HIE should include complex with metal-bound methanol. The detected presence of iridium complexes with deuteride ligands instead of hydride ligands confirm that HIE in substrate molecule undergoes via preceding deuteration of the catalyst. The lineshape analysis confirms that the H/D exchange process proceeds sequentially through mono- and di-deuterated products confirming that the ligand is lost during the process.

In contrast to the other substrates, **4-AP** undergoes H/D exchange on the same timescale as catalyst activation, while ultimately reaching similar deuteration levels to the other substrates. This suggests the **4-AP** is easier to activate than the other substrates. The acidity of the C-H bond in the substrate will be important in this step. Despite the electron-donating resonance effect in **4-AP**, which activates the *ortho* and *para* positions relative to the substituent group, the weak electron-withdrawing inductive effect affects the whole aromatic ring and the *ortho* positions relative to aromatic nitrogen become more acidic. For future studies the substrates with deactivating electron-withdrawing groups, like 4-carboxypyridine or 4-nitropyridine, would be interesting to study. Due to the more acidic *ortho* positions they are expected to deuterate quickly.

In case of the **4-PBA** substrate, the fact that the H/D exchange is not seen in the *meta* position, suggests the binding to the iridium metal-centre occurs via the aromatic nitrogen, and not via metallacyclisation involving the amide group.^{166, 187}

In the future the catalyst could be deactivated using bipyridine to prove that the deuteration stops when the substrate can no longer ligate to the catalyst. This has been employed previously to recover substrate T_1 values in the presence of the catalyst.¹⁴⁸ Alternatively, low temperature can be applied to slow down the reaction before analysis.

To more accurately model the concentration effects, the catalyst could first be activated in a solvent that does not act as a source of deuterium, for example *protio*-methanol or dichloromethane- d_2 . After the catalyst activation methanol- d_4 would be added to allow the HIE to occur.

In addition, cooling the sample containing a solution of the substrate and the catalyst to a very low temperatures using a liquid N₂ cooled NMR probe could reveal a *ortho*-ylidene ¹³C signal. Investigation of Pd and Ni pyridylidene complexes with ¹³C NMR has been reported previously.¹⁸⁸ PHIP hyperpolarisation has been known to detect short-lived trace intermediates and can be employed to detect the chemical shift of the hydride *trans* to substrate carbene.^{66, 189}

In the next chapter, the catalyst activation and H/D-labelling in substrate is probed with the SABRE signal intensity and lifetime using benchtop 43 MHz NMR spectroscopy.

Chapter 7: Reaction monitoring using SABRE-enhanced benchtop (1 T) NMR spectroscopy

7.1 Introduction

In this chapter a new method for monitoring a chemical transformation using benchtop 1 T NMR detection, combined with SABRE hyperpolarisation, is developed. This method brings together many of the results described previously in this thesis and some of the key results have been published.¹⁹⁰

To illustrate the reaction monitoring method, the reactions occurring within the SABRE system that were discussed in Chapter 6 are followed. This includes the transformation of the SABRE pre-catalyst [Ir(Cl)(COD)(IMes)] in the presence of H₂ and the substrate, **4-AP**, into the active catalyst [Ir(H)₂(IMes)(**4-AP**)₃]Cl (**4a**) and the incorporation of deuterium into the *ortho* positions of this substrate via hydrogen isotope exchange (HIE), where the source of deuterium is methanol-*d*₄. A method for monitoring this reactivity using the SABRE enhanced ¹H NMR signals of **4-AP** as a function of time and parallel non-hyperpolarised ¹H NMR spectra at high field (9.4 T) as a reference is developed. Specifically, the use of both the amplitude and lifetime of the SABRE signal to follow reactivity is explored. The SABRE lifetime measurements are achieved using the single-shot hyperT₁ method developed in Chapter 5. The method is first demonstrated at 9.4 T as a proof of concept and then is used at 1 T on a benchtop NMR spectrometer. It is shown that both catalyst activation and the HIE reactions can be followed through the change in SABRE hyperpolarisation lifetimes. Due to the low sensitivity of the benchtop spectrometer, HIE can be quenched by substituting *protio* methanol for methanol-*d*₄ and the results compared. To demonstrate that this method is applicable to systems with different kinetics, it is also applied to an analogous SABRE system where the substrate is 4-methylpyridine (**4-MP**).

Finally, a calibration approach for single-shot SABRE lifetime measurements is investigated in conjunction with a model of SABRE

developed by Barskiy *et al.*⁴⁶ to link the relaxation measurements with the concentrations of the substrate and catalyst.

7.2 Results

Reaction monitoring using thermally polarised ^1H NMR signals acquired within a benchtop NMR spectrometer is not reliable at millimolar concentrations of the substrate due to the reduced sensitivity at 43 MHz (1 T). Example ^1H NMR spectra acquired before and 1.5 min after $p\text{-H}_2$ addition to a sample of complex $[\text{Ir}(\text{COD})(\text{IMes})(\mathbf{4}\text{-AP})]\text{Cl}$ are presented in Figure 7.1. These demonstrate that even after a relatively short reaction time of 1.5 minutes, the signal-to-noise of the ^1H NMR peak for the *ortho* resonance (blue circle) is too low to be accurately quantified using thermally polarised benchtop NMR. Therefore, an alternate approach using hyperpolarisation is required.

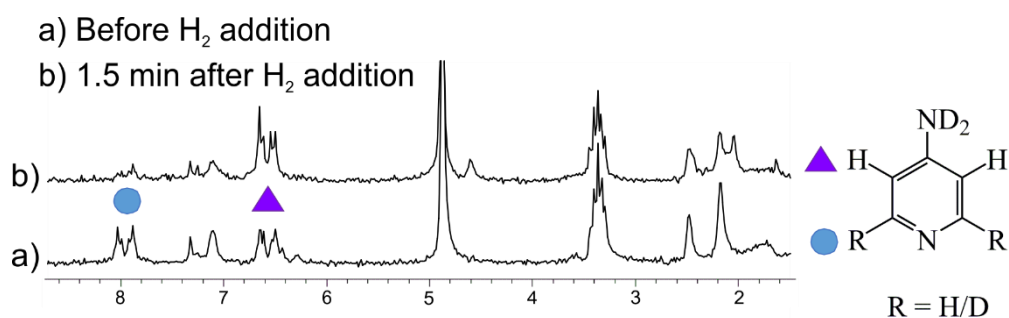


Figure 7.1 ^1H NMR spectra acquired using a 43 MHz (1 T) benchtop NMR spectrometer before addition of $p\text{-H}_2$ (bottom trace) and at 1.5 min after $p\text{-H}_2$ addition (upper trace) to a sample of 25 mM $\mathbf{4}\text{-AP}$ in presence of the SABRE catalyst (5 mM) in methanol- d_4 .

SABRE hyperpolarisation provides a significant increase in signal intensity compared to the Boltzmann-derived NMR signals and should normally be expressed as a percentage polarization rather than a simple enhancement factor (see Chapter 9, section 9.4). This is because the level of polarization generated by SABRE is independent of the detector, although sample handling effects and relaxation may impact on the observed values. However, from a sensitivity perspective, SABRE is more beneficial for 1 T NMR measurements as the thermal signal is much weaker.

A comparison of SABRE ^1H NMR spectra and standard ^1H NMR spectra, acquired in fields of 9.4 T and 1 T, for 25 mM **4-AP** in the presence of 5 mM of activated SABRE catalyst $[\text{Ir}(\text{H})_2(\text{IMes})(\mathbf{4-AP})_3]$ (**4a**) are shown in Figure 7.2. In both measurements, SABRE-enhanced peaks are visible at the chemical shifts corresponding to both bound and free substrate molecules. The standard ^1H spectrum suffers from reduced chemical shift dispersion at 1 T. Nevertheless, the SABRE enhanced peaks are well resolved. As has been established previously, comparable levels of SABRE polarisation are observed at high-field (9.4 T) and low-field (1 T).⁴² The higher polarisation level of the *meta* resonance of **4-AP** obtained using the 1 T NMR spectrometer is likely due to the easier access to the spectrometer bore which makes transfer times shorter.

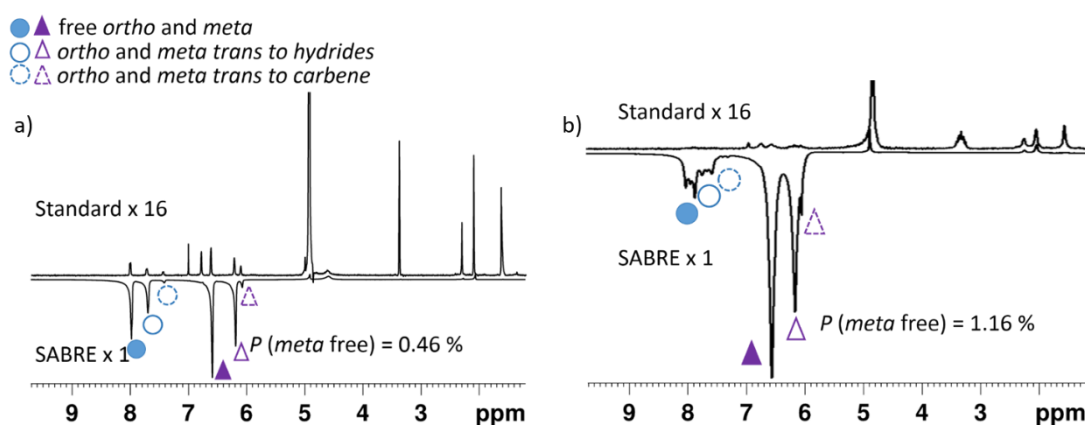


Figure 7.2 Standard ^1H NMR spectra (top) compared with SABRE-enhanced ^1H NMR spectra (bottom) of **4-AP** (5 eq, 2-fold-excess, 10 mM) in the presence of $[\text{Ir}(\text{H})_2(\text{IMes})(\mathbf{4-AP})_3]$ (**4a**) (5 mM) in methanol- d_4 acquired in a magnetic field of 9.4 T at 328 min from start of activation (a) and at 1 T at 320 min from start of activation (b).

In contrast to a conventional quantitative NMR measurement, SABRE signal intensity does not scale linearly with the substrate concentration because of complex kinetic behavior that is not simply first order in nature. Here, the thesis focuses on understanding the SABRE response in both a qualitative and quantitative manner as a function of the reaction conditions. This response can be assessed through either its amplitude or lifetime. Both of these parameters have the potential to act as probes for reaction monitoring because they can be measured using a series

of single-shot acquisitions that mean the total experiment time need not exceed a couple of minutes.^{39, 159, 191} In the following section the viability of these parameters for monitoring chemical changes in the sample during the activation and deuteration processes will be explored.

7.2.1.1 Reaction monitoring with SABRE signal intensity

The amplitude of the SABRE signal is expected to provide information on the activation process because the degree of signal amplification will increase as the concentration of the active catalyst species (**4a**) increases. However, the effect of substrate deuteration on this signal is expected to be complex. Previous work by Rayner *et al.* has suggested that deuteration can lead to increased SABRE efficiency due to a lengthening of the lifetimes of the remaining ¹H resonances within the substrate, and the concentration of the SABRE hyperpolarisation into fewer nuclei.⁹⁰ At the same time, there is also potential for deuteration to decrease SABRE polarisation transfer efficiency through changes to the *J*-coupling network that drives polarisation transfer in the low-field regime.^{56, 77-79, 90} A series of SABRE hyperpolarisation experiments were performed using a 400 MHz ¹H NMR spectrometer for detection. Fresh *para*-hydrogen was added to the head-space of the NMR tube and mixed into solution (via shaking) between each measurement in order to achieve SABRE hyperpolarisation. This hydrogen refreshment step changes the observed rate of reaction of both the activation and the deuteration processes. In order to establish a suitable control experiment, a standard ¹H NMR spectrum was recorded at each step of the experiment for comparison with the SABRE response.

The changes in the SABRE-enhanced ¹H NMR signal intensity of **4-AP** were observed with the reaction time. The evolution of the standard and SABRE-enhanced ¹H NMR signal intensities as a function of time, where *p*-H₂ is refreshed between each data point, are presented in Figure 7.3a and Figure 7.3b,c, respectively. The *meta* proton resonance of **4-AP** in free solution (6.58 ppm) is shown as a control to assess the kinetics of the SABRE catalyst activation (see section 7.2.1.1.1 for details). The observed trends in SABRE signal integral suggest that this parameter is sensitive to both of the

chemical transformations under investigation. An exponential fit of the decay in signal intensity seen for the standard ^1H NMR response of the **4-AP** *meta* proton (Figure 7.3a) indicates that the activation process has completed after 235 min. As expected, the SABRE-enhanced NMR responses of both *ortho* and *meta* resonances increase on the same timescale as the concentration of **4a** rises. Interestingly, the SABRE signal continues to grow after the activation step is complete. These results suggest that the SABRE-enhanced NMR signal is affected by both activation and deuteration processes. However, differentiation of these effects is challenging. Similar trends were observed for results collected at both 9.4 T (Figure 7.3b) and 1 T (Figure 7.3c). The smaller increase in the final *ortho* resonance signal area at 1 T could be due to peak overlap and/or relaxation effects, but has not been further investigated.

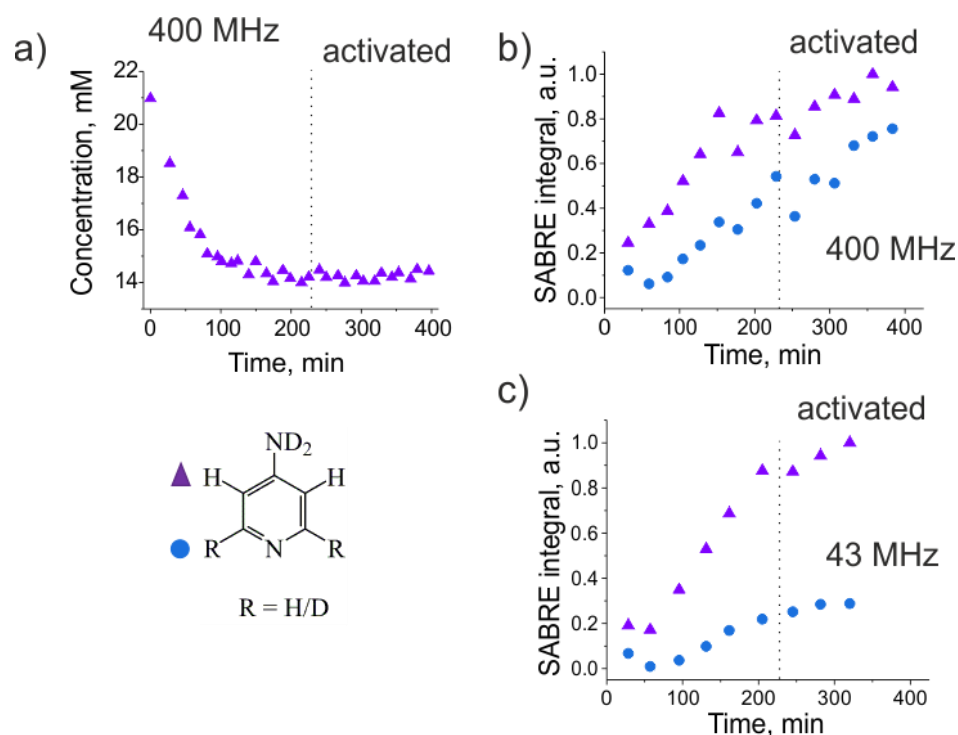


Figure 7.3 (a) Concentration of free **4-AP** as a function of time determined from standard ^1H NMR spectra acquired at 9.4 T in parallel with the SABRE measurements. The time to activation (235 min) was determined from a fit to a mono-exponential decay. Normalised raw SABRE-enhanced ^1H NMR signal intensity of the *ortho* (blue circles) and *meta* (violet triangles) protons of **4-AP** (5.2 eq relatively to **1**) during the activation of 5 mM SABRE complex in methanol- d_4 as measured using detection at (b) 9.4 T and (c) 1 T.

To summarise, the interpretation of the change in SABRE signal amplitude in terms of the underlying chemical reactivity is complicated by

the fact the SABRE response is not linearly dependent on substrate concentration in this case. In addition, any quantitative interpretation would be limited by the reproducibility of the SABRE response, which depends on many factors including *para*-hydrogen enrichment level, polarisation transfer field, hyperpolarisation time, and sample transport time. In the next subsection an additional effect on the **4-AP** *ortho* proton signal intensity is discussed which was observed during the monitoring presented above and which explains why the *meta* resonance has been used for the control experiment.

7.2.1.1.1 HIE equilibrium effect on *ortho* position in **4-AP**

The standard (thermally polarised) ^1H NMR spectra acquired in parallel with the SABRE-enhanced spectra at 9.4 T (Figure 7.3a) revealed that the signal for the *ortho* resonance changes differently with reaction time. Both the *ortho* and *meta* signal integrals are presented in Figure 7.4a. An initial decrease in the ^1H NMR signal for the *ortho* resonance is attributed to the consumption of free **4-AP** during the activation step and the HIE reaction which substitutes deuterium for ^1H in this site. Subsequently there is a prominent ^1H NMR signal increase in the *ortho* resonance which needs explanation.

One way to account of this would be to propose that equilibration within the gas phase of liberated HD and D_2 according to Figure 6-14 (Chapter 6) acts over long time periods to move the HIE equilibrium back to the **4-AP** *protio* form. Another possibility would be to involve one-proton PHIP. However, the previously reported ^1H NMR signals enhanced with one-proton PHIP possess emissive peak lineshape which is not the case here.¹⁵⁸

In order to rationalise this behaviour, the ^1H NMR *ortho* and *meta* signal integrals of **4-AP** were measured, where H_2 was added just once at the beginning of the experiment and the NMR tube remained in the spectrometer throughout the reaction; it was not shaken between each NMR acquisition (Figure 7.4b). Initially, the integrals of the two resonances are equal, as they both correspond to two protons. Both *ortho* and *meta*

protons decrease due to the consumption of **4-AP** in activation process. Deuteration of the **4-AP** *ortho* position then causes the *ortho* signal to further decrease. In this case the slow activation and deuterium incorporation is evident. When the same experiment was repeated with *p*-H₂, but where the sample was first activated by shaking to the point where 37% conversion to the active SABRE catalyst was achieved, the plot in Figure 7.4c was obtained. As the *p*-H₂ is not refreshed beyond this point, its effect is rapidly quenched as it converts to normal hydrogen under reversible exchange with the catalyst. Now the *ortho* proton signal initially decreases in intensity as expected. However, at longer reaction times the signal starts to increase slowly as H₂ replaces D₂ and HD in solution which leads to the reformation of unlabeled and mono labelled **4-AP** forms. This increase is smaller than in Figure 7.4a due to the smaller concentration of fresh H₂. The same effect was seen for the hydride ¹H NMR signals in Chapter 6, section 6.4.1.

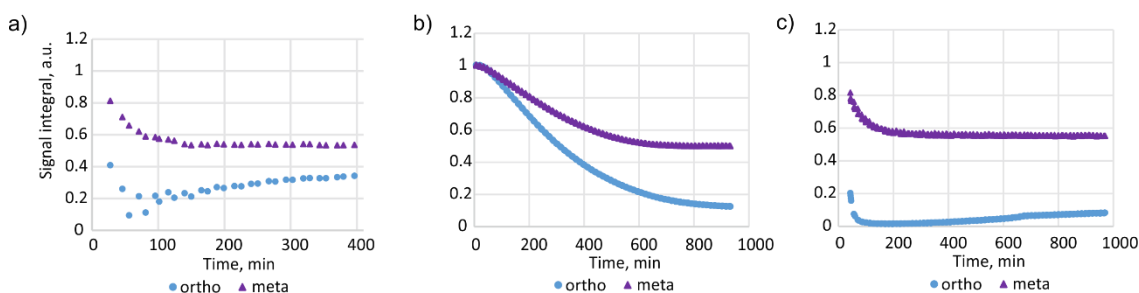


Figure 7.4 Standard ¹H NMR signal integral of the *ortho* (blue circles) and *meta* (violet triangles) signal intensity during the reaction monitoring under (a) *p*-H₂ when the sample was monitored with alternate thermal and hyperpolarised measurements and *para*-hydrogen gas was refreshed for each hyperpolarised scan (b) H₂, when H₂ was added once in the beginning, and (c) *p*-H₂, when the catalyst was activated to 37% using shaking under *p*-H₂ and then the sample was monitored without additional *p*-H₂ refreshment.

To conclude, due to the complex HIE effects in the *ortho* proton the *meta* resonance is used from the standard ¹H NMR experiments as a reference for comparison with the hyperpolarised measurements in Figure 7.3. This allows me to assess the kinetics of the substrate consumption during catalyst activation without the confounding effects of HIE.

7.2.1.2 Reaction monitoring using SABRE hyperpolarisation lifetimes

As SABRE signal intensity cannot be easily quantified and does not provide a straight-forward route to distinguish between the different types of reactivity in the system, SABRE signal lifetime (hyper T_1) is now tested for being a good probe of reactivity. The lifetime of the SABRE hyperpolarisation is limited by the longitudinal (T_1) NMR relaxation time, which is sensitive to the chemical environment and has been used previously for identifying and characterising inter- and intramolecular interactions.^{146, 147, 192, 193} In this method, the fact that the active SABRE catalyst contains bound substrate molecules that exchange with those in solution is exploited. As a result, the observed lifetime of the SABRE hyperpolarisation reflects a weighted average of contributions from these different forms.¹⁴⁸ NMR relaxation times are known to be significantly shorter for the bound substrate molecules.¹⁴⁸ Therefore, as the concentration of the active SABRE catalyst (**4a**) increases, the observed hyperpolarisation lifetime is expected to decrease. This shortening of the relaxation time in the presence of the activated complex is well-known in the SABRE literature.^{90, 148} In addition, the observed lifetime of the SABRE hyperpolarisation of the *meta* resonances of **4-AP** is expected to increase following substitution of ^2H for ^1H in the adjacent *ortho* position.^{90, 113} Therefore the time-dependent changes of the hyperpolarisation lifetimes for the *meta* resonances of **4-AP** are expected to reflect the competing effects of the formation of **4a** and the partial deuteration of **4-AP**. In contrast, the hyperpolarisation lifetimes for the *ortho* resonances of **4-AP** are expected to reflect only the formation of **4a**. This is because ^1H NMR signal will only be observed for the ^1H *ortho* resonances of 4-aminopyridine and 4-amino-2- d_1 -pyridine. In both of these cases, the observed *ortho ^1H hyperpolarisation lifetime will be dominated by interactions with the ^1H in the adjacent *meta* position and therefore is not expected to be affected significantly by the progress of the ^1H - ^2H exchange reaction.⁹⁰*

Parallel measurements of non-hyperpolarised ^1H NMR spectra and hyperpolarisation lifetimes were performed as a function of time following

the first addition of $p\text{-H}_2$ with detection on a 400 MHz NMR spectrometer in methanol- d_4 (Figure 7.5a and b). Non-hyperpolarised ^1H NMR spectra indicate that the formation of **4a** is complete by 205 min following the first addition of $p\text{-H}_2$ (Figure 7.5a). This activation time is indicated by the vertical dashed lines in Figure 7.5b-d.

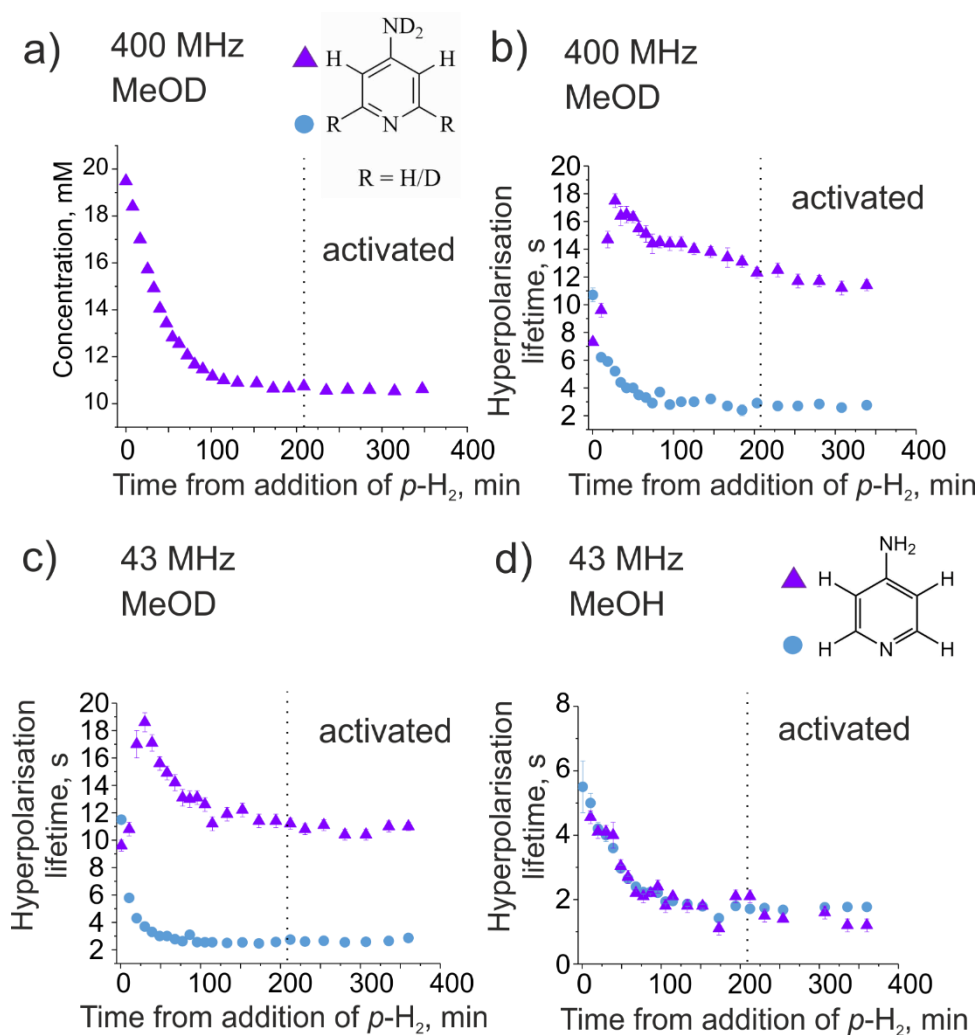


Figure 7.5 (a) **4-AP** concentration assessed by acquisition of non-hyperpolarised ^1H NMR signal intensity of the **4-AP** *meta* proton resonance, acquired as a function of time following the addition of H_2 to the methanol- d_4 solution alongside parallel hyperpolarisation lifetime measurements in (b) at 400 MHz. The *ortho* (blue circles) and *meta* (purple triangles) encode the corresponding hyper T_1 values, (c) portrays the analogous lifetime results in methanol- d_4 at 1 T, while (d) reflect the same data from *protio* methanol at 1 T. The initial concentration of **4-AP** used was 25 mM, giving a net 2-fold excess relative to $[\text{Ir}(\text{H})_2(\text{IMes})(\mathbf{4-AP})_3]\text{Cl}$ (5 mM) once the reaction is complete. Error bars represent the standard errors of the fit for each point. The time for the activation step to go to completion was estimated from an exponential fit of the ^1H NMR data in (a) and is indicated by the vertical dotted line.

Figure 7.5b shows the change in the *ortho* (blue circles) and *meta* (purple triangles) ^1H hyperpolarisation lifetimes as a function of time

following the initial addition of *p*-H₂. Each hyperpolarisation lifetime measurement is achieved using a manual shaking SABRE hyperpolarisation procedure with NMR detection at 9.4 T where the *p*-H₂ in the headspace and hence solution of the NMR tube was refreshed between each measurement. These measurements involved monitoring the *ortho* and *meta* resonances, which have already been shown to exhibit equivalent *T*₁ values for the free and bound substrate respectively at high field (section 5.3.3.2, Chapter 5).

In Figure 7.5b, the hyperpolarisation lifetimes for the *ortho* resonances of **4-AP** reduce and reach a plateau in a time period that corresponds to the formation of **4a**. In contrast, the lifetimes of the *meta* resonances show an initial rapid increase with a subsequent decrease at longer times. These observations support our hypothesis that the hyperpolarisation lifetimes of the *meta* resonances are sensitive to both the formation of **4a** and substrate deuteration, while the hyperpolarisation lifetimes of the *ortho* resonances are sensitive only to the formation of **4a**. The initial change in the lifetime of the *meta* resonances indicate a more rapid incorporation of ²H into **4-AP** than was observed under the experimental conditions discussed in section 6.5, Chapter 6, where the H₂ was added to the headspace and the sample shaken only once at the start of the experiment. The apparent increase in the rate of the HIE reaction under SABRE conditions, where *p*-H₂ is refreshed and the sample shaken vigorously between each measurement, is supported by the observed changes in lineshape of the *meta* resonances that are seen in the standard ¹H NMR spectra that were acquired at 400 MHz (Figure 7.6) during such reactions.

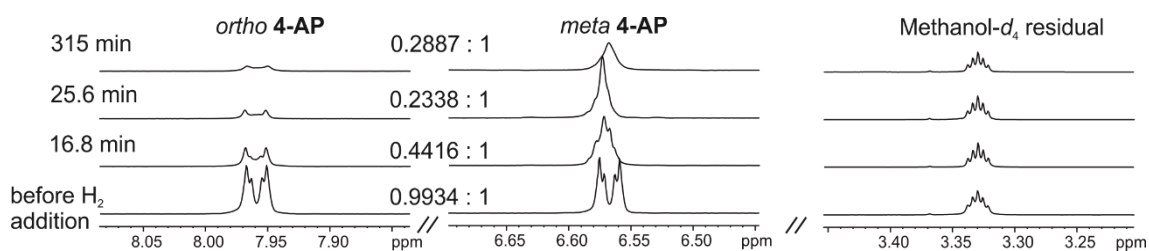


Figure 7.6 Change in the relative intensity and line-shape of the *ortho* and *meta* proton resonances of **4-AP** as a function of reaction time in the regime where the *p*-H₂ was refreshed between each scan. The *ortho* resonance line shape loses some of the second order splitting, which is characteristic of progressive ²H substitution at the second *ortho* position on the ring, but retains the doublet line-shape indicating that the *meta* resonance itself is not undergoing deuteration. The line-shape of the *meta* resonance evolves into a singlet over time which suggests that the *ortho* position has been significantly deuterated.

Time zero denotes the time at which the H₂ gas was introduced to the sample.

The use of SABRE hyperpolarisation to increase sensitivity allows us to repeat this reaction monitoring procedure on a 1 T benchtop NMR spectrometer (Figure 7.5c). The time-dependent changes in hyperpolarisation lifetime determined using the benchtop NMR instrument show the same trends as the experiments using a standard (9.4 T) NMR spectrometer. This illustrates that SABRE hyperpolarisation can be used to enable reaction monitoring at both high and low field. In fact, here benchtop NMR is used where a combination of low sensitivity and peak overlap would normally prevent this monitoring process. Furthermore, once the sensitivity limitation is overcome through the use of hyperpolarisation, there are additional benefits to using benchtop NMR. Due to its lower magnetic field strength, benchtop ¹H NMR spectra can be acquired in the presence of a protonated solvent without the need to actively suppress the solvent signal. Indeed it has been found that the SABRE hyperpolarised NMR response from a low-concentration analyte can exceed that from a protonated solvent when detected at 1 T (43 MHz).⁴² Figure 7.5d shows the change in the *ortho* (blue circles) and *meta* (purple triangles) ¹H hyperpolarisation lifetimes as a function of time following the initial addition of *p*-H₂ for the case where *protio* methanol is the solvent and a 1 T benchtop NMR spectrometer is used for detection. In the absence of the source of deuterium (methanol-*d*₄) the hyperpolarisation lifetimes of both the *ortho* and *meta* protons follow the same trend: a monotonic decrease to a plateau on the same timescale as the

formation of the activated SABRE complex, **4a**. The absence of the initial increase in the *meta* hyperpolarisation lifetime supports the hypothesis that this feature of the previous experiments originated from the deuteration effect. Therefore not only does the use of SABRE hyperpolarisation enable reaction monitoring using a benchtop NMR spectrometer, the use of this low-field (1 T) instrument provides a simple route to the deconvolution of the competing effects of SABRE catalyst activation and substrate deuteration.

To further verify the method, it has been applied to an analogous SABRE system where the substrate is 4-methylpyridine (**4-MP**). The SABRE catalyst $[\text{Ir}(\text{H})_2(\text{IMes})(\mathbf{4-MP})_3]\text{Cl}$ formation from the mixture of **1** and $[\text{Ir}(\text{COD})(\text{IMes})(\mathbf{4-MP})]\text{Cl}$ in the presence of a 4-fold excess (in starting solution) of 4-methylpyridine (**4-MP**), was monitored using the hyperpolarisation lifetime measurement procedure with benchtop (1 T) NMR detection. Figure 7.7 shows the change in the *ortho* (green square) and *meta* (gold triangles) ^1H hyperpolarisation lifetimes of **4-MP** as a function of time following the initial addition of *p*- H_2 in methanol- d_4 (Figure 7.7a) and *protio* methanol (Figure 7.7b). Figure 7.7 indicates a much faster rate of activation for **4-MP** compared to **4-AP** (Figure 7.5). This is due to the different electronic properties of **4-MP** and **4-AP** due to substituent effects. Furthermore, the hyperpolarisation lifetime behaviour for **4-MP** is the same in the two solvents. This indicates that there is no significant deuteration of **4-MP** on the timescale of this experiment. Control experiments of ^1H NMR line-shapes were acquired at 400 MHz to confirm the absence of significant deuteration on this timescale in the regime when *p*- H_2 is refreshed between the measurements (Figure 7.8).

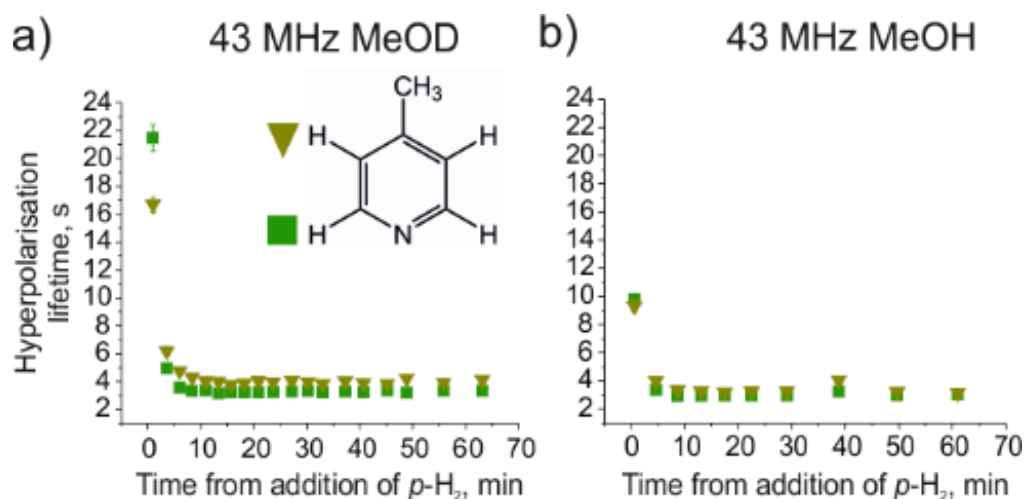


Figure 7.7 Hyperpolarisation lifetimes of the *ortho* and *meta* protons of **4-MP** as a function of time during the activation of the SABRE complex at 1 T (a) in methanol- d_4 and (b) in *protio* methanol. Initial concentration of **4-MP** is 25 mM which results in a 2-fold excess to the activated complex $[\text{Ir}(\text{H})_2(\text{IMes})(\mathbf{4}\text{-MP})_3]\text{Cl}$ (5 mM). Error bars represent the standard error from the fit of each hyperpolarisation decay curve to mono-exponential.

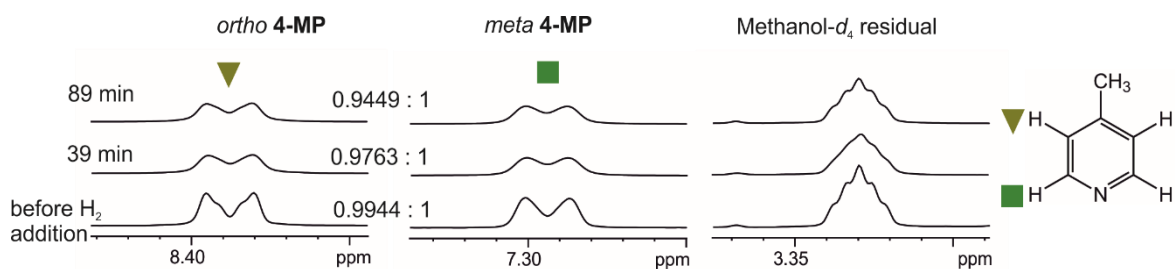


Figure 7.8 Change in the relative intensity of the **4-MP** *ortho* and *meta* resonances as a function of reaction time in the regime when the *p*- H_2 was refreshed between each scan acquired at 400 MHz. The initial solution was prepared with 9 eq of **4-MP** relative to **1**. Eleven *p*- H_2 refreshments were done in 89 min. The ^1H NMR spectra presented here were acquired (bottom) before *p*- H_2 addition, (middle) 39 min and (top) 89 min after the first *p*- H_2 addition. No significant change was observed in the line-shapes of the *ortho* and *meta* peaks of **4-MP**, indicating no significant deuteration on this timescale. Time zero denotes the time at which the *p*- H_2 gas was introduced to the sample.

To conclude, in this case, the formation of the active SABRE catalyst $[\text{Ir}(\text{H})_2(\text{IMes})(\mathbf{4}\text{-MP})_3]\text{Cl}$ is more rapid (~ 20 min) when compared to the reaction with **4-AP** (205 min) and no significant deuteration of **4-MP** is observed on the timescale of the experiment (65 min). In addition, the hyperpolarised lifetimes exhibit the same trends when the reaction is monitored in both deuterated and protonated methanol, further supporting the observation that no HIE is occurring on the timescale of the experiment.

7.2.1.3 Calibration of SABRE hyperpolarisation lifetimes

7.2.1.3.1 Calibration model

A calibration is required for reaction monitoring applications in order to quantitatively follow changes in concentration. An analytical model for the SABRE hyperpolarisation process was proposed by Barskiy *et al.*⁴⁶ The free and bound substrate molecules are assumed to be under fast exchange “even comparable to the complex relaxation time”.⁴⁶ The exchange process occurs via the formation of an intermediate 16-electron complex as studied by Cowley *et al.*⁹⁵ As a result of the fast exchange, the model gives $R_{1,avg} = \frac{1}{T_{1,avg}}$ dependence on the relative concentration of the bound to the SABRE catalyst and free substrate molecules and their individual T_1 values.⁴⁶ A derivation of the $R_{1,avg}$ adapted from Barskiy *et al.* is presented below.⁴⁶

Figure 7.9 illustrates the exchange and relaxation processes that are considered in the model, where $[C]$, $[C_1]$ and $[S]$ are the concentrations of the substrate bound to the complex, the intermediate species and the free substrate, respectively, k_s^a and k_s^d are the association and dissociation rate constants, $[C^*]$ and $[S^*]$ are the concentrations of hyperpolarised species for the substrate bound to the complex and the free substrate, respectively. $R_C = \frac{1}{T_{1,bound}}$ and $R_S = \frac{1}{T_{1,free}}$ are the relaxation rate constants for the hyperpolarised substrate bound to the complex and the free substrate, respectively.

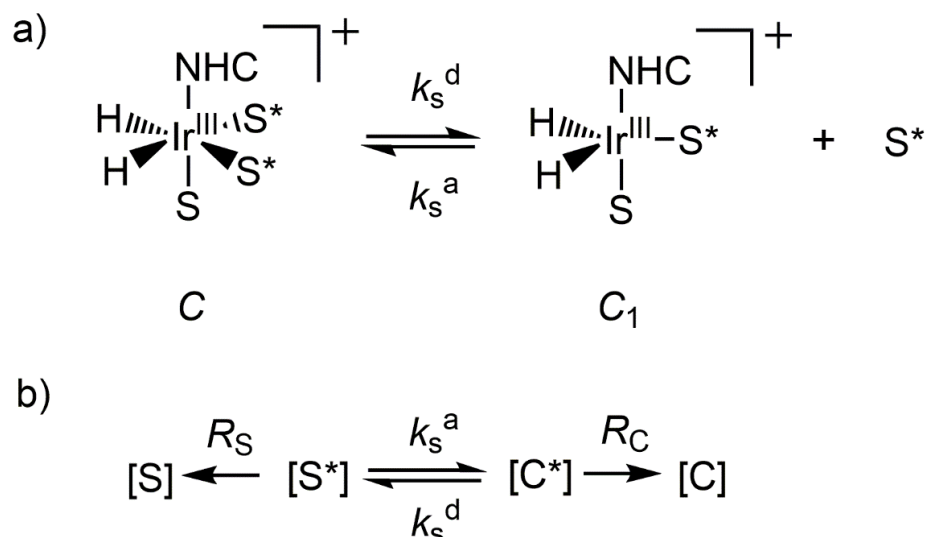


Figure 7.9 a) Scheme for the exchange of the hyperpolarised substrate (S^*) on the SABRE catalyst (C) via the formation of the intermediate 16-electron complex (C_1). b) Scheme illustrating the rates of association (k_s^a) and dissociation (k_s^d) and the relaxation rates for the free (R_S) and bound substrate (R_C), which are considered in the model proposed by Barskiy *et al.*⁴⁶

The changes in the concentrations of hyperpolarised bound and free substrate with time are expressed in Equations 7.1 and 7.2, respectively.

$$\frac{d[C^*]}{dt} = -k_s^d[C^*] + k_s^a[S^*][C_1] - R_c[C^*] \quad (7.1)$$

$$\frac{d[S^*]}{dt} = +k_s^d[C^*] - k_s^a[S^*][C_1] - R_s[S^*] \quad (7.2)$$

In this model the exchange between the bound and free substrate is assumed to be faster than the relaxation rates, thus, it can be assumed the following Equations 7.3 and 7.4 are true.

$$\frac{[C^*]}{[S^*]} = \frac{[C]}{[S]} \quad (7.3)$$

$$k_s = \frac{[S^*][C_1]}{[C^*]} = \frac{[S][C_1]}{[C]} \quad (7.4)$$

Using the fact that $[C^*] = \frac{[C][S^*]}{[S]}$, the change in concentration, $[C^*]$, is expressed in Equation 7.5. And therefore, the sum of the differentials is given by Equation 7.6.

$$\frac{d[C^*]}{dt} = \frac{[C]}{[S]} \frac{d[S^*]}{dt} \quad (7.5)$$

$$\frac{d[C^*]}{dt} + \frac{d[S^*]}{dt} = \left(1 + \frac{[C]}{[S]}\right) \frac{d[S^*]}{dt} \quad (7.6)$$

The summation of Equations 7.1 and 7.2, considering $[C^*] = \frac{[C][S^*]}{[S]}$, gives Equation 7.7. From Equation 7.6 and 7.7, Equation 7.8 is derived, which is then rearranged into Equation 7.9 to give the change in the hyperpolarised free substrate concentration, where the average relaxation rate is $R_{1,avg} = 1/T_{1,avg}$ (Equation 7.10).

$$\frac{d[C^*]}{dt} + \frac{d[S^*]}{dt} = -\left(R_s + R_c \frac{[C]}{[S]}\right) [S^*] \quad (7.7)$$

$$\left(1 + \frac{[C]}{[S]}\right) \frac{d[S^*]}{dt} = -\left(R_s + R_c \frac{[C]}{[S]}\right) [S^*] \quad (7.8)$$

$$\frac{d[S^*]}{[S^*]} = -\frac{\left(R_s + R_c \frac{[C]}{[S]}\right)}{\left(1 + \frac{[C]}{[S]}\right)} dt \quad (7.9)$$

$$\frac{1}{T_{1,avg}} = R_{1,avg} = \frac{\left(R_s + R_c \frac{[C]}{[S]}\right)}{\left(1 + \frac{[C]}{[S]}\right)} \quad (7.10)$$

Equation 7.10 derived by Barskiy *et al.* provides the relationship between the average T_1 , the T_1 values of the free and bound substrate and their concentrations.

7.2.1.3.2 Results

In this section, a calibration for the hyper T_1 dependence on the substrate and activated catalyst concentrations in *protio*-methanol is performed to avoid competing reactions like deuteration. The obtained data is fitted with the SABRE analytical model discussed above and extend it to the reaction monitoring data.

A series of hyperpolarisation lifetime measurements for different substrate concentrations and a constant catalyst concentration were performed for 4-aminopyridine in the presence of 5 mM $[\text{Ir}(\text{IMes})(\text{H})_2(\mathbf{4-AP})_3]\text{Cl}$ in MeOH at 1 T using the benchtop NMR for detection (Figure 7.10a). A second series of measurements were then performed for a range

of catalyst concentrations and a constant **4-AP** concentration (Figure 7.10b). The expected increase in T_1 values with increase in substrate concentration and decrease with increase in catalyst loading in the activated sample is observed.

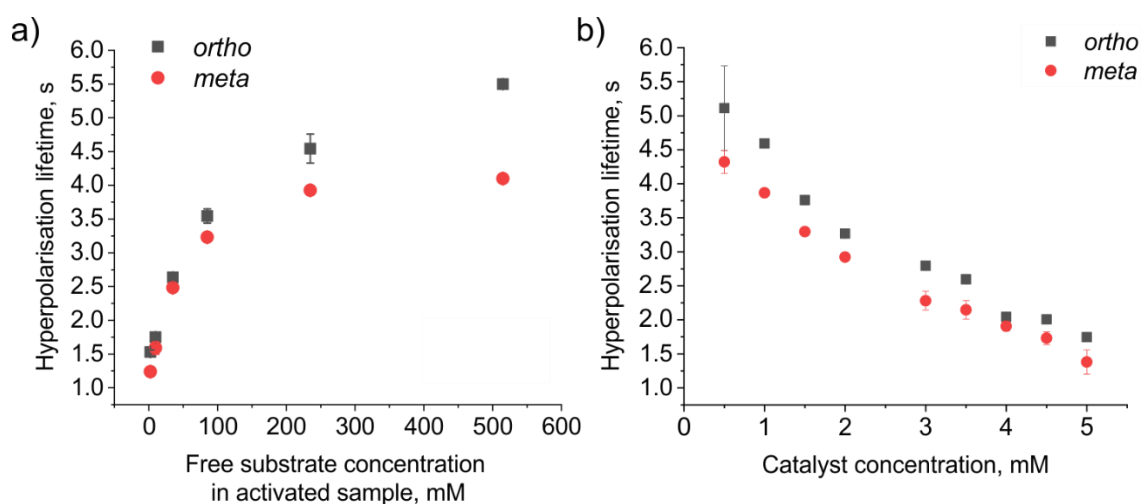


Figure 7.10 Hyperpolarisation lifetimes of **4-AP** in MeOH at 1 T benchtop NMR (a) at different concentrations (3.5 eq, 5 eq, 10 eq, 20 eq, 50 eq, 106 eq relatively to **1**) in presence of 5 mM $[\text{Ir}(\text{IMes})(\text{H})_2(\text{4-AP})_3]\text{Cl}$ and (b) at 10 mM **4-AP** in the activated sample at different concentrations of $[\text{Ir}(\text{IMes})(\text{H})_2(\text{4-AP})_3]\text{Cl}$ (0.5 mM, 1 mM, 1.5 mM, 2 mM, 3 mM, 3.5 mM, 4 mM, 4.5 mM, 5 mM).

The obtained dependences of $T_{1,\text{avg}}$ on concentration were fit to Equation 7.10, where the concentration of the bound substrate was double the catalyst concentration due to the equal probability of the substrate being bound *trans* to each of the hydrides. The result of fitting the hyper T_1 data is presented in Figure 7.11. The fitting curve exhibits an R^2 value of 0.973 for the *ortho* proton data and 0.948 for the *meta* proton data. This means that 97.3% and 94.8% of the variability in the data has been accounted for by the model function respectively. Table 7.1 presents the predicted T_1 values for the free and bound substrate generated from this fitting to the model.

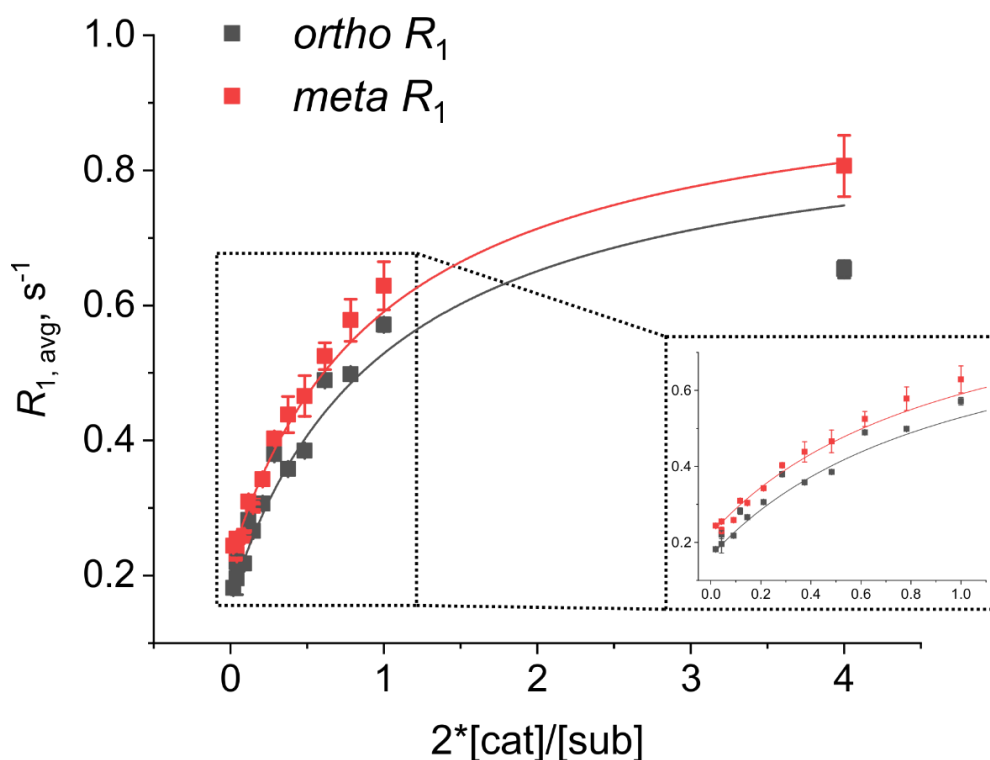


Figure 7.11 The dependence of $R_{1,avg}$ on the relative concentration of the bound to the free substrate molecules, fitted to Equation 7.10. The concentration of the bound substrate was taken as the double of the catalyst concentration due to the equal probability of both two bound *trans* to hydrides substrate molecule to exchange with the free substrate. The inserted graph is the zoomed region shown in dashed line.

Table 7.1 T_1 values of the *ortho* and *meta* protons of the free and bound substrate obtained under hyperpolarisation from fitting the data presented in Figure 7.11 to Equation 7.10. The last column refers to data measured on a sample of 150 mM **4-AP** in MeOH in presence of 5 mM $[\text{Ir}(\text{COD})(\text{IMes})(\mathbf{4-AP})]\text{Cl}$ under areduced pressure atmosphere.

	$T_{1, \text{free}}, \text{ s}$	$T_{1, \text{bound}}, \text{ s}$	$T_{1, \text{free}}, \text{ s}$
	from the fit	from the fit	measured
<i>ortho</i>	6.1 ± 0.3	1.12 ± 0.04	4.9 ± 0.2
<i>meta</i>	4.5 ± 0.1	1.04 ± 0.05	4.9 ± 0.1

For comparison purposes, it is worth noting that the extracted $T_{1, \text{bound}}$ values for the *ortho* and *meta* resonances are close to literature reported T_1 values of $\sim 1 - 2$ s for 4,6- d_2 -nicotinate in methanol- d_4 obtained at 243 K, where $T_{1, \text{free}}$ and $T_{1, \text{bound}}$ values are resolved.⁴⁰ In addition, the extracted $T_{1, \text{bound}}$ values are consistent with the values measured at low temperature in section 5.3.3.3 of Chapter 5 for **3,5-DAP** and **4-PBA** in methanol- d_4 . Extracted $T_{1, \text{free}}$ values of *ortho* and *meta* protons (6.1 ± 0.3 s and 4.5 ± 0.1

respectively) are also comparable to those measured for 150 mM **4-AP** in *protio*-methanol at 1 T in the presence of unactivated catalyst, which are 4.9 ± 0.2 s and 4.9 ± 0.1 s respectively (Table 7.1). Hence it can be confirmed that the T_1 values extracted from model are consistent with expected values.

The observed deviation of the experimental hyperpolarised data from the model for the higher catalyst to substrate ratios can be explained if the assumption in the model of fast exchange and perfectly averaged T_1 values is not fulfilled. It is noteworthy, that despite the *ortho* and *meta* resonances exhibiting averaged T_1 values for the free and bound substrate respectively they provide separate NMR signals at both high and low field. This is due to the fact that a T_1 of 6 s is associated with an R_1 of 0.17 s^{-1} , while the chemical shift difference for *ortho* free and bound resonances is 0.23 ppm (91.5 Hz at 9.4 T) and 0.35 ppm (141.5 Hz at 9.4 T) for the *meta* resonances. This suggests that the chemical exchange is sufficiently rapid to average on the timescale of the T_1 relaxation but not on the timescale of the difference in chemical shift.

Another explanation is based on the variations in the experimental data. Due to the measurement in a *protio*-solvent, the relative concentration of the substrate to catalyst is assumed to be as prepared and cannot be accurately measured with NMR spectroscopy. In order to observe the NMR spectrum of **4-AP** and the catalyst in *protio*-methanol at 400 MHz, solvent-suppression sequence has to be used. However, only one of the methanol peaks can be suppressed and the effect of the remaining large solvent peak on the spectrum baseline and integration is adverse, which has a significant affect on the signals of the low concentration catalyst. Therefore, solvent-suppressed NMR experiments in high field provided non-quantitative results and could not be used to confirm the prepared substrate to catalyst ratios.

Once the $T_{1,\text{free}}$ and $T_{1,\text{bound}}$ values have been obtained it is possible to extract the change in activated catalyst to free substrate relative

concentration with time according to Equation 7.11 by using the hyper T_1 reaction monitoring data from Figure 7.5d. The outlier data point at 173 min was omitted here for convenience; the full data set is presented in Figure A10 in Appendix. The results are presented in Figure 7.12.

$$\frac{[cat]}{[sub]} = \frac{\left(\frac{1}{T_{1,free}} - \frac{1}{T_{1,average}}\right)}{2\left(\frac{1}{T_{1,average}} - \frac{1}{T_{1,bound}}\right)} \quad (7.11)$$

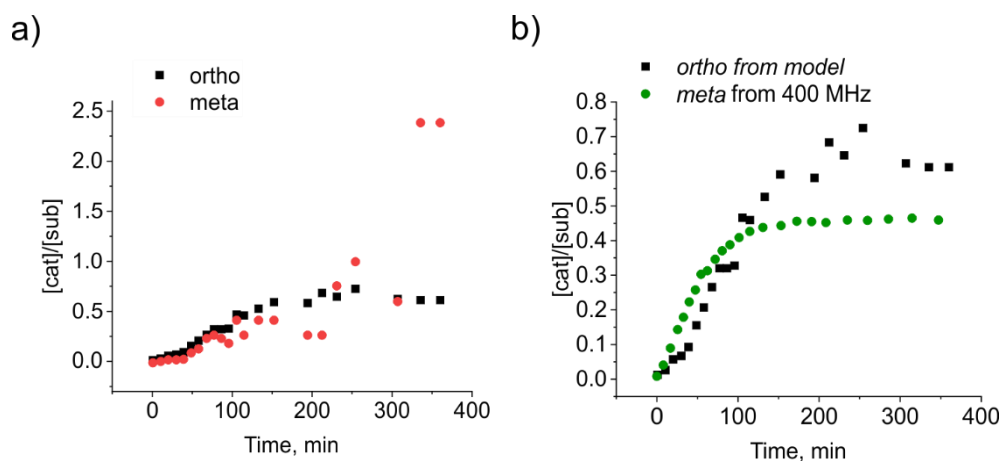


Figure 7.12 (a) The activated catalyst to substrate ratio dependence on reaction time according to the hyper T_1 data recorded at 1 T benchtop NMR spectrometer in *protio*-methanol in conjunction with Equation 7.11 for the *ortho* and *meta* sites (without an outlier data point at 173 min). (b) *Ortho* proton data from (a) alongside the activated catalyst to substrate ratio as determined from the substrate *meta* proton and the catalyst carbene signals for a thermal control measurement recorded at 400 MHz NMR for an analogous sample in methanol- d_4 based on the data in Figure 7.5a.

As predicted, the activated catalyst to substrate ratio increases throughout the reaction until a plateau is obtained (Figure 7.12a). Scatter in the *meta* hyper T_1 values is evident at long reaction times. In Figure 7.12b the *ortho* proton data is compared to the change in catalyst to substrate ratio determined from an analogous sample monitored using standard ^1H NMR at 400 MHz in methanol- d_4 . The comparison shows that both trends occur on a similar timescale and reach a plateau indicating reaction completion. In theory, the value of the activated catalyst to substrate ratio at the plateau should reach 0.5 when the initial concentrations of **4-AP** and the pre-catalyst are 25 mM and 5 mM, respectively, as three substrate molecules bind during the activation process. The standard NMR reference data (green circles in Figure 7.12b) yield a final ratio of 0.46, which deviates from

the theoretical value of 0.5. When calibrating the catalyst peak intensity to the free substrate peak, a 7.5% difference in the final value was observed depending on the chosen reference catalyst peak. This suggests that the largest source of uncertainty in the catalyst to substrate ratios is the calculation of the peak integrals. This is associated with the peak lineshapes, which have baseline components that extend further than normal under the reaction conditions and therefore the peak integrals may be underestimated. This is expected to be more significant when the hyperpolarised spectra are acquired due to the line broadening associated with the SABRE-enhanced NMR peaks caused by the shake and drop hyperpolarisation measurement procedure. The final catalyst to substrate ratio found with the hyperpolarised data (~ 0.6) is higher than that predicted based on the amounts of added reagents. This is suggested to be a combination of difference in actual concentration of reagents, when compared to the sample for the reference data, and uncertainties in the integration of NMR peaks. Nonetheless, the data will be self-consistent, and therefore, the conclusions made are appropriate.

Unlike the calibration data, the experimental hyper T_1 values were measured in the presence of a varying concentration of the intermediate dihydride complex with a bound COD ligand $[\text{Ir}(\text{COD})(\text{IMes})(\mathbf{4}\text{-AP})]\text{Cl}$. This could change the measured T_1 at the early stages of reaction when the concentration of the intermediate complex is high relative to the activated catalyst. This is due to the fact that the rate of ligand exchange is slower in this complex and hence it will make a contribution to relaxation felt by the hyperpolarised bound substrate. This effect is not accounted for in the model proposed by Barskiy *et al.*⁴⁶ Therefore, it is possible that the catalyst activation process influences the averaging of the T_1 values and would need to be accounted for in the calibration.

To conclude, the dependence of the hyper T_1 values for $\mathbf{4}\text{-AP}$ on concentration has been determined on a 1 T benchtop NMR spectrometer in the presence of the activated catalyst in *protio*-methanol. These data fit to the model proposed in the literature, which accounts for exchange

between free and bound substrate species and their individual T_1 values. The fit has an R^2 of 0.973 for the *ortho* proton and 0.948 for the *meta* proton data. $T_{1,\text{free}}$ and $T_{1,\text{bound}}$ values were obtained from the fit. These T_1 values were then used to extract the relative ratio of the catalyst to substrate during the reaction. Employment of a similar control sample for ^1H monitoring at 400 MHz in methanol- d_4 yielded different values over the same time period and suggested the problems with both the model for SABRE process and SABRE NMR peak broadening. Although, leaving the hyperpolarised sample longer in the magnet before detection should help to improve NMR peak lineshape, and therefore, accuracy of integration.

7.3 Conclusions

A method for using SABRE-enhanced ^1H NMR spectroscopy to monitor reactivity at mM level concentrations through the quantification of hyperpolarisation lifetimes was introduced. The developed approach was demonstrated using both high-field (9.4 T, 400 MHz) and benchtop (1 T, 43 MHz) NMR detection. This method was used to monitor the formation of the active SABRE catalyst from a pre-catalyst and hydrogen isotope exchange within the substrates 4-aminopyridine and 4-methylpyridine. Comparable results were obtained at both fields, illustrating the utility of this approach for reaction monitoring on a benchtop NMR spectrometer even under conditions where standard ^1H NMR cannot be used due to low sensitivity and peak overlap. In addition, the use of a low-field benchtop NMR spectrometer for detection allowed for experiments to be carried out in a *protio* solvent. For the reactivity explored herein, this provided a route to separating out the effects of the formation of the SABRE catalyst and the hydrogen isotope exchange reaction, by removing the source of ^2H for the isotope exchange, methanol- d_4 . This approach also confirmed non-significant deuteration in the 4-methylpyridine and its faster kinetics of activation compared to 4-aminopyridine. More generally, the ability to carry out reaction monitoring in a non-deuterated solvent renders this method more attractive for industrial applications, such as PAT, as it removes the need for costly sample preparation step prior to analysis. Additionally, I

performed a quantitative analysis of the data obtained in *protio*-methanol by fitting it to the model for SABRE process proposed by Barskiy *et al.*⁴⁶ The results from the hyper T_1 and standard ^1H NMR monitoring highlighted the benefits of this method and the complications associated with the accuracy of integration.

The experiments presented here were achieved using a manual SABRE hyperpolarisation protocol. In future work, a flow-based SABRE approach, where *p*- H_2 is bubbled through the solution outside of the spectrometer,⁷⁴ could provide a route to automating the reaction monitoring method. *In situ* SABRE measurements, where detection is achieved in mT- μT magnetic fields such as the Earth's magnetic field, could also be used to provide increased control over the reaction conditions throughout the monitoring process. However, in this case there would be a need for significant benchmarking to isolate the source of the hyperpolarised response as no chemical shift information is available in such ultra-low-field NMR spectra. The quantitative aspects of the method can be improved by improving the calibration of the hyperpolarisation lifetimes to link changes in lifetime to changes in the concentration of the active SABRE species; however, the effects of the intermediate complex have to be investigated thoroughly.

Chapter 8: Conclusions and future work

8.1 Conclusions

In this thesis, reactivity using the SABRE-hyperpolarised NMR response at both high (9.4 T, 400 MHz) and low (1 T, 43 MHz) field has been monitored. Specifically, an amide formation reaction, hydrogen isotope exchange (HIE) and the SABRE catalyst formation have been studied. Also an improved understanding of the SABRE hyperpolarisation of individual N-heterocyclic amines and their mixtures, spin-lattice relaxation effects in SABRE systems and ^2H -labelling of SABRE targets have been developed. Below the main outcomes of this work and discuss areas for future development are summarised.

The optimisation of the SABRE hyperpolarisation of 4-aminopyridine (**4-AP**) and N-(4-pyridyl)benzamide (**4-PBA**) was performed. This included assessing the dependence of the SABRE enhancement on concentration and polarisation transfer field in the range of 12.5 – 50 mM. The PTF dependence for the resonances of **4-PBA** were observed to be significantly different to those for **4-AP**. Both the *ortho* and *meta* proton resonances of **4-AP** demonstrated a maximum SABRE enhancement at around 60 G, which is similar to that seen for other N-heterocycles such as pyridine, pyrazinamide and nicotinamide.^{43, 74, 78, 80} In contrast, the enhancements for the *ortho* proton resonance of **4-PBA** showed two local maxima at PTF values of 20 G and 60 G in a broad profile from 10 G to 70 G. Hence, **4-PBA** proved to show reduced sensitivity to PTF effects when compared to most other N-heterocycles. One maximum for the *meta* proton resonance of **4-PBA** at 20 G was observed. A PTF curve similar to the one observed for **4-PBA** has been previously been reported for isoniazid.^{74, 80} The change in sign observed for the *meta* proton enhancements in both compounds can be potentially explained by the competing direct and indirect polarisation transfer from the hydrides to the *meta* proton via the *ortho* proton.⁵⁶

The dependence of the SABRE NMR signal intensity on the **4-PBA** concentration showed the underlying challenge in the quantification of the

substrate using the SABRE signal response. The level of the SABRE signal does not vary linearly with concentration, as would be expected for a standard thermally polarised NMR signal. The maximum signal enhancement (~190-fold) was detected for both free *ortho* and *meta* protons at 7.5 equivalents of the substrate relative to the pre-catalyst **1**, which corresponds to a 37.5 mM substrate concentration. I suggest, this reflects the minimum substrate concentration for the stabilisation of the active SABRE complex with this substrate.

Interesting results were obtained while studying the hyperpolarisation distribution in mixtures of these materials. The analysis gave an insight into the stabilisation of the active SABRE complex, which resulted in a higher SABRE-enhanced NMR signal for N-(4-pyridyl)benzamide (**4-PBA**) in the presence of **4-AP**. It was shown that the PTF plot for each of the compounds in a mixture is similar to the one of the respective compound alone, so it can be concluded that the *J* coupling network did not change greatly with the more complex compound ligation expected for this mixture. SABRE signal amplitudes were for the mixtures of 4-aminopyridine (**4-AP**) and **4-PBA** in ratios of 2.5 : 7.5, 5 : 5 and 7.5 : 2.5 (12.5 : 37.5, 25 : 25 and 37.5 : 12.5 mM) equivalence to the pre-catalyst in the range of PTF = 0.5 - 140 G. Differences in the PTF trends for the two substrates was found to allow for the selective detection of one compound over another. For example, the enhancement of the *ortho* proton of **4-AP** was 66-times higher in enhancement factor than the *meta* proton of **4-PBA** at 55 G in the 5 eq : 5 eq mixture. This is especially beneficial in case of peak overlap when low-field NMR spectroscopy is used for detection. The conditions for the detection of both compounds with a similar level of sensitivity were also found. For example, at 60 G the enhancement factors are similar for the *ortho* proton of **4-PBA** (-229-fold) and the *meta* proton of **4-AP** (-232-fold) in the 5 eq : 5 eq mixture. These experiments provide a route to develop a model for the quantification of the SABRE signal in mixtures of compounds. However more calibration measurements would be required.

The SABRE signal for both **4-AP** and **4-PBA** when measured in mixtures showed a linear trend over the range of concentrations studied. This is a promising but is a preliminary result and requires further investigation to determine the range of substrate to catalyst ratios where this linear behavior is observed. Previously, a linear correlation between SABRE signal and concentration was shown for much lower concentrations $< 1 \mu\text{M}$.^{45, 124} If further measurements prove the linear regime extends to mM concentrations, then this would provide a straight-forward route to the quantification of SABRE signals in mixtures with potential applications for the analysis of reactions with high sensitivity.

Monitoring of an amide formation reaction with SABRE was explored. In order to find the optimal reactants, a range of N-heterocyclic amines with benzoic anhydride or ethyl benzoate in different solvents were screened using HPLC-MS-UV analysis. The conversion of **4-AP** and benzoic anhydride to form **4-PBA** and benzoic acid in dichloromethane-*d*₂ was selected as the model reaction. The formation of **4-PBA** was followed using standard ¹H NMR spectroscopy and SABRE-enhanced NMR signals at 400 MHz (9.4 T). The evolution of the SABRE signal of the starting material and product with the reaction time was observed. The crowded NMR spectra were selectively enhanced by the SABRE technique, which is extremely beneficial for reaction monitoring purposes particularly if low-field NMR is to be used for detection. However, many complications associated with the reaction conditions were encountered. Changes in ¹H NMR chemical shift were observed for **4-PBA** and **4-AP** in the presence of benzoic acid, indicating the formation of their pyridinium carboxylate salts. This leads to weaker substrate binding, meaning reduced SABRE hyperpolarisation efficiency and precipitation of the product, **4-PBA**. These effects add to the fundamental challenge of SABRE signal quantification with respect to substrate concentrations.

Due to the complications in the interpretation of the dependence of the SABRE signal intensity on reactivity, the thesis next focuses on hyperpolarized signal lifetimes as a potential probe of reactivity. The

investigation started with an assessment of the dependence of the thermal magnetization lifetime, specifically the spin-lattice relaxation time constant (T_1), on the SABRE reaction conditions. The presence of paramagnetic species, such as oxygen, were shown to decrease the T_1 values by a factor of two in the case of **4-PBA**. The effects of the unactivated $[\text{Ir}(\text{COD})(\text{IMes})(\text{substrate})]\text{Cl}$ (2) and activated $[\text{Ir}(\text{H})_2(\text{IMes})(\text{substrate})_3]\text{Cl}$ (4) SABRE catalysts on the T_1 were assessed. The unactivated catalyst effects were not studied in the literature before to such extent. A slight impact on the T_1 value was shown for **4-AP** in presence of the unactivated SABRE catalyst when compared to the results for pure **4-AP** in methanol- d_4 over a substrate concentration range of 1.5 – 465 mM. The results for the activated catalyst were found to be consistent with the literature data and confirm that activation has a major effect on the substrate T_1 values, which are a weighted average of the T_1 value of the substrate bound to the catalyst and its counterpart in the free solution. This is caused by the relatively fast exchange of the substrate ligand when bound to the catalyst. This fast exchange was confirmed using exchange spectroscopy (EXSY).

One of the significant outcomes in this thesis was the development of a variable flip angle single-shot method for hyperpolarised T_1 measurement. Compared to the robust thermal methods, such as inversion and saturation recovery, this method obtains the T_1 value in a matter of 5 times the T_1 period, which is about a few minutes for small organic molecules. Moreover, consistent results with higher SNR are found using this method when compared to the constant flip angle sequence proposed in the literature. This allows changes in hyperpolarisation lifetimes in the reacting systems to be measured when the reaction timescale is much longer than $5 \cdot T_1$.

The single-shot method was employed in screening a variety of N-heterocyclic amines, where enhancement factors and SABRE lifetimes were measured as a function of their chemical structure. This study showed that in general protons with longer hyper T_1 values typically resulted in higher levels of SABRE hyperpolarisation. However, hyperpolarisation transfer is

more efficient when J coupling to the hydride ligands originating from p -H₂ is stronger. Thus, the fast relaxing *ortho* protons obtain high levels of enhancement in NMR signal (from -124 to -774 -fold) due to their closer proximity to the hydride ligands. In contrast, for 4-(aminomethyl)pyridine, which binds through both aromatic and amino group nitrogens, *ortho* protons gained relatively high hyper T_1 of 9.7 s and enhancement of (-427 ± 7) -fold. An increase in the hyper T_1 value was shown for the protons adjacent to the deuterium substituted positions due to the reduced magnetic moment of deuterium nucleus, which reduces the efficiency of dipole-dipole relaxation. For example, the *meta* protons of 4,6-nicotinamide- d_2 has a hyper T_1 of 18.2 ± 0.2 s. Similarly, the proton isolated with the deuterated amino groups in d_4 -3,5-diaminopyridine has a hyperpolarisation lifetime of 13.7 ± 0.3 s. In addition, the substrates containing substituents in the *para* position that are able to donate electron density *via* mesomeric effects were observed to reduce the SABRE enhancement factor. This effect could be due to the reduced substrate dissociation rate from the SABRE catalyst once electron density on the binding aromatic nitrogen is increased. Thus, the single-shot T_1 measurement method allows for an assessment of the target compound's likely performance with SABRE. In addition, this method was employed to detect hydrogen isotope exchange (HIE) in **4-PBA** in the presence of the associated SABRE catalyst in methanol- d_4 .

The HIE process in SABRE systems has been reported previously in the literature; however, it has not been investigated mechanistically. Here, this phenomenon was studied using thermal and hyperpolarised ¹H and ¹³C NMR spectroscopy. Evidence for HIE in four SABRE systems was shown. The formation of a deuterated SABRE complex was observed in all of the samples that contained **4-AP**, **4-MP**, **4-PBA** and pyridine, thereby indicating a contribution from the iridium catalyst in the H/D exchange process. Due to the instability of the active SABRE complex $[\text{Ir}(\text{H})_2(\text{IMes})(\text{substrate})_3]\text{Cl}$ (**4**), H/D-labelling of the substrate was followed during pre-catalyst $[\text{Ir}(\text{Cl})(\text{COD})(\text{IMes})]$ activation under hydrogen. The potential contribution of $[\text{Ir}(\text{COD})(\text{IMes})(\text{substrate})]\text{Cl}$ (**2**) and $[\text{Ir}(\text{H})_2(\text{COD})(\text{IMes})(\text{substrate})]\text{Cl}$

(3), which are present during active SABRE catalyst formation was studied. The former complex was shown not to be active for the HIE reaction. Slow substrate exchange in the intermediate complex **3** was seen with EXSY, lineshape analysis and hyperpolarised ^1H NMR spectra. Together these results suggest a very low probability that **3** contributes significantly to the HIE reaction. The catalyst responsible for the HIE reaction was deduced to be the activated SABRE complex, **4**. In case of **4-AP**, the deuteration of the substrate proceeded on the same timescale as the relatively slow activation reaction, in contrast to the **4-MP**, **4-PBA** and pyridine, which activate the SABRE complex first on a faster timescale, and then continue to undergo H/D exchange.

The competing processes of H/D exchange in the catalyst, substrate, methanol- d_4 and hydrogen gas were observed in the SABRE systems. The time-dependence of the relative proportions of the catalyst, hydrogen gas and substrate isotopologues were evaluated using standard ^1H NMR spectroscopy. The return of the proton into the catalyst was observed for **4-MP** and **4-PBA** at the expense of the substrate deuteration on longer timescales. It was suggested that there is one type of kinetics happening during the activation, and after activation is complete the system re-equilibrates. Simulations of the ^1H NMR spectra for the unlabeled, mono- and double-labelled substrates were employed to evaluate changes in the protonated and deuterated forms of pyridine, **4-AP** and **4-PBA** with time during the HIE reaction. The results confirmed that substrate dissociation from the catalyst occurred prior to the introduction of the second label. Full consumption of the protonated substrate occurred in the case of pyridine and **4-PBA**, while equilibrium amounts of the protonated form was seen in the case of **4-AP** in the final solution. In the case of **4-PBA**, full conversion to the mono-labelled form occurred prior to the insertion of the second label. I believe that these results will be interesting for the applications of SABRE for analytical purposes in the biopharmaceutical field, where ^2H -labeling is used.

Several advancements in reaction monitoring using benchtop NMR spectroscopy were achieved in this thesis. Due to the insensitivity of the low field NMR instrument, standard ^1H NMR monitoring is not possible at mM levels of concentration. Here it was demonstrated that SABRE hyperpolarisation combined with low-field NMR can be used to follow the catalyst activation and H/D exchange in the substrate. Both SABRE intensity and hyperpolarisation lifetimes were used to probe these reactions. The SABRE signal increased with both catalyst formation and substrate deuteration. Quantification with SABRE signal intensity proved challenging. Thus, the hyper T_1 values were measured with the reaction time instead. The resultant trends for the *ortho* and *meta* proton resonances of **4-AP** allowed me to distinguish these two reactions. Both *ortho* and *meta* SABRE lifetimes decreased with an increase in catalyst formation due to the averaging between bound and free substrate T_1 values. In addition, the values for *meta* proton increased with the deuterium incorporation into *ortho* positions. Absence of the HIE effect in the experiment conducted in *protio*-methanol further confirmed these observations. The results obtained using benchtop NMR spectroscopy were in a good agreement with the data acquired using a high-field NMR instrument. Calibration data for hyper T_1 was collected for **4-AP** in the presence of the activated SABRE catalyst in *protio*-methanol on the 43 MHz NMR spectrometer to validate this process. An analytical model of the SABRE process proposed in the literature was applied to fit this data. The model fitted the calibration data well and the extracted T_1 parameters were in general agreement with other experimental values. However, the reaction monitoring hyper T_1 data was less consistent with the reference data from the high-field standard ^1H NMR spectra. This reflects the challenge in obtaining an accurate **4-AP** original concentration in *protio* methanol and challenges the assumption that it was the same in both datasets. Nonetheless, the data showed predicted trends and it is expected that quantitative analysis is possible.

In summary, this method possesses great potential in industrial applications due to the low-cost instrumentation, the ability to use *protio*

solvents and the analysis of mM concentration samples. The obtained results contribute to the fundamental knowledge of the SABRE hyperpolarisation technique and inorganic chemistry. Challenges associated with the quantification of the hyperpolarised SABRE response were partly overcome in this thesis; however, further investigations are required. Provided a sufficiently slow timescale of reactivity relative to the hyper T_1 measurement, the applications of the developed method are limited by a required difference in $T_{1,\text{free}}$ and $T_{1,\text{bound}}$. At higher substrate concentrations and with smaller difference between associated T_1 values, the decay in the average T_1 will be less significant. On the other hand, in such systems, the HIE contribution to the T_1 change may be easily distinguished from the change with the catalyst activation.

8.2 Future work

Regarding future work, the resolution of several challenges that were found in this thesis could be investigated further. For example, the pH change during reaction monitoring could be accounted for by investigating the SABRE NMR signal under different pH conditions. Some studies have already been reported of the SABRE response at a range of pH values in the absence of reactivity.¹²² Indeed, the SABRE signal can be employed as a probe for pH changes in the system and to extract useful information about the undergoing processes, where both chemical shift changes and the SABRE signal intensity will be indicative of these changes.

Other reactions, like the racemization of the amines¹⁹⁴, imine formation or imine metathesis¹⁹⁵, and hydrolysis reactions can be investigated to overcome the precipitation problem. Although many preliminary studies would be required to assess the viability of monitoring these reactions with SABRE-enhanced NMR signals. These would include characterisation of the species that exhibit a hyperpolarised response in the presence of the SABRE catalyst, optimisation of the kinetics and the evaluation of any mechanism changes caused by the SABRE complex.

The complexity associated with the quantification of the SABRE NMR response could be overcome by the employment of the approach of Tessari *et al.* that shows linear SABRE signal response when a first-order regime kinetics is achieved through the use of a co-substrate.^{45, 124} For example, the reaction could be conducted in acetonitrile- d_3 that would act as a co-ligand and potentially provide a linear SABRE response with respect to the concentration of the substrate. In this case, an investigation into the optimisation of the SABRE signal intensity in acetonitrile- d_3 would be required. Alternatively, another co-ligand can be used. It is important that the chosen co-ligand is not involved in the reaction and acts exclusively to stabilise the SABRE complex. On the other hand, an easier way to apply SABRE hyperpolarisation to the reaction monitoring is by employing the newly discovered SABRE-Relay method.¹¹⁸ In this case, the target ligand does not bind to the metal-complex for hyperpolarisation but obtains hyperpolarisation transfer via a proton exchange with a polarisation carrier molecule, typically an amine.¹¹⁸ The advantages of using this method are, firstly, a wider range of reactants can be used and, secondly, the complex may be inert to the mechanism and kinetics of the reaction. In addition, the SABRE-Relay mechanism is expected to be inactive in the HIE reaction within the substrate.

For future studies, removing the competing catalyst activation reaction and observing the HIE individually is suggested. This can be achieved by activating the catalyst in a solvent that does not act as a source of deuterium, for example dichloromethane- d_2 or *protio*-methanol with high-field or low-field NMR spectroscopy respectively. Then the catalyst can then be transferred into methanol- d_4 and substrate deuteration can be observed under D_2 to ensure that any catalyst protonation can only be from the substrate using standard high-field NMR. The same can be repeated with $p\text{-H}_2$ instead of D_2 with hyperpolarised benchtop NMR spectroscopy; however, this introduces the possibility of the hydrogen gas protonating the substrate.

The reaction monitoring approach discussed here can be automated using the flow system for hyperpolarisation that was described in Chapter 3 in this thesis for SABRE signal detection of the individual compounds and their mixtures. In the case of high-field and benchtop 1 T NMR spectrometers, the sample is hyperpolarised outside the magnet and transferred in the magnet for detection. This approach can be extended to even lower field NMR spectrometers based on polarising coils.⁸⁵ Thus, the hyperpolarisation process can be performed *in situ* when a magnetic field of tens of Gauss is applied, then the field is switched off and detection happens in the Earth's magnetic field. Due to the insensitivity of the detection in the Earth's field NMR spectrometer, the developed hyper T_1 method is beneficial because it uses higher pulse angles and so provides higher SNR. In addition, changes in the hyper T_1 of all of the hyperpolarised protons can be tracked in the absence of chemical shift resolution, which is consistent with the use of this instrument. Rigorous instrumentation development and calibration is required in order to apply accurate variable flip angle pulses to Earth's field NMR spectroscopy.

The developed method measures SABRE lifetimes and can assist in developing a better fundamental understanding of the SABRE mechanism. For example, the quantification studies proposed by Tessari and co-workers assume similar relaxation effects for the substrate exchanging with the mixture of complexes, which can be readily tested using hyper T_1 measurements.¹²⁴ In addition, the SABRE analytical model developed by Barskiy *et al.* is based on an assumption of fast substrate exchange on the SABRE catalyst.⁴⁶ The knowledge of the weighted average T_1 values can provide information about the kinetic rates of the exchange in the slow regime. In such cases the kinetic equations, provided in the model, would encode the scaling factor which would indicate to what extent the exchange affects the resultant T_1 values. Experimentally, the change in the free substrate T_1 can be correlated with the rates of dissociation at variable temperatures to assess the contribution of the exchange to the average T_1 in the SABRE system.

One further aspect is the solvent cage, which in this case would be encoded through differential relaxation in the bulk solution and around the catalyst. Evidence was shown for Fe(II) and Co(III) complexes that the dissociative process involved a solvent-caged species.^{196, 197} In contrast, the H/D exchange in the reacting amine ligands of Ir (III) complex suggested the absence of the solvent cage effect.¹⁹⁴ Our preliminary studies showed that at high **4-AP** concentrations the hyper T_1 values are reduced and do not reach the free substrate T_1 . This might suggest that only substrate molecules closest to the catalyst become hyperpolarised while the other ones are restricted by diffusion and exchange rates, and thus, do not contribute to the weighted hyper T_1 . Alternatively this effect could be due to the change in the solution viscosity at the higher concentrations. This effect can be also probed with the SABRE signal lifetime and SNR, which would both reach a plateau if the limiting concentration is achieved.

In conclusion, the data and methods presented in this thesis add substantially to knowledge over a range of topics. Based on the results reported here, a first-author paper has been published and one publication is in preparation. Manuscript is attached in Accompanying material.

Chapter 9: Experimental

9.1 Sample preparation

NMR samples were prepared by mixing 5 mM of the catalyst, [Ir(Cl)(COD)(IMes)] (pre-catalyst **1**, COD = *cis,cis*-1,5-cyclooctadiene, IMes = 1,3-bis(2,4,6-trimethyl-phenyl)imidazole-2-ylidene) in 0.6 mL of a specified solvent (typically methanol- d_4). [Ir(Cl)(COD)(IMes)] was synthesised by Dr. Victoria Annis according to literature procedure.^{40, 198} Once dissolved various molar equivalents of the selected substrate were added to form the final solution, which was subsequently transferred into a 5 mm NMR tube fitted with a Young's tap (GPE scientific). The samples containing nicotinamide- d_2 were prepared with the partially deuterated form of pre-catalyst **1**, Ir(IMes- d_{22})(COD)Cl (IMes- d_{22} catalyst). The samples were degassed using a three-stage freeze-pump-thaw method using a bath of dry ice and acetone in case of methanol- d_4 and a bath of liquid nitrogen in case of dichloromethane- d_2 . The pre-catalyst and 4,6-nicotinamide- d_2 were synthesized in-house and the substrates were purchased from Alfa Aesar (3-aminopyridine), Sigma Aldrich (pyridine, 4-aminopyridine, 2-aminopyridine, 3-amino-4-methylpyridine, 3-amino-5-methylpyridine, 4-(aminomethyl)pyridine), Fluorochem (4-amino-3-methylpyridine, 3,5-diaminopyridine), Maybridge Fisher Scientific (N-(4-pyridyl)benzamide), Avocado Research Chemicals Ltd (4-methylpyridine) and used without further modification. NMR characterisation data for complexes **2**, **3** and **4** with **4-AP**, complexes **2** and **4** with **4-PBA** and complex **2** with pyridine are available in the section 9.12. NMR characterisation data for the complex [Ir(H)₂(IMes)(pyridine)₃]Cl is available in the literature.¹²¹

9.2 NMR data acquisition

All NMR spectra were acquired either on a Bruker AVIII 400 MHz system (9.4 T), a Bruker AVIII 500 MHz system (11.7 T) or a Magritek Spinsolve Carbon 43 MHz benchtop NMR spectrometer (1 T). The benchtop NMR spectrometer operates at 301.5 K while most of the experiments performed using high-field spectrometers were done at 298 K unless

otherwise stated. Although the SABRE hyperpolarisation and T_1 relaxation of small molecules is dependent on temperature, larger temperature differences are required for a significant effect to be observed.¹⁶²

9.3 Measurement of hyperpolarised signals

SABRE hyperpolarisation transfer experiments were performed using *para*-hydrogen that was produced by cooling H_2 gas over a paramagnetic catalyst predominantly containing Fe_2O_3 at an interconversion temperature of 28 K to produce $\sim 99\%$ *para*-enrichment. The *para*-hydrogen was added at a pressure of 4 bar (absolute) to the headspace of the NMR tube containing the sample prepared as described above. After the *para*-enriched H_2 was added, the sample was shaken for 5 s in order to dissolve the *p*- H_2 into solution. A polarisation transfer field (PTF) is required to satisfy the resonance conditions to allow SABRE hyperpolarisation to build-up. The magnetic field was created using either the stray field of the 400 MHz NMR spectrometer determined using a Gaussmeter (GM08, Hirst Magnetic Instruments Ltd, $\pm 0.5\%$ reproducibility), or a hand-held magnet array based on a permanent magnet Hallbach design, which generates a magnetic field of 6.1 ± 0.3 mT (61 ± 3 G), reported in the literature.⁴³ Immediately following shaking, the sample was transferred manually into the spectrometer for a single-shot NMR measurement using either a single 90° radio frequency (*RF*) pulse followed by acquisition of the free induction decay (FID) or a single-shot T_1 sequence (details below in section 9.8 and in Chapter 5).

Normally between each hyperpolarisation measurement, the headspace of the NMR tube was placed under a residual vacuum to allow evacuation of the used H_2 and subsequently refreshed once with *p*- H_2 . For the reaction monitoring the *p*- H_2 refreshment was done twice without emptying the headspace, via the diffusion between the NMR tube headspace and the line filled with fresh *p*- H_2 for 10 s. This way of refreshing *p*- H_2 was employed in order to reduce the solvent evaporation and, therefore, limit any possible changes in the reaction kinetics.

Prior to SABRE measurements, the samples were activated with *para*-hydrogen by repeating the manual shaking procedure described above. The catalyst was considered activated once the characteristic signals of the intermediate complex, $[\text{Ir}(\text{H})_2(\text{COD})(\text{IMes})(\text{substrate})]\text{Cl}$, with hydride peaks around -12 ppm and -17 ppm disappeared and a peak for the activated complex, $[\text{Ir}(\text{H})_2(\text{IMes})(\text{substrate})_3]\text{Cl}$, between -20 ppm to -30 ppm appeared in the SABRE-enhanced ^1H NMR spectrum.

9.4 Calculation of enhancement factors and polarisation levels

To determine SABRE enhancement factors and polarisation levels, a thermally-polarised reference spectrum was detected with the same acquisition parameters and with the same NMR spectrometer as the corresponding SABRE-enhanced measurement. The only salient difference is that for the thermal NMR spectrum a recycle delay of $5 * T_1$ was included prior to each experiment. Enhancement factors were calculated by taking a ratio of the hyperpolarised signal integral and the thermal signal (Equation 9.1). In order to assess the polarisation level obtained with SABRE, the Boltzmann-derived polarisation is multiplied by the enhancement factor (Equation 9.2). The Boltzmann-derived polarisation ($P_{thermal}$) at 9.4 T is 0.0032% and at 1 T is 0.00035%.

$$\varepsilon = \frac{I_{SABRE}}{I_{thermal}} \quad (9.1)$$

$$P_{SABRE} = \varepsilon * P_{thermal} \quad (9.2)$$

In cases of thermal reference peak overlap, another peak of the same compound was used for the reference integral. This is appropriate as long as the relaxation delay is sufficient, i.e. $5 * T_1$ for both resonances and the relative number of protons is accounted for.

9.5 Automated flow system for hyperpolarisation (Chapter 3)

The majority of SABRE experiments used the manual shaking approach, which produces significant polarisation levels but can be prone to reproducibility errors and typically is dependent on the user. One method

to circumvent this issue is to employ an automated flow system, a device that allows the hyperpolarisation of chemicals via SABRE outside the NMR spectrometer and subsequent automatic transfer of the reaction mixture into the detection field as detailed in Figure 9.1.⁷⁴ The apparatus contains an electrolytic cell which converts water into hydrogen gas [1] before conversion to *p*-H₂, using a commercial *p*-H₂ generator (Bruker) [2], which operates in much the same manner as the rig previously described but instead operates with an interconversion temperature of 38 K (~92 %, theoretically). A reaction chamber that is surrounded by a copper solenoid to provide the necessary PTF [3] is used to facilitate the mixing of *p*-H₂ and the substrate in the presence of the catalyst. A flow probe is located inside the spectrometer [4] for measurement, which is designed to allow pneumatic transfer of the sample from the reaction chamber to the NMR probe using N₂ gas prior to acquisition. The N₂ pressures and timings were optimised in such way that the sample transfer was reproducibly transferred into the active region of the NMR detection coil without forming bubbles. The total sample transfer time was typically ~ 1 - 2 s. The flow system controls the transfer of polarisation between *p*-H₂ and the substrate by changing the polarisation transfer field (PTF) and the polarisation transfer time (PTT). A specified current in the coil [3] that surrounds the reaction chamber generates a magnetic field in the range from -150 G to 150 G. The time over which the sample is exposed to *para*-hydrogen (PTT) can also be precisely set. Overall this system allows for complete control of the SABRE experiment, removing the user dependent aspect and allowing for both pseudo and 2D NMR experiments to be acquired with high reproducibility.

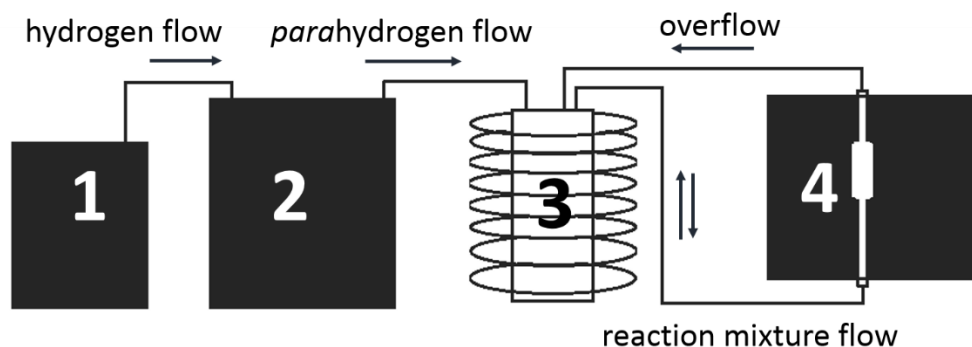


Figure 9.1 1 – Hydrogen generator; 2 – Bruker *para*-hydrogen generator; 3 – reaction chamber and the coil used to generate the polarisation transfer field; 4 – flow cell for sample monitoring inside the NMR spectrometer.

In order to perform the SABRE hyperpolarised NMR signal measurement using the flow system, the sample was prepared by mixing 5 mM of the catalyst, $[\text{Ir}(\text{Cl})(\text{COD})(\text{IMes})]$ (pre-catalyst 1, COD = *cis,cis*-1,5-cyclooctadiene, IMes = 1,3-bis(2,4,6-trimethyl-phenyl)imidazole-2-ylidene) in 3 mL of methanol- d_4 in a sample vial. Once dissolved various molar equivalents of the selected substrate(s) were added to form the final solution. After the sample was injected into the reaction chamber [3], the procedure to acquire SABRE-enhanced NMR spectra was followed. This includes 1) bubbling of *para*-hydrogen through the solution for 20 s (PTT) at the desired PTF, 2) waiting a delay time of 3 s for the separation of gaseous components from the sample by releasing the pressure in the reaction chamber; 3) transfer of the sample to the NMR spectrometer, 4) spectral acquisition following a 90 degree excitation pulse and 5) transfer of the sample back to the reaction chamber.

Prior to quantitative SABRE measurements using the flow system, the SABRE catalyst activation was done by performing repeat bubbling-transfer-acquire experiments as described above. Similar to the manual hyperpolarisation procedure (section 9.3), the catalyst was considered activated once the characteristic signals of the intermediate complex, $[\text{Ir}(\text{H})_2(\text{COD})(\text{IMes})(\text{substrate})]\text{Cl}$, with hydride peaks around -12 ppm and -17 ppm disappeared and a peak for the activated complex,

$[\text{Ir}(\text{H})_2(\text{IMes})(\text{substrate})_3]\text{Cl}$, between -20 ppm to -30 ppm appeared in the SABRE-enhanced NMR spectrum.

As reported in the literature, reproducibility of the SABRE ^1H NMR signal integral measured using the flow system is less than 6% standard deviation over 30 repeats polarisation measurements.⁴²

9.5.1.1 Reproducibility study using flow system in a mixture

Reproducibility of the enhancement factor was assessed for a standard activated sample of 5 eq : 5 eq **4-AP** and **4-PBA** (50 mM total concentration relative to the 5 mM pre-catalyst **1** in 3 mL methanol- d_4) over 11 repeat measurements. A thermal reference ^1H NMR spectrum was acquired after each respective SABRE-enhanced spectrum. This reference spectrum was used to compute the SABRE ^1H NMR signal enhancement values in order to reduce the contribution of solvent evaporation to the error in the measurements. The results are discussed in Chapter 3, section 3.5.1.

9.5.1.2 PTF for individual compounds and mixtures

The measurement of the PTF plots at different concentrations of **4-AP** and **4-PBA** were performed for the activated samples varying the polarisation transfer field (PTF) from 0.5 G (Earth's field with solenoid switched off) to 140 G while all the pressure parameters for the sample transfer and $p\text{-H}_2$ bubbling time were kept constant. The concentrations of **4-AP** and **4-PBA** mixtures were 10 eq : 0 eq; 7.5 eq : 2.5 eq; 5 eq : 5 eq; 2.5 eq : 7.5 eq; 0 eq : 10 eq (50 mM total concentration relative to the 5 mM pre-catalyst **1** in 3 mL methanol- d_4) which corresponds to 50 mM : 0 mM, 37.5 mM : 12.5 mM; 25 mM : 25 mM; 12.5 mM : 37.5 mM; 0 eq : 50 mM. The SABRE spectrum measurement at each PTF was carried out once for all mixtures, except for 5 eq : 5 eq mixture, where measurement at each PTF was performed twice and the average enhancement factor was then calculated. A thermal ^1H NMR spectrum was acquired before and after the series of SABRE spectra to verify that no significant changes occurred in the sample during the experiment.

9.6 Screening for the model reaction in the flask (Chapter 4)

A 250 mL round bottomed flask (RBF) flask was loaded with 0.25 mmol, 0.46 mmol or 0.5 mmol substrate (4-aminomethylpyridine, 4-amino-3-methylpyridine, 4-aminopyridine (**4-AP**), 3,5-aminopyridine or 3-amino-5-methylpyridine) and benzoic anhydride (**BAH**) (0.25 mmol or 0.5 mmol) or ethyl benzoate (0.5 mmol) in 5 mL solvent (methanol, dichloromethane or acetonitrile). Reaction monitoring was performed at room temperature, except for ethyl benzoate, which was done at 40 °C. The samples from the reaction flask were tested using the HPLC-MS-UV instrument at different time points.

9.6.1 HPLC-MS-UV instrument

Thermo Scientific UltiMate 3000 UHPLC instrument with diode array detector for UV-detection and mass spectrometry detection was used. The samples were taken from the reaction flask or the NMR tube with the Pasteur pipette and diluted with methanol. Then the sample was tested using HPLC, where mass-spectra and UV-spectra (at 254 nm) of the fractions were acquired.

9.7 Reaction monitoring of amide formation with standard and SABRE-enhanced ¹H NMR (Chapter 4)

9.7.1 Reaction monitoring in the absence of the SABRE catalyst

First, dissolution of benzoic anhydride (**BAH**) was checked in a separate ¹H NMR pseudo 2D experiment which includes separate ¹H 1D NMR spectra acquired at specific time points. The pre-weighted 6.84 mg of **BAH** (~1 eq relatively to the 50 mM 4-aminopyridine (**4-AP**) in the reaction conditions) was added to the 0.6 mL of DCM-*d*₂ in the NMR tube. Dissolution was confirmed to be fast and complete in the first 13 s.

For the reaction monitoring 67.88 mg of **BAH** was dissolved in 1 mL of DCM-*d*₂. 0.1 mL of this solution was added to the 0.5 mL of 60 mM **4-AP** solution in DCM-*d*₂. The delay between the addition of **BAH** and the acquisition of the first ¹H spectrum was 8 min 42 s because shimming was

performed after addition of **BAH**. The ^1H spectra were acquired every 66 seconds the next 2 hours using the 400 MHz NMR spectrometer preheated to 301.5 K for detection.

Data processing was performed in Bruker Dynamics Center 2.5.5 software by fitting the integrals from the ^1H NMR spectra to first-order kinetics. The first 14 spectra (≈ 14 min) were excluded due to the induction period of the reaction.

The decay of the starting material and build-up of the product were fitted to Equations 9.3 and 9.4, respectively.

$$I(t) = I_0 \exp(-kt) \quad (9.3)$$

$$I(t) = I_0 [1 - \exp(-kt)] + C \quad (9.4)$$

9.7.2 Reaction monitoring in SABRE conditions

4-aminopyridine (**4-AP**) (30.8 μmol , 10.6 eq relative to pre-catalyst **1**, 55 mM) was activated in the presence of 5.2 mM $[\text{Ir}(\text{Cl})(\text{COD})(\text{IMes})]$ in 0.563 mL $\text{DCM-}d_2$ in a 5 mm NMR tube equipped with Young's tap. Benzoic anhydride (**BAH**) (30.4 μmol , 10.5 eq relative to the pre-catalyst, 54 mM) was added to the activated complex and fresh $p\text{-H}_2$ was added and ^1H NMR spectra acquisition started in 2 min 38 s. Hyperpolarised and thermal ^1H spectra were acquired in parallel every 2-3 minutes using a 400 MHz NMR spectrometer for 120 min. Fresh $p\text{-H}_2$ was added to the NMR tube before each hyperpolarised measurement.

9.8 Hyperpolarised single-shot T_1 measurement (Chapter 5)

The single-shot hyperpolarised T_1 measurements were achieved by acquiring a series of 15 ^1H NMR spectra, where the excitation pulse for each acquisition was achieved using RF pulses of increasing flip angle (see section 5.4.3 in Chapter 5 for more details). To remove the influence of thermally-polarised background ^1H NMR signals from the T_1 analysis, a reference scan was acquired after each hyperpolarised T_1 measurement. This was achieved by holding the sample outside of the NMR spectrometer

for 1-1.5 minutes to ensure full relaxation of all polarisation and then manually inserting the sample into the NMR spectrometer and carrying out a single-shot T_1 experiment. The resultant thermally-polarised NMR spectra were integrated and subtracted from the hyperpolarised signals prior to T_1 analysis. Hyperpolarised relaxation times (T_1) were determined from an exponential fit of the corrected hyperpolarised signal decay according to Equation 9.5.

$$M = M_0 e^{(-t/T_1)} + M_{offset} \quad (9.5)$$

The standard error for 5 repeated variable flip angle single-shot T_1 measurements was less than 3% for the samples of 25 mM **4-AP** in MeOH in the presence of the 1 mM, 2 mM, 3 mM and 4 mM activated SABRE catalyst and less than 6% for the samples of 25 mM **4-AP** in MeOH in the presence of the 0.5 mM and 5 mM activated SABRE catalyst measured on the 1 T benchtop NMR spectrometer. In addition, the standard error of a related substrate, 3,5-diaminopyridine (25 mM), which does not undergo deuteration on the timescale of the SABRE catalyst activation, constituted less than 3% as estimated from 9 repeated measurements. Throughout the thesis the error bars for the hyper T_1 values represent reproducibility errors calculated from 3 repeated measurements unless otherwise stated.

When the rate of relaxation was derived from the measured hyper T_1 value, errors of average and free relaxation rates, $\Delta R_{1,average}$, were calculated from the standard errors of the relaxation times simply by taking the same percentage error of the rate as of the time constant (Equation 9.6).

$$\Delta R_1 = \frac{\Delta T_1}{T_1} R_1 \quad (9.6)$$

9.9 SABRE catalyst activation and HIE monitoring using standard ^1H NMR (Chapter 6)

Solutions containing the pre-catalyst **1** (5 mM) with either pyridine, **4-AP**, **4-MP** or **4-PBA** (25 mM) in methanol- d_4 form the unactivated catalyst $[\text{Ir}(\text{COD})(\text{IMes})(\text{substrate})]\text{Cl}$. 0.6 mL of this initial solution was added to a

5 mm NMR tube equipped with a Young's tap and degassed following the sample preparation procedure described above. In order to monitor the formation of the active complex $[\text{Ir}(\text{H})_2(\text{IMes})(\text{substrate})_3]\text{Cl}$ (substrate = pyridine, **4-AP**, **4-PBA** or **4-MP**), H_2 (4 bar absolute) was added to the headspace of the NMR tube. The sample was shaken vigorously for 5 s and inserted into the NMR spectrometer (Bruker AVIII 400 MHz) at 298 K. A series of ^1H spectra were acquired over a period of 15.5 hours. The time between H_2 addition and the first scan was monitored using a digital timer. The data was then Fourier transformed, phased and integrated in the exactly the same way for all spectra in the dataset.

9.9.1 Quantification of the level of deuterium incorporation

The deuteration percentage was calculated using Equation 9.7, where S_{ortho} and S_{meta} are the integrated signal intensities for the *ortho* and *meta* resonances of the free substrate, respectively.

$$D (\%) = 100 * (1 - \frac{S_{ortho}}{S_{meta}}) \quad (9.7)$$

In case of **4-PBA**, the *meta* resonance (7.86 ppm, 2H) overlaps with *ortho* (benzyl ring) resonance of the substrate bound trans to carbene in the activated catalyst (**4b**) which increases in intensity with the reaction time. Thus to account for it, the integrals of the *meta* resonance of **4-PBA** were reduced by half of the intensities of the **4b** carbene peak (6.74 ppm, s, 4H, CH^{mes}) which was able to integrate.

9.10 NMR Exchange Spectroscopy (EXSY)

The selective exchange spectroscopy (EXSY) measurement is based on the 1D Nuclear Overhauser Effect (NOE) experiment. It was performed to estimate the rate of chemical exchange between the species. The Bruker standard sequence "selnogp" has been employed to observe the magnetisation of the exchanging species.¹⁹⁹⁻²⁰¹ This sequence selectively excites only the target spin magnetisation in the transverse plane using a single pulsed-field-gradient echo that consists of a central 180 degree pulse in between of two gradients (**A** in Figure 9.2). All other spins are left

dephased and unobservable. The subsequent 90 degree pulse transfers the target magnetisation onto the $-z$ -axis, after which there is a mixing time delay (t_{mix}) during which chemical exchange can occur. The excited magnetisation is refocused with standard gradient echo pulse sequence (**B** in Figure 9.2) to account for dephasing during the mixing stage. The excited and exchanged resonances are detected using a 90 degree pulse. The recorded spectrum contains only the target resonance that has been selectively excited and the resonances that have undergone chemical exchange with the excited resonance.²⁰²

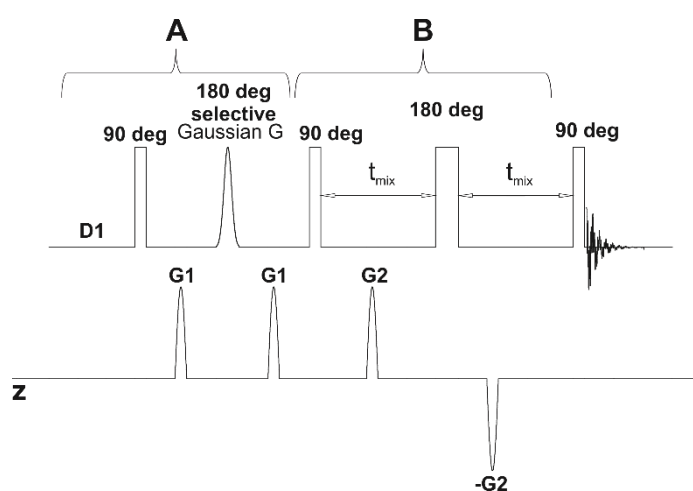


Figure 9.2 1D selective NOESY gradient pulse sequence for EXSY experiment.

An increase in intensity of a non-excited resonance indicates exchange. To determine the exchange rate, the mixing time (t_{mix}) is increased and changes in the excited resonance and the exchanged resonance intensities are detected.

In order to model the exchange between substrate species in free solution and bound to the catalyst, the scheme presented in Figure 9.3 was employed. The concentration of the species A-E, X and Y in this process can be expressed by the kinetic equations 9.8 – 9.14, where the concentration of species after time Δt is $[]_{t+\Delta t}$, the previous concentration of each species is $[]_t$, and k_d and k_a are the dissociation and association rates, which are assumed to be the same for the exchange in the complexes A-E. The concentration of species A and Y at $t = 0$ were set to the starting

concentrations of the catalyst and free substrate in the activated solution, while the starting concentrations of all other species were set equal to zero.

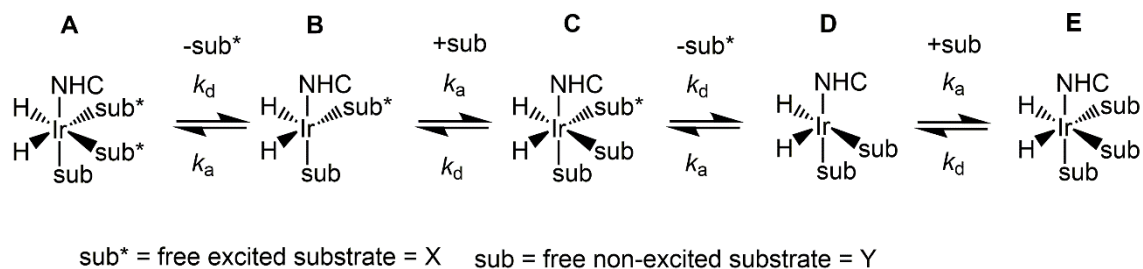


Figure 9.3 Scheme representing the exchange between substrate species in free solution and bound to the catalyst.

$$[A]_{t+\Delta t} = [A]_t - 2k_d[A]_t\Delta t + k_a[B]_t[X]_t\Delta t \quad (9.8)$$

$$[B]_{t+\Delta t} = [B]_t + 2k_d[A]_t\Delta t - k_a[B]_t[X]_t\Delta t + k_d[C]_t\Delta t - k_a[B]_t[Y]_t\Delta t \quad (9.9)$$

$$[C]_{t+\Delta t} = [C]_t - 2k_d[C]_t\Delta t + k_a[B]_t[Y]_t\Delta t + k_a[D]_t[X]_t\Delta t \quad (9.10)$$

$$[D]_{t+\Delta t} = [D]_t + k_d[C]_t\Delta t - k_a[D]_t[X]_t\Delta t + 2k_d[E]_t\Delta t - k_a[D]_t[Y]_t\Delta t \quad (9.11)$$

$$[E]_{t+\Delta t} = [E]_t - 2k_d[E]_t\Delta t + k_a[D]_t[Y]_t\Delta t \quad (9.12)$$

$$[X]_{t+\Delta t} = [X]_t + 2k_d[A]_t\Delta t - k_a[B]_t[X]_t\Delta t - k_a[D]_t[X]_t\Delta t + k_d[C]_t\Delta t \quad (9.13)$$

$$[Y]_{t+\Delta t} = [Y]_t + 2k_d[E]_t\Delta t - k_a[B]_t[Y]_t\Delta t - k_a[D]_t[Y]_t\Delta t + k_d[C]_t\Delta t \quad (9.14)$$

The concentration of the excited bound substrate is described by $2[A] + [B] + [C]$, while the concentration of the excited free substrate is $[X]$. The integrals for them, obtained using the EXSY experiment at different mixing times, were inserted in an Excel spreadsheet and the squared difference between the predicted values from the kinetic equations 9.8 – 9.14 and the experimental data were reduced using the Solver Add-in by varying the k_d and k_a values.²⁰³ Only the limiting k_d rate is reliably obtained from this modeling as the equilibrium point is unknown.

The measurements were performed for the samples containing 5 mM SABRE pre-catalyst and 50 mM substrate (**4-AP** or **4-PBA**). During the activation three substrate molecules bind to the iridium complex, thus, free substrate concentration becomes 35 mM which was used in the model as a $[Y]_0$.

Meta proton resonances were used for the EXSY experiment in the cases where the substrate undergoes *ortho* position deuteration. The bound *meta* resonance of **4-AP** at 6.17 ppm was excited and exchange was observed with the free substrate *meta* resonance at 6.57 ppm. The bound *ortho* resonance of **4-PBA** at 8.25 ppm was excited and exchange was observed with the *ortho* resonance of free substrate at 8.46 ppm. The measurements were performed for mixing times in the range of 0.01 s – 1 s, which were significantly less than the T_1 values of the free substrate. Therefore, an increase in signal of the free substrate due to the T_1 can be neglected and changes in intensity can be purely associated with the exchange between the resonances.

9.11 Mean and error calculation

The mean (\bar{x}) from n repeated measurements (x_i) was calculated using Equation 9.15. Standard deviation (SD) for n repeated measurements was calculated using the Equation 9.16. Error was calculated using Equation 9.17.

$$\bar{x} = \frac{\sum x_n}{n} \quad (9.15)$$

$$SD = \sqrt{\frac{\sum (x_n - \bar{x})^2}{n-1}} \quad (9.16)$$

$$Error = \frac{SD}{\sqrt{n}} \quad (9.17)$$

9.11.1 Error propagation

The error of the mean ($\Delta\bar{x}$) which was calculated from the values which possess their own errors (Δx_i) is given by Equation 9.18, which can be resolved into Equation 9.19.

$$\Delta\bar{x}^2 = \sum_n \left(\frac{\partial\bar{x}}{\partial x_n} \Delta x_n \right)^2 \quad (9.18)$$

$$\Delta\bar{x} = \frac{\sqrt{\sum \Delta x_n^2}}{n} \quad (9.19)$$

If the value is equal to a ratio of the values which possess their own errors, see Equation 9.20, then its error is propagated using Equation 9.21 (analogous to Equation 9.18), which can be resolved into Equation 9.22.

$$x = \frac{y}{z} \quad (9.20)$$

$$\Delta\bar{x}^2 = \frac{\partial\bar{x}}{\partial y} \Delta y + \frac{\partial\bar{x}}{\partial z} \Delta z \quad (9.21)$$

$$\Delta x = x * \sqrt{\left(\frac{\Delta y}{y}\right)^2 + \left(\frac{\Delta z}{z}\right)^2} \quad (9.22)$$

9.12 Characterisation

NMR samples were made up in a vial for dissolution and transferred to 5 mm NMR tubes equipped with Young's tap.

4-aminopyridine (4-AP)

^1H (400.1 MHz, MeOD, 253 K, ppm): 7.94 (m, 2H, *ortho*H), 6.55 (m, 2H, *meta*H).

^{13}C (100.6 MHz, MeOD, 253 K, ppm): 156.8 (C), 149.1 (*ortho*CH), 109.7 (*meta*CH).

^{15}N (50.7 MHz, MeOD, 243 K, ppm): 254.1 (N), 66.0 (NH_2).

[Ir(COD)(IMes)(4-aminopyridine)]Cl (2a) (also [Ir(COD)(IMes)(4-AP)]Cl)

Sample contained 20 mM **4-AP** and 5 mM pre-catalyst **1** in 0.6 mL methanol-*d*₄. Formation of the complex **2a** was detected with NMR in about 10 minutes after mixing **4-AP** and the pre-catalyst **1**, and **2a** was stable over a week.

¹H (500.1 MHz, MeOD, 253 K): 7.40 (s, 2H, NCHCHN), 7.21 (s, 2H, CH^{mes}), 7.13 (m, 2H, *ortho*H, 4-AP *trans* to COD), 7.05 (s, 2H, CH^{mes}), 6.32 (m, 2H, *meta*H, 4-AP *trans* to COD), 3.52 (m, 2H, CH^{COD}), 3.33 (overlap with solvent, CH^{COD}), 2.44 (s, 6H, *para*CH₃^{mes}), 2.34 (br s, 6H, *ortho*CH₃^{mes}), 1.94 (s, 6H, *ortho*CH₃^{mes}), 1.98 and 1.86 and 1.59 (br m, 8H, overlap, CH₂^{COD}).

¹³C (125.8 MHz, MeOD, 253 K): 174.2 (NCN), 155.1 (*para*C, 4-AP), 149.1 (*ortho*CH, 4-AP), 139.5 (*para*C^{mes}), 137.4 (N-C^{mes}), 135.4 (*ortho*C^{mes}), 135.2 (*ortho*C^{mes}), 129.5 (CH^{mes}), 129.0 (CH^{mes}), 125.0 (NCHCHN), 109.7 (*meta*CH, 4-AP), 80.8 (CH^{COD}), 62.7 (CH^{COD}), 19.8 (*para*CH₃^{mes}), 17.4 (*ortho*CH₃^{mes}), 32.3 (overlap, CH₂^{COD}), 29.06 (overlap, CH₂^{COD}).

¹⁵N (50.7 MHz, MeOD, 243 K): 195.6 (aromatic N, 4-AP), 195.0 (carbene N), 72.1 (NH₂, 4-AP).

[Ir(H)₂(COD)(IMes)(4-aminopyridine)]Cl (3a) (also [Ir(H)₂(COD)(IMes)(4-AP)]Cl)

Sample containing 25 mM **4-AP** and 5 mM pre-catalyst **1** in 0.6 mL methanol-*d*₄ was degassed using a three-stage freeze-pump-thaw method. H₂ gas was added while the sample was kept in the dry ice-acetone bath and inserted into the pre-cooled to 240 K NMR spectrometer.

¹H NMR (500 MHz, MeOD, 240 K): 7.65 (m, 2H, *ortho*H, 4-AP *trans* to hydride), 7.35 (s, 2H, N-CH-CHN), 7.09 (s, 2H, CH^{mes}), 7.03 (s, 2H, CH^{mes}), 6.27 (m, 2H, *meta*H, 4-AP *trans* to hydride), 4.87 and 4.56 and 4.08 and 3.64 (m, 4H, CH^{COD}), 2.41 (s, 6H, *para*CH₃^{mes}), 2.00 (s, 6H, *ortho*CH₃^{mes}), 1.98 (s, 6H, *ortho*CH₃^{mes}), 2.30 and 2.10 and 2.07 and 1.97 and 1.95 and

1.82 and 1.48 (br m, 12H, overlap, CH₂^{CO^D}), -12.15 (br s, 2H, hydride), -16.97 (br s, 2H, hydride).

¹³C NMR (125.8 MHz, MeOD, 240 K): 157.2 (*ortho*C, 4-AP *trans* to hydride), 154.3 (NCN), 154.0 (*para*C, 4-AP *trans* to hydride), 139.4 (*para*C^{mes}), 136.9 (N-C^{mes}), 135.3 (*ortho*C^{mes}), 128.7 and 129.8 (CH^{mes}), 124.2 (NCHCHN), 110.3 (*meta*C, 4-AP *trans* to hydride), 89.79 and 87.50 and 83.4 and 79.2 (CH^{CO^D}), 34.3 and 32.0 and 29.6 and 25.8 (CH₂^{CO^D}), 19.1 (*para*CH₃^{mes}), 16.90 (*ortho*CH₃^{mes}).

[Ir(H)₂(IMes)(4-aminopyridine)₃]Cl (4a) (also [Ir(H)₂(IMes)(4-AP)₃]Cl)

Sample containing 25 mM 4-AP and 5 mM pre-catalyst 1 in 0.6 mL methanol-*d*₄ was degassed using a three-stage freeze-pump-thaw method. H₂ gas was added to the sample and left at room temperature or in ~40 deg. water bath for activation until characteristic hydride at ~ -23 ppm appears in ¹H NMR spectrum.

¹H NMR (400.1 MHz, MeOD, 253 K): 7.65 (m, 4H, *ortho*H, 4-AP *trans* to hydride), 7.37 (m, 2H, *ortho*H, 4-AP *cis* to hydride), 7.01 (s, 2H, NCHCHN), 6.75 (s, 4H, CH^{mes}), 6.15 (m, 4H, *meta*H, 4-AP *trans* to hydride), 6.04 (m, 2H, *meta*H, 4-AP *cis* to hydride), 2.26 (s, 6H, *para*CH₃^{mes}), 2.05 (s, 12 H, *ortho*CH₃^{mes}), -22.97 (s, 2H, hydride).

¹³C NMR (100.6 MHz, MeOD, 253 K): 155.93 (NCN), 155.26 (*ortho*C, 4-AP *cis* to hydride), 155.11 (*para*C, 4-AP *cis* to hydride), 155.08 (*para*C, 4-AP *trans* to hydride), 154.44 (*ortho*C, 4-AP *trans* to hydride), 139.27 (*ortho*C^{mes}), 138.96 (*para*C^{mes}), 136.14 (N-C^{mes}), 129.28 (CH^{mes}), 122.95 (NCHCHN), 110.0 (*meta*C, 4-AP *trans* to hydride), 109.77 (*meta*C, 4-AP *cis* to hydride), 20.92 (*para*CH₃^{mes}), 18.90 (*ortho*CH₃^{mes}).

¹⁵N (50.7 MHz, MeOD, 253 K): 214.10 (N, 4-AP *trans* to hydride), 196.90 (N, 4-AP *cis* to hydride), 194.00 (carbene N), 67.29 (NH₂, 4-AP *cis* to hydride, at 243 K), 66.35 (NH₂, 4-AP *trans* to hydride, at 243 K).

N-(4-pyridyl)benzamide (4-PBA)

^1H NMR (500.1 MHz, MeOD, 260 K, ppm): 8.46 (m, 2H, *ortho*H^{Py}), 7.98 (m, 2H, *ortho*H^{Ar}), 7.91 (m, 2H, *meta*H^{Py}), 7.66 (t, 1H, $J = 7.3$ Hz, *para*H^{Ar}), 7.56 (m, 2H, *meta*H^{Ar})

^{13}C NMR (125.8 MHz, MeOD, 260 K, ppm): 168.0 (NHCO), 149.2 (*ortho*C^{Py}), 147.0 (*para*C^{Py}), 133.0 (NHCO_C^{Ar}), 132.4 (*para*C^{Ar}), 128.6 (*meta*C^{Ar}), 127.6 (*ortho*C^{Ar}), 114.4 (*meta*C^{Py}),

^{15}N NMR (50.7 MHz, MeOD, 260 K, ppm): 283.4 (N), 127.8 (NH).

[Ir(COD)(IMes)(N-(4-pyridyl)benzamide)]Cl (2b) (also [Ir(COD)(IMes)(4-PBA)]Cl)

Sample contained 25 mM 4-PBA and 5 mM pre-catalyst 1 in 0.6 mL methanol- d_4 . Formation of the complex 2b was detected with NMR in about 10 minutes after mixing 4-PBA and the pre-catalyst 1, and 2b was stable over a week.

^1H (500.1 MHz, MeOD, 260 K): 7.42 (s, 2H, N-CH-CH-N), 8.01 (m, 2H, *ortho*H^{Ar}, 4-PBA *trans* to COD), 7.72 (overlap, 4H, *ortho*H^{Py}, *meta*H^{Py}, 4-PBA *trans* to COD), 7.69 (m, 2H, *para*H^{Ar}, 4-PBA *trans* to COD), 7.58 (m, 2H, *meta*H^{Ar}, 4-PBA *trans* to COD), 7.25 (s, 2H, CH^{mes}), 7.05 (s, 2H, CH^{mes}), 3.64 (m, 2H, CH^{COD}), 3.34 (m, 2H, CH^{COD}), 2.47 (s, 6H, *para*CH₃^{mes}), 2.36 (br s, 6H, *ortho*CH₃^{mes}), 1.93 (s, 6H, *ortho*CH₃^{mes}), 2.05, 1.91, 1.65 (br m, 8H, overlap, CH₂^{COD}).

^{13}C (125.8 MHz, MeOD, 260 K): 173.2 (NCN), 167.9 (NHCO), 150.7 (*ortho*C^{Py}, 4-PBA), 146.7 (*para*C^{Py}, 4-PBA), 139.8 (*para*C^{mes}), 137.4 (N-C^{mes}), 135.2 (*ortho*C^{mes}), 132.4 (NHCO_C^{Ar}, 4-PBA), 132.4 (*para*C^{Ar}), 128.6 (*meta*C^{Ar}), 127.6 (*ortho*C^{Ar}), 129.3 (CH^{mes}), 125.1 (N-CH-CH-N), 115.4 (*meta*C^{Py}, 4-PBA), 81.5 (CH^{COD}), 64.4 (CH^{COD}), 32.2 (overlap, CH₂^{COD}), 28.8 (overlap, CH₂^{COD}), 19.8 (*para*CH₃^{mes}), 17.2 (*ortho*CH₃^{mes}).

^{15}N NMR (MeOD, 50.7 MHz, 260 K): 225.0 (aromatic N, 4-PBA), 195.7 (carbene N), \sim 128 (NH₂, 4-PBA).

[Ir(H)₂(IMes)(N-(4-pyridyl)benzamide)₃]Cl (4b) (also [Ir(H)₂(IMes)(4-PBA)₃]Cl)

Sample containing 50 mM 4-PBA and 5 mM pre-catalyst 1 in 0.6 mL methanol-*d*₄ was degassed using a three-stage freeze-pump-thaw method. H₂ gas was added to the sample and left at room temperature or in \sim 40 deg. water bath for activation until characteristic hydride at \sim -23 ppm appears in ^1H NMR spectrum.

^1H NMR (MeOD, 500 MHz, 253 K): 8.26 (m, 4H, *ortho*H^{py}, 4-PBA *trans* to hydride), 7.99 (m, 2H, *ortho*H^{py}, 4-PBA *cis* to hydride), 7.98 (overlap, 4H, *ortho*H^{ar} ring, 4-PBA *trans* to hydride), 7.86 (d, 2H, J^{HH} = 8 Hz, *ortho*H^{ar} ring, 4-PBA *cis* to hydride), 7.67 (t, 2H, J^{HH} = 7.3 Hz, *para*H^{ar}, 4-PBA *trans* to hydride), 7.65 (overlap, 4H, *meta*H^{ar}, 4-PBA *trans* to hydride), 7.60 (t, 1H, J^{HH} = 11 Hz, *para*H^{ar}, 4-PBA *cis* to hydride), 7.56 (m, 4H, *meta*H^{py}, 4-PBA *trans* to hydride), 7.50 (t, 2H, *meta*H^{ar}, J^{HH} = 7 Hz, 4-PBA *cis* to hydride), 7.44 (d, 2H, J^{HH} = 6 Hz, *meta*H^{py}, 4-PBA *cis* to hydride), 7.10 (s, 2H, N-CH-CHN), 6.74 (s, 4H, CH^{mes}), 2.23 (s, 6H, *para*CH₃^{mes}), 2.11 (s, 12H, *ortho*CH₃^{mes}), -22.77 (s, 2H, hydride).

^{13}C NMR (MeOD, 125.7 MHz, 255 K): 152.9 (NCN), 167.9 (CO, 4-PBA *trans* to hydride), 167.5 (CO, 4-PBA *cis* to hydride), 155.6 (*ortho*C^{py}, 4-PBA *cis* to hydride), 154.5 (*ortho*C^{py}, 4-PBA *trans* to hydride), 146.0 (*para*C^{py}, 4-PBA *cis* to hydride), 145.7 (*para*C^{py}, 4-PBA *trans* to hydride), 138.2 (*para*C^{mes}), 137.6 (*ortho*C^{mes}), 135.1 (N-C^{mes}), 134.0 (NCOC, 4-PBA *trans* to hydride), 133.8 (NCOC, 4-PBA *cis* to hydride), 132.3 (*para*C^{ar}, 4-PBA *trans* to hydride), 132.2 (*para*C^{ar}, 4-PBA *cis* to hydride), 128.4 (overlap, *ortho*C^{ar} and *meta*C^{ar}, 4-PBA *trans* to hydride; *meta*C^{ar}, 4-PBA *cis* to hydride), 128.3 (CH^{mes}), 127.5 (*ortho*C^{ar}, 4-PBA *cis* to hydride), 122.3 (NCHCHN), 114.9 (*meta*C^{py}, 4-PBA *cis* to hydride), 114.6 (*meta*C^{py}, 4-PBA *trans* to hydride), 19.6 (*para*CH₃^{mes}), 17.7 (*ortho*CH₃^{mes}).

^{15}N NMR (MeOD, 50.7 MHz, 253 K): 194.2 (carbene N), 240.2 (N, 4-PBA *trans* to hydride), 222.4 (N, 4-PBA *cis* to hydride), 128.2 (NH, 4-PBA *cis* to hydride), 128.0 (NH, 4-PBA *trans* to hydride).

4-methylpyridine (4-MP)

^1H (500.1 MHz, MeOD, 263 K): 8.40 (m, 2H, *ortho*H), 7.34 (m, 2H, *meta*H), 2.43 (s, 3H, CH_3).

^{13}C (125.8 MHz, MeOD, 263 K): 149.2 (C), 148.1 (*ortho*CH), 125.2 (*meta*CH), 19.6 (CH_3).

^{15}N (50.7 MHz, MeOD, 255 K): 188.7 (N).

[Ir(COD)(IMes)(4-methylpyridine)]Cl (**2c**) (also [Ir(COD)(IMes)(4-MP)]Cl)

Sample contained 25 mM **4-MP** and 5 mM pre-catalyst **1** in 0.6 mL methanol- d_4 . Formation of the complex **2c** was detected with NMR in about 10 minutes after mixing **4-MP** and the pre-catalyst **1**, and **2c** was stable over a week.

^1H (500.1 MHz, MeOD, 263 K): 7.70 (overlap, 2H, *ortho*H, 4-MP *trans* to COD), 7.41 (s, 2H, NCHCHN), 7.24 (br s, 2H, CH^{mes}), 7.15 (m, 2H, *meta*H, 4-MP *trans* to COD), 7.02 (br s, 2H, CH^{mes}), 3.66 (t, 2H, $J^{\text{HH}} = 2.8$ Hz, CH^{COD} , *trans* to 4-MP), 3.28 (t, 2H, $J^{\text{HH}} = 2.8$ Hz, CH^{COD} , *trans* to carbene), 2.46 (s, 6H, $\text{paraCH}_3^{\text{mes}}$), 2.43 (s, 3H, CH_3 , 4-MP *trans* to COD), 2.37 (br s, 6H, *ortho* CH_3^{mes}), 1.86 (br s, 6H, *ortho* CH_3^{mes}), 2.05, 1.90, 1.65, 1.64 (overlap, CH_2^{COD}).

^{13}C (125.8 MHz, MeOD, 263 K): 173.0 (NCN), 150.1 (*para*C, 4-MP), 149.9 (*ortho*CH, 4-MP), 139.8 (*para* C^{mes}), 135.7 and 135.3 (*ortho* C^{mes}), 133.2 (N- C^{mes}), 129.1 (CH^{mes}), 126.5 (*meta*CH, 4-MP), 125.2 (NCHCHN), 81.8 (CH^{COD} , *trans* to carbene), 64.4 (CH^{COD} , *trans* to 4-MP), 19.8 (*para* CH_3^{mes}), 19.5 (CH_3 , 4-MP), 17.3 (*ortho* CH_3^{mes}), 28.5 (overlap, CH_2^{COD}), 32.1 (overlap, CH_2^{COD}).

^{15}N (50.7 MHz, MeOD, 263 K): 233.5 (aromatic N, 4-MP), 195.4 (carbene N).

[Ir(H)₂(IMes)(4-methylpyridine)₃]Cl (4c) (also [Ir(H)₂(IMes)(4-MP)₃]Cl)

Sample containing 25 mM 4-MP and 5 mM pre-catalyst 1 in 0.6 mL methanol-*d*₄ was degassed using a three-stage freeze-pump-thaw method. H₂ gas was added to the sample and left at room temperature or in ~40 deg. water bath for activation until characteristic hydride at ~ -23 ppm appears in ^1H NMR spectrum.

^1H NMR (500.1 MHz, MeOD, 255 K): 8.15 (m, 4H, *ortho*H, 4-MP *trans* to hydride), 7.88 (m, 2H, *ortho*H, 4-MP *cis* to hydride), 7.11 (s, 2H, NCHCHN), 6.95 (m, 4H, *meta*H, 4MP *trans* to hydride), 6.82 (m, 2H, *meta*H, 4-MP *cis* to hydride), 6.67 (s, 4H, CH^{mes}), 2.34 (s, 6H, CH₃, 4-MP *trans* to hydride), 2.22 (s, 6H, *para*CH₃^{mes}), 2.16 (s, 3H, CH₃, 4-MP *cis* to hydride), 2.05 (s, 12H, *ortho*CH₃^{mes}), -22.64 (s, 2H, hydride).

^{13}C (125.8 MHz, MeOD, 255 K): 154.6 (*ortho*C, 4-MP *cis* to hydride), 153.6 (*ortho*C, 4-MP *trans* to hydride), 152.0 (NCN), 148.4 (*para*C, 4-MP *cis* to hydride), 148.0 (*para*C, 4-MP *trans* to hydride), 138.1 (*para*C^{mes}), 137.5 (N-C^{mes}), 135.1 (*ortho*C^{mes}), 128.3 (CH^{mes}), 122.54 (NCHCHN), 125.91-125.95 (overlap, *meta*C, 4-MP *trans* to hydride, *meta*C, 4-MP *cis* to hydride), 26.0 (CH₃, 4-MP *trans* to hydride, 4-MP *cis* to hydride), 19.7 (*para*CH₃^{mes}), 17.7 (*ortho*CH₃^{mes}).

^{15}N (50.7 MHz, MeOD, 255 K): 247.4 (N, 4-MP *trans* to hydride), 194.5 (carbene N), 130.8 (N, 4-MP *cis* to hydride).

Pyridine (py)

^1H (500 MHz, MeOD, 263 K): 8.56 (m, 2H, *ortho*H), 7.91 (t, 1H, *para*H), 7.49 (m, 2H, *meta*H)

^{13}C (125 MHz, MeOD, 263 K): 148.7 (*ortho*CH), 137.5 (*para*CH), 124.6 (*meta*CH)

^{15}N (50.6 MHz, MeOD, 263 K): 198.1 (N).

[Ir(COD)(IMes)(pyridine)]Cl (2d) (also [Ir(COD)(IMes)(py)]Cl)

Sample contained 25 mM pyridine and 5 mM pre-catalyst **1** in 0.6 mL methanol-*d*₄. Formation of the complex **2d** was detected with NMR in about 10 minutes after mixing pyridine and the pre-catalyst **1**, and **2d** was stable over a week.

^1H (500 MHz, MeOD, 263 K): 7.88 (overlap, 2H, *ortho*H, py *trans* to COD), 7.81 (tt, $J^{\text{HH}} = 1.4$ Hz, $J^{\text{HH}} = 7.7$ Hz, 1H, *para*H, py *trans* to COD), 7.42 (s, 2H, N-CH-CH-N), 7.30 (m, 2H, *meta*H, py *trans* to COD), 7.24 (br s, 2H, CH^{mes}), 7.02 (br s, 2H, CH^{mes}), 3.68 (t, 2H, $J^{\text{HH}} = 2.9$ Hz, CH^{COD}, *trans* to py), 3.29 (t, 2H, $J^{\text{HH}} = 2.9$ Hz, CH^{COD}, *trans* to carbene), 2.46 (s, 6H, *para*CH₃^{mes}), 2.37 (br s, 6H, *ortho*CH₃^{mes}), 1.86 (br s, 6H, *ortho*CH₃^{mes}), 2.05, 1.90, 1.65 (overlap, CH₂^{COD}).

^{13}C (125.7 MHz, MeOD, 263 K): 172.8 (NCN), 150.7 (*ortho*CH, py), 139.7 (*para*C^{mes}), not seen (N-C^{mes}), 137.4 (*para*CH, py), 135.5 (*ortho*C^{mes}), 129.2 (CH^{mes}), 125.9 (*meta*CH, py), 125.3 (N-CH-CH-N), 81.6 (CH^{COD}, *trans* to carbene), 64.8 (CH^{COD}, *trans* to py), 19.8 (*para*CH₃^{mes}), 17.3 (*ortho*CH₃^{mes}), 28.5 (overlap, CH₂^{COD}), 32.1 (overlap, CH₂^{COD}).

^{15}N (50.6 MHz, MeOD, 263 K): 242.4 (N, py), 195.6 (carbene N).

Abbreviations

NMR	Nuclear Magnetic Resonance
PHIP	<i>Para</i> -hydrogen Induced Polarisation
SABRE	Signal Amplification By Reversible Exchange
<i>p</i> -H ₂	<i>para</i> -hydrogen
COD	<i>cis,cis</i> -1,5-cyclooctadiene
PTF	Polarisation Transfer Field
PTT	Polarisation Transfer Time
G	Gauss
T	Tesla
s, sec	second
min	minute
hr	hour
py	pyridine
4-AP	4-aminopyridine
4-MP	4-methylpyridine
4-PBA	N-(4-pyridyl)benzamide
3,5-DAP	3,5-diaminopyridine
IMes	1,3-bis(2,4,6-trimethylphenyl)imidazole-2-ylidene
ICy	1,3-bis(cyclohexyl)imidazole-2-ylidene
ImMe ₂ NPr ⁱ ₂	1,3-bis(isopropyl)-4,5-dimethylimidazole-2-ylidene
IME	1,3-bis(methyl)imidazole-2-ylidene
Tp ^{Me2}	hydrotris(3,5-dimethylpyrazolyl)borate
1	[Ir(Cl)(COD)(IMes)], pre-catalyst
2	[Ir(COD)(IMes)(substrate)]Cl
3	[Ir(H) ₂ (COD)(IMes)(substrate)]Cl
4	[Ir(H) ₂ (IMes)(substrate) ₃]Cl
2a	[Ir(COD)(IMes)(4-AP)]Cl
2b	[Ir(COD)(IMes)(4-PBA)]Cl
2c	[Ir(COD)(IMes)(4-MP)]Cl
2d	[Ir(COD)(IMes)(py)]Cl
3a	[Ir(H) ₂ (COD)(IMes)(4-AP)]Cl
4a	[Ir(H) ₂ (IMes)(4-AP) ₃]Cl
4b	[Ir(H) ₂ (IMes)(4-PBA) ₃]Cl
4c	[Ir(H) ₂ (IMes)(4-MP) ₃]Cl
4d	[Ir(H) ₂ (IMes)(py) ₃]Cl
EXSY	Exchange Spectroscopy
NOE	Nuclear Overhauser Effect
MS	Mass-spectrometry

Appendix

Additional information

Table A1 Standard deviation and standard error for the *ortho* and *meta* protons of **4-AP** and **4-PBA** assessed for their 5 eq : 5 eq mixture in presence of the activated SABRE catalyst in methanol-*d*₄.

		<i>ortho</i> 4-PBA	<i>ortho</i> 4-AP	<i>meta</i> 4-PBA	<i>meta</i> 4-AP
Thermal	SD, %	5.6	3.2	4.1	3.2
signal	Standard error, %	1.7	1.0	1.2	1.0
SABRE	SD, %	3.5	2.3	7.6	2.7
signal	Standard error, %	1.1	0.7	2.3	0.8
Enhancem	SD, %	5.6	4.0	7.1	3.9
ent factor	Standard error*, %	2.0	1.2	2.6	1.3

* Standard error was calculated using the error propagation (see Equation 9.22 in Chapter 9, section 11).

Table A2 Reproducibility of the enhancement factors measured for the **4-AP** and **4-PBA** *ortho* and *meta* protons in the 5 eq : 5 eq mixture in presence of the SABRE catalyst in methanol-*d*₄ under 4 bar *p*-H₂.

	<i>ortho</i> 4-PBA	<i>ortho</i> 4-AP	<i>meta</i> 4-PBA	<i>meta</i> 4-AP
1	-195.39	-294.17	-21.04	-210.81
2	-202.47	-294.79	-25.70	-213.13
3	-201.22	-283.87	-23.88	-203.57
4	-188.80	-275.39	-25.63	-197.54
5	-195.49	-295.78	-22.40	-211.76
6	-217.81	-306.93	-23.66	-216.54
7	-199.27	-282.34	-21.51	-199.22
8	-200.86	-314.25	-24.43	-221.43
9	-179.83	-281.56	-21.08	-198.09
10	-179.89	-283.43	-23.76	-200.64
11	-190.27	-287.58	-24.01	-204.66
Average	-195.57	-290.92	-23.37	-207.04
SD, %	5.56	4.02	7.12	3.93
Standard error, %	1.68	1.21	2.15	1.18
Standard error*, %	2.0	1.2	2.6	1.3

* Standard error was calculated using the error propagation (see Equation 9.22 in Chapter 9, section 11).

Table A3 Reproducibility of the ratios of enhancement factors measured for the **4-AP** and **4-PBA** *ortho* and *meta* protons in the 5 eq : 5 eq mixture in presence of the SABRE catalyst in methanol-*d*₄ under 4 bar *p*-H₂.

	<i>o</i> : <i>m</i> 4-PBA	<i>o</i> : <i>m</i> 4-AP	<i>o</i> : <i>o</i> 4-AP : 4-PBA	<i>m</i> : <i>m</i> 4-AP : 4-PBA	<i>o</i> : <i>m</i> 4-AP : 4-PBA	<i>m</i> : <i>o</i> 4-AP : 4-PBA
1	9.20	1.39	1.51	10.02	13.98	1.08
2	7.88	1.38	1.45	8.29	11.47	1.05
3	8.43	1.39	1.41	8.52	11.89	1.01
4	7.37	1.39	1.46	7.71	10.74	1.05
5	8.73	1.40	1.51	9.45	13.21	1.08
6	9.21	1.42	1.41	9.15	12.97	0.99
7	9.26	1.42	1.42	9.26	13.13	1.00
8	8.22	1.42	1.56	9.06	12.86	1.10
9	8.53	1.42	1.57	9.40	13.36	1.10
10	7.57	1.41	1.58	8.44	11.93	1.12
11	7.92	1.41	1.51	8.52	11.98	1.08
Average	8.40	1.41	1.49	8.90	12.50	1.06
SD, %	8.07	0.93	4.25	7.38	7.71	4.03
Standard error, %	2.43	0.28	1.28	2.23	2.33	1.22
Standard error*, %	3.3	1.7	2.3	2.9	2.9	2.4

* Standard error was calculated using the error propagation (see Equation 9.22 in Chapter 9, section 11).

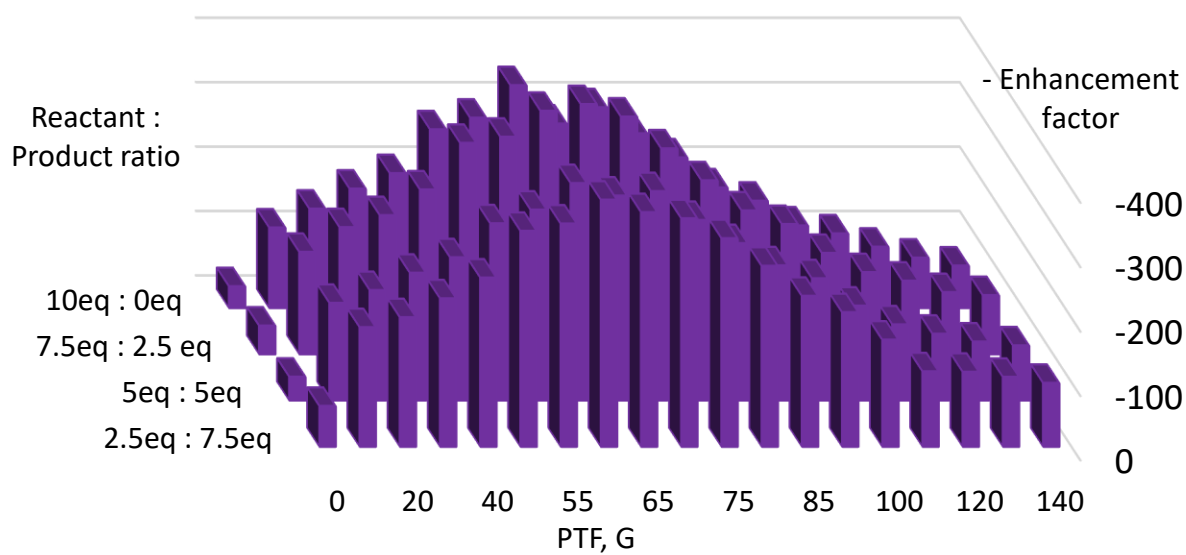


Figure A9.4 Polarisation transfer field (PTF) and relative concentrations dependence on enhancement factor of **4-AP** *ortho* proton.

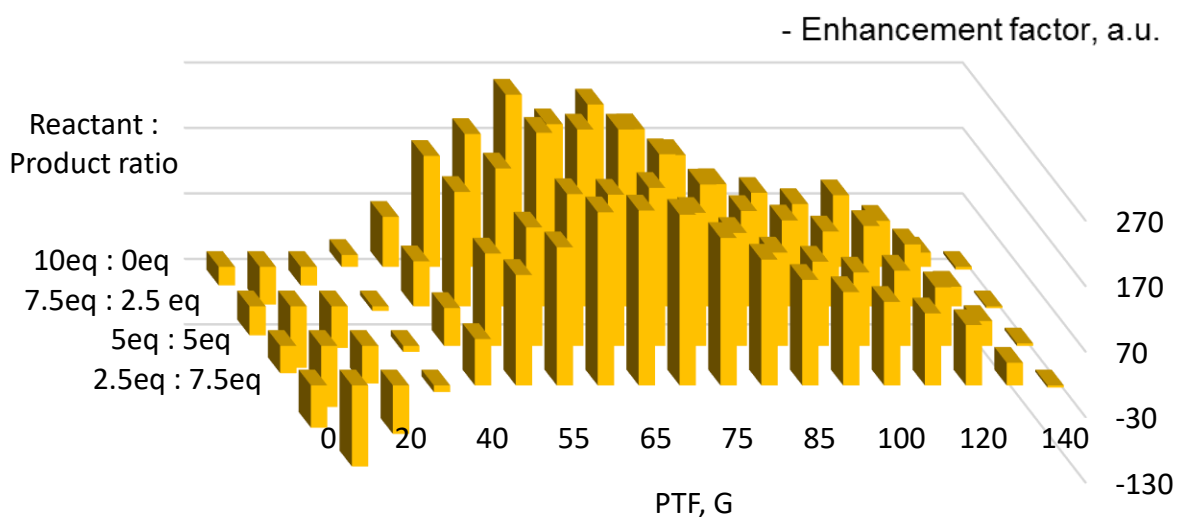


Figure A9.5 Polarisation transfer field (PTF) and relative concentrations dependence on enhancement factor of **4-AP** *meta* proton.

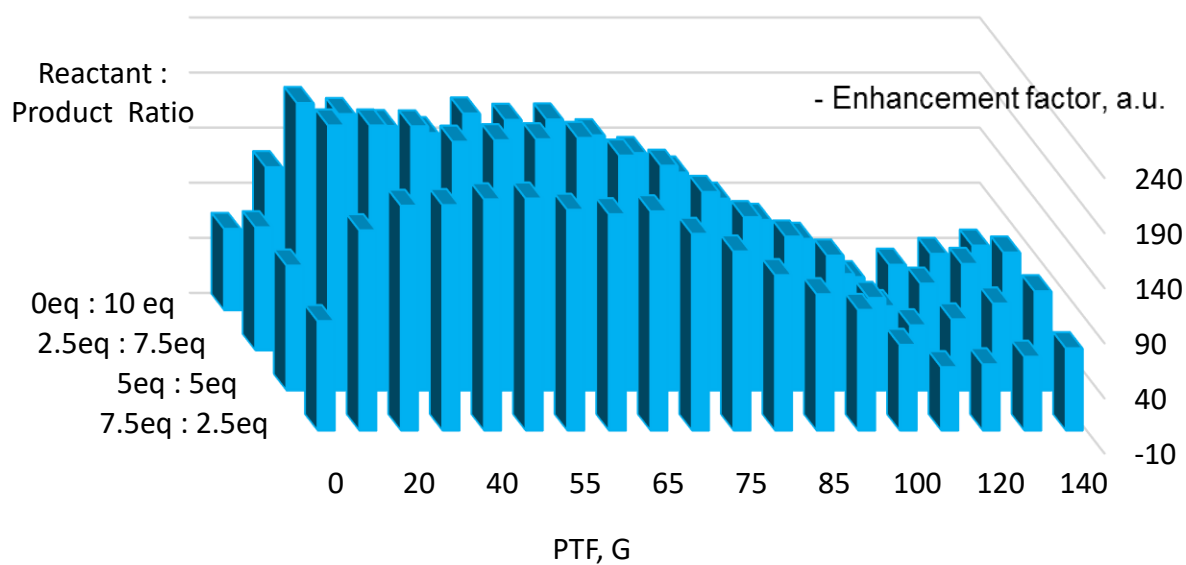


Figure A9.6 Polarisation transfer field (PTF) and relative concentrations dependence on enhancement factor of **4-PBA** *ortho* proton.

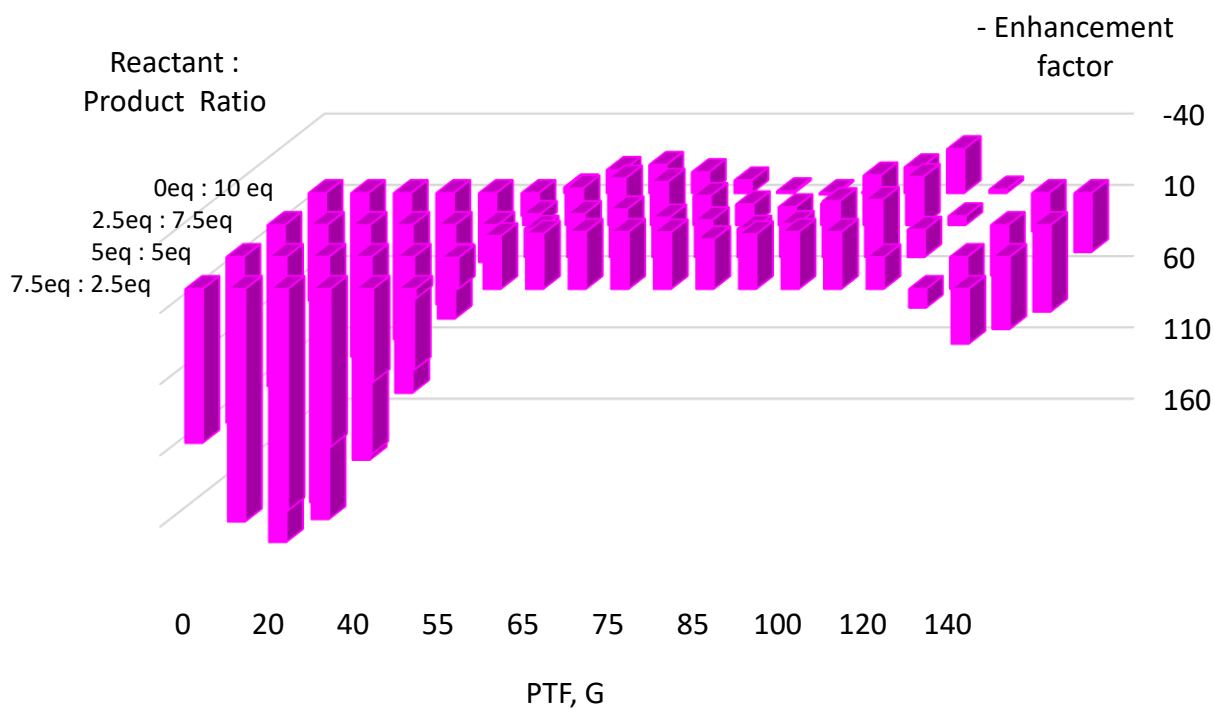


Figure A9.7 Polarisation transfer field (PTF) and relative concentrations dependence on enhancement factor of **4-PBA** *meta* proton.

Table A4 NMR chemical shifts of individual compounds and mixtures in DCM for reaction monitoring characterisation.

Compound	In mixture with	Chemical shifts, ppm
BAH	pure	8.15 (m, 2H, <i>ortho</i>), 7.71 (tt, 1H, $J^{\text{HH}} = 7.4$ Hz, $J^{\text{HH}} = 1.3$ Hz, <i>para</i>), 7.55 (m, 2H, <i>meta</i>)
BA	pure	8.12 (m, 2H, <i>ortho</i>), 7.65 (tt, 1H, $J^{\text{HH}} = 7.4$ Hz, $J^{\text{HH}} = 1.3$ Hz, <i>para</i>), 7.51 (m, 2H, <i>meta</i>)
	+ 4-AP	8.07 (d, 2H, $J^{\text{HH}} = 7.6$ Hz, <i>ortho</i>), 7.52 (m, 1H, <i>para</i>), 7.43 (m, 2H, <i>meta</i>)
	+ 4-PBA	8.09 (m, 2H, <i>ortho</i>), 7.61 (overlap, 1H, <i>para</i>), 7.49 (overlap, 2H, <i>meta</i>)
4-AP	pure	8.15 (m, 2H, <i>ortho</i>), 6.52 (m, 2H, <i>meta</i>), 4.24 (br s, 2H, NH ₂)
	+ BA	8.24 (m, 2H, <i>ortho</i>), 6.62 (m, 2H, <i>meta</i>), 5.14 or 4.77 (br s, NH ⁺ aromatic or NH ₃ ⁺ amino)
	+ 4-PBA	8.14 (m, 2H, <i>ortho</i>), 6.52 (m, 2H, <i>meta</i>), 4.25 (br s, 2H, NH ₂)
4-PBA	pure	8.52 (m, 2H, <i>ortho in Py</i>), 8.00 (br s, 1H, NH amino), 7.88 (m, 2H, <i>ortho in Ar</i>), 7.61 (overlap, 2H, <i>meta in Py</i> , 1H, <i>para in Ar</i>), 7.53 (m, 2H, <i>meta in Ar</i>)
	+ BA	8.57 (m, 2H, <i>ortho in Py</i>), 8.29 (br s, NH ₂ ⁺ amino or NH ⁺ aromatic), 7.90 (m, 2H, <i>ortho in Ar</i>), 7.72 (m, 2H, <i>meta in Py</i>), 7.61 (overlap, 1H, <i>para in Ar</i>), 7.52 (overlap, 2H, <i>meta in Ar</i>), 5.83 (br s, NH ₂ ⁺ amino or NH ⁺ aromatic)
	+ 4-AP	8.73 (br s, 1H, NH amino), 8.50 (m, 2H, <i>ortho in Py</i>), 7.89 (m, 2H, <i>ortho in Ar</i>), 7.64 (m, 2H, <i>meta in Py</i>), 7.58 (m, 1H, <i>para in Ar</i>), 7.50 (m, 2H, <i>meta in Ar</i>)

Table A5 Change in **4-AP** T_1 values in presence of unactivated catalyst [Ir(COD)(IMes)(4-AP)]Cl (5 mM) with increase of **4-AP** concentration. Error bars represent the fitting errors.

4-AP concentration, mM	<i>ortho</i>	<i>ortho</i> bound	<i>meta</i>	<i>meta</i> bound
1.5	9 ± 0.2	1.52 ± 0.01	10.01 ± 0.05	3.26 ± 0.05
10	8.8 ± 0.03	1.45 ± 0.03	10.66 ± 0.03	3.25 ± 0.05
17.5	9.3 ± 0.03	1.49 ± 0.02	10.72 ± 0.05	3.24 ± 0.04
20	9.19 ± 0.003	1.630 ± 0.008	9.37 ± 0.01	3.11 ± 0.03
35	9.69 ± 0.02	1.50 ± 0.02	10.92 ± 0.03	3.26 ± 0.06
52.5	10.68 ± 0.01	1.43 ± 0.01	10.91 ± 0.02	3.34 ± 0.05
98	10.55 ± 0.01	1.47 ± 0.01	10.89 ± 0.03	3.05 ± 0.05
465	9.46 ± 0.01	1.18 ± 0.05	9.749 ± 0.006	2.6 ± 0.1

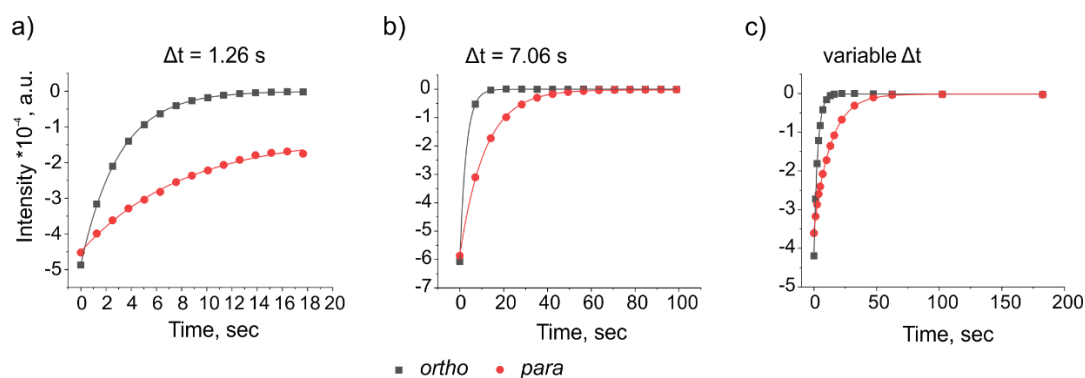


Figure A9.8 Hyperpolarisation lifetime curves for 3,5-diaminopyridine (**3,5-DAP**) *ortho* (7.35 ppm) and *para* (6.47 ppm) protons acquired in presence of [Ir(H)₂(IMes)(**3,5-DAP**)₃]Cl in methanol-*d*₄ on a 1 T NMR spectrometer with constant time delays of a) 1.26 s and b) 7.06 s and c) variable time delays.

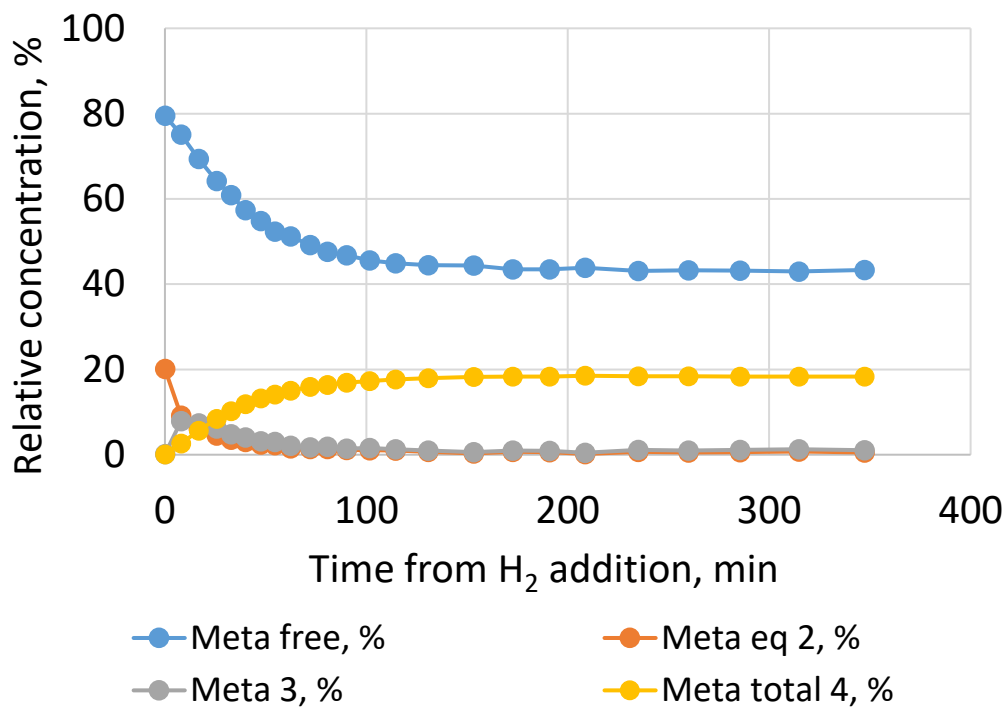


Figure A9.9 ¹H NMR signal intensities of the **4-AP** meta proton peak of the free substrate in solution and bound to **2a**, **3a** and **4a** as a function of reaction time when *para*-hydrogen is refreshed between NMR measurements.

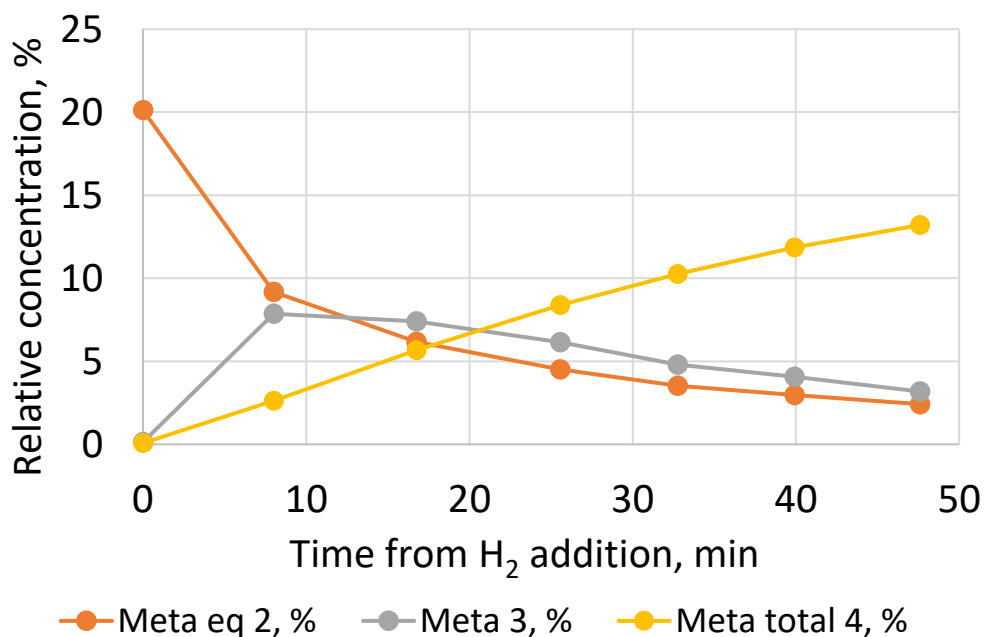


Figure A9.10 ¹H NMR signal intensity of the **4-AP** meta proton peak of the substrate in free solution and bound to **2a**, **3a** and **4a** as a function of reaction time when *para*-hydrogen was refreshed between measurements over the first 50 mins of reaction.

York - Chemistry - Mass Spectrometry Service Report

op577-4ap-ref

Analysis Information

Analysis Filename: sbd74657os_P1-B-2_01_10073.d
 Acquisition Date: 21/01/2019 13:27:07
 Method: ESI_low mass_2c1s.m
 Instrument: compact
 Submission Name: sbd74657os
 Positive

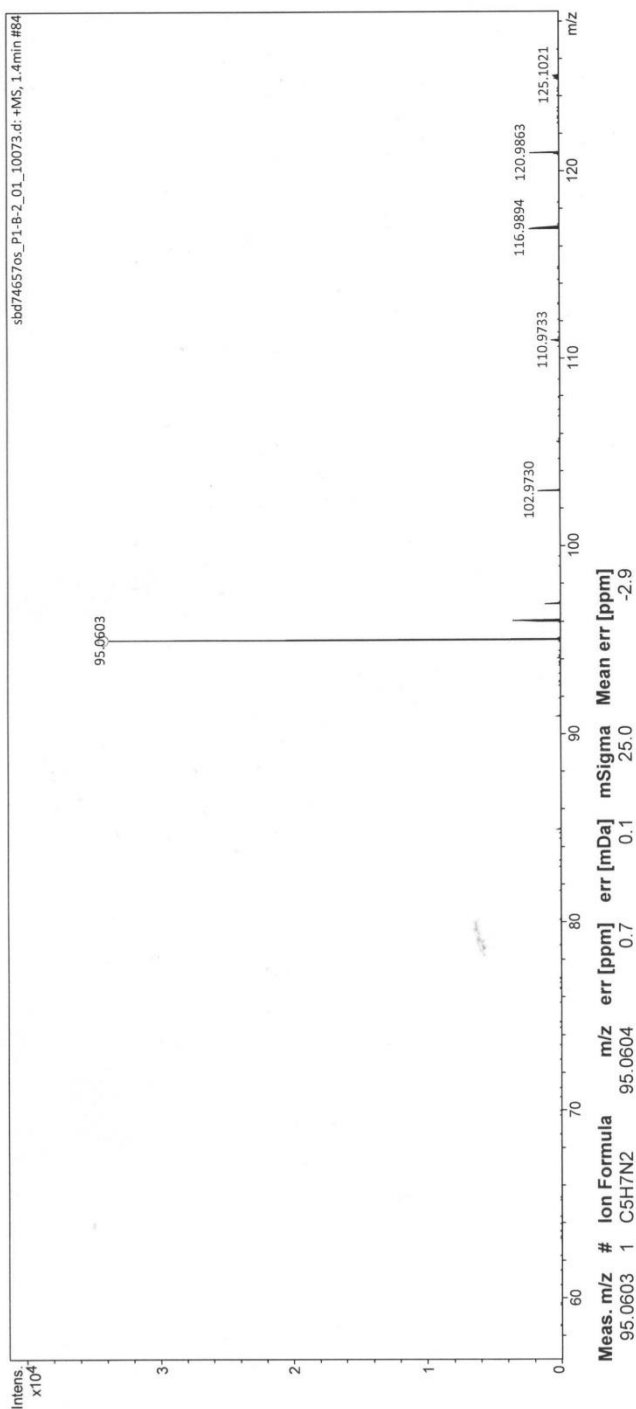


Figure A9.11 MS-ESI spectrum for pure solution of **4-AP** in methanol-*d*₄.

York - Chemistry - Mass Spectrometry Service Report

op577/18/01/19-4a
p

Analysis Information

Analysis Filename: sbd74568os_P1-B-3_01_10074.d
 Method: ESI_lowmass_2c1s.m
 Submission Name: sbd74568os
 Acquisition Date: 21/01/2019 13:33:17
 Instrument: compact
 Positive

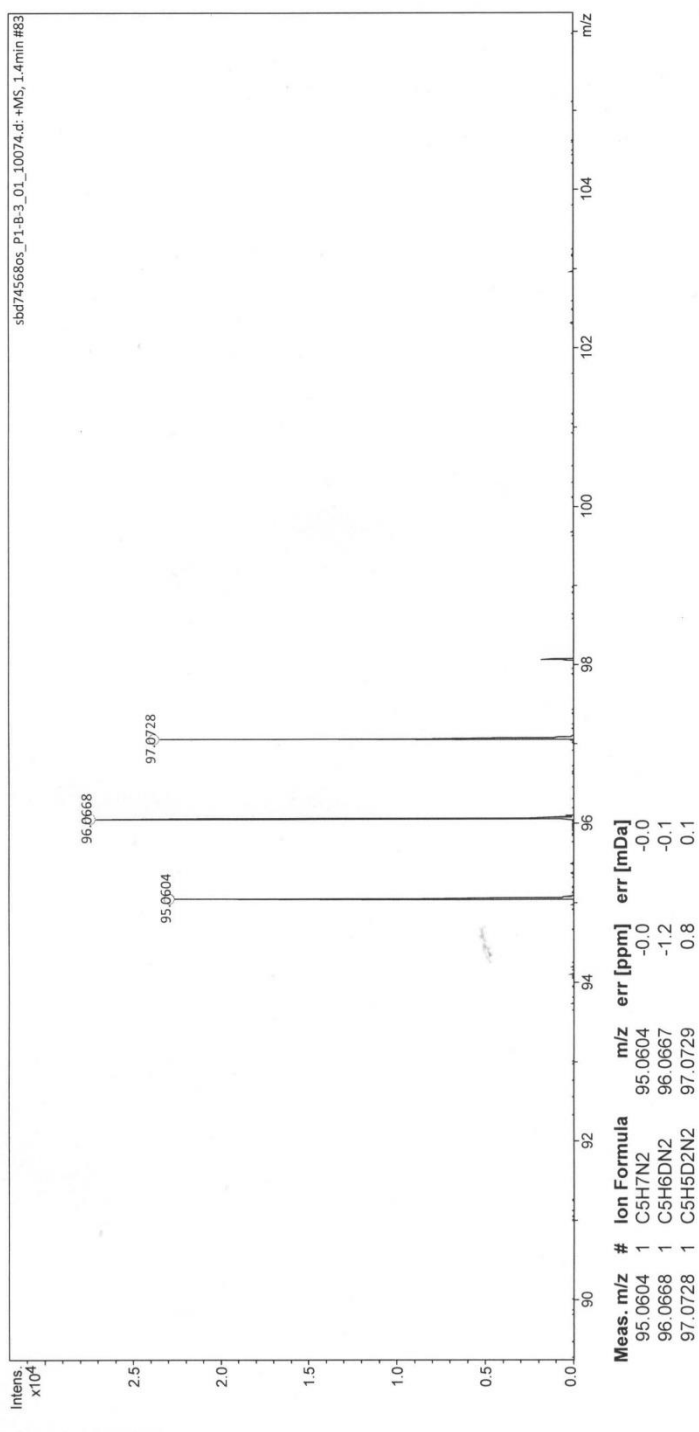


Figure A9.12 MS-EI spectrum of **4-AP** when its *ortho* position is deuterated to the level of ~60% (by ^1H NMR spectroscopy) in presence of $[\text{Ir}(\text{H})_2(\text{IMes})(\mathbf{4-AP})_3]\text{Cl}$ in methanol- d_4 under hydrogen gas.

Table A6 J -couplings and linebroadening parameters used in the analysis of **4-AP**.

J -coupling	Simulated value
${}^3J(\text{Hortho}, \text{Hmeta}) / \text{Hz}$	5.83
${}^5J(\text{Hortho}, \text{Hmeta}) / \text{Hz}$	0.63
${}^4J(\text{Hortho}, \text{Hortho}) / \text{Hz}$	2.39
${}^4J(\text{Hmeta}, \text{Hmeta}) / \text{Hz}$	0.33
Broadening parameter for SPINACH	Simulated value
<i>ortho</i>	0.008
<i>meta</i>	0.0105
<i>total</i>	0.00925

Table A7 J -couplings and linebroadening parameters used in the analysis of pyridine.

J -coupling	Simulated value
${}^3J(\text{Hortho}, \text{Hmeta}) / \text{Hz}$	5.03
${}^3J(\text{Hpara}, \text{Hmeta}) / \text{Hz}$	7.69
${}^5J(\text{Hortho}, \text{Hmeta}) / \text{Hz}$	0.87
${}^4J(\text{Hortho}, \text{Hortho}) / \text{Hz}$	1.43
${}^4J(\text{Hmeta}, \text{Hmeta}) / \text{Hz}$	0.01
${}^4J(\text{Hortho}, \text{Hpara}) / \text{Hz}$	1.79
Broadening parameter for SPINACH	Simulated value
<i>ortho</i>	0.009
<i>meta</i>	0.0125
<i>para</i>	0.0125
<i>total</i>	0.009

Table A8 J -couplings and linebroadening parameters used in the analysis of **4-PBA**.

J -coupling	Simulated value
${}^3J(\text{Hortho}, \text{Hmeta}) / \text{Hz}$	5.83
${}^5J(\text{Hortho}, \text{Hmeta}) / \text{Hz}$	0.63
${}^4J(\text{Hortho}, \text{Hortho}) / \text{Hz}$	2.39
${}^4J(\text{Hmeta}, \text{Hmeta}) / \text{Hz}$	0.33
Broadening parameter for SPINACH	Simulated value
<i>total</i>	0.009

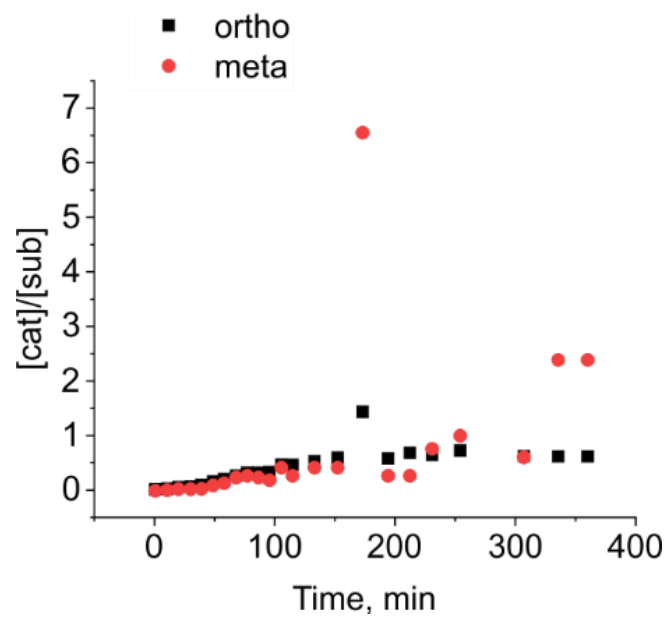


Figure A9.13 The activated catalyst to substrate ratio dependence on reaction time according to the hyper T_1 data recorded at 1 T benchtop NMR spectrometer in *protio*-methanol in conjunction with Equation 7.11 in Chapter 7 for the *ortho* and *meta* sites.

References

1. US Department of Health and Human Services Food and Drug Administration, *Guidance for Industry PAT — A Framework for Innovative Pharmaceutical Development, Manufacturing, and Quality Assurance*, 2004.
2. L. L. Simon, H. Pataki, G. Marosi, F. Meemken, K. Hungerbühler, A. Baiker, S. Tummala, B. Glennon, M. Kuentz, G. Steele, H. J. M. Kramer, J. W. Rydzak, Z. Chen, J. Morris, F. Kjell, R. Singh, R. Gani, K. V. Gernaey, M. Louhi-Kultanen, J. O'Reilly, N. Sandler, O. Antikainen, J. Yliruusi, P. Froberg, J. Ulrich, R. D. Braatz, T. Leyssens, M. von Stosch, R. Oliveira, R. B. H. Tan, H. Wu, M. Khan, D. O'Grady, A. Pandey, R. Westra, E. Delle-Case, D. Pape, D. Angelosante, Y. Maret, O. Steiger, M. Lenner, K. Abbou-Oucherif, Z. K. Nagy, J. D. Litster, V. K. Kamaraju and M.-S. Chiu, *Org. Process Res. Dev.*, 2015, **19**, 3-62.
3. J. Wiss, *Chemistry Today*, 2015, **33**, 30-33.
4. D. Landgrebe, C. Haake, T. Höpfner, S. Beutel, B. Hitzmann, T. Scheper, M. Rhiel and K. F. Reardon, *Appl. Microbiol. Biotechnol.*, 2010, **88**, 11-22.
5. R. Foley, S. Hennessy and I. W. Marison, *Appl. Spectrosc.*, 2012, **66**, 33-39.
6. P. Roychoudhury, R. O'Kennedy, B. McNeil and L. M. Harvey, *Anal. Chim. Acta*, 2007, **590**, 110-117.
7. N. Petersen, P. Ödman, A. E. C. Padrell, S. Stocks, A. E. Lantz and K. V. Gernaey, *Biotechnol. Prog.*, 2010, **26**, 263-271.
8. C. Schaefer, D. Clicq, C. Lecomte, A. Merschaert, E. Norrant and F. Fotiadu, *Talanta*, 2014, **120**, 114-125.
9. R. J. Wells, J. M. Hook, T. S. Al-Deen and D. B. Hibbert, *J. Agric. Food Chem.*, 2002, **50**, 3366-3374.
10. A. Nordon, C. A. McGill and D. Littlejohn, *Analyst*, 2001, **126**, 260-272.
11. U. Holzgrabe, R. Deubner, C. Schollmayer and B. Waibel, *J. Pharm. Biomed. Anal.*, 2005, **38**, 806-812.
12. K. M. Appleby, R. E. Mewis, A. M. Olaru, G. G. R. Green, I. J. S. Fairlamb and S. B. Duckett, *Chem. Sci.*, 2015, **6**, 3981-3993.
13. D. A. Foley, C. W. Doecke, J. Y. Buser, J. M. Merritt, L. Murphy, M. Kissane, S. G. Collins, A. R. Maguire and A. Kaerner, *J. Org. Chem.*, 2011, **76**, 9630-9640.
14. D. A. Foley, J. Wang, B. Maranzano, M. T. Zell, B. L. Marquez, Y. Xiang and G. L. Reid, *Anal. Chem.*, 2013, **85**, 8928-8932.
15. D. A. Foley, M. T. Zeil, B. L. Marquez and A. Kaerner, *Pharm. Technol.*, 2011, **November 2011**, 19-21.
16. F. Dalitz, M. Cudaj, M. Maiwald and G. Guthausen, *Prog. Nucl. Magn. Reson. Spectrosc.*, 2012, **60**, 52-70.
17. K. Singh and B. Blümich, *Trends Anal. Chem.*, 2016, **83**, 12-26.
18. A. Nordon, C. A. McGill and D. Littlejohn, *Appl. Spectrosc.*, 2002, **56**, 75-82.

19. H. Metz and K. Mäder, *Int. J. Pharm.*, 2008, **364**, 170-175.
20. S. U. Schumacher, B. Rothenhäusler, A. Willmann, J. Thun, R. Moog and M. Kuentz, *J. Pharm. Biomed. Anal.*, 2017, **137**, 96-103.
21. V. Sans, L. Porwol, V. Dragone and L. Cronin, *Chem. Sci.*, 2015, **6**, 1258-1264.
22. L. Porwol, A. Henson, P. J. Kitson, D. L. Long and L. Cronin, *Inorg. Chem. Front.*, 2016, **3**, 919-923.
23. K. Singh, E. Danieli and B. Blümich, *Anal. Bioanal. Chem.*, 2017, **409**, 7223-7234.
24. B. Musio, E. Gala and S. V. Ley, *ACS Sustainable Chem. Eng.*, 2018, **6**, 1489-1495.
25. M. Foroozandeh, R. W. Adams, N. J. Meharry, D. Jeannerat, M. Nilsson and G. A. Morris, *Angew. Chem., Int. Ed.*, 2014, **53**, 6990-6992.
26. J. M. Fonville, S. E. Richards, R. H. Barton, C. L. Boulange, T. M. D. Ebbels, J. K. Nicholson, E. Holmes and M.-E. Dumas, *J. Chemom.*, 2010, **24**, 636-649.
27. M. E. Halse, *Trends Anal. Chem.*, 2016, **83**, 76-83.
28. J. H. Ardenkjaer-Larsen, S. Boebinger Gregory, A. Comment, S. Duckett, S. Edison Arthur, F. Engelke, C. Griesinger, G. Griffin Robert, C. Hilty, H. Maeda, G. Parigi, T. Prisner, E. Ravera, J. van Bentum, S. Vega, A. Webb, C. Luchinat, H. Schwalbe and L. Frydman, *Angew. Chem., Int. Ed.*, 2015, **54**, 9162-9185.
29. J. H. Ardenkjaer-Larsen, *J. Magn. Reson.*, 2016, **264**, 3-12.
30. P. Berthault, G. Huber and H. Desvaux, *Prog. Nucl. Magn. Reson. Spectrosc.*, 2009, **55**, 35-60.
31. T. G. Walker and W. Happer, *Rev. Mod. Phys.*, 1997, **69**, 629-642.
32. S. B. Duckett and R. E. Mewis, *Acc. Chem. Res.*, 2012, **45**, 1247-1257.
33. J. Hovener, N. Pravdivtsev Andrey, B. Kidd, C. R. Bowers, S. Glöggler, V. Kovtunov Kirill, M. Plaumann, R. Katz-Brull, K. Buckenmaier, A. Jerschow, F. Reineri, T. Theis, V. Shchepin Roman, S. Wagner, M. M. Zacharias Niki, P. Bhattacharya and Y. Chekmenev Eduard, *Angew. Chem., Int. Ed.*, 2018, **0**.
34. S. S. Tee, V. DiGialleonardo, R. Eskandari, S. Jeong, K. L. Granlund, V. Miloushev, A. J. Poot, S. Truong, J. A. Alvarez, H. N. Aldeborgh and K. R. Keshari, *Sci. Rep.*, 2016, **6**, 32846.
35. M. L. Hirsch, N. Kalechofsky, A. Belzer, M. Rosay and J. G. Kempf, *J. Am. Chem. Soc.*, 2015, **137**, 8428-8434.
36. S. B. Duckett and C. J. Sleigh, *Prog. Nucl. Magn. Reson. Spectrosc.*, 1999, **34**, 71-92.
37. J. Natterer and J. Bargon, *Prog. Nucl. Magn. Reson. Spectrosc.*, 1997, **31**, 293-315.
38. D. Gołowicz, K. Kazimierczuk, M. Urbańczyk and T. Ratajczyk, *ChemistryOpen*, 2019, **8**, 196-200.
39. R. W. Adams, J. A. Aguilar, K. D. Atkinson, M. J. Cowley, P. I. P. Elliott, S. B. Duckett, G. G. R. Green, I. G. Khazal, J. López-Serrano and D. C. Williamson, *Science*, 2009, **323**, 1708.
40. P. J. Rayner, P. Norcott, K. M. Appleby, W. Iali, R. O. John, S. J. Hart, A. C. Whitwood and S. B. Duckett, *Nat. Commun.*, 2018, **9**, 4251.

41. J. F. P. Colell, M. Emondts, A. W. J. Logan, K. Shen, J. Bae, R. V. Shchepin, G. X. Ortiz, P. Spannring, Q. Wang, S. J. Malcolmson, E. Y. Chekmenev, M. C. Feiters, F. P. J. T. Rutjes, B. Blümich, T. Theis and W. S. Warren, *J. Am. Chem. Soc.*, 2017, **139**, 7761-7767.
42. P. M. Richardson, A. J. Parrott, O. Semenova, A. Nordon, S. B. Duckett and M. E. Halse, *Analyst*, 2018, **143**, 3442-3450.
43. P. M. Richardson, S. Jackson, A. J. Parrott, A. Nordon, S. B. Duckett and M. E. Halse, *Magn. Reson. Chem.*, 2017, **56**, 641-650.
44. S. Lehmkuhl, M. Wiese, L. Schubert, M. Held, M. Küppers, M. Wessling and B. Blümich, *J. Magn. Reson.*, 2018, **291**, 8-13.
45. N. Eshuis, N. Hermkens, B. J. A. van Weerdenburg, M. C. Feiters, F. P. J. T. Rutjes, S. S. Wijmenga and M. Tessari, *J. Am. Chem. Soc.*, 2014, **136**, 2695-2698.
46. D. A. Barskiy, A. N. Pravdivtsev, K. L. Ivanov, K. V. Kovtunov and I. V. Koptuyug, *Phys. Chem. Chem. Phys.*, 2016, **18**, 89-93.
47. P. M. Richardson, R. O. John, A. J. Parrott, P. J. Rayner, W. Iali, A. Nordon, M. E. Halse and S. B. Duckett, *Phys. Chem. Chem. Phys.*, 2018, **20**, 26362-26371.
48. N. Eshuis, R. L. E. G. Aspers, B. J. A. van Weerdenburg, M. C. Feiters, F. P. J. T. Rutjes, S. S. Wijmenga and M. Tessari, *Angew. Chem. Int. Ed.*, 2015, **54**, 14527-14530.
49. P. J. Hore, *Nuclear Magnetic Resonance*, Oxford University Press, Oxford, 2011.
50. J. Keeler, in *Understanding NMR spectroscopy*, ed. J. Keeler, Wiley, Chichester, 2nd edn., 2010, ch. 3, pp. 23-46.
51. M. Edgar, *Annu. Rep. Prog. Chem. Sect. B: Org. Chem.*, 2013, **109**, 256-274.
52. J. Keeler, in *Understanding NMR spectroscopy*, ed. J. Keeler, Wiley, Chichester, 2nd edn., 2010, ch. 4, pp. 47-75.
53. J. Keeler, in *Understanding NMR spectroscopy*, ed. J. Keeler, Wiley, Chichester, 2nd edn., 2010, ch. 12, pp. 441-482.
54. B. Blümich, *Trends Anal. Chem.*, 2016, **83**, 2-11.
55. J. W. Leachman, R. T. Jacobsen, S. G. Penoncello and E. W. Lemmon, *J. Phys. Chem. Ref. Data*, 2009, **38**, 721-748.
56. R. A. Green, R. W. Adams, S. B. Duckett, R. E. Mewis, D. C. Williamson and G. G. R. Green, *Prog. Nucl. Magn. Reson. Spectrosc.*, 2012, **67**, 1-48.
57. B. A. Tom, S. Bhasker, Y. Miyamoto, T. Momose and B. J. McCall, *Rev. Sci. Instrum.*, 2009, **80**, 016108.
58. S. T. Massie and D. M. Hunten, *Icarus*, 1982, **49**, 213-226.
59. J. Leachman, M. J. Street and T. Graham, *AIP Conf. Proc.*, 2012, **1434**, 1261-1267.
60. G. E. Schmauch and A. H. Singleton, *Ind. Eng. Chem. Res.*, 1964, **56**, 20-31.
61. I. F. Silvera, *Rev. Mod. Phys.*, 1980, **52**, 393-452.
62. S. B. Duckett and N. J. Wood, *Coord. Chem. Rev.*, 2008, **252**, 2278-2291.
63. P. H. Emmett and R. W. Harkness, *J. Am. Chem. Soc.*, 1932, **54**, 403-404.

64. C. R. Bowers and D. P. Weitekamp, *J. Am. Chem. Soc.*, 1987, **109**, 5541-5542.
65. C. R. Bowers and D. P. Weitekamp, *Phys. Rev. Lett.*, 1986, **57**, 2645-2648.
66. T. C. Eisenschmid, R. U. Kirss, P. P. Deutsch, S. I. Hommeltoft, R. Eisenberg, J. Bargon, R. G. Lawler and A. L. Balch, *J. Am. Chem. Soc.*, 1987, **109**, 8089-8091.
67. M. G. Pravica and D. P. Weitekamp, *Chem. Phys. Lett.*, 1988, **145**, 255-258.
68. A. Koch and J. Bargon, *Inorg. Chem.*, 2001, **40**, 533-539.
69. L. T. Kuhn, U. Bommerich and J. Bargon, *J. Phys. Chem. A*, 2006, **110**, 3521-3526.
70. J. P. Dunne, S. Aiken, S. B. Duckett, D. Konya, K. Q. Almeida Leñero and E. Drent, *J. Am. Chem. Soc.*, 2004, **126**, 16708-16709.
71. A. Permin and R. Eisenberg, *Inorg. Chem.*, 2002, **41**, 2451-2458.
72. E. Vinogradov and A. K. Grant, *J. Magn. Reson.*, 2008, **194**, 46-57.
73. T. Ratajczyk, T. Gutmann, S. Dillenberger, S. Abdulhussaein, J. Frydel, H. Breitzke, U. Bommerich, T. Trantzschele, J. Bernarding, P. C. M. M. Magusin and G. Buntkowsky, *Solid State Nucl. Magn. Reson.*, 2012, **43-44**, 14-21.
74. R. E. Mewis, K. D. Atkinson, M. J. Cowley, S. B. Duckett, G. G. R. Green, R. A. Green, L. A. R. Highton, D. Kilgour, L. S. Lloyd, J. A. B. Lohman and D. C. Williamson, *Magn. Reson. Chem.*, 2014, **52**, 358-369.
75. I. Prina, L. Buljubasich and R. H. Acosta, *J. Magn. Reson.*, 2015, **251**, 1-7.
76. R. W. Adams, S. B. Duckett, R. A. Green, D. C. Williamson and G. G. R. Green, *J. Chem. Phys.*, 2009, **131**, 194505.
77. K. L. Ivanov, A. N. Pravdivtsev, A. V. Yurkovskaya, H.-M. Vieth and R. Kaptein, *Prog. Nucl. Magn. Reson. Spectrosc.*, 2014, **81**, 1-36.
78. N. Eshuis, R. L. E. G. Aspers, B. J. A. van Weerdenburg, M. C. Feiters, F. P. J. T. Rutjes, S. S. Wijmenga and M. Tessari, *J. Magn. Reson.*, 2016, **265**, 59-66.
79. T. Theis, M. L. Truong, A. M. Coffey, R. V. Shchepin, K. W. Waddell, F. Shi, B. M. Goodson, W. S. Warren and E. Y. Chekmenev, *J. Am. Chem. Soc.*, 2015, **137**, 1404-1407.
80. H. Zeng, J. Xu, J. Gillen, M. T. McMahon, D. Artemov, J.-M. Tyburn, J. A. B. Lohman, R. E. Mewis, K. D. Atkinson, G. G. R. Green, S. B. Duckett and P. C. M. van Zijl, *J. Magn. Reson.*, 2013, **237**, 73-78.
81. D. A. Barskiy, R. V. Shchepin, A. M. Coffey, T. Theis, W. S. Warren, B. M. Goodson and E. Y. Chekmenev, *J. Am. Chem. Soc.*, 2016, **138**, 8080-8083.
82. Q. Gong, A. Gordji-Nejad, B. Blümich and S. Appelt, *Anal. Chem.*, 2010, **82**, 7078-7082.
83. R. V. Shchepin, L. Jaigirdar, T. Theis, W. S. Warren, B. M. Goodson and E. Y. Chekmenev, *J. Phys. Chem. C*, 2017, **121**, 28425-28434.
84. T. Theis, P. Ganssle, G. Kervern, S. Knappe, J. Kitching, M. P. Ledbetter, D. Budker and A. Pines, *Nat. Phys.*, 2011, **7**, 571.

85. J.-B. Hövener, N. Schwaderlapp, T. Lickert, S. B. Duckett, R. E. Mewis, L. A. R. Highton, S. M. Kenny, G. G. R. Green, D. Leibfritz, J. G. Korvink, J. Hennig and D. von Elverfeldt, *Nat. Commun.*, 2013, **4**.
86. A. M. Olaru, A. Burt, P. J. Rayner, S. J. Hart, A. C. Whitwood, G. G. R. Green and S. B. Duckett, *Chem. Commun.*, 2016, **52**, 14482-14485.
87. M. J. Burns, P. J. Rayner, G. G. R. Green, L. A. R. Highton, R. E. Mewis and S. B. Duckett, *J. Phys. Chem. B*, 2015, **119**, 5020-5027.
88. K. V. Kovtunov, L. M. Kovtunova, M. E. Gemeinhardt, A. V. Bukhtiyarov, J. Gesiorski, V. I. Bukhtiyarov, E. Y. Chekmenev, I. V. Koptuyug and B. M. Goodson, *Angew. Chem., Int. Ed.*, 2017, **56**, 10433-10437.
89. A. M. Olaru, T. B. R. Robertson, J. S. Lewis, A. Antony, W. Iali, R. E. Mewis and S. B. Duckett, *ChemistryOpen*, 2018, **7**, 97-105.
90. P. J. Rayner, M. J. Burns, A. M. Olaru, P. Norcott, M. Fekete, G. G. R. Green, L. A. R. Highton, R. E. Mewis and S. B. Duckett, *Proc. Natl. Acad. Sci. U. S. A.*, 2017, **114**, E3188-E3194.
91. R. H. Crabtree and M. W. Davis, *J. Org. Chem.*, 1986, **51**, 2655-2661.
92. K. D. Atkinson, M. J. Cowley, P. I. P. Elliott, S. B. Duckett, G. G. R. Green, J. López-Serrano and A. C. Whitwood, *J. Am. Chem. Soc.*, 2009, **131**, 13362-13368.
93. Atkins P. W., Overton T. L. and W. M. T. Rourke J. P., Armstrong F. A., in *Shriver & Atkins' inorganic Chemistry*, ed. A. P. W., Oxford University Press, New York, USA, 5th edn., 2010, ch. 22, pp. 551-552.
94. A. R. Chianese, A. Kovacevic, B. M. Zeglis, J. W. Faller and R. H. Crabtree, *Organometallics*, 2004, **23**, 2461-2468.
95. M. J. Cowley, R. W. Adams, K. D. Atkinson, M. C. R. Cockett, S. B. Duckett, G. G. R. Green, J. A. B. Lohman, R. Kerssebaum, D. Kilgour and R. E. Mewis, *J. Am. Chem. Soc.*, 2011, **133**, 6134-6137.
96. B. J. A. van Weerdenburg, S. Glogglar, N. Eshuis, A. H. J. Engwerda, J. M. M. Smits, R. de Gelder, S. Appelt, S. S. Wymenga, M. Tessari, M. C. Feiters, B. Blumich and F. P. J. T. Rutjes, *Chem. Commun.*, 2013, **49**, 7388-7390.
97. C. A. Tolman, *Chem. Rev.*, 1977, **77**, 313-348.
98. L. Cavallo, A. Correa, C. Costabile and H. Jacobsen, *J. Organomet. Chem.*, 2005, **690**, 5407-5413.
99. M. Fekete, O. W. Bayfield, O. Bayfield, S. B. Duckett, S. Hart, R. E. Mewis, N. Pridmore, P. J. Rayner and A. Whitwood, *Inorg. Chem.*, 2013, **52**, 13453-13461.
100. H. Zeng, J. Xu, M. T. McMahon, J. A. B. Lohman and P. C. M. van Zijl, *J. Magn. Reson.*, 2014, **246**, 119-121.
101. P. Spannring, I. Reile, M. Emondts, P. P. M. Schleker, N. K. J. Hermkens, N. G. J. v. d. Zwaluw, B. J. A. v. Weerdenburg, P. Tinnemans, M. Tessari, B. Blümich, F. P. J. T. Rutjes and M. C. Feiters, *Chem. Eur. J.*, 2016, **22**, 9277-9282.
102. F. Shi, P. He, Q. A. Best, K. Groome, M. L. Truong, A. M. Coffey, G. Zimay, R. V. Shchepin, K. W. Waddell, E. Y. Chekmenev and B. M. Goodson, *J. Phys. Chem. C*, 2016, **120**, 12149-12156.
103. A. J. Ruddlesden, R. E. Mewis, G. G. R. Green, A. C. Whitwood and S. B. Duckett, *Organometallics*, 2015, **34**, 2997-3006.

104. D. J. Heal, S. L. Smith, J. Gosden and D. J. Nutt, *J. Psychopharmacol.*, 2013, **27**, 479-496.
105. M. El Mansari, B. P. Guiard, O. Chernoloz, R. Ghanbari, N. Katz and P. Blier, *CNS Neurosci Ther.*, 2010, **16**, e1-e17.
106. A. Björklund and S. B. Dunnett, *Trends Neurosci.*, 2007, **30**, 185-187.
107. H. M. Pinheiro, E. Touraud and O. Thomas, *Dyes Pigm.*, 2004, **61**, 121-139.
108. M. P. K. Pereira L., Alves M., *Aromatic Amines Sources, Environmental Impact and Remediation*, Springer, Cham, 2015.
109. Y. O. Mezhuev, Y. V. Korshak and M. I. Shtilman, *Russ. Chem. Rev.*, 2017, **86**, 1271-1285.
110. J. S. Thomson, J. B. Green, T. B. McWilliams and S. K. T. Yu, *J. High Resolut. Chromatogr.*, 1994, **17**, 415-426.
111. L. S. Jackson, *J. Agric. Food Chem.*, 2009, **57**, 8161-8170.
112. A. R. Blight, *Ther. Adv. Neurol. Disord.*, 2011, **4**, 99-109.
113. C. Taglang, D. E. Korenchan, C. von Morze, J. Yu, C. Najac, S. Wang, J. E. Blecha, S. Subramaniam, R. Bok, H. F. VanBrocklin, D. B. Vigneron, S. M. Ronen, R. Sriram, J. Kurhanewicz, D. M. Wilson and R. R. Flavell, *Chem. Commun.*, 2018, **54**, 5233-5236.
114. F. A. Gallagher, M. I. Kettunen, S. E. Day, D.-e. Hu, M. Karlsson, A. Gisselsson, M. H. Lerche and K. M. Brindle, *Magn. Reson. Med.*, 2011, **66**, 18-23.
115. E. Cerutti, A. Viale, C. Nervi, R. Gobetto and S. Aime, *J. Phys. Chem. A*, 2015, **119**, 11271-11279.
116. S. Glogglar, R. Muller, J. Colell, M. Emondts, M. Dabrowski, B. Blumich and S. Appelt, *Phys. Chem. Chem. Phys.*, 2011, **13**, 13759-13764.
117. A. W. J. Logan, T. Theis, J. F. P. Colell, W. S. Warren and S. J. Malcolmson, *Chem. Eur. J.*, 2016, **22**, 10777-10781.
118. W. Iali, P. J. Rayner and S. B. Duckett, *Sci. Adv.*, 2018, **4**, eaao6250.
119. W. Iali, P. J. Rayner, A. Alshehri, A. J. Holmes, A. J. Ruddlesden and S. B. Duckett, *Chem. Sci.*, 2018, **9**, 3677-3684.
120. S. S. Roy, P. Norcott, P. J. Rayner, G. G. R. Green and S. B. Duckett, *Chemistry*, 2017, **23**, 10496-10500.
121. L. S. Lloyd, A. Asghar, M. J. Burns, A. Charlton, S. Coombes, M. J. Cowley, G. J. Dear, S. B. Duckett, G. R. Genov, G. G. R. Green, L. A. R. Highton, A. J. J. Hooper, M. Khan, I. G. Khazal, R. J. Lewis, R. E. Mewis, A. D. Roberts and A. J. Ruddlesden, *Catal. Sci. Technol.*, 2014, **4**, 3544-3554.
122. A. M. Oлару, M. J. Burns, G. G. R. Green and S. B. Duckett, *Chem. Sci.*, 2017, **8**, 2257-2266.
123. V. Daniele, F.-X. Legrand, P. Berthault, J.-N. Dumez and G. Huber, *ChemPhysChem*, 2015, **16**, 3413-3417.
124. N. Eshuis, B. J. A. v. Weerdenburg, M. C. Feiters, F. P. J. T. Rutjes, S. S. Wijmenga and M. Tessari, *Angew. Chem., Int. Ed.*, 2015, **54**, 1481-1484.
125. E. B. Dücker, L. T. Kuhn, K. Münnemann and C. Griesinger, *J. Magn. Reson.*, 2012, **214**, 159-165.

126. M. E. Merritt, C. Harrison, C. Storey, F. M. Jeffrey, A. D. Sherry and C. R. Malloy, *Proc. Natl. Acad. Sci.*, 2007, **104**, 19773.
127. D. M. Wilson, R. E. Hurd, K. Keshari, M. Van Criekeing, A. P. Chen, S. J. Nelson, D. B. Vigneron and J. Kurhanewicz, *Proc. Natl. Acad. Sci.*, 2009, **106**, 5503.
128. M. H. Lerche, S. Meier, P. R. Jensen, S.-O. Hustvedt, M. Karlsson, J. Ø. Duus and J. H. Ardenkjær-Larsen, *NMR Biomed.*, 2011, **24**, 96-103.
129. J. Bae, Z. Zhou, T. Theis, W. S. Warren and Q. Wang, *Sci. Adv.*, 2018, **4**, eaar2978.
130. J. Clayden, N. Greeves, S. Warren and P. Wothers, in *Organic Chemistry*, Oxford University Press, New York, USA, 2nd edn., 2012, ch. 12, pp. 280-289.
131. M. B. Djordjevic and R. S. Porter, 1983, **23**, 650-657.
132. D. S. Wishart, C. G. Bigam, J. Yao, F. Abildgaard, H. J. Dyson, E. Oldfield, J. L. Markley and B. D. J. J. o. B. N. Sykes, 1995, **6**, 135-140.
133. J. W. Akitt, in *NMR and chemistry: an introduction to modern NMR spectroscopy*, ed. J. W. Akitt, Chapman & Hall, London, 3rd edn., 1992, ch. 6.1, pp. 135-158.
134. J. Keeler, in *Understanding NMR spectroscopy*, ed. J. Keeler, Wiley, Chichester, 2nd edn., 2010, ch. 9, pp. 241-317.
135. N. Bloembergen, E. M. Purcell and R. V. Pound, *Phys. Rev.*, 1948, **73**, 679-712.
136. V. I. Bakhmutov, John Wiley & Sons, Ltd, Chichester, West Sussex, England, 2004, ch. 5.4, p. 65.
137. J. W. Akitt, in *NMR and chemistry: an introduction to modern NMR spectroscopy*, ed. J. W. Akitt, Chapman & Hall, London, 3rd edn., 1992, ch. 3.1, pp. 41-42.
138. A. Abragam, Oxford University Press, London, UK, 1962, ch. VIII E-F, pp. 289-316.
139. J. W. Akitt, in *NMR and chemistry. An introduction to the Fourier transform -- multinuclear era*, ed. J. W. Akitt, Chapman and Hall, New York, 2nd edn., 1984, ch. 4.4, pp. 68-75.
140. N. R. Skrynnikov, S. F. Lienin, R. Brüschweiler and R. R. Ernst, *J. Chem. Phys.*, 1998, **108**, 7662-7669.
141. P.-O. Westlund, *Phys. Chem. Chem. Phys.*, 2010, **12**, 3136-3140.
142. J. W. Akitt, in *NMR and chemistry: an introduction to modern NMR spectroscopy*, ed. J. W. Akitt, Chapman & Hall, London, 3rd edn., 1992, ch. 4.6, pp. 97-98.
143. I. Hancu, W. T. Dixon, M. Woods, E. Vinogradov, A. D. Sherry and R. E. Lenkinski, *Acta Radiol.*, 2010, **51**, 910-923.
144. V. I. Bakhmutov, *Practical NMR relaxation for chemists*, John Wiley & Sons, Ltd, Chichester, West Sussex, England, 2004.
145. V. I. Bakhmutov and E. V. Vorontsov, *Rev. Inorg. Chem.*, 1998, **18**, 183.
146. J. Kim, M. Liu and C. Hilty, *J. Phys. Chem. B*, 2017, **121**, 6492-6498.
147. D. Kumar, Y. Krishnan, M. Paranjothy and S. Pal, *J. Phys. Chem. B*, 2017, **121**, 2864-2872.
148. R. E. Mewis, M. Fekete, G. G. R. Green, A. C. Whitwood and S. B. Duckett, *Chem. Commun.*, 2015, **51**, 9857-9859.

149. P. J. McDonald, J. P. Korb, J. Mitchell and L. Monteilhet, *Phys. Rev. E*, 2005, **72**, 011409.
150. D. G. Gusev, D. Nietlispach, A. B. Vymenits, V. I. Bakhmutov and H. Berke, *Inorg. Chem.*, 1993, **32**, 3270-3276.
151. R. V. Shchepin, L. Jaigirdar and E. Y. Chekmenev, *J. Phys. Chem. C*, 2018, **122**, 4984-4996.
152. R. L. Vold, J. S. Waugh, M. P. Klein and D. E. Phelps, *J. Chem. Phys.*, 1968, **48**, 3831-3832.
153. S. Braun, H.-O. Kalinowski and S. Berger, in *100 and More Basic NMR Experiments. A Practical Course*, ed. M. Bar, VCH Verlagsgesellschaft, VCH Publishers, Weinheim, Federal Republic of Germany; New York, NY, USA, 1996, ch. 6.1, pp. 125-129.
154. D. C. Look and D. R. Locker, *Rev. Sci. Instrum.*, 1970, **41**, 250-251.
155. J. L. Markley, W. J. Horsley and M. P. Klein, *J. Chem. Phys.*, 1971, **55**, 3604-3605.
156. C. L. Young, in *IUPAC Solubility Data Series, Hydrogen and Deuterium*, ed. C. L. Young, Pergamon Press, Oxford, UK, 1981, vol. 5/6, ch. 1.6, pp. 191 - 193.
157. R. E. Mewis, *Magn. Reson. Chem.*, 2015, **53**, 789-800.
158. D. A. Barskiy, K. V. Kovtunov, I. V. Koptug, P. He, K. A. Groome, Q. A. Best, F. Shi, B. M. Goodson, R. V. Shchepin, A. M. Coffey, K. W. Waddell and E. Y. Chekmenev, *J. Am. Chem. Soc.*, 2014, **136**, 3322-3325.
159. R. Kaptein, K. Dijkstra and C. E. Tarr, *J. Magn. Reson.*, 1976, **24**, 295-300.
160. I. J. Day, J. C. Mitchell, M. J. Snowden and A. L. Davis, *J. Magn. Reson.*, 2007, **187**, 216-224.
161. K. X. Moreno, K. Nasr, M. Milne, A. D. Sherry and W. J. Goux, *J. Magn. Reson.*, 2015, **257**, 15-23.
162. M. L. Truong, T. Theis, A. M. Coffey, R. V. Shchepin, K. W. Waddell, F. Shi, B. M. Goodson, W. S. Warren and E. Y. Chekmenev, *J. Phys. Chem. C*, 2015, **119**, 8786-8797.
163. J. A. Aguilar, P. I. P. Elliott, J. López-Serrano, R. W. Adams and S. B. Duckett, *Chem. Commun.*, 2007, 1183-1185.
164. S. Knecht, A. S. Kiryutin, A. V. Yurkovskaya and K. L. Ivanov, *J. Magn. Reson.*, 2018, **287**, 74-81.
165. A. B. Permin and R. Eisenberg, *J. Am. Chem. Soc.*, 2002, **124**, 12406-12407.
166. G. J. Ellames, J. S. Gibson, J. M. Herbert and A. H. McNeill, *Tetrahedron*, 2001, **57**, 9487-9497.
167. A. Di Giuseppe, R. Castarlenas and L. A. Oro, *C. R. Chim.*, 2015, **18**, 713-741.
168. R. H. Crabtree, E. M. Holt, M. Lavin and S. M. Morehouse, *Inorg. Chem.*, 1985, **24**, 1986-1992.
169. J. R. Heys, *J. Labelled Compd. Radiopharm.*, 2007, **50**, 770-778.
170. A. Y. L. Shu, W. Chen and J. R. Heys, *J. Organomet. Chem.*, 1996, **524**, 87-93.

171. J. A. Brown, A. R. Cochrane, S. Irvine, W. J. Kerr, B. Mondal, J. A. Parkinson, L. C. Paterson, M. Reid, T. Tuttle, S. Andersson and G. N. Nilsson, *Adv. Synth. Catal.*, 2014, **356**, 3551-3562.
172. W. D. Jones and F. J. Feher, *Acc. Chem. Res.*, 1989, **22**, 91-100.
173. A. S. Goldman and K. I. Goldberg, in *Activation and Functionalization of C—H Bonds*, American Chemical Society, 2004, vol. 885, ch. 1, pp. 1-43.
174. W. J. Kerr, R. J. Mudd, P. K. Owens, M. Reid, J. A. Brown and S. Campos, *J. Labelled Compd. Radiopharm.*, 2016, **59**, 601-603.
175. W. J. Kerr, M. Reid and T. Tuttle, *Angew. Chem., Int. Ed.*, 2017, **56**, 7808-7812.
176. E. Alvarez, S. Conejero, M. Paneque, A. Petronilho, M. L. Poveda, O. Serrano and E. Carmona, *J. Am. Chem. Soc.*, 2006, **128**, 13060-13061.
177. Y. A. Hernández, J. López-Serrano, M. Paneque, M. L. Poveda, F. Vattier, V. Salazar, E. Álvarez and E. Carmona, *Chem. Eur. J.*, 2011, **17**, 9302-9305.
178. M. A. Esteruelas, F. J. Fernández-Alvarez and E. Oñate, *Organometallics*, 2007, **26**, 5239-5245.
179. D. G. Johnson, J. M. Lynam, N. S. Mistry, J. M. Slattery, R. J. Thatcher and A. C. Whitwood, *J. Am. Chem. Soc.*, 2013, **135**, 2222-2234.
180. D.-H. Lee, J. Chen, J. W. Faller and R. H. Crabtree, *Chem. Commun.*, 2001, 213-214.
181. B. Eguillor, M. A. Esteruelas, J. García-Raboso, M. Oliván and E. Oñate, *Organometallics*, 2009, **28**, 3700-3709.
182. D. H. Nguyen, J. J. Perez-Torrente, M. V. Jimenez, F. J. Modrego, D. Gomez-Bautista, F. J. Lahoz and L. A. Oro, *Organometallics*, 2013, **32**, 6918-6930.
183. S. R. Klei, J. T. Golden, P. Burger and R. G. Bergman, *J. Mol. Catal. A-Chem.*, 2002, **189**, 79-94.
184. S. B. Duckett, G. K. Barlow, M. G. Partridge and B. A. Messerle, *J. Chem. Soc., Dalton Trans.*, 1995, 3427-3429.
185. I. Kuprov, N. Wagner-Rundell and P. J. Hore, *J. Magn. Reson.*, 2007, **189**, 241-250.
186. I. Kuprov, *J. Magn. Reson.*, 2011, **209**, 31-38.
187. T. Junk and W. J. Catallo, *Chem. Soc. Rev.*, 1997, **26**, 401-406.
188. E. Stander-Grobler, O. Schuster, G. Heydenrych, S. Cronje, E. Tosh, M. Albrecht, G. Frenking and H. G. Raubenheimer, *Organometallics*, 2010, **29**, 5821-5833.
189. S. K. Hasnip, S. A. Colebrooke, C. J. Sleight, S. B. Duckett, D. R. Taylor, G. K. Barlow and M. J. Taylor, *J. Chem. Soc., Dalton Trans.*, 2002, 743-751.
190. O. Semenova, P. M. Richardson, A. J. Parrott, A. Nordon, M. E. Halse and S. B. Duckett, *Anal. Chem.*, 2019, **91**, 6695-6701.
191. K. Golman, J. H. Ardenkjær-Larsen, J. S. Petersson, S. Månsson and I. Leunbach, *Proc. Natl. Acad. Sci.*, 2003, **100**, 10435.
192. D. Fairhurst, T. Cosgrove and S. W. Prescott, *Magn. Reson. Chem.*, 2016, **54**, 521-526.
193. D. M. Grant, C. L. Mayne, F. Liu and T. X. Xiang, *Chem. Rev.*, 1991, **91**, 1591-1624.

194. M. J. Stirling, J. M. Mwansa, G. Sweeney, A. J. Blacker and M. I. Page, *Org. Biomol. Chem.*, 2016, **14**, 7092-7098.
195. M. Ciaccia and S. Di Stefano, *Org. Biomol. Chem.*, 2015, **13**, 646-654.
196. J. Farias de Lima, A. K. Nakano and N. Y. Murakami Iha, *Inorg. Chem.*, 1999, **38**, 403-405.
197. C. Bartocci, F. Scandola, A. Ferri and V. Carassiti, *J. Am. Chem. Soc.*, 1980, **102**, 7067-7072.
198. O. Torres, M. Martín and E. Sola, *Organometallics*, 2009, **28**, 863-870.
199. H. Kessler, H. Oschkinat, C. Griesinger and W. Bermel, *J. Magn. Reson.*, 1986, **70**, 106-133.
200. J. Stonehouse, P. Adell, J. Keeler and A. J. Shaka, *J. Am. Chem. Soc.*, 1994, **116**, 6037-6038.
201. K. Stott, J. Stonehouse, J. Keeler, T.-L. Hwang and A. J. Shaka, *J. Am. Chem. Soc.*, 1995, **117**, 4199-4200.
202. T. D. W. Claridge, in *High-Resolution NMR Techniques in Organic Chemistry*, Elsevier Science & Technology, Amsterdam, Netherlands, 3rd edn., 2016, ch. 9.6.2, pp. 346-347.
203. K. M. Appleby, PhD thesis, University of York, 2016.